Project No. 14-6863

Advanced Models for Nondestructive Evaluation of Aging Nuclear Power Plant Cables

Reactor Concepts Research Development and Demonstration (RCRDD)

Nicola Bowler
Iowa State University

Collaborators
Washington State University

Alison Hahn, Federal POC
Jeremy Busby, Technical POC

NEUP Nuclear Energy University Programs
U.S. Department of Energy

Advanced Models for Nondestructive Evaluation of Aging Nuclear Power Plant Cables

October 1, 2014 – December 31, 2017

Final report
Submitted July 14, 2018

Nicola Bowler,[1,3] Chien-Ping Chiou,[2,3] Shuaishuai Liu,[1] Chamila De Silva,[1] Zhihui Shao,[1] Ying-Bin Guo,[2,3] Adam Gjersvik,[2,3] and Michael I. Byler[1,2]
[1]Department of Materials Science and Engineering
[2]Department of Aerospace Engineering
[3]Center for Nondestructive Evaluation
Iowa State University
Ames, Iowa 50011

Scott P. Beckman, Bo Z. Xu, and Irmak Sargin
School of Mechanical and Materials Engineering
Washington State University
Pullman, Washington 99164

Leonard S. Fifield, Mark K. Murphy, Andy J. Zwoster, Qian Huang, and M. Ian Childers
Energy and Environment Directorate
Pacific Northwest National Laboratory
Richland, Washington 99354

DOE Award Number: DE-NE0008269
Recipient: Iowa State University
Principal investigator: Dr. Nicola Bowler, Professor
E-mail: nbowler@iastate.edu
Tel.: 515-294-3202

Executive Summary

Background: Nuclear power plant (NPP) cables must function correctly for proper power supply and control of the nuclear reactor. This is especially important for public and environmental safety at critical times such as during reactor shut-down following loss of coolant. Over extended periods of service, the cable insulation and jacket polymer materials suffer from degradation due to exposure to environmental stressors such as heat and ionizing radiation. The focus of this project has been the development of detailed descriptions of the way in which insulation polymers degrade, from a materials science perspective, and the development of new electrical techniques to monitor cable polymer condition nondestructively.

Objectives: The objectives of this project have been to i) perform detailed characterization experiments upon cable insulation polymers that have experienced thermal and radiation exposure mimicking that received during NPP operation, including the exploration of novel cable nondestructive evaluation methods; capacitive, THz and infrared methods; ii) identify the most sensitive indicators of aging in these materials, and iii) develop advanced, validated models describing microstructural and chemical changes that are observed in cable insulation polymers due to thermal and radiation exposure.

Methods: Accelerated aging was performed on the two most common United States NPP cable insulation polymers (cross-linked polyethylene (XLPE) and ethylene propylene rubber (EPR)) under various conditions of elevated temperature and gamma radiation dose. Aging mechanisms were elucidated through extensive thermal, mechanical and microscopic characterization of the aged samples, and materials modeling. Dielectric and IR spectra were measured on pristine and aged samples. Data was analyzed statistically, via multiple linear regression, partial least squares and probabilistic neural network approaches.

Impact: Extant cable monitoring techniques do not deal successfully with all polymer types. This research has laid a foundation upon which new electrical nondestructive test methods for cable polymer condition monitoring may be developed, hence launching the development of new test methods for cable insulation monitoring based on measuring electrical rather than mechanical parameters.

Collaboration: This project has benefitted from collaboration between experts in materials science and engineering, materials modeling, electrical engineering, and nondestructive evaluation. The majority of the characterization measurements were carried out at Iowa State University. Materials modeling was carried out primarily at Washington State University. Irradiation of samples took place at Pacific Northwest National Laboratory (PNNL), where a student intern from Iowa State was hosted for one summer, setting up the aging experiments. A research student from the University of Bologna, Italy, joined the project for their thesis research at Iowa State University with samples provided by PNNL. The project benefitted from regular involvement of senior engineers in US-based industry partners. Project investigators presented findings at various national and international conferences and workshops.

Table of Contents

Abbreviations and acronyms

ATR	Attenuated total reflection
CSPE	Chlorosulfonated polyethylene
DBDE	Decabromodiphenyl ether
DFT	Density functional theory
DSC	Differential scanning calorimetry
EAB	Elongation at break
EDS	Energy dispersive x-ray spectroscopy
EPR	Ethylene-propylene rubber
FTIR	Fourier transform infrared spectroscopy
GCMS	Gas chromatography – mass spectrometry
HEF	High exposure facility
IM	Indenter modulus
LAMMPS	Large-scale Atomic/Molecular Massively Parallel Simulator
MS	Mass spectrometry
NVT	Number, volume, and temperature
OIT	Oxidation induction time
PCA	Principal component analysis
PCs	Principal components
PE	Polyethylene
PVC	Polyvinyl chloride
Py	Pycnometry
PLS	Partial least squares
PNN	Probabilistic neural network
SEM	Scanning electron microscopy
TGA	Thermogravimetric analysis
THz	Terahertz
XLPE	Cross-linked polyethylene

Activities Summary

Tasks and Schedule

Tasks and schedule, proposed and actual, for this project are listed in Table 1. Several tasks continued for a few months beyond their original schedule. The reason for this is that the sample-preparation tasks 1.2 and 3.1 took three months longer than originally scheduled, and the characterization tasks depended on samples being available. A three-month no-cost extension was granted on the project, leading to the project concluding on December 31, 2017 with tasks complete and on budget.

Table 1. Logical path to work accomplishment and schedule. ♦ indicates originally proposed schedule. + indicates tasks that continued into subsequent quarters.

	Year 1		**Year 2**		**Year 3**		**Y4**
	1/2	2/2	1/2	2/2	1/2	2/2	1/4
Task 1: Develop models relating polymer changes to spectral changes							
1.1: Conduct detailed literature survey of aging response of EPR & XLPE to heat, neutron/gamma irradiation, and water immersion	♦						
1.2: Design and conduct accelerated aging of EPR & XLPE samples (to complement published data identified in Task 1.1)		♦	♦	+			
1.3: Thermal and mechanical characterization of aged samples		♦	♦	♦	+		
1.4: Dielectric, THz and infrared characterization of aged samples			♦	♦	+	+	+
1.5: Develop models of spectral changes due to aging				♦	♦	+	
1.6: Develop and validate models relating microstructural and chemical changes in aged polymers to observed spectral changes		♦	♦	♦	♦	+	
Task 2: Identify spectral range(s) showing most sensitivity to polymer degradation							
2: Identify spectral indicators of degradation		♦	♦	♦	♦	+	
Task 3: Develop models relating NDE signals to cable polymers state							
3.1: Conduct accelerated aging of EPR & XLPE-based cables (simultaneously with Task 1.2)		♦	♦	♦	♦	+	
3.2: Measure broadband capacitance on cables aged in Task 3.1 with interdigital patch or clamp capacitors applied to cable jacket				♦	♦	+	+
3.3: Measure THz signals on cables aged in Task 3.1				♦	♦	+	
3.4: Model THz signals					♦	+	+
3.5: Validate models on aged cables						♦	+

Task Reports

1.1 Literature survey of cable polymer aging response

Aging mechanisms of two polymeric insulation materials that are used widely in nuclear power plant low-voltage cables; cross-linked polyethylene (XLPE) and ethylene propylene rubber/ethylene propylene diene terpolymer (EPR/EPDM), were reviewed. The task was completed two months early and the review was published in the International Journal of Prognostics and Health Management, available freely online at: http://www.phmsociety.org/references/ijphm-archives/2015/Sp3.

The article abstract is reproduced here for convenience.

Article Abstract

Aging mechanisms of two polymeric insulation materials that are used widely in nuclear power plant low-voltage cables; cross-linked polyethylene (XLPE) and ethylene propylene rubber/ethylene propylene diene terpolymer (EPR/EPDM), are reviewed. A summary of various nondestructive methods suitable for evaluation of cable insulation is given. A capacitive sensor capable of making local nondestructive measurements of capacitance and dissipation factor on cable polymers, and potentially suitable for *in situ* cable monitoring, is introduced. Correlating values of elongation-at-break, indenter modulus, capacitance and dissipation factor measured on a set of 47 aged flame-resistant EPR samples shows a higher correlation between indenter modulus and dissipation factor than between indenter modulus and elongation-at-break.

1.2 Accelerated Aging of Samples

Samples were aged thermally without and with gamma ray exposure at the High Exposure Facility, Pacific Northwest National Laboratory. Due to the high demand of this specialized facility for this and other projects, this task was completed in June 2016, three months later than originally scheduled.

Hypotheses

- The ability to independently control gamma dose rate and temperature during simultaneous exposure can help to identify and understand degradation behavior phenomena such as synergistic effects and 'inverse temperature' effects in nuclear cable relevant materials;
- A large number of aging conditions achieved in one aging experiment can help to reveal the effects of dose rate and total dose on associated material property changes.

Polymer components of nuclear power plant cables are known to experience material degradation as a result of exposure to heat and to gamma radiation, but the combined effects of the two sources of stress are not well understood.

The 'inverse temperature' effect describes a phenomenon whereby a material aged at a lower temperature experiences more severe aging than one aged at a higher temperature. This effect is due to differences in degradation mechanisms below and above phase transitions (e.g. melting point) of the material.

Approach

Firewall® III multi-conductor shielded instrumentation cable (Product Code I46-0021) was purchased from RSCC Wire Cable LLC and studied in this work, Figure 1 and

Table 2. Cross-linked polyethylene (XLPE) insulation specimens were extracted from this low voltage (600 V) multi-conductor cable prior to exposure, both with conductor intact and with conductor removed. Further XLPE samples with the same formulation as that found in the previously-mentioned control cable, but with the flat tape geometry needed for some of our analyses, were kindly provided by RSCC for the use of this project. Pure polyethylene (PE) in the form of Poly Hi Solidur Low Density Polyethylene was also studied.

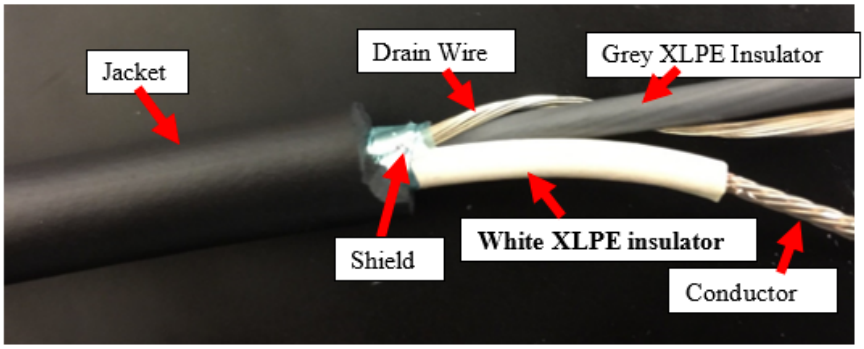

Figure 1. RSCC 2/C cable (product code I46-0021).

Table 2. Dimensional information for RSCC 2/C cable studied here.

Product Code	Number of conductors	Insulation thickness (mm)	Insulated conductor diameter (mm)	Jacket thickness (mm)	Nominal overall diameter (mm)
I46-0021	2	0.64	2.79	1.14	7.87

The high exposure facility (HEF) in the 318 Building at PNNL comprises a 15.2 m x 3.7 m x 3.7 m room with a connecting control room/entry way. The capability has historically been used for laboratory instrument calibrations, dosimeter irradiations, and radiation biology research. A carousel under the floor of the HEF houses seven, NIST-traceable radiation sources: Five Cs-137 sources and two Co-60 sources with activities from 0.42 mCi to 5,000 Ci. A selected source is pneumatically raised from carousel below the floor up to the aperture of a steel column, Figure 2, during exposure. When raised to the exposure position, a collimated beam emerges with a 30° collimator angle, centered 1.5 m above the floor, Figure 3. At the time of this project, photon exposure rates ranging from 30 nGy/h to 1,200 Gy/h were accessible based on sample position in the room relative to the source. Laser positioning tools provide for precise alignment and calculation of sample positions. A video display in the control room provides monitoring capability for instrumentation during irradiation and calibration. Dose rates and attenuation due to oven walls and samples etc., are measured using an ion gauge.

Figure 2. View of backside of irradiator column in the High Exposure Facility at Pacific Northwest National Laboratory.

Figure 3. Oven ready for positioning against the irradiator collimator opening.

Gamma irradiation of cable materials—Control of dose rate

The same Co-60 source (2.64 Gy/h at 100 cm as of 9/1/15) was used for all irradiation experiments for this project in fiscal year 2016. The activity of the source decays by approximately 1.1 % per month. The highest dose rate achievable with this source for samples placed within the column opening, 18.5 cm from the source, was ~1,200 Gy/h. A rack within the oven provided a range of dose rates available corresponding to each row of the rack, from the highest dose rate closest to the source of 540 Gy/h at row 1 to the lowest dose rate at the 24th row of 120 Gy/h, Figure 5. A second, similar rack positioned behind the oven from the source provided dose rates between 10 and 100 Gy/h. A summary of the temperatures, dose rates and total doses of samples aged within the oven nearest to the Co-60 source is provided in Table 3. Exposure conditions for PE samples in particular are provided in Table 4.

Table 3. Summary of the range of aging conditions applied to samples aged within the oven closest to the Co-60 source.

Temperatures	60 °C, 90 °C, 115 °C
Exposure Times	0 - 25 days
Gamma Dose Rates	0, 120 - 540 Gy/hr
Total Doses	0, 10- 324 kGy

Table 4. Aging conditions applied to PE samples.

Sample ID	Aging T (°C)	Aging duration (d)	Dose rate (Gy/h)	Dose (kGy)
E0	Ambient	n/a	0	0
E1	25	20	90	43.2
E2	25	20	80	38.4
E3	25	20	70	33.6
E4	25	20	60	28.8
E5	~ 40	20	1,200	576
E6	~ 40	20	880	422

Thermal exposure of cable materials

Due to heating from the Co-60 source, the temperature within the column aperture is approximately 40 °C. The underground HEF room maintains a stable temperature of 25 °C. For exposure of samples to higher, controlled temperatures ovens are used. It is thought to be important to maintain flowing air around samples during exposure to encourage uniform heating of samples and to ensure that oxygen that may contribute to aging mechanisms is not limited in the vicinity of the samples. A circulating air, 800-Watt, mechanical convection oven (Model 10AF, Quincy Lab, Inc., Chicago, IL) is used to control the aging temperature of the material. These ovens were found to withstand the ultra-high doses involved over the experiment duration. Each oven was retrofit to independently control the air circulating fan and the heating element. The bimetal thermostat controls were replaced with Red Lion Model T48 temperature control modules (Red Lion Controls, York, PA) in order to improve the temperature stability to approximately ± 1°C. Long thermocouple cables were utilized to remove the control electronics from the gamma beam and thus significantly extend useful lifetime. In addition to the set point thermocouple, two addition thermocouples were placed in the oven to achieve temperature monitoring at three different locations (front, center and back) of the oven. Over the multi-day irradiations all thermocouple readings were recorded every minute utilizing the VersaLog Model VL-TC data logger and software (Accsense Inc., Chesterland, OH) and a common laptop computer.

Control of Total Dose

The HEF is available for use intermittently. Total dose experienced by samples exposed at various dose rates is controlled by planned placement and removal of samples in the course of the exposure experiment. The series of crosslinked polyethylene (XLPE) sample exposures at a given oven setting was performed in five rounds of five-day exposures, resulting in the lowest total exposure time of five days (120 h) and the highest total exposure time of 25 days (600 h). The key assumption used in the experimental plan is that significant material aging occurs only during exposure and that exposure times are additive. With this assumption, five rounds of five-day exposure is equivalent to one round of 25 days exposure.

Simultaneous Thermal and Gamma Radiation Aging

An illustration of the setup by which heat and gamma radiation can be applied simultaneously to the studied materials is given in Figure 3. The oven is placed in the gamma beam and used to host the samples and control their aging temperature during irradiation. The distance from the center of the Co-60 source to the first row of samples on the rack in the oven is 26.5 cm. The first rack row is 2.0 cm from the inner oven wall.

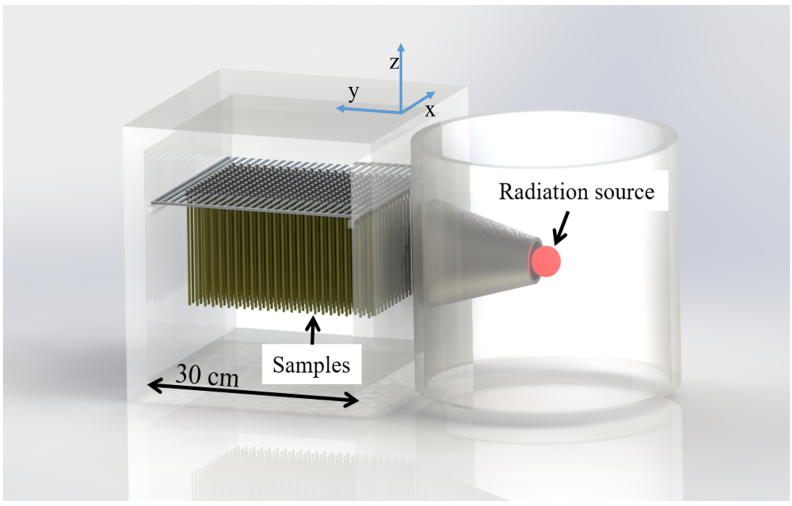

Figure 4. Three-dimensional model of the gamma-irradiation aging setup.

Figure 5. Low voltage cross-linked polyethylene (XLPE) insulated cable (lower left). XLPE insulation samples in oven rack (above). Example XLPE sample set (right). Image analysis of tensile performance (lower center).

Significant results

Samples

Three temperatures were selected for simultaneous aging experiments for this project: 60, 90, and 115 °C. The series of five rounds of five-day exposures at 115 °C were completed in FY15 during the first year of the project. In the second year of the project, FY16, the 60 and 90 °C series were completed. Twenty-six distinct distances from the Co-60 source, corresponding to distinct gamma dose rates, were employed at each temperature. Sample sets of between seven and eight samples each were exposed at selected locations for times from 120 to 600 hours. In this way, more than 500 individually labeled and tracked cross-linked polyethylene (XLPE) samples were used in each of the 60 and 90 °C series in FY16. An additional 80 ethylene-

propylene rubber (EPR) samples were included in the 90 °C series and 80 each of EPR and polyethylene (PE) samples included in the 60 °C series. Sample masses were recorded before and after exposure.

Eighty different aging conditions were achieved in each round of the experiment, in which all samples were aged at the same temperature but exposed to different dose rates and different total doses of gamma radiation.

As illustrated in Table 5, samples among the eighty distinct exposure conditions can be grouped in order to study the effect of either dose rate or total dose. For the purpose of studying the total dose effect, samples aged at the same temperature and same dose rate for different durations can be selected, as indicated by gray shading in Table 5. For the purpose of studying the dose rate effect, samples aged at the same temperature and exposed to the same total doses can be selected, as highlighted in bold font in Table 5. Superscripts a, b, c, d indicate samples grouped by similar total dose. Such comparisons can be made also at the different aging temperatures selected, to study the effect of temperature on sample aging.

Uncertainty Analysis

Radiation intensity falls off with the inverse of the square of the distance from the radiation source. The distance of each sample to the radiation source is slightly different, even for samples on the same row in the oven, due to the radial nature of the gamma beam emitted from the Co-60 source. Furthermore, over the 10 cm length of any one sample, there is some variation in radiation intensity along its length. The uncertainty in the dose rate at each sample and the total dose received by each sample caused by this factor and other factors is analyzed as follows.

The dose rates at multiple locations within each oven were measured using a small volume ionization chamber (Exradin Model A12). These dose rate measurements were performed in empty ovens as well in ovens fully loaded with samples (multiple rack rows and multiple points along rows), and the dose rate values were provided in terms of dose to air (air-kerma in Gy/h). Using this measured data, the dose rate at which the center of each sample is exposed was inferred by curve fitting to the measured dose rates. Along each sample, the dose rate distribution D_z was calculated by employing the distance to the radiation source and the dose rate at its center point. If D_z is the dose rate distribution along a particular sample, then the average dose rate A to that sample is calculated by evaluating the integral equation (1), where L represents the sample length.

Dose rate distribution within the oven is displayed in Figure 6. It can be seen that at each row, the dose rate is higher in the center and lower at the edge of the rack. At each row, the average dose rate in the center is D_m, and that at the edge is D_e. R is defined as the difference ratio between D_m and D_e, equation (2).

$$A = \frac{1}{L}\int_{-L/2}^{L/2} D(z)dz \qquad (1)$$

$$R = \frac{D_e - D_m}{D_m} \qquad (2)$$

Table 5. Eighty different gamma radiation aging conditions are achieved by one round of aging experiment.

Row in oven	Dose Rate (Gy/h)	5 days	10 days	15 days	20 days	25 days
		Total Dose (kGy)				
1	504-533	--	121-128	181-192	--	302-320
2	459-484	55-58	--	--	221-233	276-291
3	424-445	**51-53**[a]	**102-107**[b]	**153-160**[c]	**203-214**[d]	--
4	388-406	47-49	--	140-146	--	233-244
5	361-377	43-45	87-90	130-136	173-181	--
6	334-347	40-42	--	--	**160-167**[c]	**200-208**[d]
7	306-318	37-38	73-76	110-114	147-152	184-191
8	288-298	35-36	--	**104-107**[b]	--	173-179
9	269-278	32-33	--	--	129-133	**162-167**[c]
10	251-258	30-31	60-62	90-93	120-124	--
11	232-239	28-29	--	83-86	--	139-143
12	223-229	27	**53-55**[a]	80-82	**107-110**[b]	--
13	204-209	--	49-50	73-75	--	122-125
14	194-199	23-24	--	--	93-96	117-119
15	185-189	--	44-45	67-68	--	111-113
16	175-179	21-22	--	63-65	--	**105-108**[b]
17	166-169	20	--	--	--	--
18	156-159	19	--	--	--	--
19	147-149	18	35-36	53-54	70-72	--
20	137-139	16-17	33	**49-50**[a]	66-67	--
21	127-130	15-16	--	--	61-62	76-78
22	127-130	--	31	46-47	--	76-78
23	118-120	14	--	42-43	--	71-72
24	118-120	14	28-29	42-43	**57**[a]	--

Take the first and 24th row as examples. For the first row, D_m = 533 Gy/h, D_e = 504 Gy/h, R = 5.4. For the 24th row, D_m = 120 Gy/h, D_e = 118 Gy/h, R = 1.7. Figure 10 shows the difference ratio R value for all 24 rows. A smaller difference ratio R indicates a more even dose rate distribution in a row. It can be seen from Figure 6 and Figure 7 that the dose rate difference decreases with increasing row number, that is, with increasing distance from the radiation source.

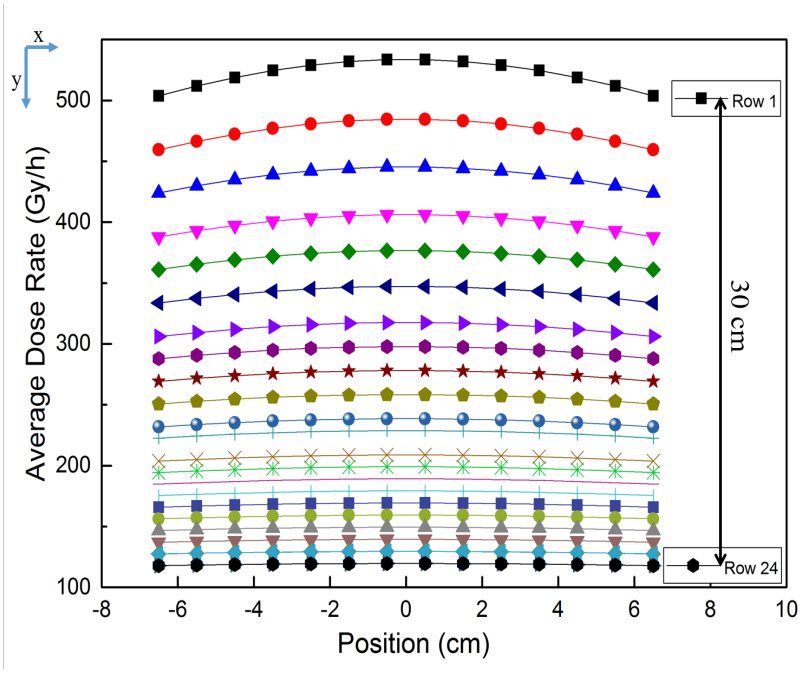

Figure 6. Average dose rate distribution in the oven as a function of position. Rows 1 and 24 are separated by 30 cm.

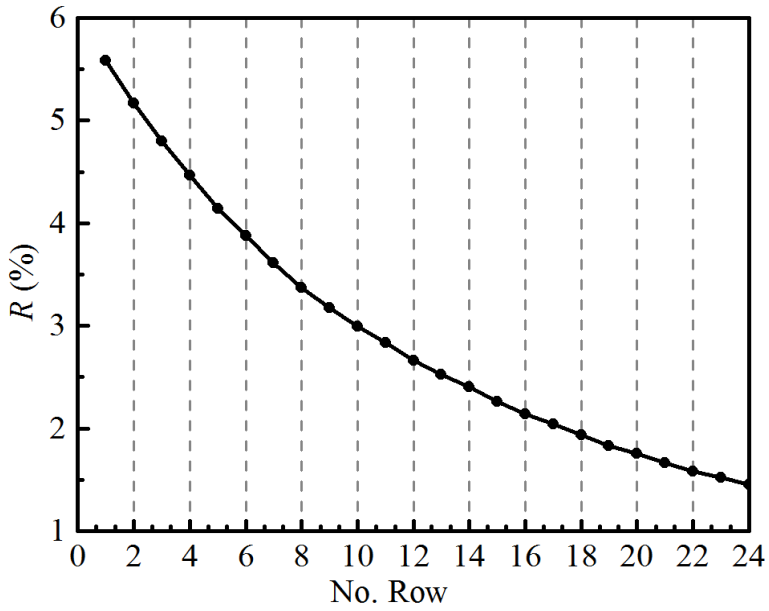

Figure 7. Difference ratio (R) between center average dose rate D_m and edge average dose rate D_e for each row. Rows 1 and 24 are separated by 30 cm.

Summary

An experimental set-up was designed that achieved a large number of aging conditions of polymeric insulation material in one aging experiment, with controlled temperature, gamma dose rate and total dose.

Key Conclusions

- A variety of sample aging conditions, in which samples were aged by thermal and gamma radiation simultaneously, were achieved by actively maintaining sample temperature, adjusting sample position relative to the radiation source and by varying the exposure time.
- Cables in NPP containment buildings are expected to be exposed to gamma radiation up to hundreds of kGy within 40 years of service. Cables in the designed accelerated aging experiment in this work have a radiation dose range from 14 to 320 kGy.

1.3 Thermal, mechanical, and chemical characterization of aged samples

Thermal, mechanical, and chemical characterization of aged samples was due to be completed at the end of Year 2 (September 30, 2016) but took longer due to samples becoming available later than originally scheduled. Some characterization experiments focused on elucidating the composition of the filled commercial XLPE. Collection of thermal, mechanical, and chemical characterization data on the aged samples was completed by February 28, 2017.

Hypotheses

- Thermal, mechanical, and chemical characterization of aged samples will provide data from which thermo-irradiative aging mechanisms in the sample material can be deduced.
- Thermal, mechanical, and chemical characterization of aged samples will reveal the most sensitive indicators of thermo-irradiative aging in the samples.

Approach

Alongside the primary purpose of the materials characterization tasks as originally conceived – to measure the effects on material properties of simultaneous thermo-irradiative aging on PE and XLPE polymer insulation – another purpose emerged during this study: the necessity of knowing as precisely as possible the composition of the starting material (commercially-formulated XLPE insulation that contains fillers for various purposes including anti-oxidants and flame retardant). Thus, alongside the characterization of aged samples we also report characterization of pristine sample material.

Materials composition of the filled XLPE has been identified using SEM-EDS, FTIR and GC-MS on pristine material. A variety of materials characterization methods including TGA, DSC, elemental analysis, OIT, FTIR, gel-content, TGA-DSC-MS, and GC-MS were conducted on pristine and aged sample materials to study the aging mechanisms.

Complete results of this task are available in the PhD thesis by Shuaishuai Liu, "Composition identification, aging mechanisms and nondestructive aging indicator of commercial filled cross-linked polyethylene (XLPE) cable insulation materials," PhD thesis, Dept. Mater. Sci. Engng., Iowa State Univ., Ames, IA, 2017. Online at:
https://lib.dr.iastate.edu/cgi/viewcontent.cgi?article=7172&context=etd

The thesis abstract is reproduced here for convenience, followed by selected results from the thesis and other relevant results not included in the thesis.

Thesis Abstract

This work studies the chemical composition, physical make-up, and aging mechanisms of thermally-exposed and gamma-irradiated, commercial, cross-linked, polyethylene (XLPE) cable insulation material used in Nuclear Power Plants (NPPs), using various analytical characterization techniques. Understanding of cable aging behaviors is important for cable safety inspection, which is required as both routine inspection and in safety inspection in the process of extending the operating license of NPPs. The fillers and additives in the XLPE cable insulation materials were identified and quantified using scanning electron microscopy, energy dispersive X-ray spectroscopy, carbon-hydrogen elemental weight ratio tests, thermogravimetric analysis, and pyrolysis gas chromatography-mass spectroscopy. Laboratory-based accelerated aging experiments were designed and conducted for aging electrical cables, achieving 240 different

aging conditions including thermal-only aging and simultaneous thermal and gamma radiation aging. Aging mechanisms of the XLPE cable insulation materials were studied, including discussion of the changes in antioxidant, flame retardants, and the XLPE polymer chains as the samples age. Additional analytical techniques used for studying the aging mechanisms included gel-fraction measurements, nuclear magnetic resonance spectroscopy, differential scanning calorimetry, permittivity and dielectric loss tangent measurements, and oxidation induction time measurements. A nondestructive aging indicator was identified, that is promising for future development of a nondestructive cable aging testing method.

Significant results

Material composition of RSCC insulation XLPE

Identification of Components

Figure 8(a) is the SEM image of the fracture surface of the material. Elemental maps were collected for the same region of the material at the same time, Figure 8(b). Brighter spots in an elemental map correspond to a greater concentration of that element. It is observed that there are fillers of various sizes in the material, and the fillers are composed of elements of Zn, S, Sb, O, and Br. In order to further identify the brominated component(s) and any other components that are not visible in the EDX maps, the studied material was pyrolyzed and the pyrolyzates were analyzed in a mass spectrometer. Figure 9 shows the temperature profile of the gas evolved from the sample in the temperature range from 80 to 800 °C. It is observed that, within the studied temperature range, there were five featured signals/peaks in the signal intensity in the evolved gas analysis, indicated by the arrows in Figure 9. For convenience of reference, these are numbered as No 1, No 2, No 3, No 4 and No 5. Their corresponding mass spectrum was further analyzed for the identification of the components, Figure 10. The NIST library installed in the data analysis software was used to identify the species associated with these peaks. No 1 was identified with 1,3,5-Triazine-2,4,6(1H,3H,5H)-trione. No 2 and No 3 were identified with poly(1,2-dihydro-2,2,4-trimethylquinoline) (pTMQ). No 4 was identified with polyethylene. No 5 was identified as mixture of brominated components, being $C_{12}H_3Br_5O$, $C_{12}H_2Br_6O$, $C_{12}HBr_7O$, $C_{12}H_2Br_8O$, $C_{12}HBr_9O$ and $C_{12}Br_{10}O$, as shown in Figure 10. The evolved temperature profiles of the six brominated compounds were obtained, Figure 11. It is observed in Figure 11 that the brominated compounds can be grouped into two categories according to their evolving temperature profile. One category is shared by $C_{12}H_3Br_5O$, $C_{12}H_2Br_6O$, and $C_{12}H_2Br_8O$, and the other by $C_{12}HBr_7O$, $C_{12}HBr_9O$, and $C_{12}Br_{10}O$. The compounds in each category follow a similar evolving temperature profile which is different from that followed by compounds in the other category.

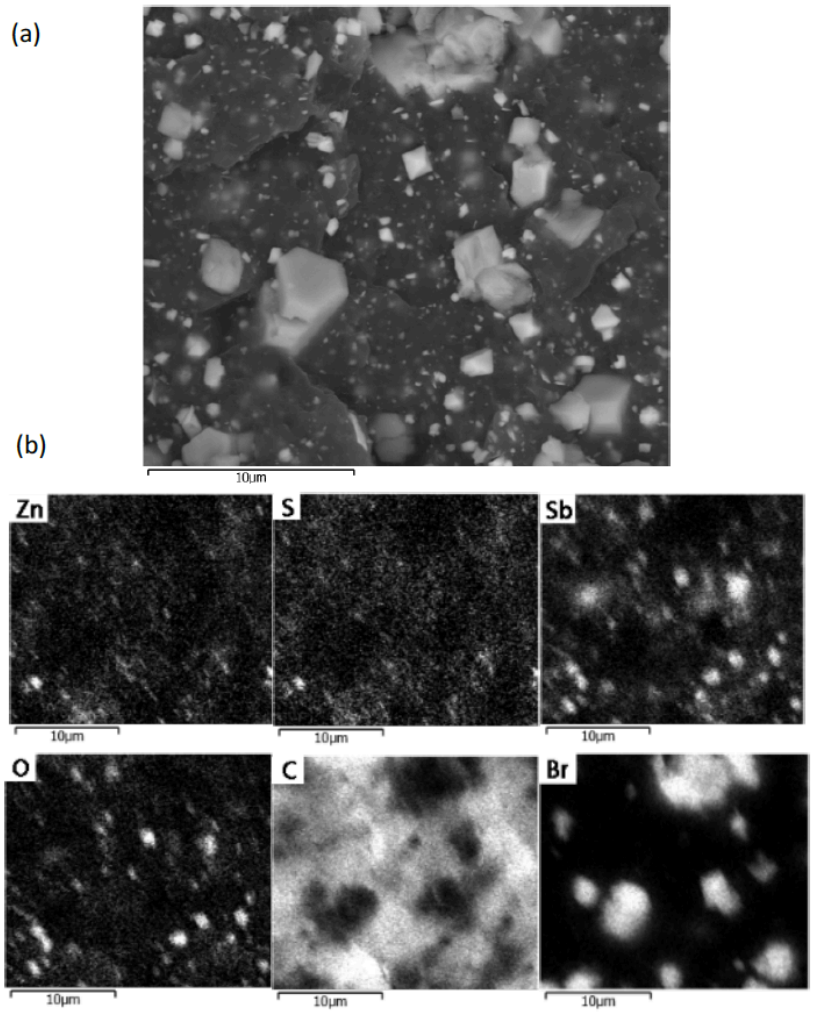

Figure 8. (a) SEM image and (b) element maps of the cross-section of pristine XLPE straw material.

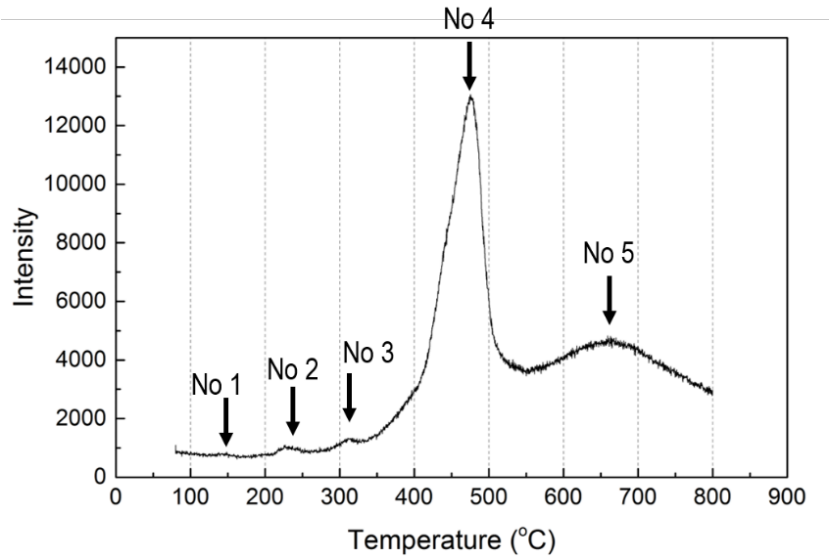

Figure 9. Evolved gas temperature profile of pristine XLPE.

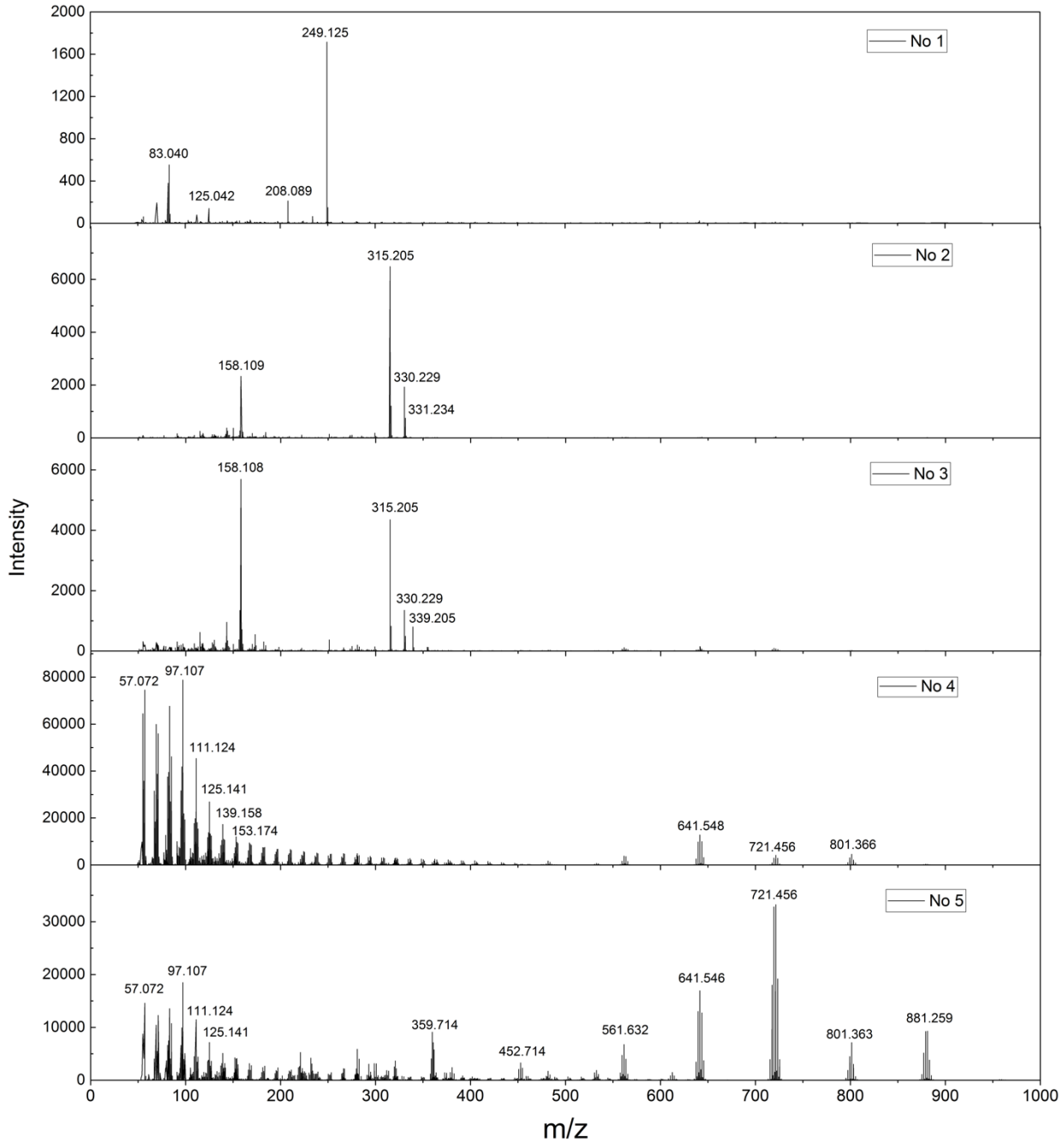

Figure 10. The mass spectra of peaks identified in Figure 9 evolved gas analysis.

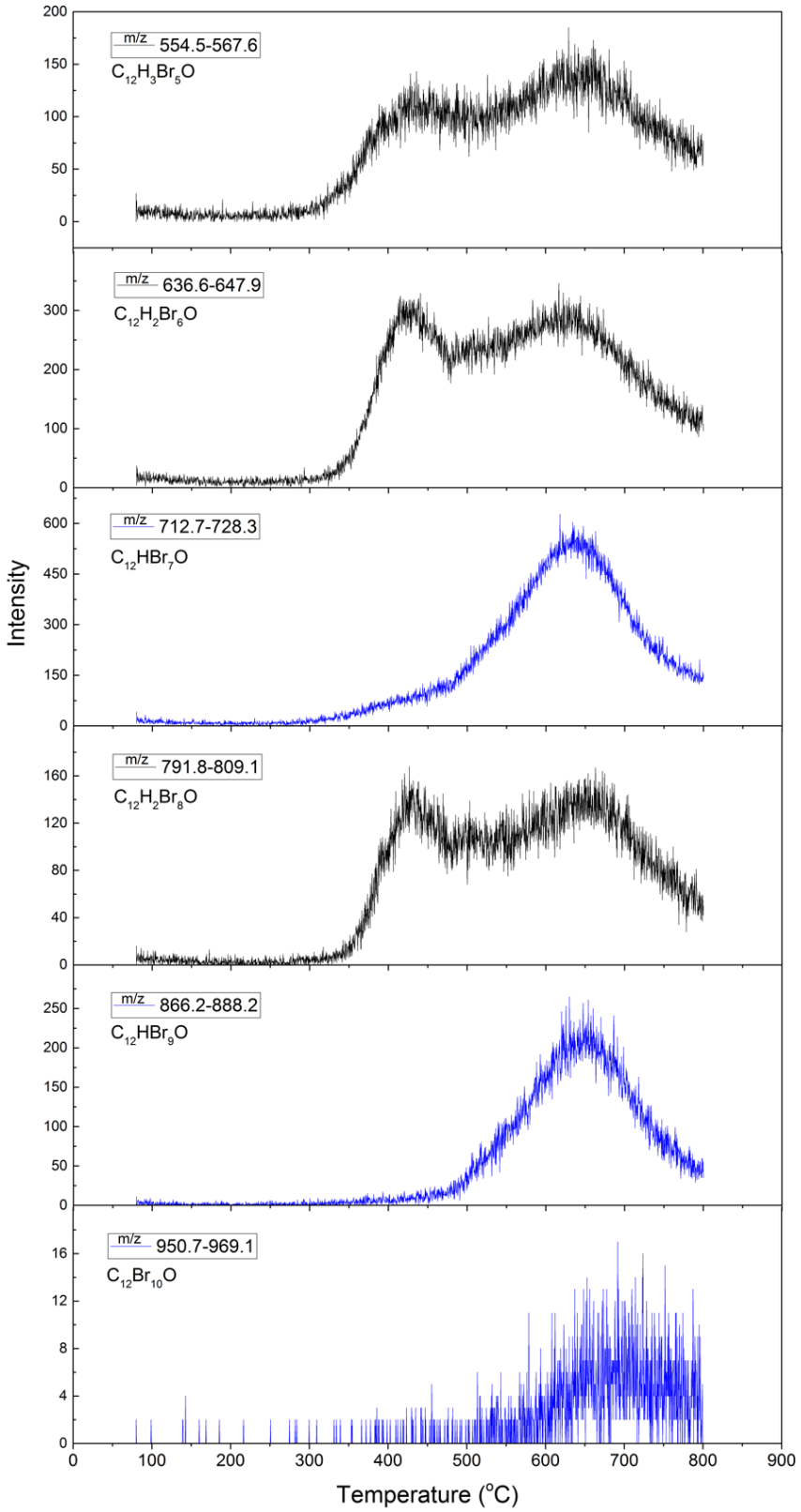

Figure 11. Evolving temperature profile of brominated compounds. The compounds fall into two categories, indicated by blue and black.

Thermogravimetric analysis was used to estimate the weight ratio of the inorganic fillers in the material. Figure 12 shows the TGA curve of the material, obtained in simulated air atmosphere. The TG curve is stable after about 600 °C with 17 % residue remaining, and the corresponding heat flow beyond this temperature reaches zero. Figure 13 shows the sum mass spectrum covering the full temperature range from 80 to 800 °C. It can be seen in Figure 13 that the signal intensity of the Octa-BDE and its decomposition products is almost equal to that of DBDE and its decomposition products, marked by black and blue arrows respectively, consistent with the color used in Figure 11. The carbon and hydrogen elemental weight ratios were measured to evaluate the percentage of XLPE polymer in the material. There was found to be 52.68 ± 0.07 % of carbon and 8.6 ± 0.1 % of hydrogen present.

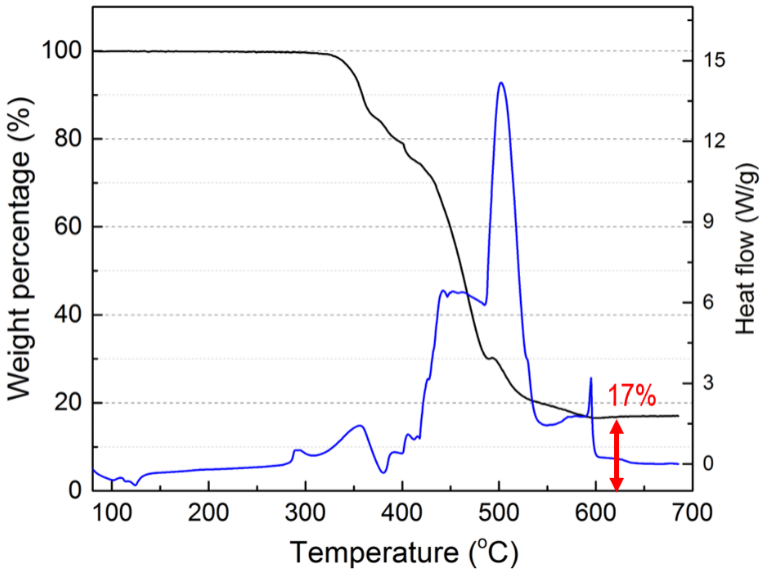

Figure 12.Thermogravimetric curve and its first derivative, measured on pristine XLPE.

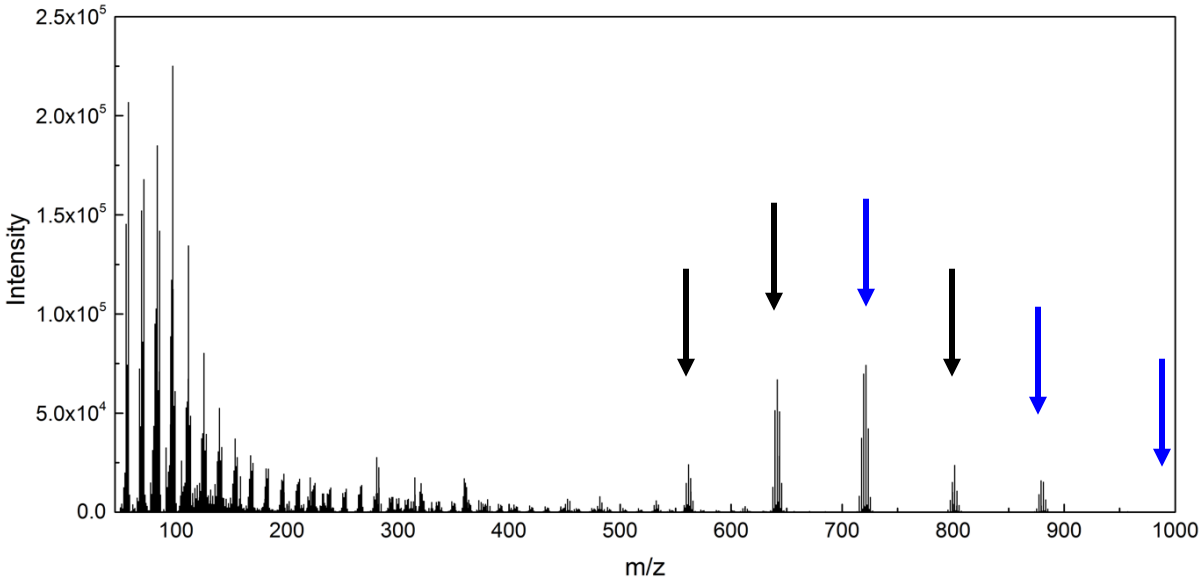

Figure 13. Sum mass spectrum of the pyrolyzates evolved in the temperature range 80 – 800 ºC. Black arrows refer to Octa-BDE and its pyrolyzates, blue arrows refer to DBDE and its pyrolyzates.

The polymer matrix of the material is XLPE. From EDX elemental analysis, Figure 8(b), it can be deduced that the fillers in the polyethylene matrix are ZnS, Sb_2O_3, and one or more brominated component(s). ZnS is often used as the white pigment in polymers [1].

It was identified by applying the pyrolysis GCMS technique that the brominated compounds suggested in Figure 8(b) are a group of brominated flame retardants. The brominated pyrolyzates detected were mainly $C_{12}H_3Br_5O$, $C_{12}H_2Br_6O$, $C_{12}H_2Br_8O$ (Octa-BDE), $C_{12}HBr_7O$, $C_{12}HBr_9O$, and $C_{12}Br_{10}O$ (DBDE). Due to the fact that the brominated flame retardants are designed to decompose when heated [2], it is very likely that not all of the above listed brominated pyrolyzates exist in the pristine material. Some of them could be molecules arising from decomposition of the original brominated compounds. Comparing the pyrolysis temperature profiles of the brominated pyrolyzates, Figure 11, $C_{12}H_3Br_5O$, $C_{12}H_2Br_6O$, and $C_{12}H_2Br_8O$ (Octa-BDE) show similar evolving temperature profiles, while $C_{12}HBr_7O$, $C_{12}HBr_9O$, and $C_{12}Br_{10}O$ (DBDE) show other similar evolving temperature profiles. It is therefore speculated that $C_{12}H_3Br_5O$ and $C_{12}H_2Br_6O$ derive from the thermal decomposition of $C_{12}H_2Br_8O$ (Octa-BDE), while $C_{12}HBr_7O$ and $C_{12}HBr_9O$ derive from the thermal decomposition of $C_{12}Br_{10}O$ (DBDE) and, further, that Octa-BDE and DBDE are the two brominated flame retardant compounds existing in the pristine material. Antimony oxide, Sb_2O_3, is often used together with brominated compounds as a flame retardant, because they show a synergistic effect when used together [3].

Small amounts of 1,3,5-Triazine-2,4,6(1H,3H,5H)-trione and pTMQ were detected by pyrolysis GCMS as shown in Figure 9 and Figure 10. 1,3,5-Triazine-2,4,6(1H,3H,5H)-trione is often used as cross-linking agent for polyethylene [2]. Poly(1,2-dihydro-2,2,4-trimethylquinoline) is used as an antioxidant for polyethylene [2, 3].

Quantification of Components

Thermogravimetric analysis, Figure 12, shows that there is 17 wt% of inorganic fillers in the material, identified as ZnS and Sb_2O_3 by EDX results. These inorganic fillers do not burn away when the material is heated up to 800 °C in air, remaining as residue following TGA testing.

It is shown in the sum mass spectrum of Figure 13 that the signal strengths due to Octa-BDE and DBDE are approximately equal. It is hence speculated that there are approximately equal amounts of Octa-BDE and DBDE in the studied material, assuming the mass spectrometry response factor of Octa-BDE and DBDE is the same. Further assuming that the polyethylene matrix takes x %, Octa-BDE takes y %, and DBDE takes y % of the weight of the material, equations (1) and (2) can be solved to obtain x and y according to the carbon weight ratio.

$$\frac{12}{13.8}x + \frac{144}{959.17}y + \frac{144}{801.38}y + \frac{144}{173.25} \times 2 = 52.68 \quad (1)$$

$$x + 2y + 17 + 2 = 100 \quad (2)$$

Equations (3) and (4) can be solved to obtain x and y according to the hydrogen weight ratio.

$$\frac{1.8}{13.8}x + \frac{2}{801.38}y + \frac{15}{173.25} \times 2 = 8.55 \quad (3)$$

$$x + 2y + 17 + 2 = 100 \quad (4)$$

From equations (1) and (2), it is calculated that $x = 53$ % and $y = 14$ %. From equations (3) and (4), it is calculated that $x = 8$ % and $y = 64$ %. The average numbers of x and y are taken as the weight percentage of XLPE and brominated compounds in the pristine material, which gives approximately 60 % of polyethylene polymer matrix and 20 % of brominated flame retardants.

The weight ratio of 1,3,5-Triazine-2,4,6(1H,3H,5H)-trione is negligible. The weight percentage of pTMQ as antioxidant is assumed to be 2 %, which is the average quantity of antioxidant used in XLPE polymers [2].

The identified components of the materials and their corresponding approximate quantities are summarized in Table 6.

Table 6. Summary of the identified components and their approximate weight percentage and function, of XLPE-based insulation material.

Component	**Approximate weight ratio (%)**	**Function**
Cross-linked polyethylene	60	Polymer matrix
Decabromodiphenyl ether ($C_{12}Br_{10}O$)	10	Flame retardants
Octabromodiphenyl ether ($C_{12}H_2Br_8O$)	10	
Sb_2O_3	17	
ZnS		White pigment
Poly(1,2-dihydro-2,2,4-trimethylquinoline)	2	Antioxidant, metal deactivator
1,3,5-Triazine-2,4,6(1H,3H,5H)-trione	trace	Cross-linking booster

Material characterization and aging mechanism of XLPE

It has been identified that the main fillers of the commercial XLPE material studied in this work are inorganic fillers ZnS and Sb_2O_3, antioxidant 1,3,5-Triazine-2,4,6(1H,3H,5H)-trione, brominated flame retardants DBDE and Octa-BDE. The problem of understanding the aging mechanisms of the material can be approached as understanding the changes of 1) inorganic fillers, 2) antioxidant, 3) brominated flame retardants, 4) XLPE polymer, and 5) the material properties as a whole piece. No changes were expected for inorganic fillers. The following sections discuss the changes of the material observed by optical spectroscopy, elemental analysis, DSC, gel content measurement, OIT measurement, Py-GCMS, and tensile testing. A detailed discussion of the change in antioxidant with aging is provided in this report by incorporating a submitted journal article manuscript, Appendix B.1 Quantitative analysis of changes in antioxidant in crosslinked polyethylene (XLPE) cable insulation material exposed to heat and gamma radiation," page 115.

Optical microscopy

Optical observation shows that the color of aged samples becomes darker yellow compared with that of pristine material, Figure 14. Research has suggested that oxidation (exemplified in the carbonyl bond, C=O) causes the color of plastics to become yellower.

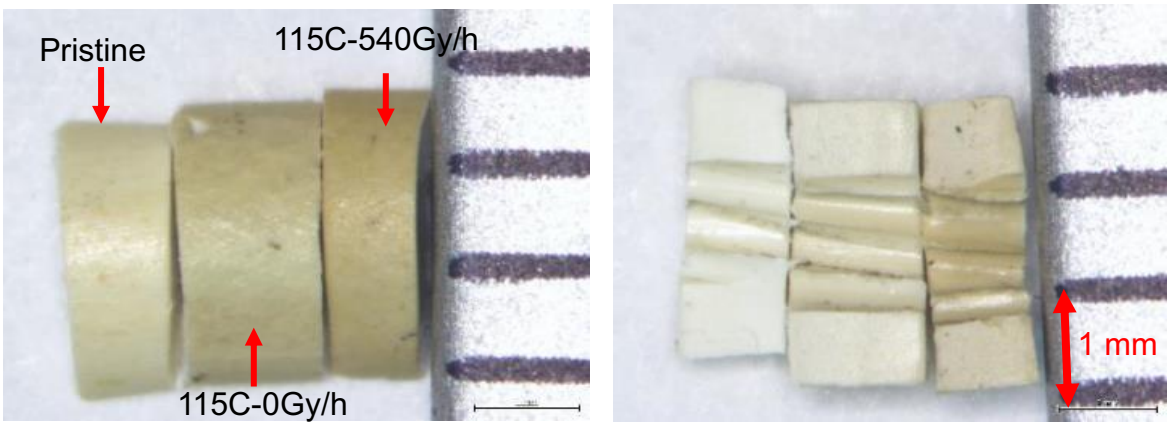

Figure 14. Optical Microscopic Images from inner side (right) and outer side (left) of samples. In each image are three samples of pristine, 25 days of thermally-only aged, and with gamma radiation aged cable insulation material.

Elemental analysis

The elemental ratio of carbon and oxygen for pristine and variously-aged XLPE samples were measured, Table 7. Compared with a pristine sample, the carbon wt% of irradiated samples decreases while the oxygen wt% increases. The decrease of carbon element ratio indicates that gases of small molecular weight such as CH_4 and C_2H_6 may exit the material during the aging process whereas the increase of oxygen element ratio indicates that oxygen participates in the chemical reactions that happen during aging, and/or oxygen is absorbed by the material in the aging process.

Table 7. Elemental analysis of carbon and oxygen of differently aged samples.

Sample ID: Temp-dose rate-days	**Carbon wt%**	**Oxygen wt%**
Pristine	52.8 ± 0.4	3.4 ± 0.2
60–540–25	51.4 ± 0.4	3.9 ± 0.2
90–540–25	51.4 ± 0.4	4.0 ± 0.2
115–540–25	51.6 ± 0.4	3.9 ± 0.2

Changes in antioxidant by pyrolysis gas chromatography-mass spectrometry (Py-GCMS) and in OIT by DSC

An article: Shuaishuai Liu, Stephen W Veysey, Leonard S Fifield, Nicola Bowler, "Quantitative analysis of changes in antioxidant in crosslinked polyethylene (XLPE) cable insulation material exposed to heat and gamma radiation," *Polymer Degradation and Stability*, was submitted in March 2018 and revised July 2018. The work describes the use of Py-GCMS for antioxidant quantification, which is discussed in the light of OIT measured by DSC. The revised manuscript is included in this report as Appendix B.1 Quantitative analysis of changes in antioxidant in crosslinked polyethylene (XLPE) cable insulation material exposed to heat and gamma radiation," page 115, and the article abstract is reproduced here for convenience.

Article abstract

Quantitative analysis of the antioxidant poly(1,2-dihydro-2,2,4-trimethylquinoline) (pTMQ) was conducted on pristine, thermally-aged, and gamma radiation-aged commercial cross-linked polyethylene-(XLPE-)based cable insulation material aged at temperatures 60, 90, and 115 °C, with gamma radiation exposure dose rates of 0, 120, 300, and 540 Gy/h for 15 days. The quantification of antioxidant was performed using pyrolysis gas chromatography-mass spectrometry (Py-GCMS). Oxidation induction time (OIT) was measured using differential scanning calorimetry (DSC) and correlation was made between the quantified depletion of antioxidant and measured OIT. It was observed that, in the case of isothermal aging, the quantity of antioxidant and OIT decreased with increasing gamma radiation dose. In the case of samples exposed to the same gamma radiation dose, the quantity of antioxidant and OIT were observed to decrease with increasing aging temperature. Depletion in the quantity of antioxidant relative to that in the pristine material ranged from 7 to 93 % for differently aged samples. The measured decline in OIT ranged from 0 to 80 %. Change in the quantity of antioxidant in the material was observed to follow the same trend as the change in OIT when the samples were aged under various conditions, with a correlation coefficient of 0.82. The observations are explained in terms of the reaction between the antioxidant and free radicals created during exposure of the samples to thermal and gamma radiation.

Changes in brominated flame retardants by Py-GCMS and NMR

Figure 15 and Figure 16 show the mass spectra of the pyrolyzates of pristine and differently aged samples within the retention time from 18 to 22 min. Signals within this retention time correspond to pyrolyzates of brominated flame retardants. Figure 15 shows the spectra of pristine and thermally-only aged samples at 60, 90, and 115 °C. No significant changes were observed for thermally aged samples, compared with the pristine sample. Figure 16 shows the spectra of pristine and samples aged by thermal and gamma radiation simultaneously. It is observed that with increasing gamma radiation exposure doses, the signal intensity between 18 and 19 min increases, while that between 21 and 22 min decreases.

Figure 17 shows the NMR spectra in the range from 100 to 120 ppm of three samples: pristine, thermally aged for 25 days at 90 °C, and thermally aged for 25 days at 90 °C with simultaneous gamma radiation dose 190 kGy. The peaks correspond to the carbon atoms of brominated compounds in the material. No significant difference is observed between the spectrum of the pristine sample and that of thermally aged sample. When exposed to a gamma radiation dose of 190 kGy, however, it is observed that the weight-normalized signal intensity increases.

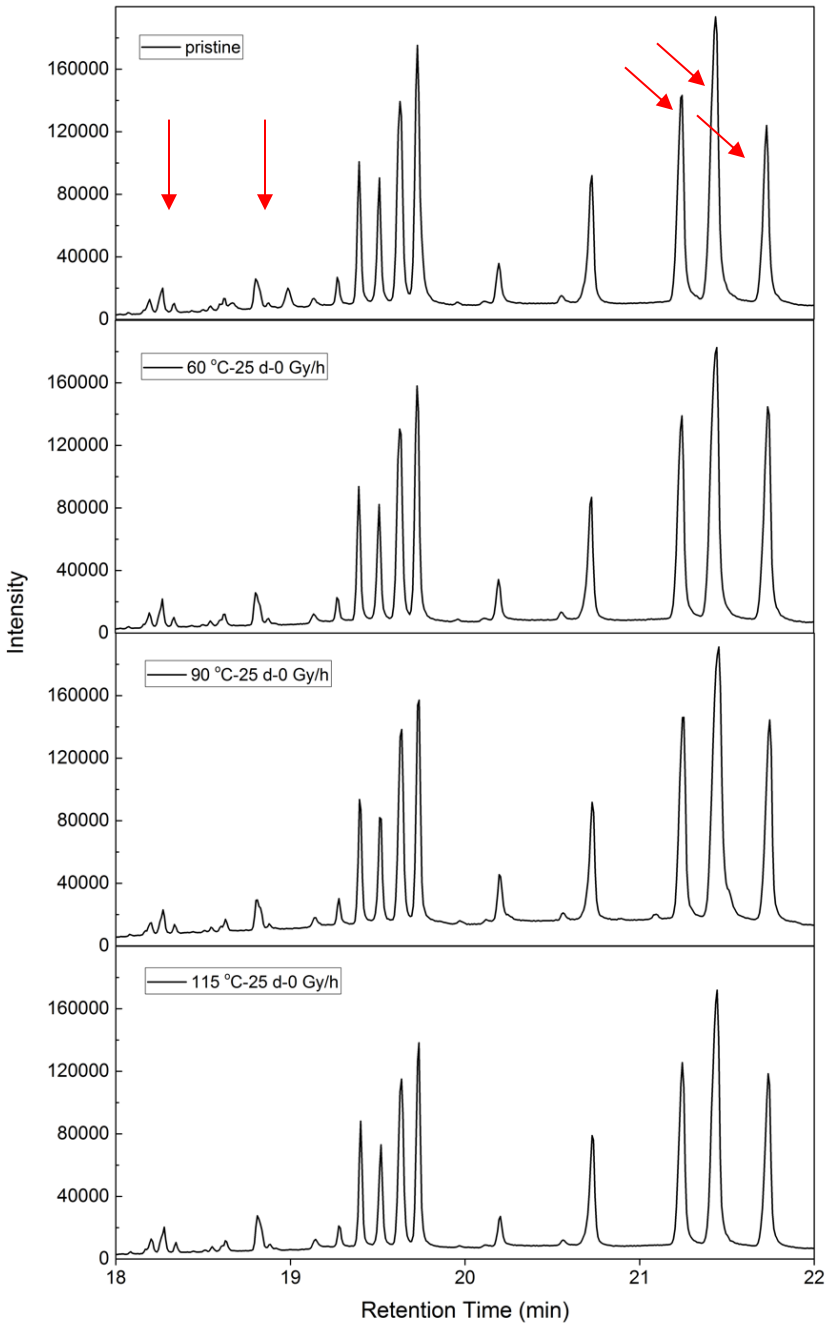

Figure 15. Mass spectra of pyrolyzates of pristine and thermally-aged samples at temperatures 60, 90, and 115 °C within the retention time range from 18 to 22 min. Red arrows indicate the peaks that changed with gamma radiation exposure.

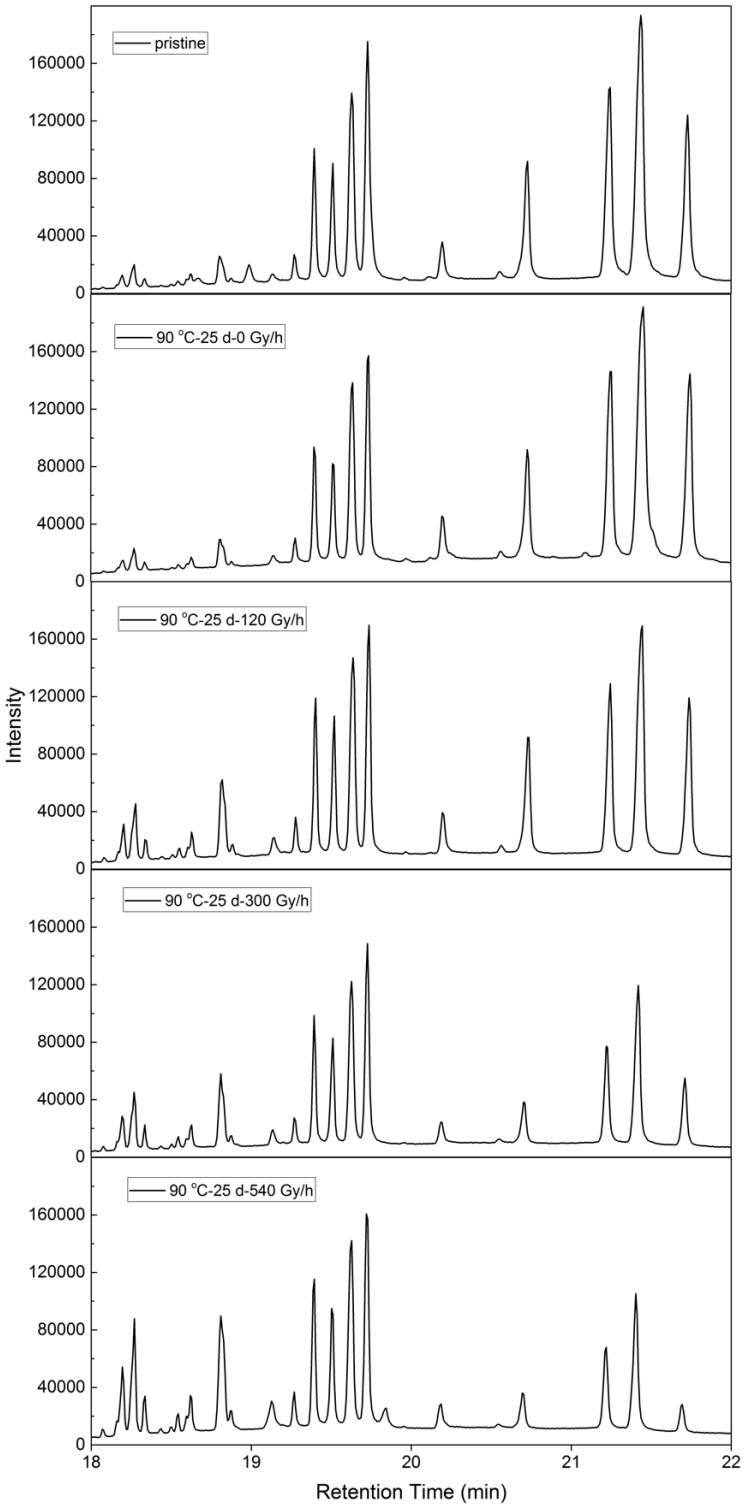

Figure 16. Mass spectra of pyrolyzates of pristine and simultaneous thermal and gamma radiation aged samples at 90 °C and various radiation doses within the retention time range from 18 to 22 min.

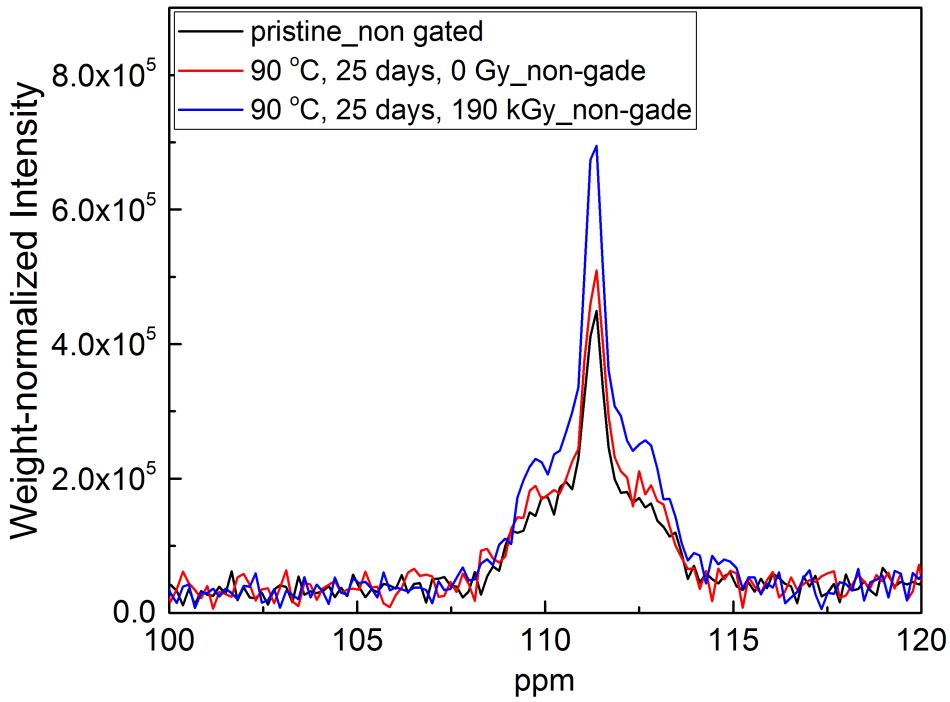

Figure 17. 13-C solid state NMR at ppm range from 100 to 120. Peaks at 112 ppm correspond to carbon signals in brominated compounds

Changes in cross-linked polyethylene polymer by differential scanning calorimetry (DSC), gel-fraction measurement and NMR spectroscopy

DSC

Figure 18(a) shows the cooling DSC curves, and (b) the re-heating curves, of a pristine sample and some aged at 90 °C with various radiation dose rates. No changes in the DSC curves were observed for thermally-only aged samples compared with the pristine sample. When gamma radiation was present, however, the re-crystallization and the melting features shift to lower temperatures. At the same temperature and same dose rates, the features shift to lower temperatures when aged for longer durations, corresponding to higher total doses. Samples that were aged at 60 °C and 115 °C show similar trends to those aged at 90 °C. Their DSC curves are not shown in detail here but are included in reference [4]. Selected curves for samples aged at 60, 90 and 115 °C are presented for the purpose of comparing the effect of different aging temperatures, as shown in Figure 19. When the sample was thermally aged without gamma radiation, no changes in the DSC curves were observed, for all three aging temperatures, compared with that of pristine sample. When the samples were exposed to gamma radiation, at all three temperatures the re-crystallization and melting features shift to lower temperatures. The maximum temperature shift takes place for the recrystallization feature of the sample that was aged for 25 days at 540 Gy/h, with a shift of 7.3 °C.

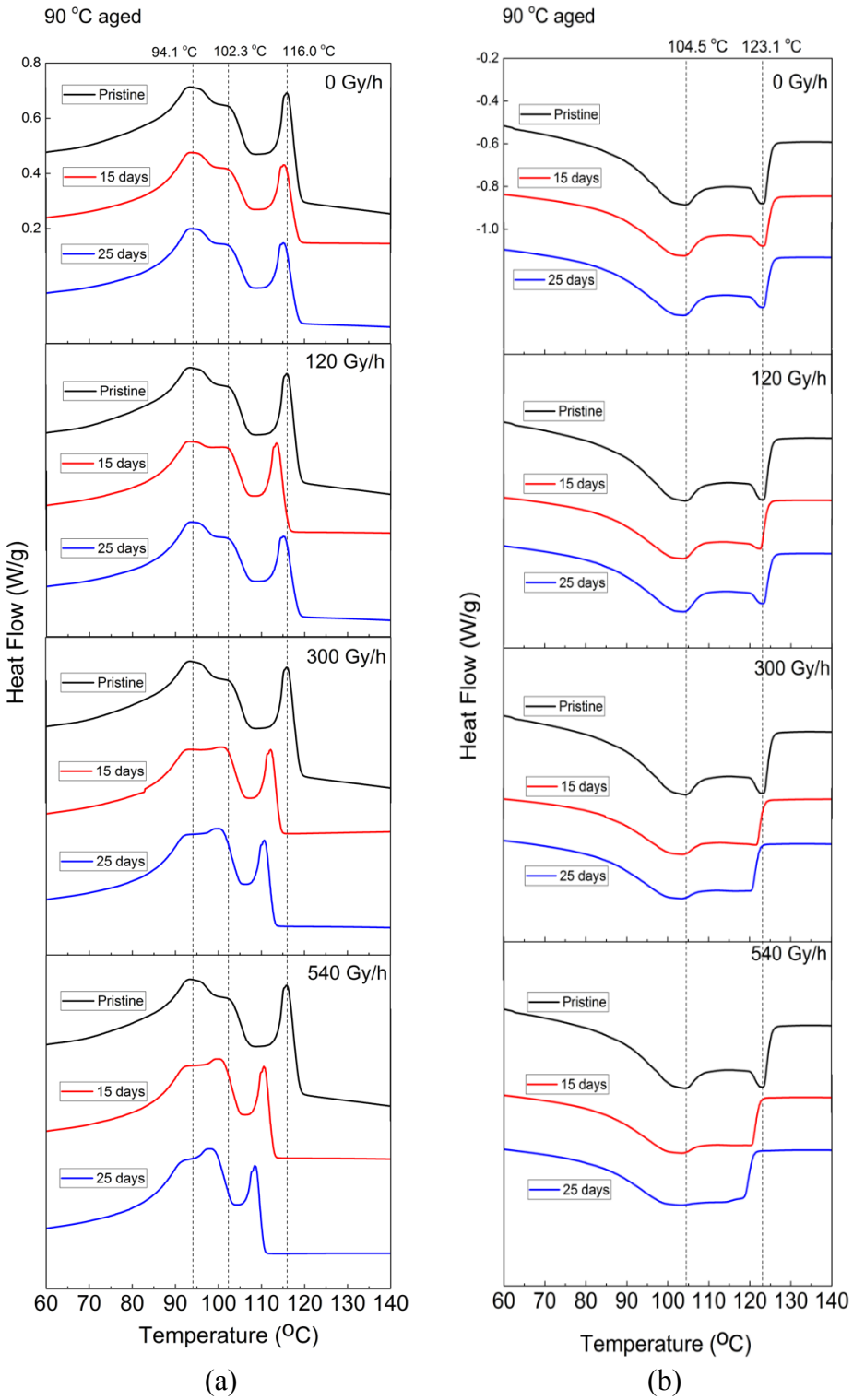

Figure 18. DSC curves of samples that were aged at 90 ℃ for different durations and at different dose rates. In (a) are the cooling DSC curves and in (b) are re-heating DSC curves. Those that were aged at 60 °C and 115 °C show the same changing trends and therefore the plots are not displayed here, they can be found in reference [4].

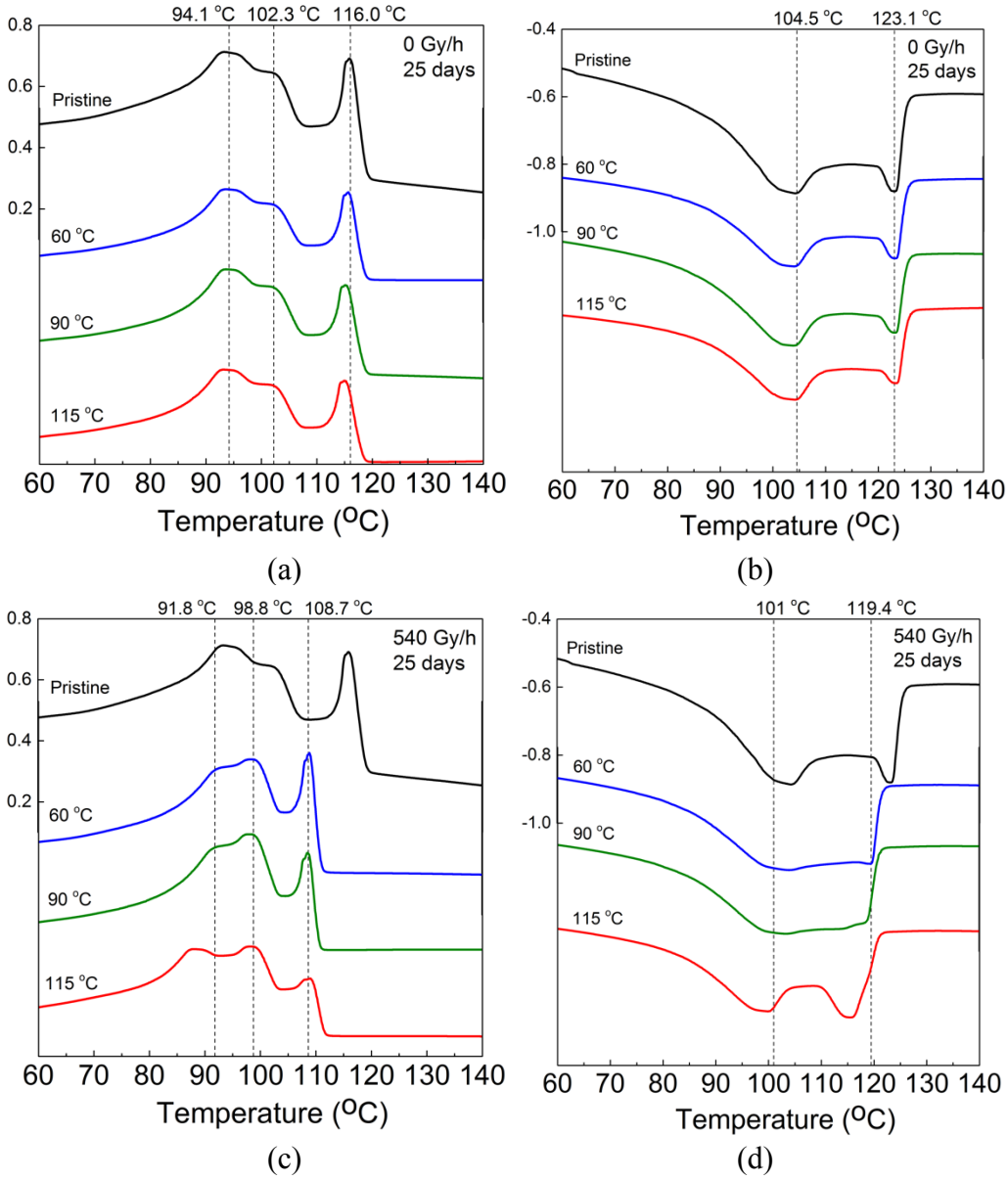

Figure 19. DSC curves of samples that were aged for 25 days at three temperatures: 60, 90 and 115 ℃, without and with (540 Gy/h) gamma radiation. In (a) and (b) are the cooling and re-heating DSC curves of samples without gamma radiation exposure, respectively. In (c) and (d) are the cooling and re-heating DSC curves of samples exposed to gamma radiation at 540 Gy/h for 25 days, respectively.

Gel content

Exposure of XLPE to elevated temperatures and gamma radiation leads to generation of reactive radicals that, in the presence of oxygen, result in molecular matrix changes including those due to chain scission and cross-linking. The monolithic nature of the cross-linked polymer matrix makes dissolution and assessment of well-defined molecular weight distribution impractical. The gel-swell method has been developed to quantify changes in polymer matrix for such insoluble material samples. The method assesses degree of solvent uptake and quantity of extractives from a sample. These values are especially useful for comparing relative changes with polymer material aging. In FY16, PNNL established equipment and a process for performing gel-swell

characterization on XLPE for tracking changes based on thermal and gamma radiation exposure, Figure 20.

Figure 21 shows the results of the gel fraction measurements for different samples. For samples that were aged at 60 °C, the gel-fraction value drops compared to that of the pristine material. For samples that were aged at 90 °C and 115 °C, an increase in gel-fraction value is observed, and the 115 °C aged samples show a higher increase. It is also observed that for samples aged at 60 and 90 °C samples, the gel-fraction values show a declining trend when the gamma exposure dose is high, that is, the gel-fraction value of samples that were exposed to gamma radiation for 190 kGy decrease compared to that of samples with gamma exposure of 110 kGy.

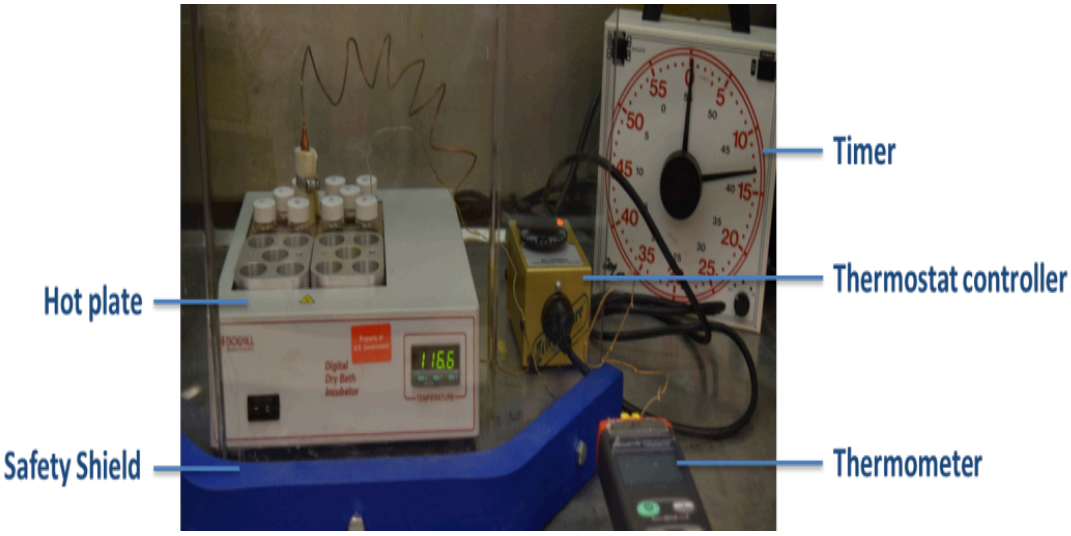

Figure 20. Equipment for performing gel content measurements on aged XLPE samples.

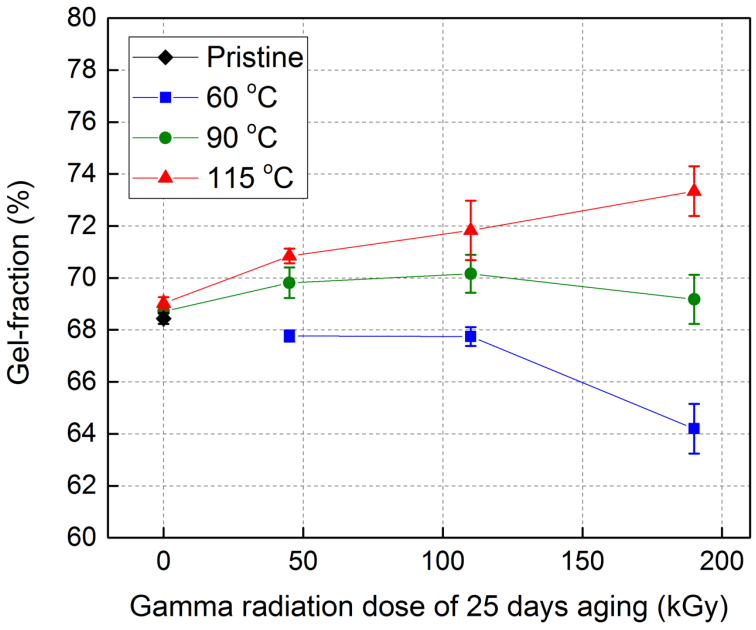

Figure 21. Gel-fraction percentage of pristine and differently aged XLPE samples.

NMR spectra

Figure 22 shows the NMR spectra in the range from 25 to 40 ppm for a pristine sample, a sample aged for 25 days at 90 °C, and one aged for 25 days with simultaneous thermal (90 °C) and gamma radiation dose 190 kGy. The peaks correspond to the carbon atoms of the XLPE polymer. No significant difference is observed between the NMR spectrum of the pristine sample and that of thermally aged sample. When exposed to gamma radiation for 190 kGy, however, it is observed that the weight-normalized signal intensity decreases, indicating that the quantity of carbon atoms in the XLPE polymer chains decreases after exposure to gamma radiation of 190 kGy. This indicates that there may possibly be small molecules such as CH_4 and C_2H_6 emitted during aging of XLPE in the presence of gamma radiation. The decomposition of DBDE and Octa-BDE into smaller brominated compounds might also consume the carbon atoms from the polymer chain.

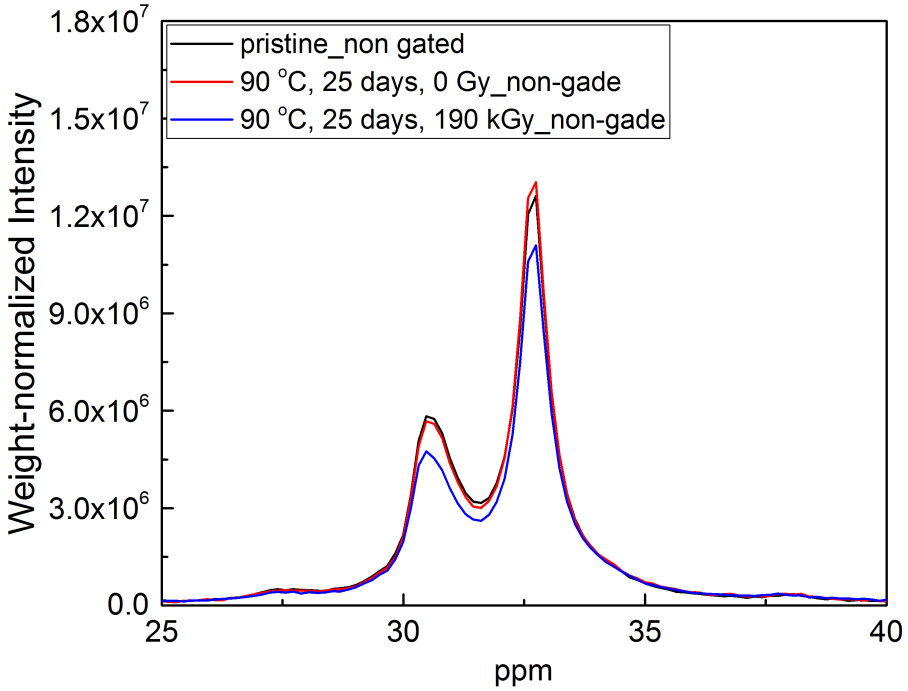

Figure 22. C-13 solid state NMR from 25 to 40 ppm. The peaks correspond to carbon signals of XLPE polymer chains.

Tensile testing

Elongation at break, or breaking strain, often shows a strong inverse correlation with polymer aging for elastomeric polymers. Elongation at break was measured on tubular samples of XLPE insulation whose inner conductor had been removed. At the end of Year 2 results were obtained for all samples aged at 90 and 115 °C, whereas those for samples aged at 60 °C were completed in Year 3.

For each aging temperature EAB was measured following guidance from IEC/IEEE 62582-3 [5]. Three to five nominally identical samples taken from the same row of the rack in the oven were used to determine EAB. Each 5-cm-long sample was clamped at both ends and the 3-cm-long gauge section marked to provide accurate monitoring of strain by video image. The samples were strained at a rate of 50 mm/min using an Instron Series IX test machine while being videoed using an HD Flip video camera with tripod. To ensure that each sample was protected from breaking at the test grips, a gray, XLPE protective piece was fitted to the sample in

alignment with the line drawn on the sample. The protective piece was used for multiple tests but needed to be replaced every 75 to 100 tests depending on how quickly it became worn. When tightening the XLPE in the test grips, each side of the sample was tightened until the torque wrench measured 20 Nm. Once the sample had been secured, the Instron grips were slowly separated until any slack in the sample was eliminated, Figure 23. To measure elongation of the XLPE, the test was videoed on a level HD Flip Video camera which was mounted on a tripod at the same height as the sample. A ruler was attached to the left side of the test grip and positioned vertically. When the sample was clamped in the Instron, it was positioned near the front of the grip (closest to the ruler) to mitigate against optical distortion of the measurement, upon video review. The tests were recorded and reviewed to obtain the initial and final gauge measurements from which the elongation-at-break was computed.

After breaking, the video was examined to determine the elongation at break. Results averaged over a few nominally-identical samples, with error bars indicating one standard deviation in the data, are shown in Figure 24 for XLPE aged at 90 °C for 15 days and in Figure 25 for XLPE aged at 115 °C for 15 days. It can be seen that there is no obvious difference in EAB for samples aged in the different rows i.e. as a function of radiation dose and dose rate for samples aged at 90 and 115 °C. This behavior is also observed for samples aged for 5, 10, 20 and 25 days. Comparing the results of Figure 24 and Figure 25 it can be seen that there is also no statistically significant difference between EAB measured on samples aged at 90 and at 115 °C. Performing statistical analysis on EAB data for samples aged at 60 and 90 °C reveals some subtle trends, however, as follows.

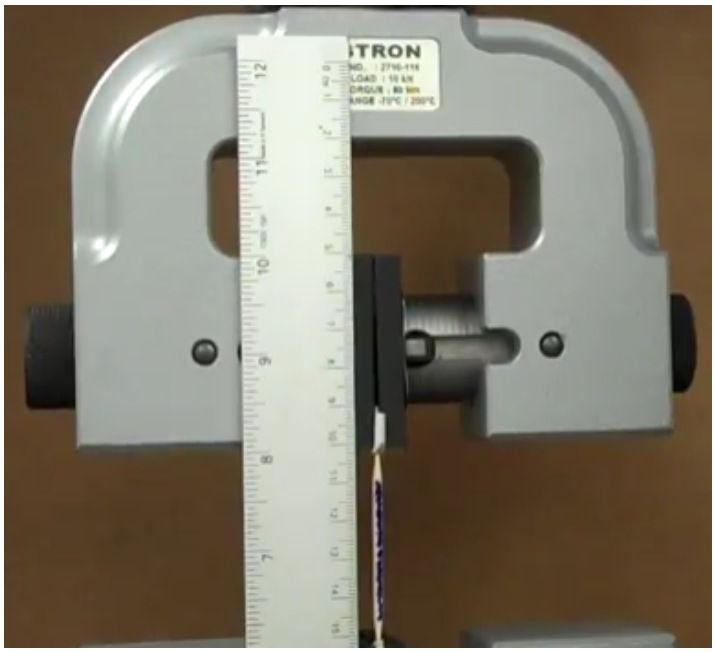

Figure 23. Equipment set-up for measuring elongation-at-break on aged XLPE samples.

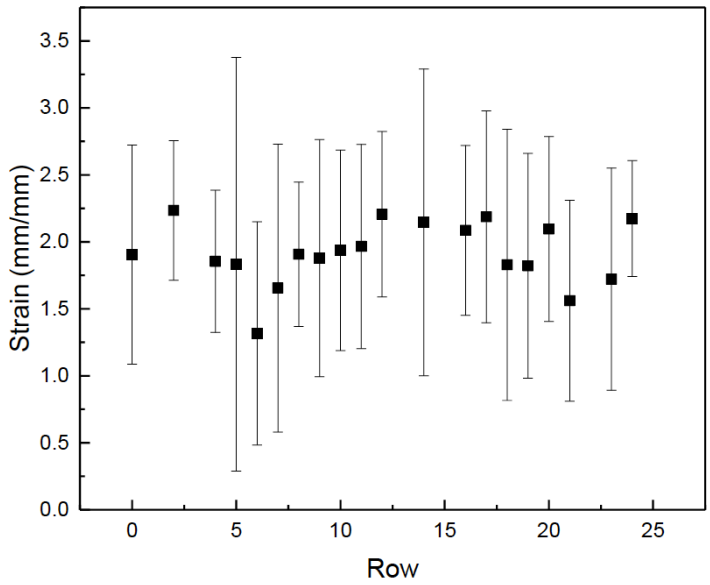

Figure 24. Mean EAB for samples aged at 90 ℃ for 15 days. Higher row numbers are farther from the Co-60 radiation source.

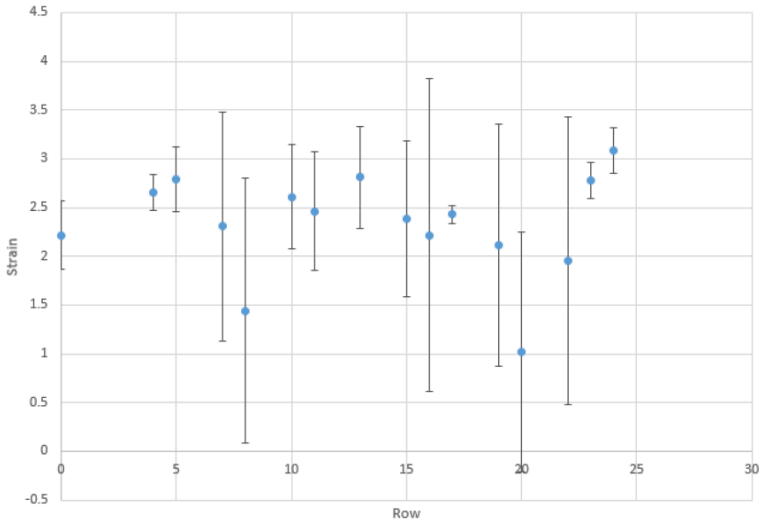

Figure 25. Mean EAB for samples aged at 115 ℃ for 15 days. Higher row numbers are farther from the Co-60 radiation source.

Plotting EAB for samples aged at 60 and 90 °C as a function of $1/R^2$, where R is the distance of the sample from the radiation source, results in the plots shown in Figure 26 and Figure 27. It is physically reasonable to make linear fits to these data sets since radiation intensity falls off as $1/R^2$. The slopes of these linear fits are tabulated in Table 8. Fewer data were available for samples aged at 115 °C so these are not plotted.

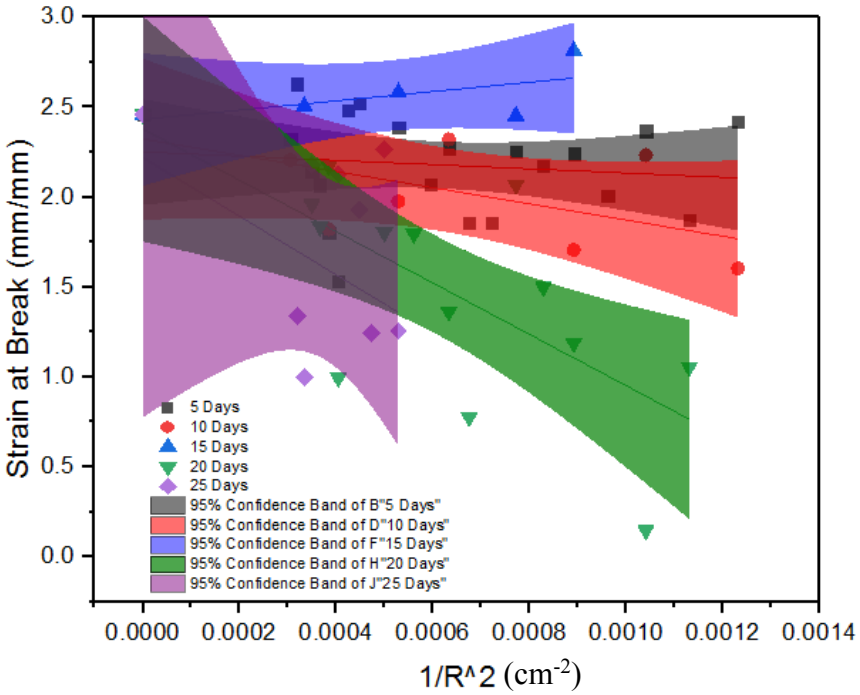

Figure 26. Mean EAB measured on samples aged at 60 ℃.

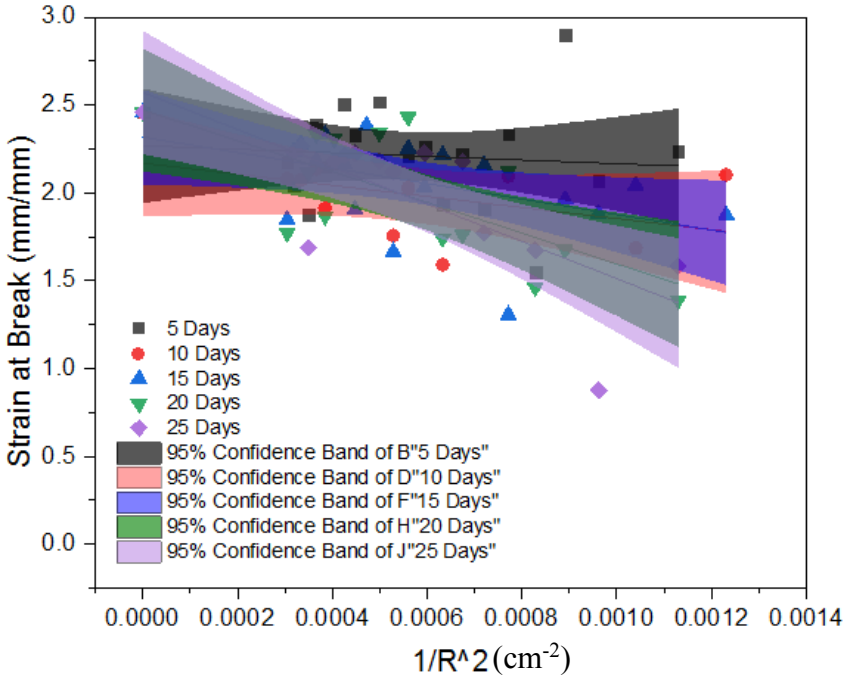

Figure 27. Mean EAB measured on samples aged at 90 ℃.

Table 8. Slope (cm^2) of EAB versus $1/R^2$, where R is distance from radiation source to sample, shown in Figure 26 and Figure 27.

	Number of days aged				
Aging temperature (°C)	5	10	15	20	25
60	–120 ± 200	–450 ± 250	260 ± 190	–1,400 ± 420	–1,630 ± 1,550
90	–100 ± 20	–320 ± 210	–440 ± 200	–880 ± 260	–1,060 ± 30

The results for samples aged at 60 ºC listed in Table 8 do not show a trend. For samples aged at 90 ºC, a monotonic increase in the magnitude of the slope is observed as the number of aging days increases, and in most cases the increase in slope magnitude is statistically significant, with non-overlapping uncertainties from one data point to the next. This result reflects the larger reduction in EAB for samples aged at 90 ºC that occurs as aging time (total dose) increases.

Summary

- The studied cable insulation material is a complicated system with XLPE as polymer matrix, DBDE, Octa-BDE, and Sb_2O_3 as flame retardants, and ZnS as white pigment;
- Oxidation causes XLPE to become darker yellow in color;
- Elemental analysis shows that, compared with a pristine sample, the carbon wt% of irradiated samples decreases while the oxygen wt% increases as the samples age;
- The changes in the quantity of antioxidant in the material follow the same trend as the changes in OIT of the material when aged under various conditions, with a correlation coefficient of 0.82;
- Depletion of antioxidant is not the only factor that contributes to the reduction in OIT of the studied material;
- For samples aged at 90 ºC, elongation-at-break increases significantly as aging time (total dose) increases.

Key conclusions

- When XLPE insulation material is aged simultaneously by thermal and gamma radiation,
  - oxygen is absorbed from the environment participating in the aging reactions;
  - the polymer backbones of the studied material are broken into shorter chains, chain-branching increases and at the same time the chain cross-linking process takes place, dominating over the chain breaking process;
  - the level of antioxidant decreases during the aging process by decomposition and volatilization;
  - small-molecule gases such as CH_4 and C_2H_6 may be released.
- When XLPE insulation material is aged isothermally,
  - the antioxidant quantity and OIT decrease with increasing gamma radiation dose and, at fixed gamma radiation dose, they decrease with increasing aging temperature.
- OIT can be an effective indicator of the antioxidant depletion severity in XLPE-based cable insulation materials.

References

1. M. Sheridan, *The Vanderbilt Rubber Handbook*, R. T. Vanderbilt Company, Inc, Norwalk, CT, 2010.
2. M. Bolgar, J. Hubball, J. Groeger, and S. Meronek, *Handbook for the Chemical Analysis of Plastic and Polymer Additives*, second edition, CRC Press, 2015.
3. M. Ash, *Handbook of Green Chemicals*, Synapse Info Resources, 2004.
4. S. Liu, "Composition identification, aging mechanisms and nondestructive aging indicator of commercial filled cross-linked polyethylene (XLPE) cable insulation materials," PhD thesis, Dept. Mater. Sci. Engng., Iowa State Univ., Ames, IA, 2017. Online at: https://lib.dr.iastate.edu/cgi/viewcontent.cgi?article=7172&context=etd
5. IEC/IEEE 62582-3 International Standard "Nuclear power plants – Instrumentation and control important to safety – Electrical equipment condition monitoring methods – Part 3: Elongation at break", Edition 1.0 2012-11

1.4 Dielectric, THz and infrared characterization of aged samples

Dielectric, terahertz, and infrared characterization of aged samples was due to be completed at the end of Year 2 (September 30, 2016) but took longer due to samples becoming available later than originally scheduled and due to the purchase of a new accessory for FTIR for the purpose of capturing low-wavenumber spectral data. Initial characterization of all samples was completed at the end of Year 2 as planned. Work continued to improve the data in various ways throughout Year 3 of the project: dielectric data were collected over a broader frequency range (from 0.01 Hz to 1 MHz rather than from 1 Hz to 1 MHz) using a more accurate instrument in order to access sensitive low-frequency permittivity indicators of XLPE aging, suggested by the preliminary data; and infrared data were collected over a broader range of wavenumbers using a new fixture in order to access sensitive low-wavenumber indicators of filled XLPE aging, suggested by the preliminary data. Collection of dielectric and infrared spectral characterization data on the aged samples was completed by November 30, 2017. Dielectric breakdown strength data collection and analysis was completed by March 31, 2018.

Hypotheses

- Dielectric spectral data may sensitively indicate aged state of XLPE-based insulation material;
- Changes in dielectric spectra may provide insight into the aging mechanisms at work as XLPE-based insulation material ages;
- Dielectric breakdown strength may correlate with degree of aging;
- Particular wavenumbers in the IR spectrum may indicate aged state of XLPE-based insulation material;
- Changes in IR spectra may provide insight into the aging mechanisms at work as XLPE-based insulation material ages.

Approach

Sample preparation

The XLPE sample material studied in this work was obtained from RSCC and is of the same formulation as XLPE material found in RSCC® Firewall® III nuclear-grade Instrumentation Cable, in which it forms the insulation layer. The XLPE sample tape has thickness approximately 0.7 mm and width approximately 20 mm. This XLPE sample material is a polymer-matrix composite containing additives and fillers designed to perform various functions. Based on our analysis, these components and their assumed functions are as detailed in Table 6, page 26.

The XLPE samples were suspended in an oven that was placed inside the High Exposure Facility (HEF) of the Radiological Exposures & Metrology Laboratory at Pacific Northwest National Laboratory (PNNL). Simultaneous thermal and gamma radiation aging of the samples was achieved by controlling the oven temperature as it was placed in the gamma-ray field from an encapsulated cobalt-60 source in the HEF.

The dose rate to each individual sample depends primarily on its distance from the radiation source. Total dose received by each sample was therefore controlled by position of the sample within the oven and the number of days of exposure. Various radiation doses to the samples were

achieved by aging them for different periods of time. Different aging temperatures were achieved by running multiple rounds of the experiment with the oven temperature at 60, 90, and 115 °C. Table 9 displays the aging conditions of the samples studied in this paper. Further details of the accelerated aging process and sample preparation can be found in references [1, 2].

Table 9. Aging conditions of the studied tape samples. Samples listed were aged at 90 °C. Dose rate is in terms of air kerma. Thickness reported is the mean and standard deviation of five measured values.

Sample	Dose Rate (Gy/h)	Exposure Time (d)	Total Dose (kGy)	Thickness (mm)
DR0D0	0	0	0	0.70 ± 0.02
DR0D5	0	5	0	0.70 ± 0.02
DR0D10	0	10	0	0.702 ± 0.008
DR0D15	0	15	0	0.69 ± 0.01
DR0D20	0	20	0	0.685 ± 0.008
DR450D0	450	0	0	0.70 ± 0.02
DR450D5	450	5	54	0.70 ± 0.04
DR450D10	450	10	108	0.684 ± 0.009
DR450D15	450	15	162	0.688 ± 0.003
DR450D20	450	20	216	0.70 ± 0.02
DR140D20	140	20	67	0.68 ± 0.02
DR280D20	280	20	134	0.70 ± 0.01
DR350D20	350	20	168	0.682 ± 0.008

Dielectric spectroscopy

In Year 2 of this project, preliminary dielectric data were collected over the frequency range from 20 Hz to 1 MHz using an Agilent E4980A precision LCR meter. During this process, it emerged that the most sensitive dielectric indicators to aging of filled XLPE likely occur in the frequency range from 0.01 to 10 Hz and, for this reason, dielectric data were collected again over the frequency range from 0.01 Hz to 1 MHz using a Novocontrol dielectric spectrometer.

Dielectric spectra were measured by connecting a custom-designed sample cell to a Novocontrol dielectric spectrometer. Measured capacitance was increased by designing a custom sample cell with rectangular electrodes, thereby reducing uncertainty in the measured permittivity values. Brass electrodes with dimensions 40 x 15 mm^2 and 50 x 20 mm^2 were mounted in a poly-methyl methacrylate (PMMA) structure, Figure 28. The corners of the rectangular electrodes were rounded with an arc radius of 2 mm.

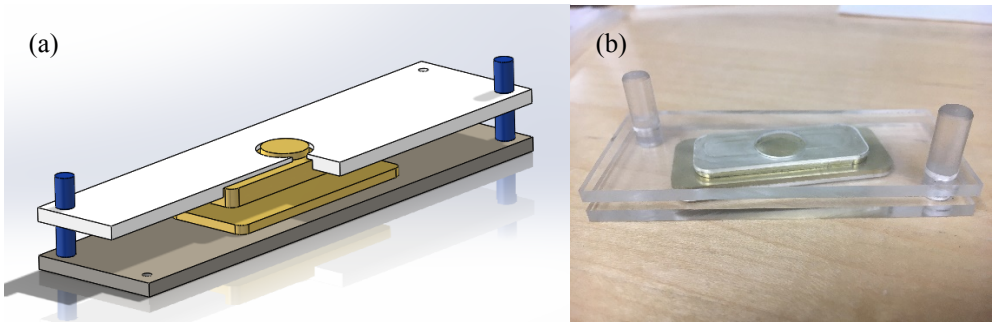

Figure 28. Sample cell structure: (a) design in SolidWorks™, and (b) photograph. Electrodes dimensions are 40 x 15 mm² and 50 x 20 mm² with corner radius 2 mm.

Before mounting it in the sample cell, each sample was wiped clean using acetone and allowed to dry. Spectra were recorded at three locations on each sample, as depicted in Figure 29. Frequency was swept from 1 Hz to 1 MHz, with three data values recorded for every frequency value. Mean values and the corresponding standard error are presented in the results. All dielectric spectral measurements were conducted at ambient temperature (20.3 °C) and relative humidity (26 %).

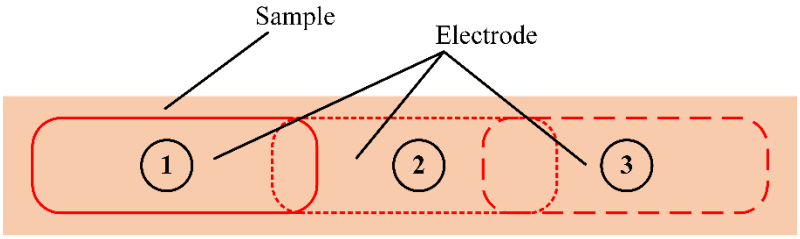

Figure 29. Dielectric spectra were measured at three positions on each sample.

Dielectric breakdown strength

In Year 1 of this project, preliminary dielectric breakdown strength data were collected on XLPE-insulated wires with the central conductor present. This work was discussed in the first annual report on this project. The wire geometry is an unconventional geometry for the collection of dielectric breakdown strength data, however, and the verification of the technique will require work outside of the scope of this original proposal. Conventional dielectric breakdown tests were performed on XLPE tape samples once all other testing had been completed, since dielectric breakdown testing is destructive to the sample.

To measure dielectric breakdown strength, the prod-plate electrode system shown in Figure 30 was employed. The breakdown system includes two electrodes: the top electrode, machined from tungsten, is a prod with hemispherical tip diameter 0.5 mm. The bottom electrode, machined from brass, is a cylinder with flat circular upper surface and diameter 5 mm. During a dielectric breakdown strength test, the top electrode is connected to the high-voltage terminal, the bottom electrode is connected to ground, and the sample is placed between them, in contact with both.

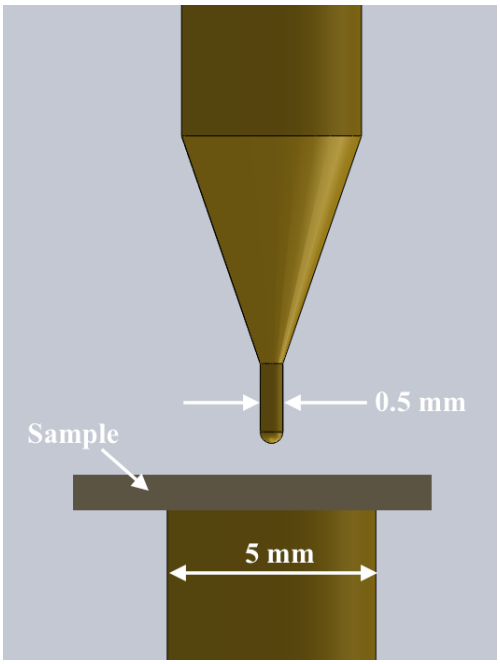

Figure 30. Electrode system for measuring breakdown strength, rendered in SolidWorks™.

Before each breakdown test, the sample was wiped clean using acetone and allowed to dry. Then, the sample was placed between the top and bottom electrodes of the breakdown test set-up, ensuring flat and complete contact between the surfaces. Then, the whole system was immersed into an insulating liquid bath filled with Envirotemp® FR3® fluid to avoid surface flashover. During the breakdown test, 50 Hz alternating voltage was applied with ramp rate 500 V/s until breakdown occurred. The breakdown current threshold was set to 0.1 mA.

Many of the samples were observed to have become discolored and distorted by aging. To make it possible to conduct dielectric breakdown measurements, distorted samples were trimmed to remove excessively bent regions or gently flattened if necessary, when the curvature was not as severe. Breakdown voltage was recorded at 20 nominally identical positions on each sample.

Sample thickness was measured at five different points on each sample using a digital micrometer with sensitivity ~1 μm. The mean and standard deviation of measured thickness values are reported in Table 9. The value of dielectric breakdown strength was obtained by dividing the measured breakdown voltage by the sample thickness. After every ten breakdown tests the bath fluid was stirred to disperse any by-products released into it during the breakdown test.

Fourier-transform infrared (FTIR) spectroscopy

FTIR is a modern infrared innovation for fast qualitative identification and quantitative characterization of a variety of materials, based on the materials' spectral "fingerprints" primarily in the mid-infrared regions.

The project has access to an Agilent 680 FTIR spectrometer (Figure 31) that has wide mid-infrared spectrum in the range from 20 to 8000 wavenumbers (cm^{-1}) at resolution better than 0.06 wavenumbers. This 680 FTIR spectrometer also features high-end step-scan functionality, as well as capabilities in specular reflection and attenuated total reflection (ATR) spectroscopy.

The Agilent 680 FTIR spectrometer is also equipped with a GladiATR accessory made by PIKE Technologies. This accessory utilizes highest performance diamond crystals to sustain exceptionally strong energy throughput and is capable of reaching the infrared region as low as 20 wavenumbers (Figure 32). Such frequency extension is particularly important to capture absorption peaks in the wavenumber range from 400 to 550 which are attributed to DBDE [3], and is one of the components of this XLPE-based insulation material. Additionally, the project has access to a field-deployable FTIR spectrometer, Agilent 4100 Exoscan (Figure 33), which is similarly capable of specular reflection, diffused reflection and attenuated total reflection spectroscopy.

Although through-transmission (T-T) spectroscopy is the standard FTIR technique, the primary focus in this project will be on the direct contact mode ATR for its advantages of being non-destructive and with almost no need for sample preparation. This is particularly suitable for testing the thick and opaque polymer samples (Figure 33).

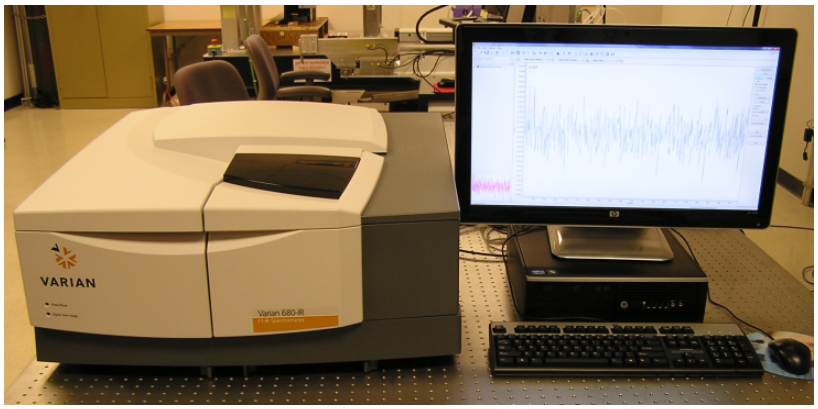

Figure 31. Agilent 680 benchtop FTIR spectrometer.

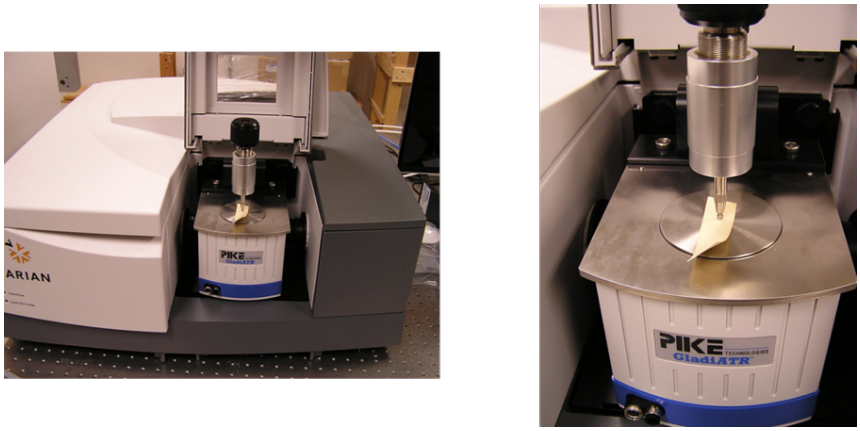

Figure 32. The desktop Agilent 680 FTIR spectrometer combined with the GladiATR ATR accessory, detailed at right.

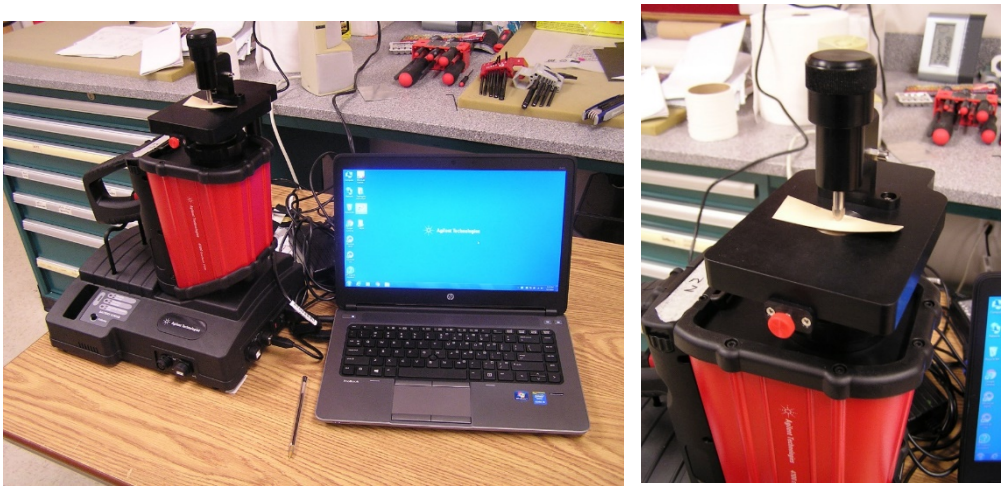

Figure 33. The hand-held, field-deployable FTIR spectrometer, Agilent 4100 Exoscan.

Due to the substantial thickness of the XLPE tape samples, in the first two quarters of 2016 we switched to contact mode FTIR measurements using ATR spectroscopy. With partial support from this project, we purchased an Agilent 4100 Exoscan FTIR spectrometer to carry out the work.

Figure 34 shows the ATR-FTIR spectrum of a sample aged thermally at 115 °C for 25 days, without gamma radiation. The plot is the average spectrum obtained from five measurement locations on both front and back surfaces of the sample. At each location, frequency was swept 32 times between wavenumbers 650 and 4,000 cm^{-1} using resolution of 2 cm^{-1}. The system software then interpolated further down to 1 cm^{-1}. We have also smoothed out the spectra by using a running average technique. We found a strong positive correction between the level of aging and the spectral strength of a peak at around 1,710 cm^{-1}, which corresponds to the C=O bond stretch mode. A negative correlation was also found in the common C-H functional group in the range from 2,800 to 3,000 cm^{-1}. The peak around wavenumber at 1,470 is due to scissoring of the CH_2 bond. We also observed an interesting raising of the baseline for wavenumbers below 1,500 cm^{-1}, which is positively correlated with degree of aging as well. This baseline rise may be attributed to the collective contributions from many smaller peaks in this region. A detailed description of the IR spectrum of PE is provided in reference [4].

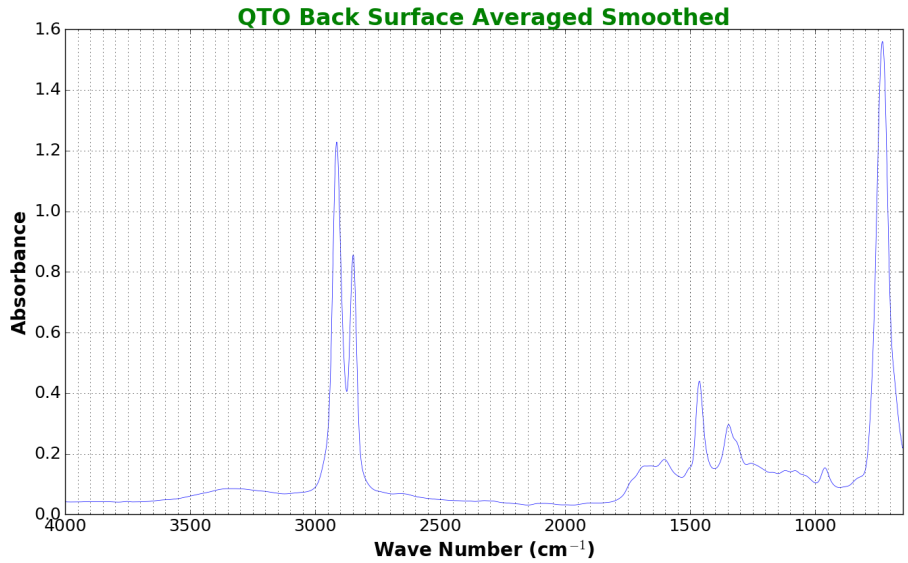

Figure 34. Mid-infrared spectrum of an XLPE sample thermally aged at 115 ℃ for 25 days, without gamma radiation.

In quarter 3 of 2016, complete ATR spectral absorbance measurements were made on the E-series of PE samples which have various degrees of aging, Table 4. As shown in Figure 35, this set of data reconfirmed the trends seen in the initial tests: positively correlated peak at wavenumber 1,710 cm^{-1}, positively correlated baseline shifting below wavenumber 1,500 cm^{-1}, and the negatively correlated twin peaks around wavenumbers 2,800 to 3,000 cm^{-1}. It is clearly seen that the spectral intensity increases significantly for the two most highly aged samples, E5 and E6. More details in the wavenumber region from 650 to 1,950 cm^{-1} are plotted in Figure 36 with the baseline E0 spectrum subtracted.

To improve the data quality, all raw data were processed by averaging, smoothing and baseline subtraction, first derivative and integration. The advanced treatments not only more clearly revealed the trending of the main peaks identified above, but also revealed weaker absorptions around wavenumbers 1,180 and 1,370 cm^{-1} in the more heavily aged samples. The precise locations of the absorption peaks were identified using an automated peak detection algorithm.

Also in this quarter, XLPE samples with various degrees of aging were likewise measured. The peak at wavenumber 732 cm^{-1} was observed to increase tremendously while the peak at 1,710 cm^{-1} disappeared. Figure 37 shows the spectra of XLPE samples aged at 90 °C and 540 Gy/h for 15 and 25 days, respectively, with all major peak locations labeled.

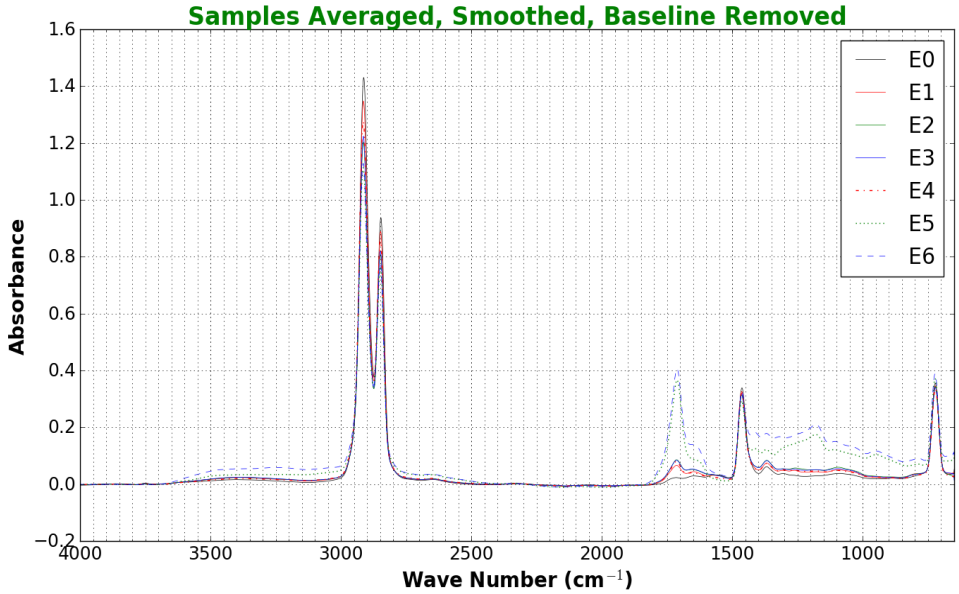

Figure 35. Processed FTIR spectra of the E-series PE samples. Aging conditions for the E-series samples are provided in Table 4.

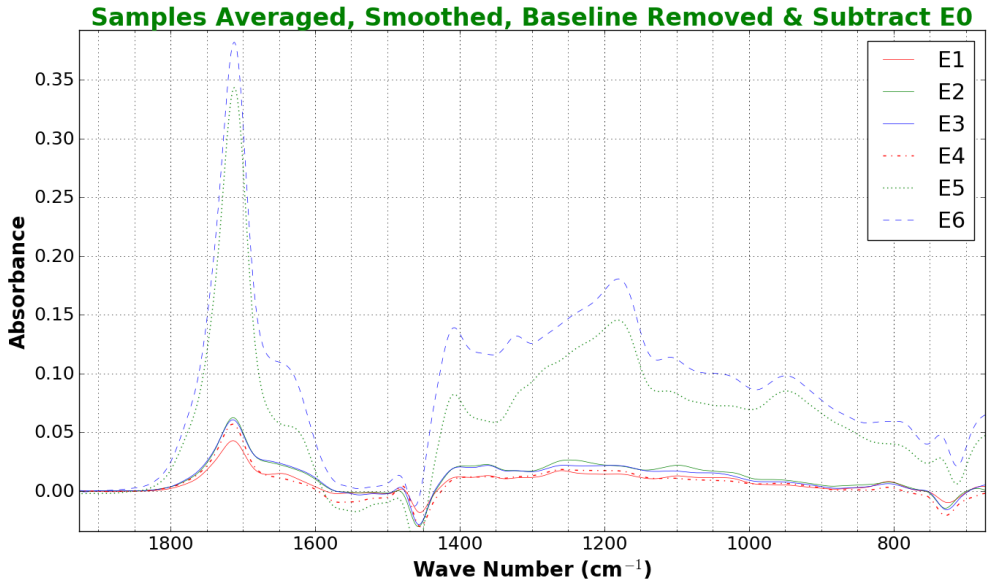

Figure 36. Processed spectra in the wavenumber range from 650 to 1,950 cm^{-1} of the E-series PE samples, Table 4, with the E0 sample baseline measurement subtracted.

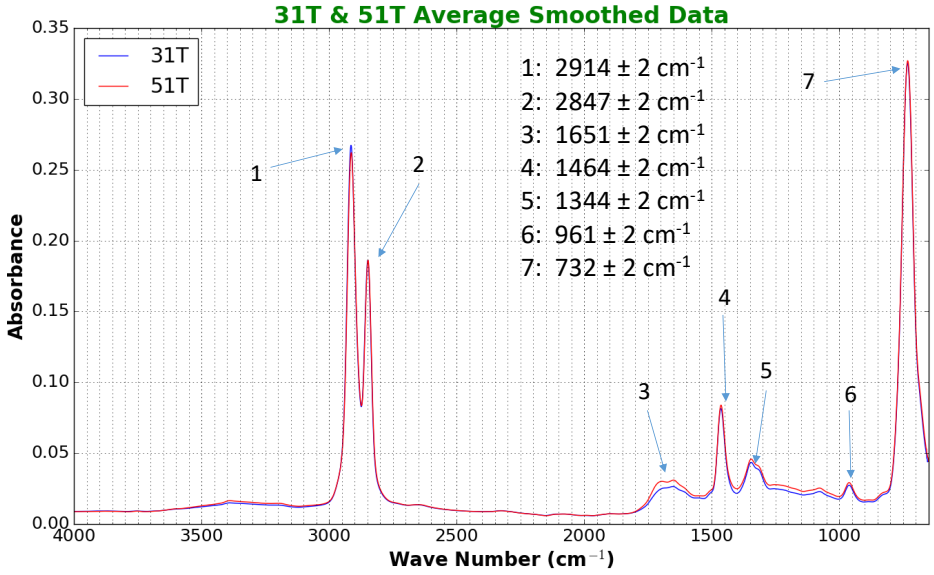

Figure 37. Spectra of XLPE samples aged at 90 ℃ and 540 Gy/h for 15 days (shown in blue) and 25 days (shown in red), respectively.

Significant results

Dielectric data gathered during the course of this project, and analysis of it, has formed the basis of two publications:

1. Z. Shao, M. I. Byler, S. Liu, N. Bowler, L. S. Fifield, and M. K. Murphy, "Dielectric Response of Cross-Linked Polyethylene (XLPE) Cable Insulation Material to Radiation and Thermal Aging," *2nd IEEE International Conference on Dielectrics (ICD2018)*, Budapest, Hungary, July 1-5, 2018, accepted May 2018.
2. Z. Shao, M. I. Byler, S. Liu, C.-P. Chiou, L. S. Fifield, M. K. Murphy, A. Gjersvik, and N. Bowler, "Dielectric Loss and Breakdown Response of XLPE to γ-Radiation and Thermal Exposure," *IEEE Trans. Dielectr. Electr. Insul.*, to be submitted.

The first of these manuscripts is reproduced in full in the Appendix of this report, beginning on page 148. The results to be included in the second are reproduced below.

Dielectric spectroscopy

Effect of aging time

The dielectric loss tangent spectra of samples aged at 90 °C, with radiation exposures detailed in Table 9, are shown in Figure 38. Comparing results for samples aged without radiation exposure, Figure 38 (a), with those for samples aged in the presence of gamma radiation, Figure 38(b), it can be seen that the dielectric response of the material changes dramatically following exposure to gamma radiation. To facilitate direct comparison between the dielectric response of samples aged with and without gamma radiation, values of dielectric loss tangent measured at 100 Hz and 1 MHz are plotted in Figure 39 as a function of exposure time, for samples aged without and with gamma radiation at dose rate 450 Gy/h. Loss tangent is a sensitive function of aging time for samples exposed to gamma radiation, but not for samples aged only thermally. Similar results have been obtained for samples aged at 60 [1, 5] and 115 °C [1].

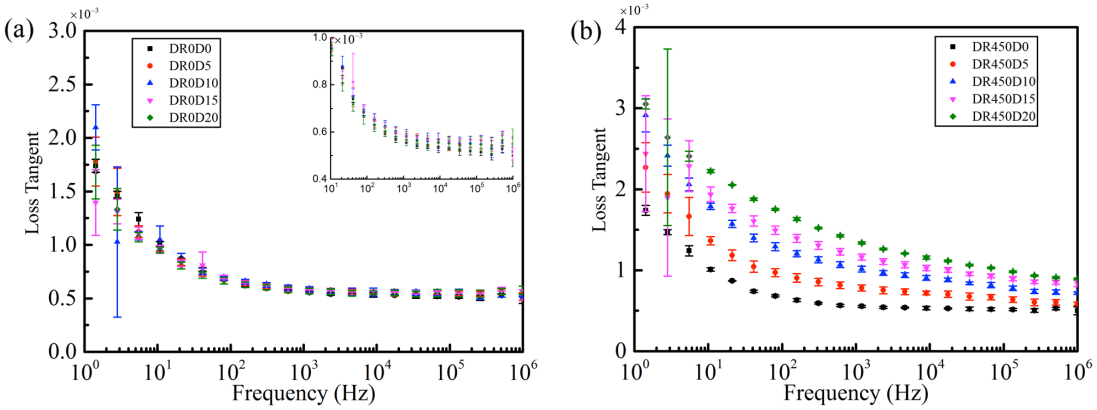

Figure 38. Dielectric loss tangent as a function of frequency for samples aged at 90 °C for up to 20 days (a) thermally and (b) with simultaneous thermal and gamma radiation at dose rate 450 Gy/h. Inset in (a) shows expanded view.

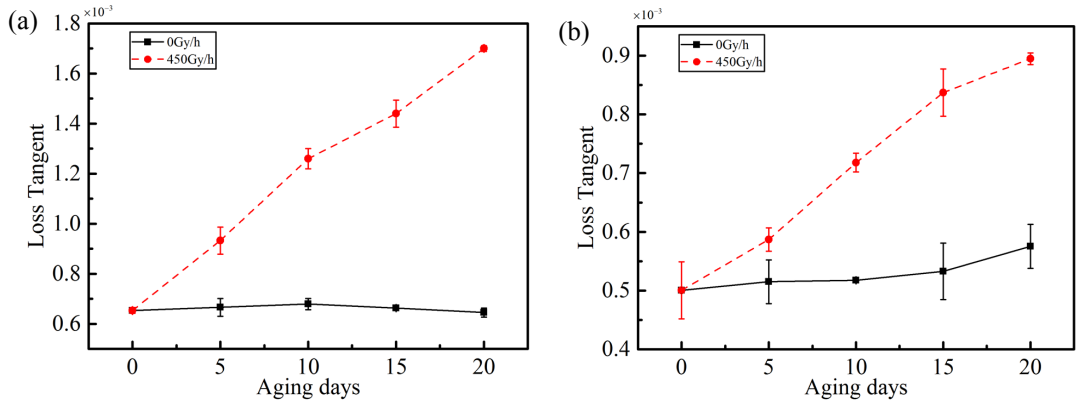

Figure 39. Dielectric loss tangent as a function of aging time at 90 °C for samples aged thermally and with simultaneous thermal and gamma radiation at dose rate 450 Gy/h, for (a) 100 Hz and (b) 1 MHz.

Effect of dose rate

The dielectric loss tangent of XLPE samples aged at different dose rates is presented in Figure 40, for five and 20 days of exposure at 90 °C. As depicted in Figure 40, the dielectric loss tangent increases with the dose rate of gamma radiation for almost the entire frequency range measured, from 1 Hz to 1 MHz. Dielectric loss tangent values measured at frequencies 100 Hz and 1 MHz are plotted in Figure 41 as a function of dose rate. For five days of aging the dielectric loss tangent increases almost linearly with dose rate for the range of values studied here. For 20 days of exposure at 90 °C the loss tangent appears to saturate for dose rates greater than approximately 350 Gy/h.

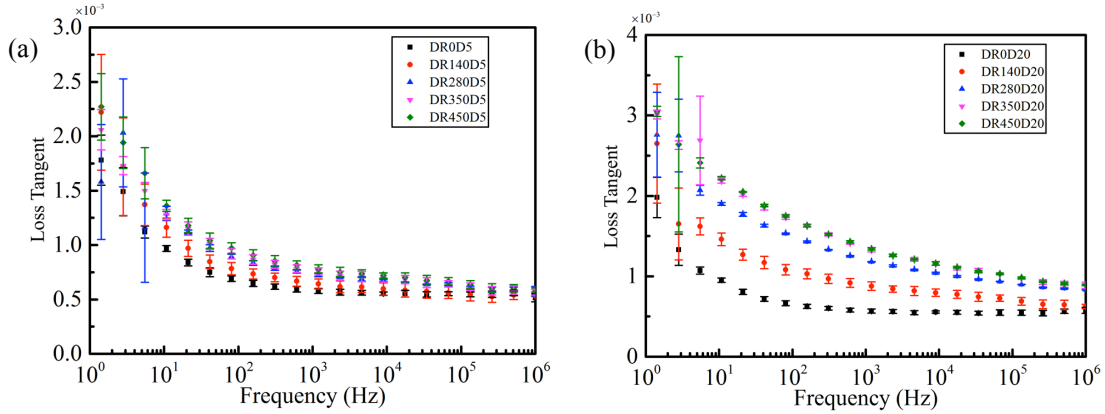

Figure 40. Dielectric loss tangent as a function of frequency for samples aged with simultaneous thermal and gamma radiation at various dose rates for (a) five and (b) 20 days at 90 °C.

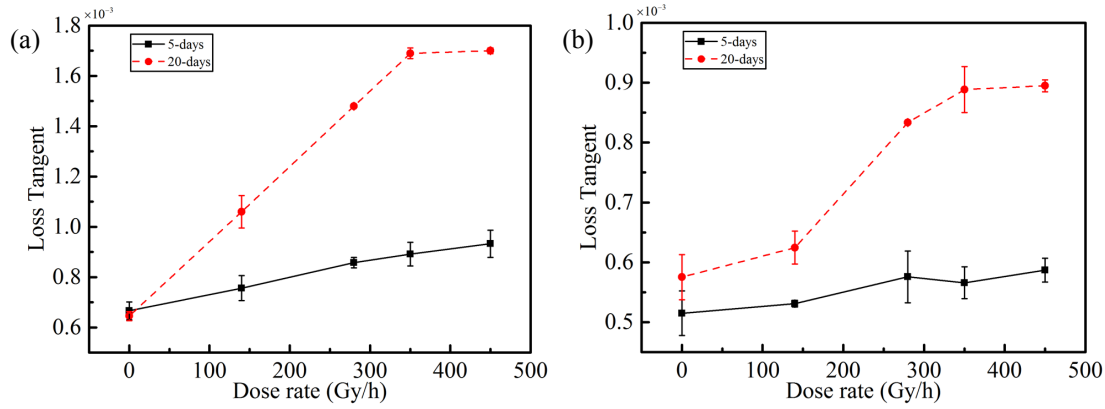

Figure 41. Dielectric loss tangent as a function of dose rate for samples aged for five and 20 days at 90 °C, for (a) 100 Hz and (b) 1 MHz.

Dielectric breakdown strength

Figure 42 shows two-parameter Weibull cumulative distribution functions (CDFs) and box plots for dielectric breakdown strength of XLPE samples aged at 90 °C without (a), (b) and with (c) to (f) exposure to gamma radiation.

The expression for the cumulative distribution function (CDF) for the two-parameter Weibull distribution is given by

$$F(E_{bd};\alpha,\beta) = 1 - \exp\left[-\left(\frac{E_{bd}}{\alpha}\right)^{\beta}\right] \quad (1)$$

where F is the probability of electrical breakdown strength E_{bd} of the insulator under test, α is the scale parameter, and β is the shape parameter. With data sets of at least 20 values, one can safely use the least-squares regression technique to estimate the two parameters with good accuracy [6].

According to normal practice in the construction of box plots, data points that lie below Q1 – 1.5 × IQR or above Q3 + 1.5 × IQR are marked as outlying data points, using the symbol + in Figure 42. By definition, IQR = Q3 – Q1, where Q3 is the 75th percentile value and Q1 is 25th percentile value of breakdown strength for any particular sample.

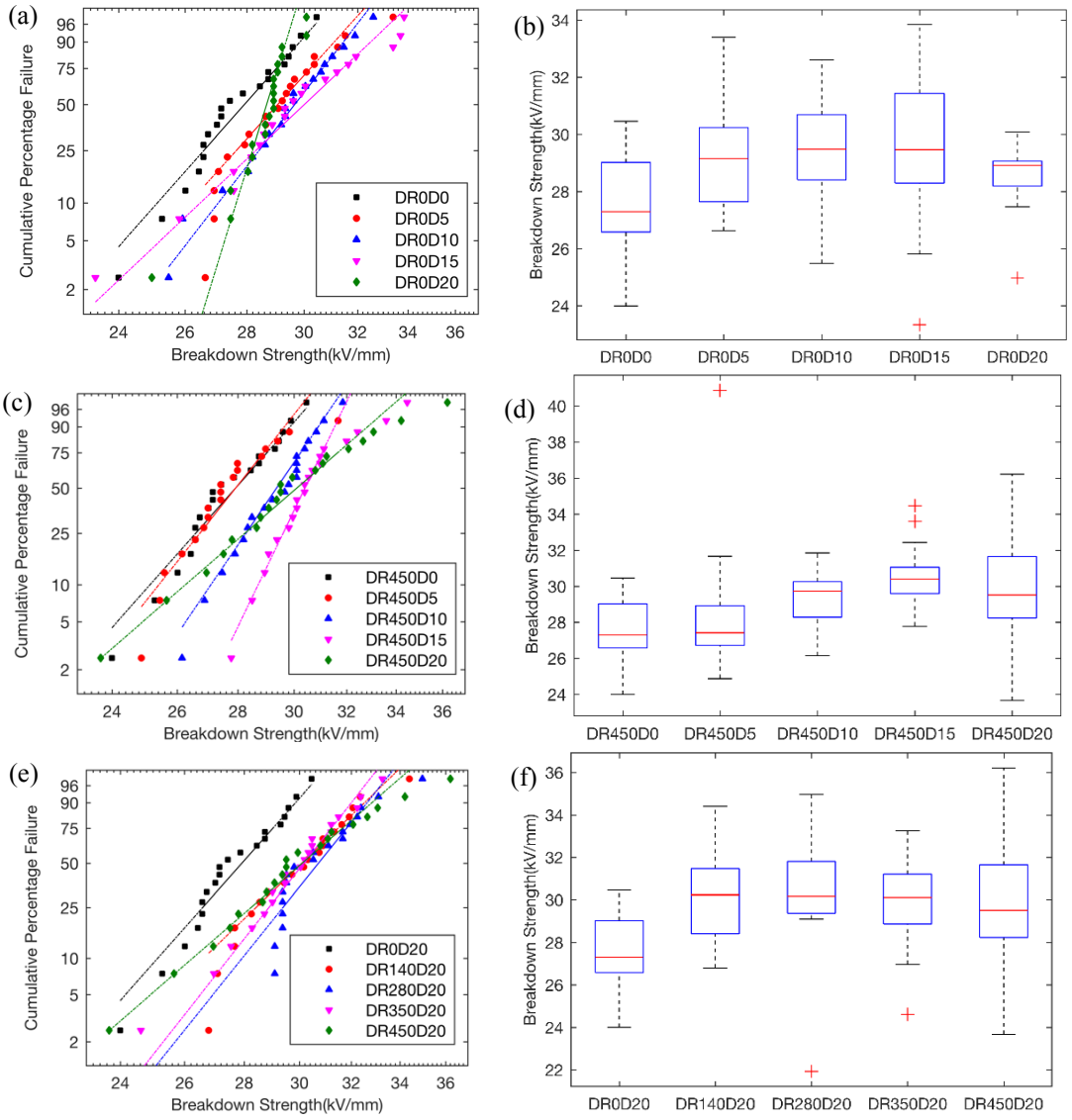

Figure 42. Dielectric breakdown strength presented as two-parameter Weibull plots (left column) and box plots (right column) for samples aged at 90 °C (a) and (b) thermally, (c) and (d) with simultaneous thermal and gamma radiation for different numbers of days at dose rate 450 Gy/h, and (e) and (f) for samples aged with simultaneous thermal and gamma radiation at various dose rates for 20 days.

Fourier-transform infrared (FTIR) spectroscopy

In Figure 43, Figure 44, and Figure 45, ATR-FTIR data acquired on all XLPE tape samples, Table 9, using the desktop Agilent 680 spectrometer are plotted for samples aged at 60, 90 and 115 °C, respectively. Each spectral line represents the average of five spectra measured on the same sample. With the ATR accessory, the lower end of these spectra is extended from 650 down to 400 cm^{-1} wavenumbers, showing additional spectral information in the wavenumber range from 500 to 550 cm^{-1}, which is attributed to the presence of DBDE. It appears that spectra clearly vary in this spectral range for samples aged at 60 and 90 °C, and less so for those aged at

115 °C. Elsewhere, in the hump at wavenumber 1,651 cm^{-1} and the upward shift observed for wavenumbers below 1,500 cm^{-1}, we also observe differences.

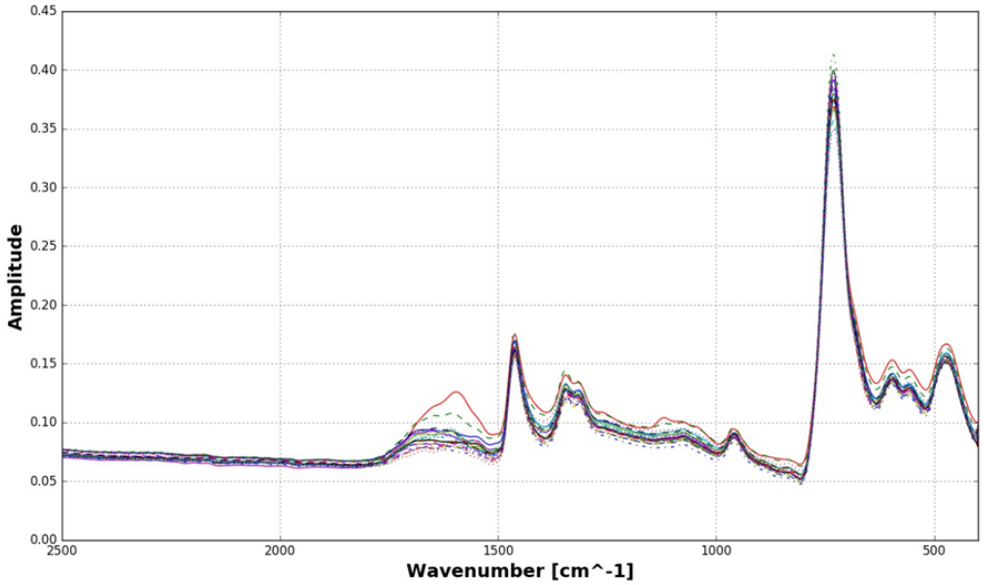

Figure 43. ATR-FTIR spectra of XLPE samples aged at 60 ℃ with various gamma radiation dose rates and total doses, Table 5.

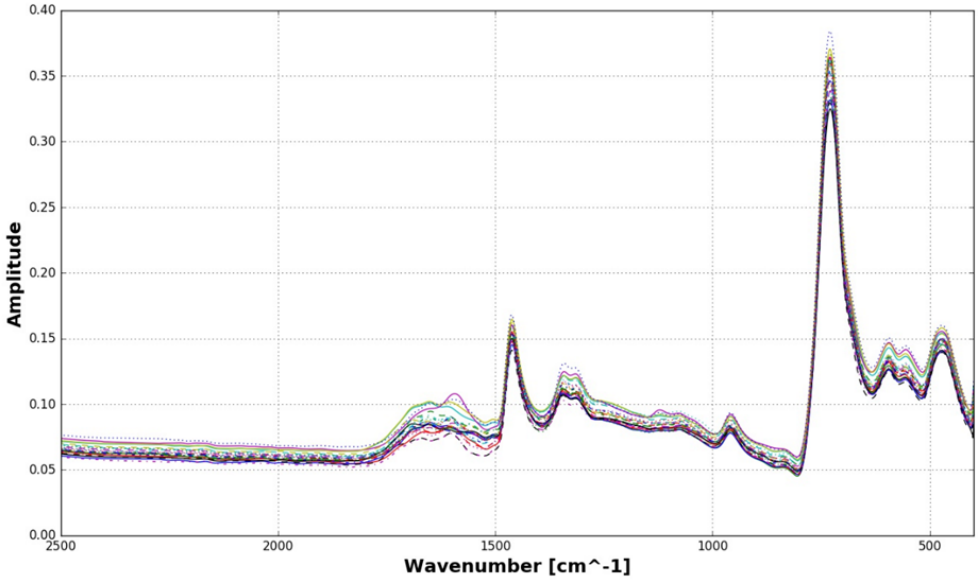

Figure 44. ATR-FTIR spectra of XLPE samples aged at 90 ℃ with various gamma radiation dose rates and total doses, Table 5.

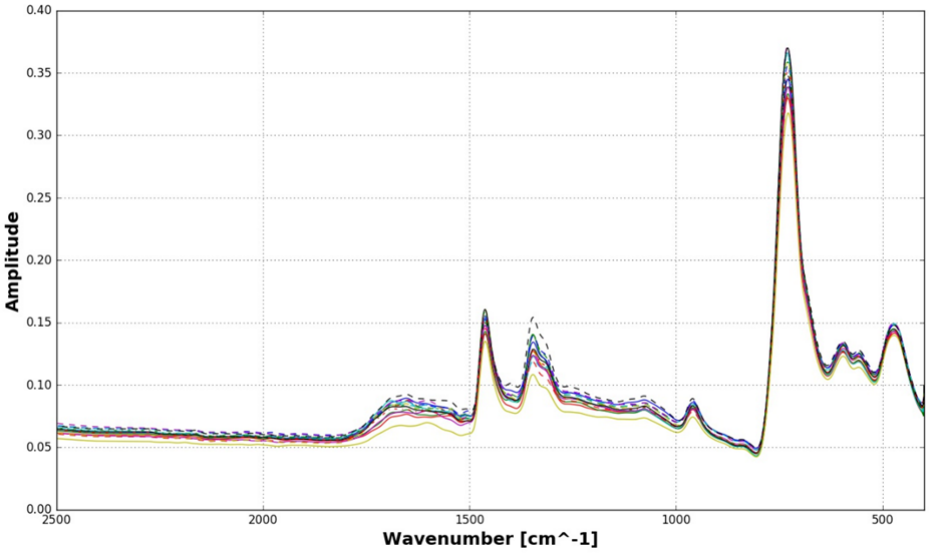

Figure 45. ATR-FTIR spectra of XLPE samples aged at 115 ℃ with various gamma radiation dose rates and total doses, Table 5.

Chemometric regression analysis by partial least-squares (PLS)

To further detect and quantify the aging mechanism and level of aging between the samples as indicated by the IR spectra, a partial least-squares (PLS) regression model was employed to analyze the FTIR data. The input data presented in PLS matrix form were the ATR-FTIR spectral columns by row of sample location. For the target variable, we selected total dose, presented as a vector for all sample locations, as the first parameter to be investigated. The results using 35 PE spectral data (7 samples with 5 repeats each) showed that even with five principal fitting components (or regression coefficients) the model predictions show a linear trend against the known experimental dose values. When the numbers of fitting components are increased to 100, the nearly perfect 1:1 (so-called 45° line) correspondence was reached between the model prediction and experimental data. Although this is the typical overfitting situation, it clearly shows that the PE spectral data are self-consistent and carry the needed feature to detect the dose difference.

Performing principal component analysis to determine the data distribution along the principal directions and the optimal number of principal components to be used in the analysis, the leave-one-out (jackknife) cross validation was conducted, which is evaluated by the so-called R-squared value (i.e. the coefficient of determination) on the quality of fitting between the model prediction and experimental data. The cross-validation of PE data is exceptional reaching R-squared value of 0.99 using 17 components and the spectra in the wavenumber range from 400 to 2500 cm^{-1}.

Testing the FTIR data measured on samples aged at 60 °C XLPE using all 24 available samples with five location repeats it was found that the PLS calibration performs very well. Figure 46 shows that the cross validation reaches its maximum 0.82 R-squared value with the first 23 principal components, using the wavenumber range from 400 to 2500 cm^{-1}. Using the first 23 principal components, the calibration obtains a very good fitting with R-squared value of 0.98, Figure 47. For samples aged at 90 °C, cross validation reaches 0.86 R-squared value with 10 components and maximum 0.91 R-squared value with 25 components. For samples aged at 115

°C, the cross validation maximizes with 28 components at 0.88 R-squared value, and again very good fitting with R-squared value of 0.99.

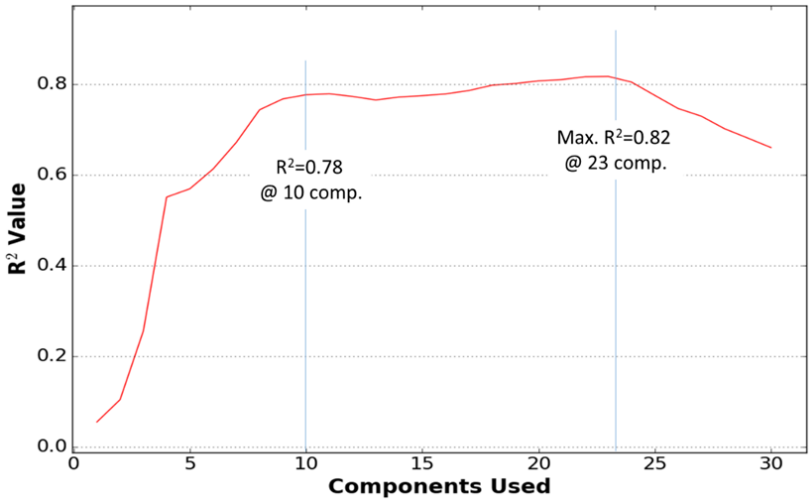

Figure 46. PLS cross-validation on FTIR data taken on XLPE samples aged at 60 °C, using data measured in the wavenumber range from 400 to 2500 cm^{-1}.

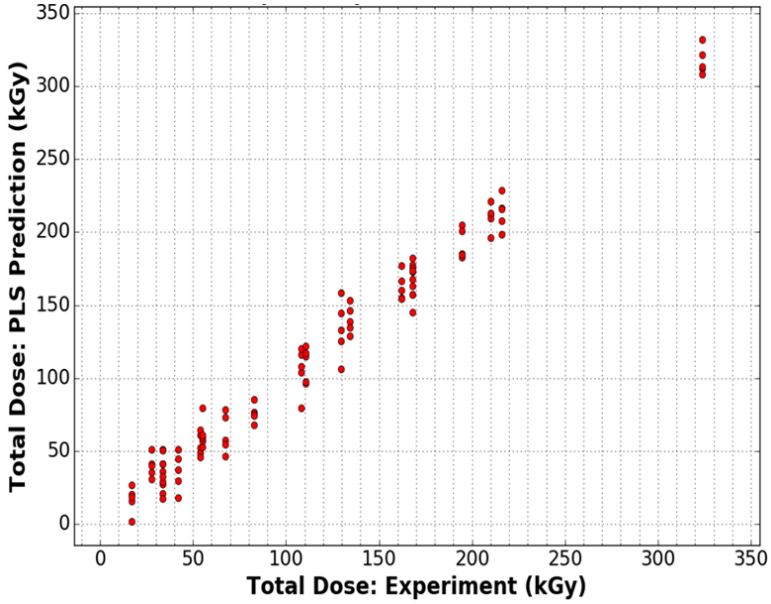

Figure 47. PLS calibration results on FTIR data taken on XLPE samples aged at 60 °C, using data measured in the wavenumber range from 400 to 2500 cm^{-1}, using the first 23 spectral components.

Classification by probabilistic neural network (PNN)

In addition to direct regression (as done via PLS), the classification of data by their specific characteristics is of interest e.g. classification of the IR data measured on samples aged at 60, 90 and 115 °C data based on these aging temperatures. As for the PLS analysis, the data used in the PNN classification process were the ATR-FTIR data acquired using the desktop Agilent 680 spectrometer. The sample sets consist of 24 XLPE tape samples aged at 60 °C, 24 aged at 90 °C and 16 aged at 115 °C, a total of 64 samples. Since the spectra of interest reside in the lower frequency region, in the PNN work we truncated the spectra at 2500 cm^{-1}, using only the

wavenumber range from 400 to 2500 cm^{-1}. The target variable is total dose, as it exhibits the most variation with distinct values associated with each sample.

We performed three types of tests. In the first test, the five repeated measurements on the same sample were averaged out so that each sample is represented by only the averaged data set, and the total 320 data sets reduce to 64. For the second test, three measurements were randomly selected from the five repeats and the data sets are only reduced to 192. For the third test, all 320 data sets were treated as independent data, although the five repeats were actually measured from the same sample. We then performed 1,500 test runs for each of the three types of tests with one training and one testing session in each run. In every test run, we randomly selected 20 % of the truncated spectral data sets from each of the 60, 90 and 115 °C classes and set those aside as testing data. The remaining data sets were used as training data. The 20 % randomized selection of the test data sets were constrained not to be repeated, so that the 1,500 test runs were truly independent. In the training session, we used the standard "leave-one-out", i.e. jackknife method to maintain training quality. From the histogram built on the 1,500 runs, first test (one average data per sample) has an average of 87 % and peak of 92 % data sets (spectra) correctly classified into the right categories according to aging temperature of the XLPE sample. In the case of the second test (three random selected data sets of five repeats) correctly classifies on average 78% of cases (Figure 48) and, in the case of the third test (in which all five repeats are used) results in 80% rate (Figure 49). For each of the three test types, some runs reach 100% and none of the 1,500 runs goes below 50% mark. We further tested classifying the data within a group by subdividing the 90 °C data into two subgroups according to 'low' (less than 100 kGy) and 'high' (greater than 100 kGy) total dose. Again, PNN delivers a promising performance with a mean 80 % correct classification of data into the two subgroups.

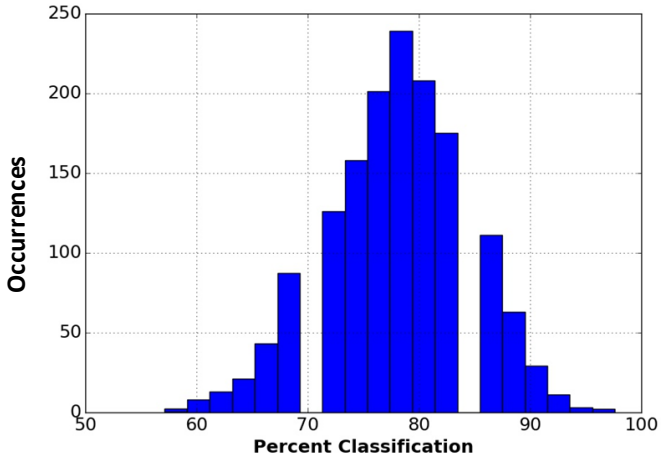

Figure 48. Number of occurrences of PNN percent correct classification of FTIR data according to aging temperature of the XLPE samples, using three sets of spectral data.

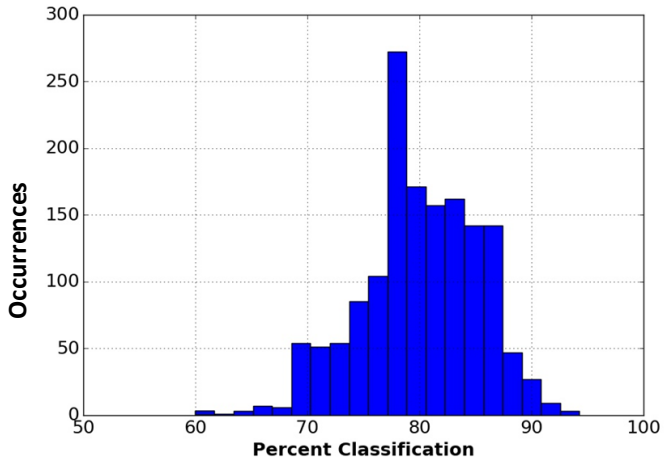

Figure 49. Number of occurrences of PNN percent correct classification of FTIR data according to aging temperature of the XLPE samples, using the full set of spectral data (five spectra).

Summary and Key Conclusions

Dielectric spectroscopy and dielectric breakdown strength

- No significant change in loss tangent was observed for XLPE aged thermally without gamma radiation;
- Dielectric loss tangent has been demonstrated to be a promising indicator of XLPE aging due to gamma radiation exposure, showing significant increase as exposure increased. This suggests that dielectric loss tangent is a sensitive indicator of XLPE material changes associated with radiation exposure;
- For samples aged at 90 °C, dielectric breakdown strength declined as gamma radiation exposure increased. No significant change in dielectric breakdown strength was observed for XLPE aged thermally without gamma radiation, or for samples aged at 60 °C with gamma radiation.

Fourier-transform infrared (FTIR) spectroscopy

- ATR has been found to be particularly effective for measuring spectra from thick and opaque PE and XLPE samples. ATR-FTIR data were collected without any alteration to or further preparation of the samples;
- Oxidation of the samples is clearly seen from the appearance of the strong spectral peak at wavenumber 1,710, associated with the C=O bond, and a rise in the baseline below 1,500 cm^{-1};
- The relative infrared intensity difference between samples of the same pool (e.g. the E-series) should allow quantification of the aging effects due to the distance to the gamma radiation source (i.e. dose rate), exposure time (i.e. total dose), etc;
- The PLS regression model works quite well in predicting total dosage from ATR-FTIR spectral data. The R-squared values for all four sample categories are at least 0.82, indicating a strong robustness;
- The PNN classification of sample groups according to aging temperature was tested with 1,500 independent runs at each of the three aging temperatures and the mean correct classification was found to be at least 78 %;

- The PNN classification of samples further into groups according to high and low total gamma radiation dose received, within the group of samples aged at 90 °C, was demonstrated.

General

- FTIR and oxygen percentage tests showed that thermal aging with radiation generated –OH and C=O bonds, whereas thermal aging without radiation generated only C=O bonds.

References

1. S. Liu, "Composition identification, aging mechanisms and nondestructive aging indicator of commercial filled cross-linked polyethylene (XLPE) cable insulation materials," PhD thesis, Dept. Mater. Sci. Engng., Iowa State Univ., Ames, IA, 2017. Online at: https://lib.dr.iastate.edu/cgi/viewcontent.cgi?article=7172&context=etd
2. L. Fifield, S. Liu and N. Bowler, "Simultaneous Thermal and Gamma Radiation Experimental Facility for Materials Accelerated Aging," *2016 Conference on Electrical Insulation and Dielectric Phenomena*, Toronto, Canada, pp. 11-14.
3. NIST Chemistry Webbook. Online at: https://webbook.nist.gov/cgi/cbook.cgi?Name=Decabromodiphenyl+ether+&Units=SI&cIR=on
4. S. Krimm, C. Y. Liang and G. B. B. M. Sutherland, "Infrared Spectra of High Polymers II Polyethylene," J. Chem. Phys., 25, 3, 1956, 549-562.
5. Z. Shao, M. I. Byler, S. Liu, N. Bowler, L. S. Fifield, and M. K. Murphy, "Dielectric Response of Cross-Linked Polyethylene (XLPE) Cable Insulation Material to Radiation and Thermal Aging," *2nd IEEE International Conference on Dielectrics (ICD2018)*, Budapest, Hungary, July 1-5, 2018.
6. "IEEE Guide for the Statistical Analysis of Electrical Insulation Breakdown Data," IEEE Std 930-2004 (Revision of IEEE Std 930-1987), 2005.

1.5 Develop models of mechanical property changes and polymer changes due to aging

The development of models of spectral changes due to aging was completed in the second quarter of Year 3. A kinetic rate model describing chain scission and cross-linking in polyethylene, stimulated by gamma radiation, was completed in the first quarter of Year 4 (during the no-cost extension period).

Hypotheses

- Molecular dynamics simulations may be employed to predict changes in mechanical properties (stress-stain curves), infrared and Raman spectra for polyethylene that has been oxidized to varying degrees;
- A kinetic rate model that correctly captures the reactions occurring in irradiated polyethylene can account for changes in the degree of cross-linking and chain scission that occur in the material as aging progresses;
- Through these simulations, the mechanisms at work in radiation-induced, thermo-oxidative aging of polyethylene are better explained.

Approach

Mechanical properties

This section includes a summary of work published in B. Z. Xu, N. Bowler, and S. P. Beckman, First Principles and Molecular Dynamics Modeling Investigation on Polyethylene, *Annual Conference on Electrical Insulation and Dielectric Phenomena*, Toronto, Canada, October 16-19, 2016. Online at: http://ieeexplore.ieee.org/document/7785553/

Mechanical stress-strain curves for polyethylene as it ages via oxidation are developed using molecular dynamics simulations. The work also includes calculations of infrared and Raman spectra for various degrees of oxidation of polyethylene.

Classical potential molecular dynamics calculations

Polyethylene is modeled using classical potentials and a united atom model. The classical Lennard-Jones interatomic potentials are used within the LAMMPS molecular dynamics software [1]. A Nose-Hoover thermostat is used to regulate the system temperature [2]. The simulations are performed for three chain lengths, comprised of 100, 1000, and 2000 monomers, with two different numbers of chains, 10 and 20, resulting in a total of 10^4-10^5 atoms. The impact of temperatures and strain rate are also considered for each stress-strain response curve. A total of 30 simulations are performed and averaged to account for the statistical variation found in the polymer system.

Amorphous polyethylene

The initial chain structure of amorphous polyethylene is created using a previously reported Monte Carlo, self-avoiding random walk method [3]. A face-centered cubic lattice is superimposed on the simulation cell with the nearest neighbor distance of 1.55 Å, which is the spacing between the ethylene monomers in the polymer chain. Monomers are added to the lattice in a probabilistic stepwise manner. The probability of chain growth in a given direction is based on the bond angle and equilibrated at 0 K in the LAMMPS software to generate the amorphous polymer structure used in the molecular dynamics simulations. The simulation begins by thermalizing the structure for 5×10^5 time steps using NVT dynamics at 500 K. Next the system

is cooled to the desired simulation temperature where it is held for an additional 5×10^5 time steps. The amorphous polyethylene is then deformed under a uniaxial tensile strain and the mechanical response is simulated. The amorphous polyethylene structure, represented using the united atom model, is shown in Figure 50.

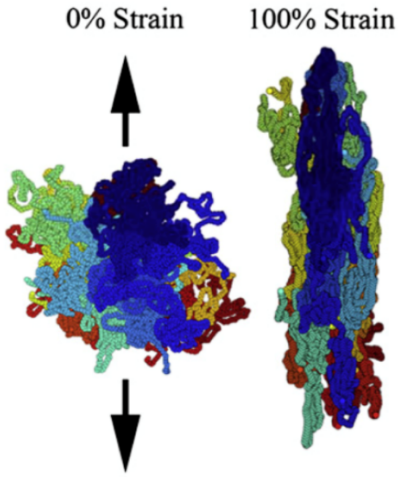

Figure 50. The atomic structure for 10 chains of polyethylene each with a length of 1000 monomers in a united atom representation. Each color represents a different polymer chain. On the left is the relaxed structure prior to straining and on the right is a system after 100% uniaxial strain is applied.

Scission versus crosslinking using a kinetic rate model

This section includes a summary of work to be published in Irmak Sargin, and Scott P. Beckman, "Crosslinking and chain scission of irradiated polyethylene," *IEEE Trans. Dielectr. Electr. Insul.*, to be submitted. The draft manuscript is included in the Appendix of this report.

Chain scission and crosslinking are two modes of damage that are of particular interest. Two common types of electrical insulation used in nuclear power plants are ethylene propylene rubber and cross-linked polyethylene, hence, here we focus on polyethylene. We present a kinetic rate model to investigate the concentrations of chain scission and crosslinking in polyethylene as a function of radiation dose, temperature, and time. Our preliminary work, shown here, follows closely the pioneering work of Min *et al.* [4]. The results here assume a homogeneous isotropic system, i.e., a mean field model. Two environmental parameters are selected: radiation dose rate, which is selected to mimic accelerated aging experiments and oxygen diffusion, which is taken in two limits that likely bracket the actual behavior.

Significant results

Mechanical properties

The molecular dynamics calculated stress-strain curves for varying chain lengths and number of chains are shown in the top plot of Figure 51. The chain length takes values 100, 1000, and 2000 -mers, the numbers of chains takes values of 10 and 20, while the temperature is fixed at 250 K and strain rate at 10^9/s. The middle plot in figure 2 shows the calculated stress-strain curves when the chain number/length is held fixed at 10/1000 -mer, the strain rate is fixed at 10^9/s and the temperature is varied over the values 250, 295, 320, 350, and 380 K. The stress-strain curves for strain rates 10^7, 10^8, 10^9, 10^{10}, and 10^{11}/s, with fixed chain number/length, 10/1000 -mer, and temperature, 250 K, are shown in the bottom plot of Figure 51.

The stress-strain curves in Figure 51 have three distinct regimes: elastic, softening, and hardening. Initially the stress increases almost linearly, which indicates an elastic regime and corresponds to the stretching of bonds. After reaching a local maximum, called the upper yield point, plastic deformation begins. The initially pinned polymer chains become mobile and move past one another to align. The alignment occurs with relative ease and is a region of softening. At the so-called lower yield point softening ends and hardening begins. The polymer chains no longer slide past each other simply and additional force is needed to plastically deform the system. Examining the top plot in Figure 51 it is observed that the chain length has a greater impact on the stress-strain curves than the number of chains. Increasing the length of the polymer leads to a higher strength due to chain entanglement. From the middle plot it is found that at elevated temperatures the upper yield point is depressed. This is due to thermal contributions to overcoming the pinning of polymer chains. It can be approximated that the upper yield points disappear for $T > 335$ K. This suggests that the pinning must have an energy barrier of approximately 29 meV. In addition, the impact of temperature on strength can be observed in the hardening regime, where again thermal fluctuations play a significant role the plastic deformation processes, resulting in a reduced strength.

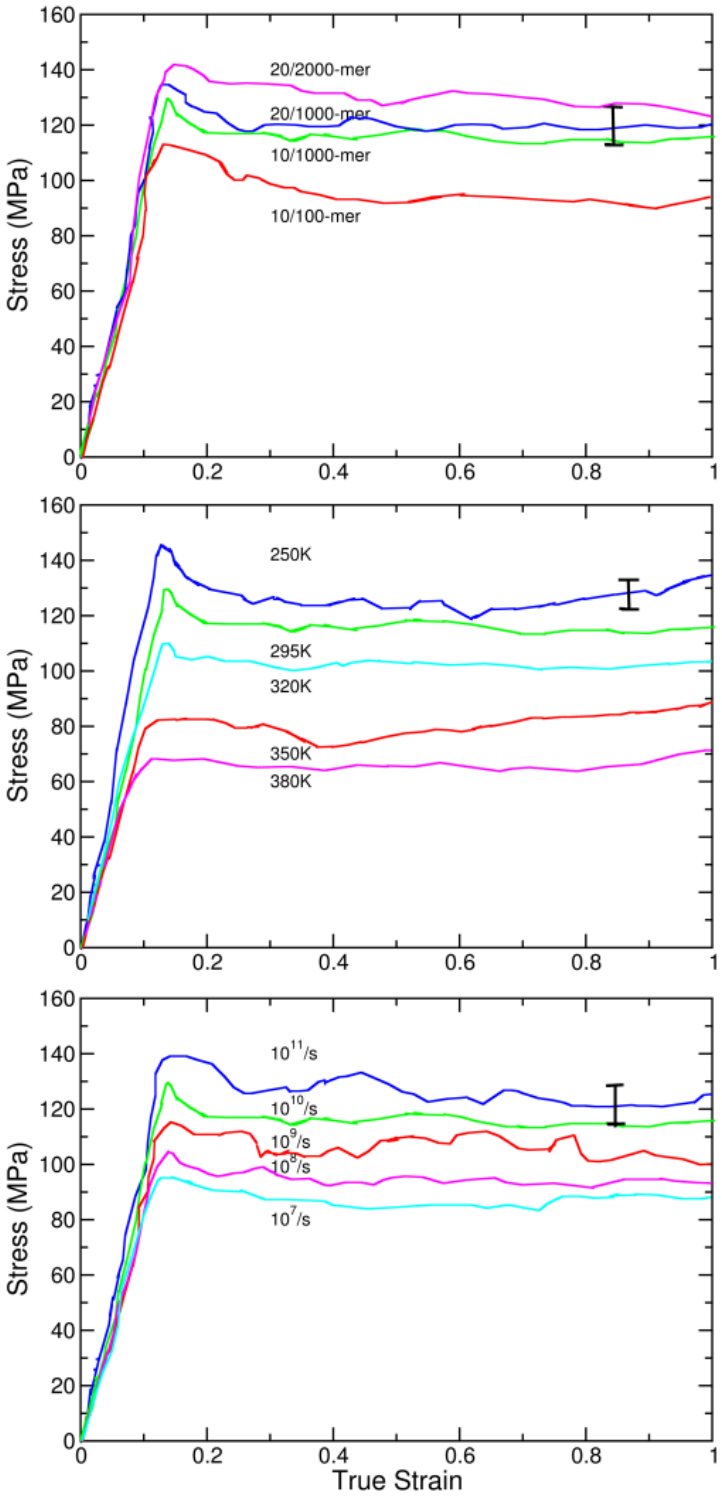

Figure 51. Stress-strain relations for amorphous polyethylene. The top plot shows the stress-strain relations at different chain number/lengths. The middle plot shows the stress-strain relations of different temperatures. The bottom plot shows the stress-strain relations at different strain rates. The error bars shown on select curves come from 30 statistically independent calculations and are characteristic of the uncertainty in all of the calculations.

Scission versus crosslinking using a kinetic rate model

Radiation parameters of 50 and 100 Gy/hr and an exposure of 1 day are picked to mimic accelerated aging experiments that have dose rates on the order of 100-300 Gy/hr and exposure periods of days to weeks. To compare to an extremely low dose rate, which is still greater than true *in situ* rates, we also examine 0.1 Gy/hr. The initial oxygen concentration is defined as the concentration of O_2 in air at standard temperature and pressure. Although this is likely high, it is a reasonable first approximation. For infinitely slow diffusion, the oxygen concentration never replenishes once consumed. For the infinitely fast diffusion, the oxygen concentration is constant. The concentration of polyethylene is the density of low-density polyethylene. The concentration of all radicals and reaction products is defined as zero. The results are plotted in Figure 52.

It can be seen from Figure 52 that the alkyl radicals generated by irradiation persist after the source is removed, diffuse relatively slowly, and are not easily eliminated from the system, allowing for damage to accrue over time. For relatively high dose rates, the damage increases by about an order of magnitude the week after irradiation and for low dose rates the damage increases by two orders of magnitude. The concentration of damage sites scale non-linearly with total dosage, decreasing the dose rate by three orders of magnitude decreases the damage by nine orders of magnitude. Both the crosslinking and scission data have positive curvature during the exposure, and the crosslinking curve has greater slope. After the source is removed the curvature of the crosslinking data becomes negative and eventually the two intersect. The time prior to intersection seems to scale with the total dosage. Increasing the oxygen concentration increases the rates of reaction and pushes the intersection point to greater times. However, there is no significant difference between the infinitely fast and infinitely slow O_2 diffusion results.

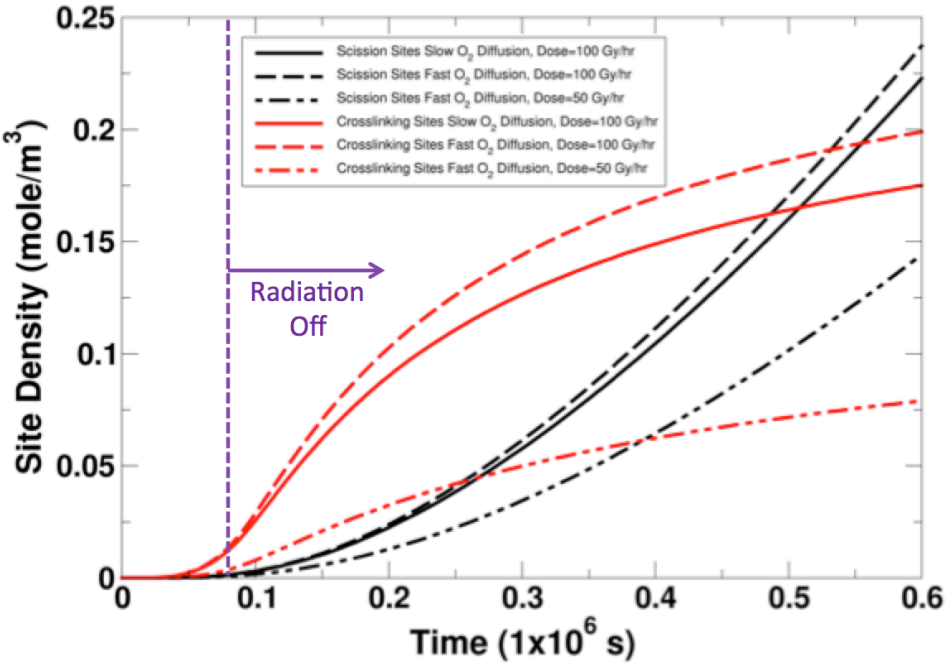

Figure 52. Scission and crosslinking sites density as a function of time for different dose rates.

Summary and Key Conclusions

Mechanical properties

Molecular dynamics simulations have shown:

- The polymer chain length has a greater impact on the stress-strain curves than the number of chains.
- Increasing the length of the polymer leads to a higher strength due to chain entanglement.
- At elevated temperatures, the upper yield point is depressed due to thermal contributions to overcoming the pinning of the polymer chains.
- The impact of temperature on strength can be observed in the hardening regime, where again thermal fluctuations play a significant role the plastic deformation processes, resulting in a reduced strength.

Scission versus crosslinking using a kinetic rate model

A mean field kinetic rate model has been used to investigate the concentrations of scission and crosslinking over time for different dose rates. The most important implications from these results are:

- For low total doses, crosslinking reactions are dominant;
- For high dose rates, such as those used in accelerated aging experiments, there is a lengthy transient time during which the reactions continue post-irradiation. These effects are the result of continuing chain scission after the radiation is turned off;
- The calculated effect of temperature on diffusion indicates that the post-irradiation specimen storage temperature is more important than the exposure temperature;
- As radiation dose rate is reduced, the concentration of scission damage sites dominates over cross-linking - for extremely low dose rates scission dominates the behavior even during the irradiation process;
- Analytical models for crosslinking and chain scission concentrations have been developed, that predict both irradiation and post-irradiation durations and crossover points;
- The agreement between the kinetic and analytical models shows that such models can be used as an alternative to the empirical superposition approach to describing polymer aging.

References

1. S. Plimpton, Fast Parallel Algorithms for Short-Range Molecular Dynamics. Journal of Computational Physics, 117, 1-19 (1995).
2. S. Nose, A Unified Formulation of the Constant Temperature Molecular Dynamics Methods. The Journal of Chemical Physics, 81, 511 (1984).
3. K. Binder, Monte Carlo and Molecular Dynamics Simulations in Polymer Science. Oxford University Press; 1995.
4. D. Min, S. Li, N. Hirai and Y. Ohki, Modeling of Oxidation Process and Property Changes of Ethylene-Propylene-Diene Copolymer. *IEEE Transactions on Dielectrics and Electrical Insulation*, 23, 537-548 (2016).

2 Identify spectral indicators due to aging

The identification of spectral indicators due to aging relied upon availability of characterization data. The task was completed at the end of the third quarter of Year 3 (June 30, 2017).

Hypothesis

- Through statistical analysis the most sensitive indicators of polymer-based insulation material aging can be determined;
- Multiple linear regression models can be used to construct equations that predict the values of one dimension as a function of dose rate and total dose (number of days of exposure).

Approach

Two statistical approaches have been used in identifying key indicators of nuclear power plant cable insulation degradation, Principal Component Analysis (PCA) and Pearson product-moment correlation coefficient.

PCA is used to reduce the dimensionality of a data set which consists of a large number of interrelated variables, while retaining as much as possible of the variation present in the original data set. This is done by linear transformation of an original set of variables into a smaller set of variables called Principal Components (PCs). Principal components are uncorrelated and ordered so that the first few retain most of the variation present in all of the original variables.

In this study, PCA is used for finding polymer characterization methods that show maximum variation and for extracting key indicators of insulation aging. The characterization data set consists of seven kinds of single-point data and three kinds of spectral data therefore the total data set carries ten dimensions that need to be analyzed. The anticipated outcome of applying PCA is to develop a small number of principal components, lower than the number of measurement types, to provide a reasonable characterization of the data set measured on the aged polymer material. Principal component analysis will be continued in an expanded scale in future when more characterization data becomes available.

The Pearson product-moment correlation coefficient (Pearson's correlation) is a measure of the strength of the linear relationship between two variables. The correlation coefficient **r** provides both the strength and direction of the relationship between variables. Values of r can be in the range from -1 to 1. The value -1 indicates perfect negative correlation between two variables, 0 indicates no linear relationship and 1 indicates a perfect positive linear relationship between variables. During the collection of all the data needed to perform PCA we are looking at Pearson correlation as a preliminary way of observing the correlations between measured variables and total gamma-radiation dose or dose rate.

Complete results of this task are available in the MS thesis by Chamila De Silva, "Principal component analysis (PCA) as a statistical tool for identifying key indicators of nuclear power plant cable insulation degradation," MS thesis, Dept. Mater. Sci. Engng., Iowa State Univ., Ames, IA, 2017. Online at:
https://lib.dr.iastate.edu/cgi/viewcontent.cgi?article=7127&context=etd

A summary was also presented in the conference paper: C. C. De Silva, S. P. Beckman, S. Liu, and N. Bowler, Principal Component Analysis (PCA) as a Statistical Tool for Identifying Key Indicators of Nuclear Power Plant Cable Insulation Degradation, *18th International Conference on Environmental Degradation of Materials in Nuclear Power Systems – Water Reactors*, Portland, Oregon, USA, August 13-17, 2017, pp. 11-23. Online at: https://link.springer.com/chapter/10.1007/978-3-319-68454-3_2

The MS thesis abstract is reproduced here for convenience.

Thesis Abstract

This thesis describes the use of Principal Component Analysis (PCA) as a statistical method to identify key indicators of degradation in nuclear power plant cable insulation. Seven kinds of single-point data* were measured on cross-linked polyethylene (XLPE) that had undergone aging at various doses and dose rates of gamma radiation from a cobalt 60 source, and at various elevated temperatures. To find the key indicators of degradation of aged cable insulation, PCA was used to reduce the dimensionality of the data set while retaining the variation present in the original data set. The analysis revealed that, for material aged at both 60 °C and at 90 °C, oxidation induction time and elongation at break data have the greatest negative correlations with the total dose to which the sample has been exposed. Furthermore, multiple linear regression models were used to construct equations that predict the values of one dimension as a function of dose rate and total dose (number of days of exposure). In this data set, oxidation induction time was found to be the only dimension that was successfully predicted via multiple regression equations for XLPE samples aged at both 60 °C and at 90 °C.

*Single-point data were: oxidation induction time (min), indenter modulus (Nm^{-1}), insulation mass loss (%) (both without and with central conductor), elongation-at-break, and density ($g\ cm^{-3}$) (both without and with central conductor).

Summary and Key Conclusions

- OIT was shown to exhibit a strong correlation with aging conditions;
- The strong correlation between OIT and the aging conditions was a critical factor in obtaining a satisfactory multiple linear regression model relating OIT and aging conditions;
- For material aged at 90 °C, elastic modulus shows a positive correlation with total dose while mass loss, oxidation induction time and density show negative correlations with the same parameter.

3.1 Accelerated aging of cables

As for task 1.2, cables were aged thermally without and with gamma ray exposure at the High Exposure Facility, Pacific Northwest National Laboratory.

Hypotheses

- Accelerated aging of intact wires and cables, rather than pure polymer samples, most closely mimics cable aging in the service environment;
- A large number of aging conditions achieved in one aging experiment can help to reveal the effects of dose rate and total dose on associated cable property changes.

Approach

XLPE-insulated wires

One set of samples comprised XLPE-insulated wires shown in Figure 5 at right, with approximate diameter 2.79 mm and insulation thickness approximately 0.64 mm, Table 2. These were aged as described in Section 1.2 Accelerated Aging of Samples. Two insulated wire samples were exposed at selected locations with respect to the gamma radiation source, for times from 120 to 600 hours. In this way, approximately 60 cross-linked polyethylene (XLPE)-insulated wire samples were prepared for both 60 °C and 90 °C series exposure temperatures.

EPR/PVC cables

Another set of samples comprised eighteen EPR/PVC cable samples, Figure 53, of approximately 45 cm in length, and aged thermally at 140 °C in an air-circulating oven for various durations up to 53 days. The three multi-strand copper conductors are approximately 1.84 mm diameter. The EPR-insulated wires (black, pink, and blue EPR) are approximately 3.40 mm diameter. The black PVC jacketed cable is approximately 10.4 mm diameter.

Summary and Key Conclusions

In relation to the hypotheses mentioned above,

- Aging of intact wires and cables, rather than pure polymer samples, allowed evaluation of characterization methods that may eventually be field-deployable, reported in Section 3.2 Measure broadband capacitance on cables;
- The effects of dose rate and total dose on associated cable property changes was observed, reported in Section 3.2 Measure broadband capacitance on cables.

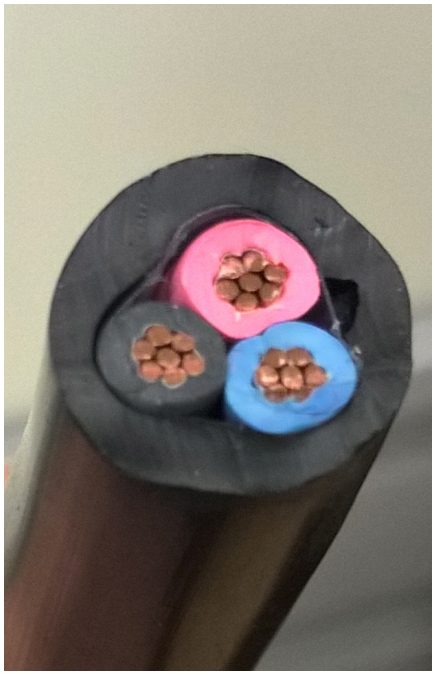

Figure 53. Photograph of EPR-insulated, PVC-jacketed three-conductor cable.

3.2 Measure broadband capacitance on cables

This task was scheduled to begin in the third quarter of Year 2 (April 1, 2016) and in fact began August 16, 2016, when a student dedicated to this aspect of the project was able to begin work. At the end of Year 2, interdigital sensor design was progressing well but the student then departed Iowa State University for personal reasons. Rather than completing this work at the end of the second quarter in Year 3, as originally planned, it proceeded into the fourth quarter of Year 3 and was completed on November 30, 2017. A second type of broadband capacitance measurement, beyond that originally proposed for this project, was pursued through a funded collaboration with the University of Bologna, Italy, that provided additional leveraging of the effort on this project and is reported under this NEUP project as well.

Hypotheses

- The capacitance and/or dissipation factor measured by an interdigital capacitive sensor applied to the exterior of an insulated wire can provide information about the condition of the polymeric insulation;
- A distributed measurement of capacitance made upon an intact, multi-conductor cable by applying a potential difference across its conductors can provide information about the condition of the polymeric insulation.

Approach

XLPE-insulated wires

Sample preparation

Samples were prepared as describe in Section 3.1 Accelerated aging of cables. The samples were hung on a rack, which was then placed in an oven inside the high exposure facility (HEF) at Pacific Northwest National Laboratory (PNNL). Simultaneous thermal and gamma radiation aging of the samples is achieved by putting the oven in the radiation environment and controlling the oven temperature. The dose rate to each individual sample depends primarily on its distance from the radiation source. Various radiation doses to the samples were achieved by aging them for different periods of time. Different aging temperatures were achieved by running multiple rounds of experiment at 60, 90, and 115 ˚C, respectively.

Table 10 displays the aging conditions of the samples studied in this task.

Samples were stored in a low-humidity (dessicant) environment when not being tested, to reduce the influence of moisture on the measurements. To clean the samples, a static free paper napkin was used to wipe the sample prior to measurement.

Capacitance measurements

Capacitance measurements were made using a custom interdigital capacitive sensor reported elsewhere [1]. The capacitive sensor was connected to an LCR meter via an SMA cable, positioned securely, and an open/short calibration conducted prior to measurement, with the calibration reference plane being the end of the SMA cable that connects to the wires feeding the sensor.

Table 10. Aging conditions of the studied XLPE-insulated wire samples.

Name	Dose rate (Gy/h)	Aging Days	Total Dose (kGy)
DR0D0	0	0	0
DR0D5	0	5	0
DR0D10	0	10	0
DR0D15	0	15	0
DR0D20	0	20	0
DR450D0	450	0	0
DR450D5	450	5	54
DR450D10	450	10	108
DR450D15	450	15	162
DR450D20	450	20	216
DR0D20	0	20	0
DR140D20	140	20	67.2
DR280D20	280	20	134.4
DR350D20	350	20	168
DR450D20	450	20	216

Figure 54. Photograph of interdigital capacitive sensor described elsewhere [1]. The sensor accommodates wires with diameter up to approximately 3 mm. Number of electrode digits: N = 14, width of each digit: w = 0.1 mm, separation between each digit: g = 0.3 mm, and digit length: l = 25 mm.

Data was collected over the frequency range 2 kHz to 200 kHz with data points distributed evenly on a $\log_{10}$ scale. Ten measurements were made per sample, five by simply translating the sensor to different positions along the sample length, and five more after the sample was rotated by 90°. Reported data is the average of these ten values collected at each frequency. Reported uncertainties comprise the standard deviation of these recorded values.

EPR/PVC three-conductor cables

The capacitance of intact, thermally-aged EPR/PVC cable was measured by connecting the conductor ends to either positive voltage or ground, in sequence, and measuring the capacitance

over frequency range from 0.01 Hz to 1 MHz for the purpose of seeking an indication of aging in the EPR insulation by change of its permittivity.

Complete results of this task are available in the MS thesis by Mario Vincenzo Imperatore, "Dielectric spectroscopy as a condition monitoring diagnostic technique for thermally aged PVC/EPR nuclear power plant cables," MS thesis, Dept. Electr. Inform. Engng., Univ. Bologna, Bologna, Italy, 2016. Online at: http://amslaurea.unibo.it/13002/

A summary was also presented in the conference paper: M. V. Imperatore, L. S. Fifield, D. Fabiani, and N. Bowler, Dielectric Spectroscopy on Thermally Aged, Intact, Poly-vinyl Chloride/Ethylene Propylene Rubber (PVC/EPR) Multipolar Cables, *Annual Conference on Electrical Insulation and Dielectric Phenomena*, Fort Worth, TX, USA, October 22-25, 2017, pp. 173-176. Online at: http://ieeexplore.ieee.org/document/8257522/

An extract from the thesis abstract is reproduced here for convenience.

Thesis Abstract Extract

Among these, dielectric spectroscopy has proven itself an excellent diagnostic technique to assess the state of low-voltage NPP cables but literature regarding the effect of ageing on electrical properties of low-voltage insulation is still lacking and the long-term relations between physical/chemical degradation mechanisms and electrical property variations have not been studied in detail for low-voltage cable materials, especially for intact, multi-polar cables. Therefore this thesis aims at contributing to the studies about the impact of ageing on cable electrical parameters, in order to understand the evolution of these with cable degradation.

This thesis work, conducted at the Iowa State University in Ames, USA, in particular, has the purpose to perform dielectric spectroscopy measurements on thermally-aged, whole, intact, three-polar, low voltage cable samples. With a special consideration to the Non-Destructive aspect, philosophy of this method is that the assessment of cable state can be carried out without the need to destroy the cable section during the measurement, as it happens for techniques like EaB, so that it can be put back in its original position after the measurement. According to this philosophy, furthermore, a potential continuation in this subject could be the extension of this method to on-line measurements, with proper methods, which would mean also losing the need to interrupt NPP service to assess cable state.

The conference paper abstract is reproduced here for convenience.

Conference Paper Abstract

As a contribution to condition monitoring diagnostics on low voltage cables used in nuclear power plants, this work shows that broadband dielectric spectroscopy can be an effective technique to assess aging state of these cables. Broadband dielectric spectroscopy has been performed on three-conductor (tri-core) cables, insulated by EPR with PVC jacket. The main challenge has been to perform the measurement on the intact cables, by means of a custom-built connector, conceiving a non-destructive and non-intrusive technique. Results show that capacitance and dissipation factor can provide information about the aging state of the cable, without the need to destroy the sample in the measurement process.

Sample preparation

Eighteen cable sections, each about 45 cm long and taken from a reel of Okonite® - FMR® Okoseal® low voltage cable, were thermally aged for different durations. The cable sections were aged in a mechanical convection oven at 140 °C for durations up to 53 days (1,269 hours).

Significant Results

XLPE-insulated wires

Capacitance and loss tangent measured upon pristine and aged XLPE-insulated wire samples are plotted in Figure 55 through Figure 60. Data for samples aged at 60 °C are plotted in Figure 55, Figure 56, and Figure 57 which show results for samples aged thermally at 60 °C in the absence of gamma radiation (Figure 55), aged at 60 °C and exposed to gamma radiation at dose rate 450 Gy/h for 0, 5, 10, 15, and 20 days (Figure 56), and aged thermally at 60 °C and exposed to gamma radiation at dose rates 0, 140, 280, 350, and 450 Gy/h for 20 days (Figure 57). A similar set of data for samples aged at 90 °C are plotted in Figure 58, Figure 59, and Figure 60 which show results for samples aged thermally at 90 °C in the absence of gamma radiation (Figure 58), aged at 90 °C and exposed to gamma radiation at dose rate 450 Gy/h for 0, 10, 15, and 20 days (Figure 59), and aged thermally at 90 °C and exposed to gamma radiation at dose rates 0, 140, 280, 350, and 450 Gy/h for 20 days (Figure 60).

All these results show an increase in capacitance and loss tangent after aging. In the case of samples aged thermally in the absence of gamma radiation, measured capacitance increases by approximately 0.2 pF (2.6 %) for samples aged at 60 °C and by approximately 0.15 pF (2.0 %) for samples aged at 90 °C, over the frequency range from 2 kHz to 200 kHz. Loss tangent increases by up to approximately 0.001 (~30 %) for all samples. All of the data sets show a significant distinction between the measured value of capacitance and loss tangent for the pristine sample and for the aged samples. The uncertainty associated with the capacitance and loss tangent measured on each sample is sufficiently small that the pristine and aged samples can be distinguished from each other, but is sufficiently large that capacitance and loss tangent measured on the aged samples cannot be distinguished from each other in terms of aging duration, total dose received, or rate of gamma radiation dosage.

EPR/PVC three-conductor cables

Elongation-at-break and specific capacitance measured at 10 Hz are compared in Figure 61 for the three colors of EPR that exist in the tri-core cable under test.

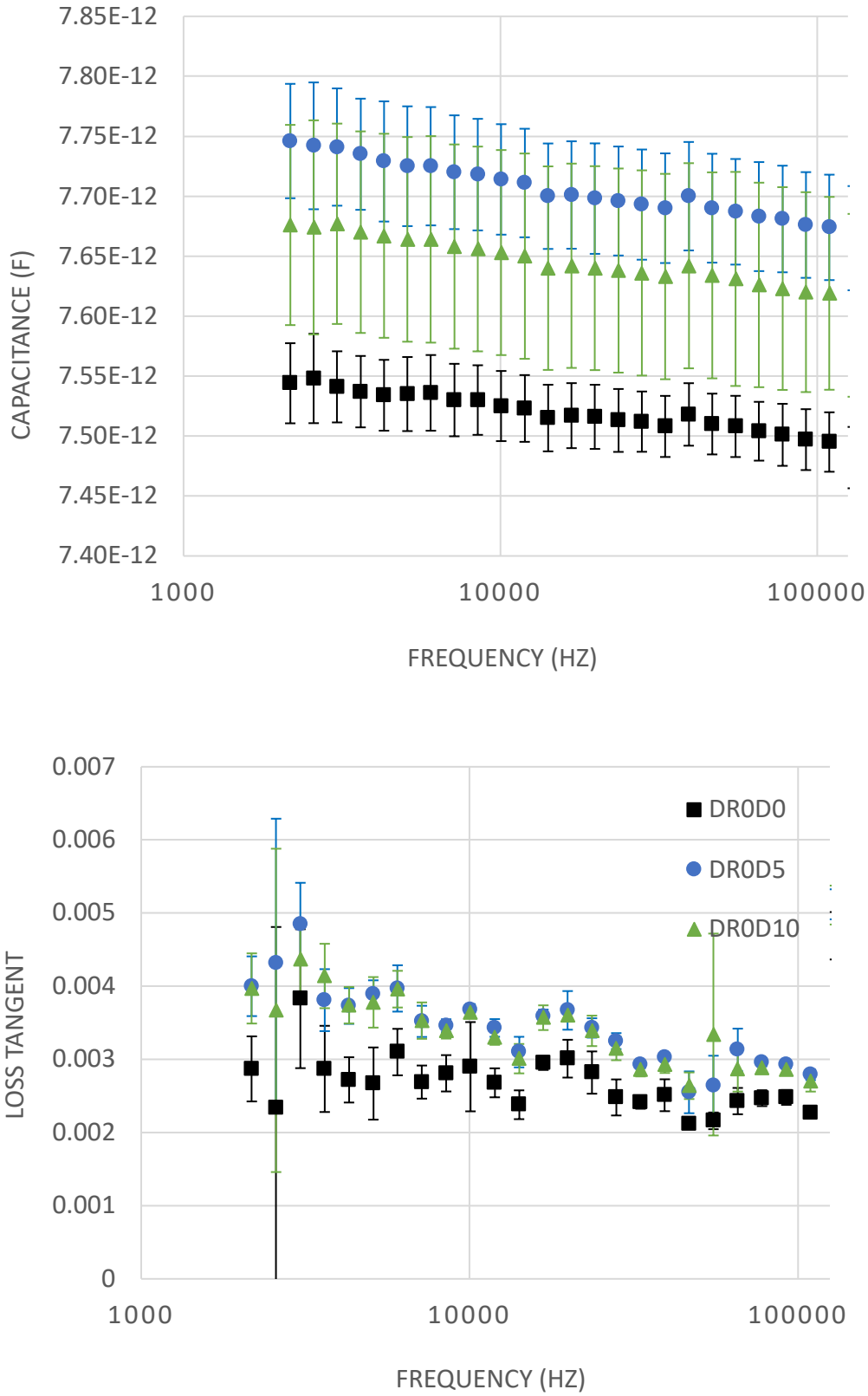

Figure 55. Capacitance and loss tangent measured using a custom capacitive clamp sensor on XLPE-insulated wires aged thermally at 60 °C for 0, 5, and 10 days.

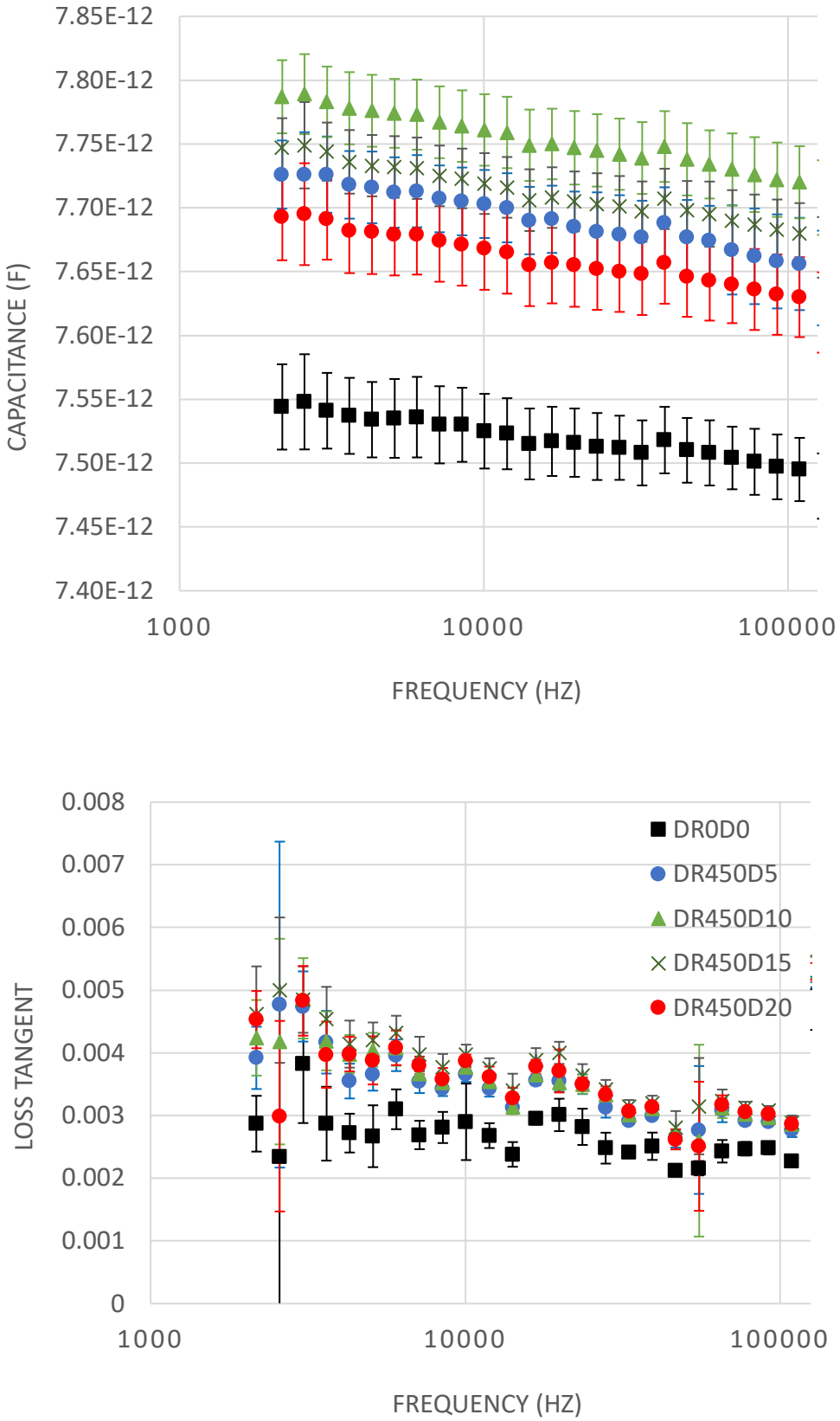

Figure 56 Capacitance and loss tangent measured using a custom capacitive clamp sensor on XLPE-insulated wires aged thermally at 60 °C and exposed to gamma radiation at dose rate 450 Gy/h for 0, 5, 10, 15, and 20 days.

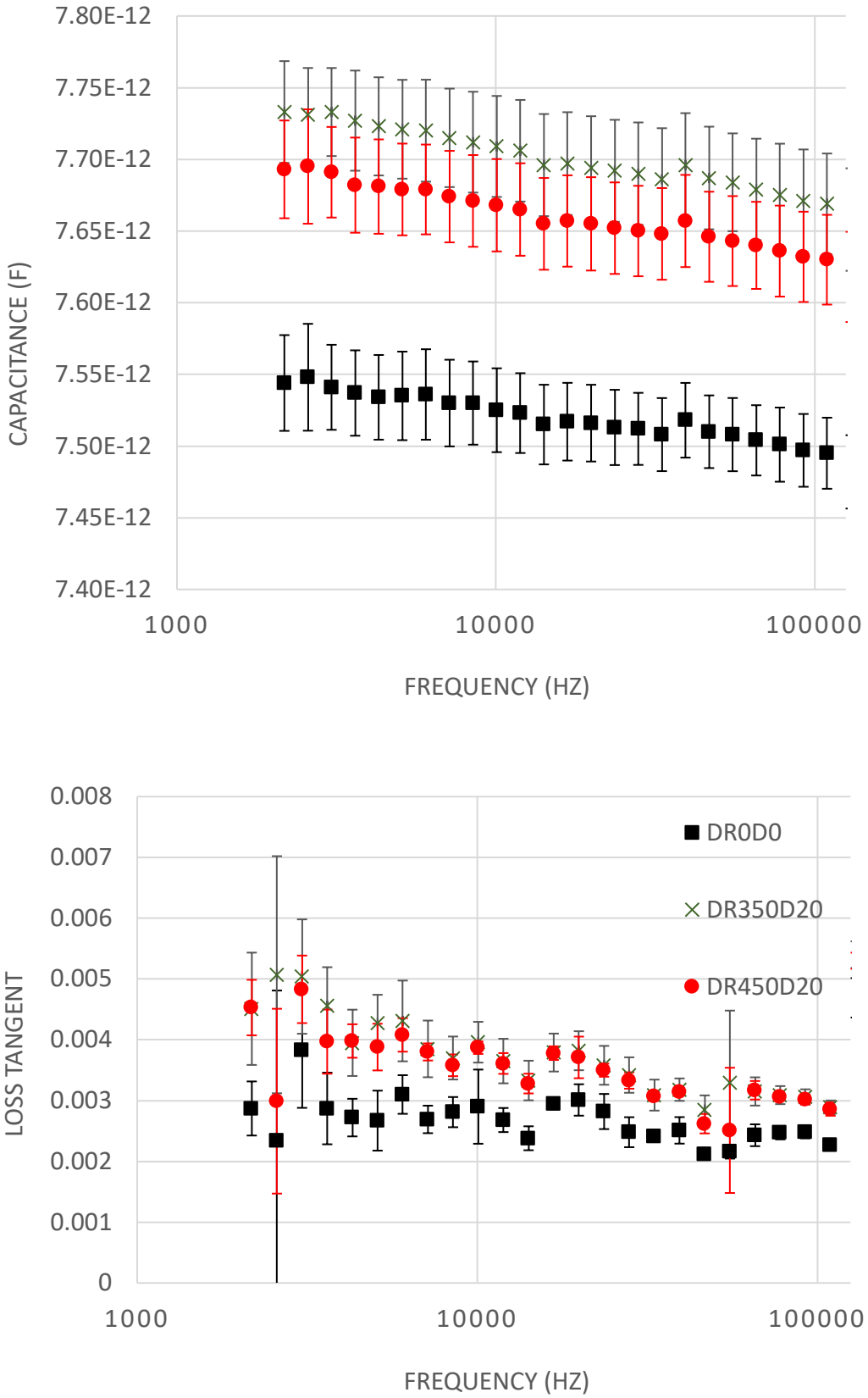

Figure 57 Capacitance and loss tangent measured using a custom capacitive clamp sensor on XLPE-insulated wires aged thermally at 60 °C and exposed to gamma radiation at dose rates 0, 350, and 450 Gy/h for 20 days.

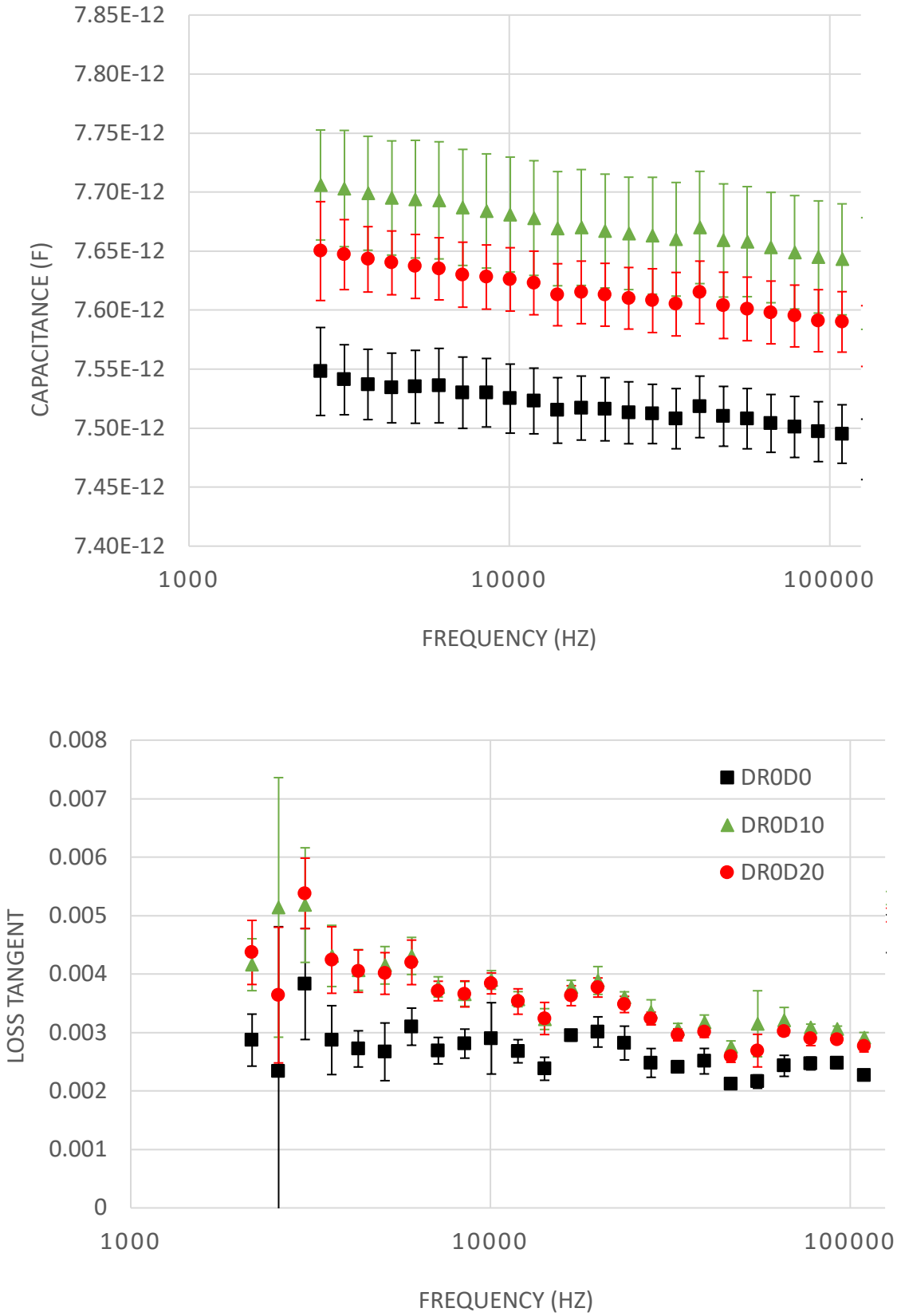

Figure 58 Capacitance and loss tangent measured using a custom capacitive clamp sensor on XLPE-insulated wires aged thermally at 90 °C for 0, 10, and 20 days.

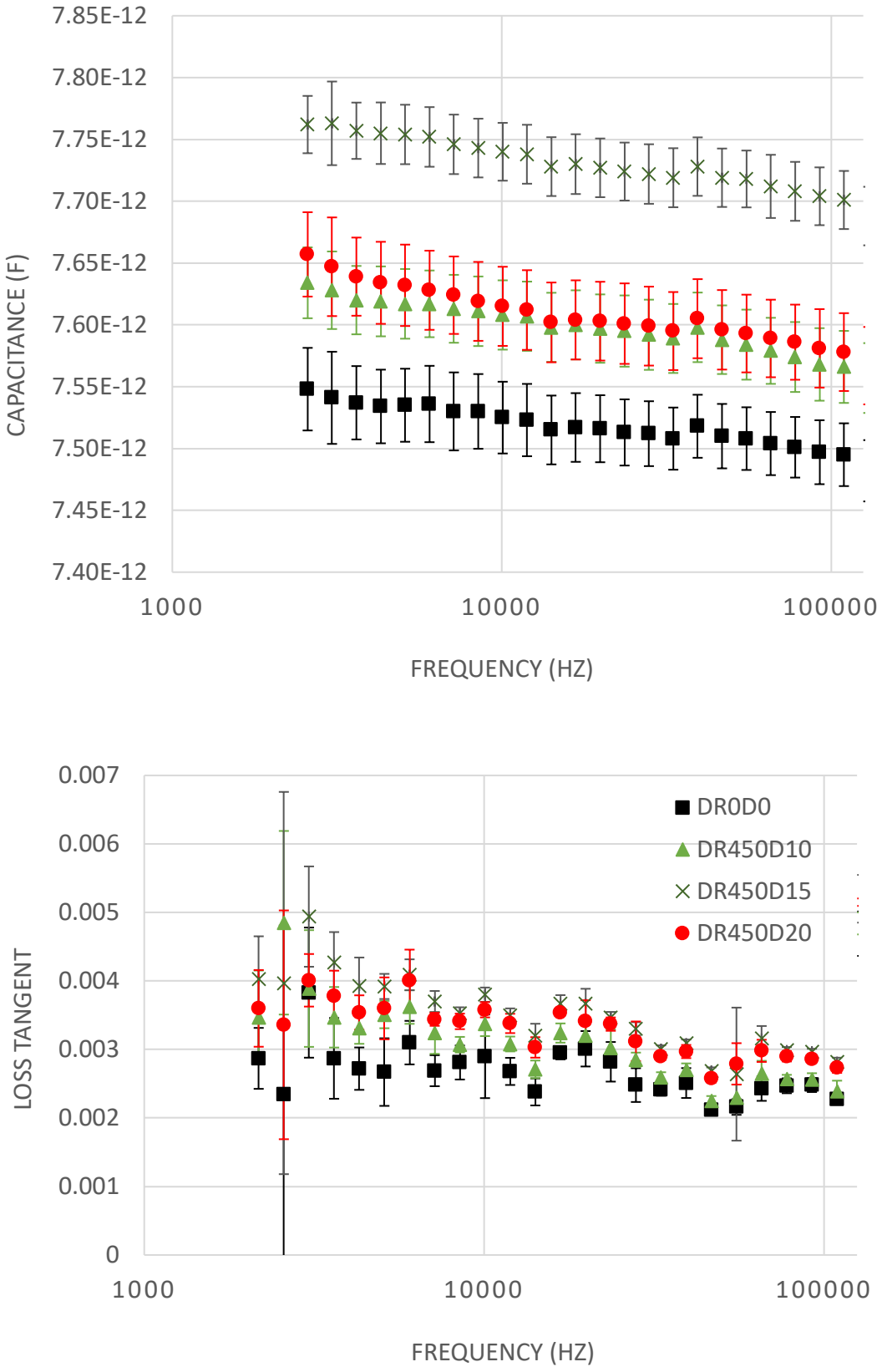

Figure 59 Capacitance and loss tangent measured using a custom capacitive clamp sensor on XLPE-insulated wires aged thermally at 90 °C and exposed to gamma radiation at dose rate 450 Gy/h for 0, 10, 15, and 20 days.

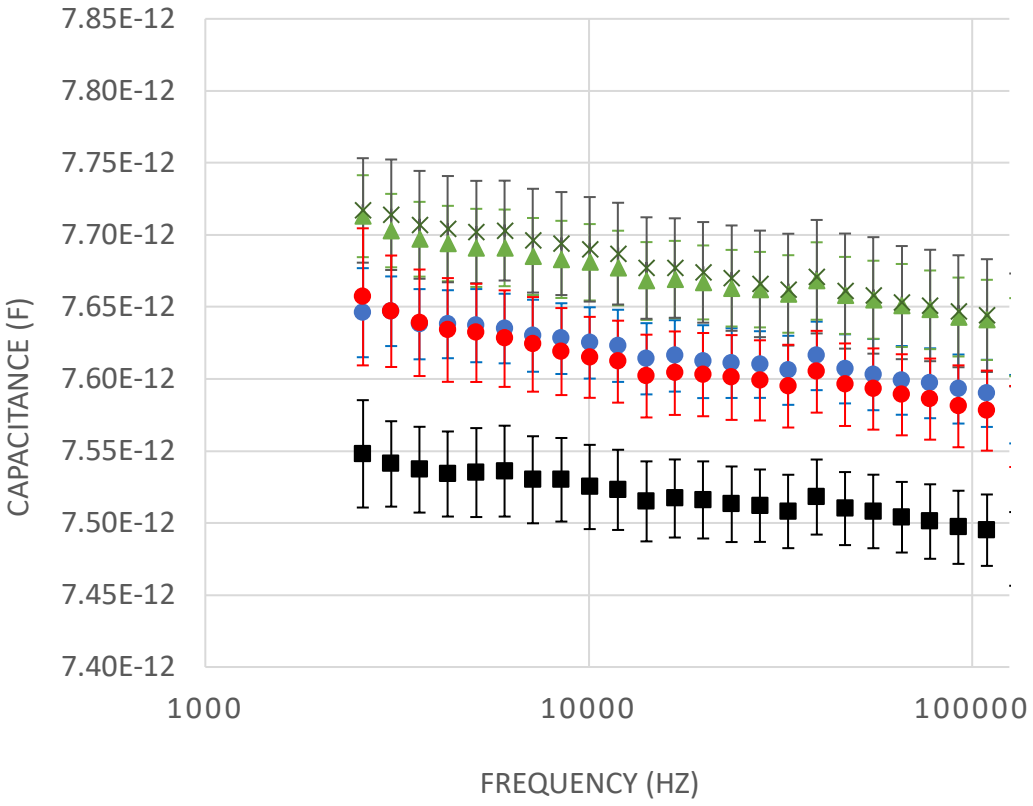

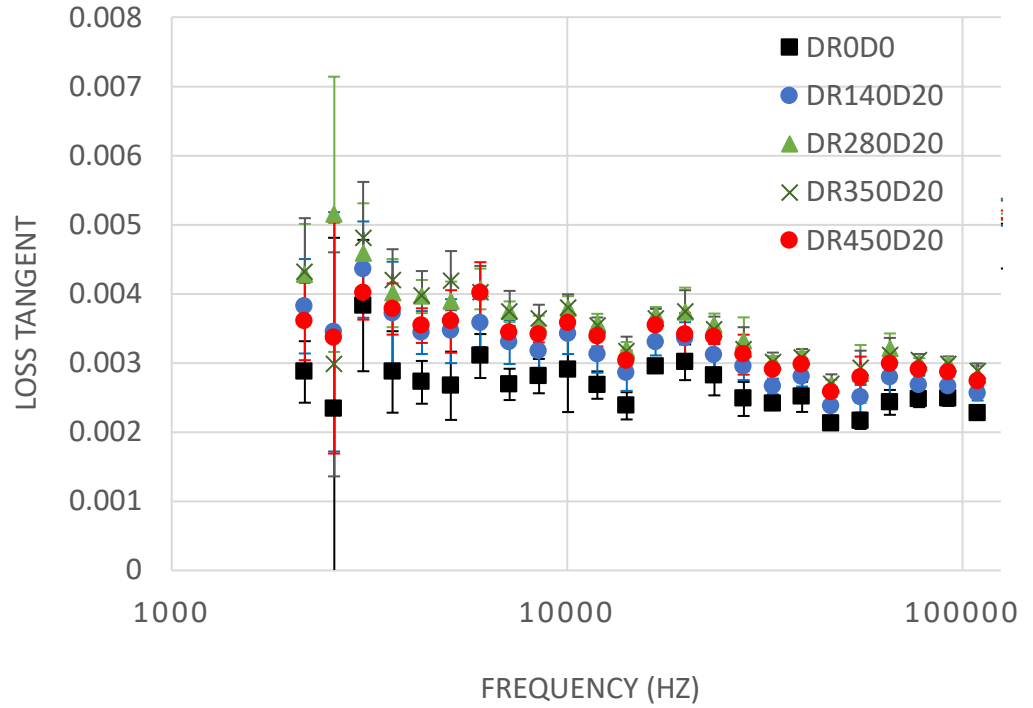

Figure 60 Capacitance and loss tangent measured using a custom capacitive clamp sensor on XLPE-insulated wires aged thermally at 90 °C and exposed to gamma radiation at dose rates 0, 140, 280, 350, and 450 Gy/h for 20 days.

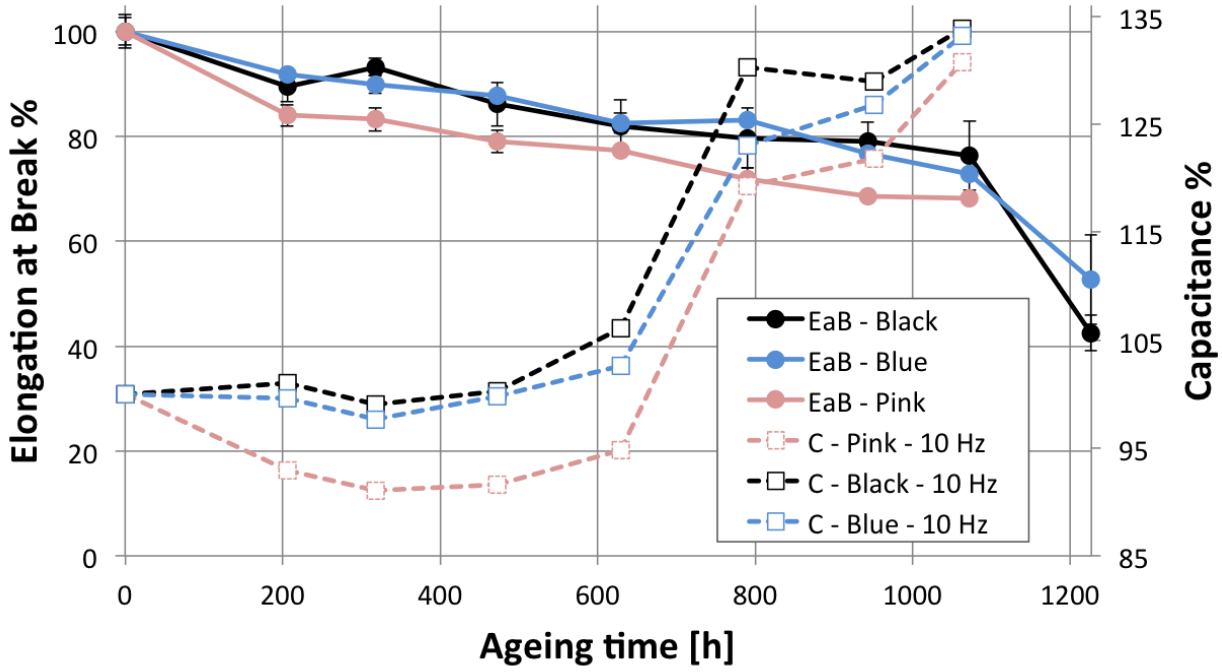

Figure 61. Comparison between elongation at break and specific capacitance at 10 Hz.

Summary and Key Conclusions

XLPE-insulated wires

- The capacitance and dissipation factor measured by an interdigital capacitive sensor applied to the exterior of a wire insulated with XLPE-based insulation material showed a significant distinction between pristine and thermally-aged wires, both without and with gamma irradiation.

EPR/PVC three-conductor cables

Dielectric properties of EPR insulation material were found to be very sensitive to aging. In particular, dissipation factor (loss tangent) at 1 kHz can be considered a leading diagnostic marker for these samples. In more detail:

- EaB declines gradually until approximately 1,100 hours of aging, followed by a sharper decrease to about 50 % at approximately 1,200 hours;
- Dissipation factor (loss tangent) and relative capacitance, both at 10 Hz and 1 kHz, show a progressive increase which starts at approximately 600 hours;
- Capacitance increases are between 33 % (10 Hz) and 22 % (1 kHz), smaller than EaB decreases;
- Dissipation factor increases are between 185 % (10 Hz) and 194 % (1 kHz): almost doubling after only 800 hours of aging.

Reference

1. R. T. Sheldon and N. Bowler, An Interdigital Capacitive Sensor for Nondestructive Evaluation of Wire Insulation, IEEE Sensors J., 14, 961-970, 2014.

3.3 Measure THz signals on aged cables

The original proposal of measuring terahertz signals on aged cables became, in the light of early results on this project, lower priority than taking additional near-infrared spectral data and so the effort originally intended for terahertz signals was redirected to refining infrared and near-infrared data taken on aged XLPE samples. Collection of infrared and near-infrared data was completed at the end of Year 3 of the project (September 30, 2017). Analysis continued to the conclusion of the project (December 31, 2017).

3.4 Calculate spectra

This task was completed March 31, 2017.

Hypothesis

Dielectric properties, infrared and Raman spectra can be predicted for crystalline polyethylene and oxidized crystalline polyethylene, giving insight into expected spectral changes in consequence of oxidative aging of PE and XLPE.

Approach

In our theoretical DFT calculations, a crystalline polyethylene model, obtained by C. W. Bunn from X-ray diffraction (XRD) was used. The theoretical background to this work is provided in Appendix A, page 103.

Pure crystalline polyethylene

Bunn reported that at low temperature, polyethylene crystallizes into an orthorhombic base-centered structure with space group Pnma [1]. In the unit cell, there are four carbon atoms and eight hydrogen atoms. Both the carbon and hydrogen atoms were reported to occupy the 4cm Wyckoff positions. The Cartesian coordinates for these positions are (x, 0.25, z), (-x+0.5, 0.75, z+0.5), (-x, 0.75, -z), (x+0.5, 0.25, -z+0.5). For carbon atoms, x=0.033 and z=0.066. Four hydrogen atoms have different x and z values from the other four hydrogen atoms. The first four hydrogen atoms have x=0.1898 and z=0.052, and the other four have x=0.0339 and z=0.2607. The lattice parameters are a=7.4Å, b=4.93Å, c=2.543Å. Using these experimental data, a pure crystalline polyethylene model is constructed, as shown in Figure 62. In Figure 62, the blue atoms are carbon atoms and the green atoms are hydrogen atoms. It is obvious that the polymer chain is in the y direction.

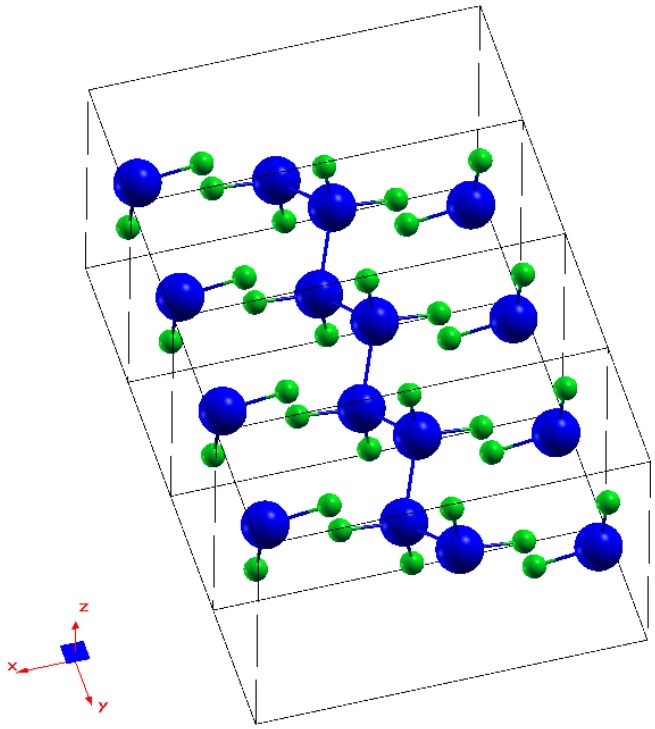

Figure 62. Pure crystalline polyethylene model. The blue atoms represent carbon atoms and the green atoms represent hydrogen atoms. The polymer chain is along the y direction.

Oxidized crystalline polyethylene

Some point defects may be introduced into the pure crystalline polyethylene model to simulate the aged polyethylene. The most common ageing effect is the oxidization of the polymer. Therefore, we also constructed some oxidized crystalline polyethylene models. As shown in Figure 63, the pure crystalline structure C_4H_8 was changed to C_4H_6O by replacing the carbon of the center chain by a carbonyl. The reason why only one oxygen atom was added to the pure polyethylene model is that, in our opinion, this is the easiest model that we can use to see effects of oxidization due to ageing. In order to see how properties change with oxidization, the concentration of oxygen atoms were changed by adding one oxygen atom to different sizes of supercells of pure crystalline polyethylene. In our calculations, four models: C_4H_8, C_4H_6O, $C_8H_{14}O$, and $C_{12}H_{22}O$ were investigated.

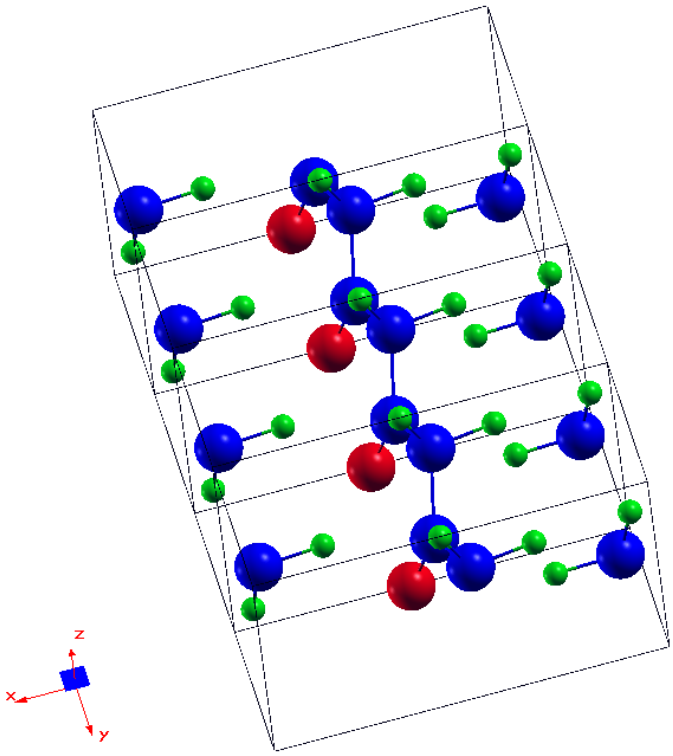

Figure 63. Oxidized crystalline polyethylene model. The blue atoms represent carbon atoms, the green atoms represent hydrogen atoms and the red atoms represent oxygen atoms. The formula is C_4H_6O.

Significant Results

Calculation details

All the calculations are performed using the density functional theory method encoded in QuantumEspresso. Both the generalized gradient approximations (GGA) and local density approximations (LDA) are used for the exchange-correlation potential along with Troullier-Matins normconserving pseudopotentials in place of the all-electron potentials. The calculations are converged when the plane wave representation of the wave function is truncated at 950 eV. The Brillouin zone is sampled using an 8×8×8 k-point mesh.

Optimized structure

The lattice parameters and atomic positions are optimized by DFT total energy calculations. Table 11 shows our results compared with some other reported theoretical and experimental data. Our results are in good agreement with those of other theoretical and experimental work.

Table 11. Results of the structure of LDPE in comparison with independent results.

	GGA (our)	LDA (our)	X-RAY [2]	Neutron (4K) [3]	Theory [4]
Bond length $r_{c\text{-}c}$(Å)	1.53	1.52	1.53	1.578	1.54
Bond length $r_{c\text{-}H}$(Å)	1.11	1.12	N/A	1.06	1.11
Bond angle CCC (°)	113.53	113.51	112	107.7	113.65
Bond angle CHC (°)	106.06	105.43	N/A	109	109.3
Lattice parameter a (Å)	7.304	6.549	7.4	7.121	7.35
Lattice parameter b (Å)	5.017	4.446	4.93	4.851	4.998
Lattice parameter c (Å)	2.565	2.515	2.543	2.548	2.572

Static dielectric properties

The original linear response method calculates the dielectric matrix (DM) that is the linear response of the electronic charge density to the external perturbation. The dielectric matrix includes so many interesting properties that are far more than what is needed for phonon calculations. The negative aspect of the DM method is that it requires inverting the dielectric matrix for phonon calculations, which is very expensive in numerical computations. The Plane-Wave Self-Consistent Field (PWSCF) method takes the approach of finding directly the linear response of the charge density to the external perturbation without calculating the details of the dielectric matrix. Combined with the local density approximation (LDA), the linear perturbation term of the total energy is evaluated. To save computation time, a self-consistent scheme is used to obtain the linear term of the change of the charge density.

By using the PWSCF method, the dielectric constants have been obtained for pristine and oxidized crystalline polyethylene: C_4H_8, $C_{12}H_{22}O$, $C_8H_{14}O$, and C_4H_6O:

$$C_4H_8 \begin{bmatrix} 2.739 & 0 & 0 \\ 0 & 2.818 & 0 \\ 0 & 0 & 2.858 \end{bmatrix}$$

$$C_{12}H_{22}O\begin{bmatrix} 2.492 & 0 & 1.318 \\ 0 & 3.004 & 0 \\ 1.318 & 0 & 3.217 \end{bmatrix}$$

$$C_8H_{14}O\begin{bmatrix} 2.591 & 0 & 1.479 \\ 0 & 3.086 & 0 \\ 1.479 & 0 & 3.324 \end{bmatrix}$$

$$C_4H_6O\begin{bmatrix} 2.637 & 0 & 1.534 \\ 0 & 3.131 & 0 \\ 1.534 & 0 & 3.361 \end{bmatrix}$$

Converting these calculated dielectric constants to three principal dielectric constants by using

$$\begin{pmatrix} K'_{11} & K'_{12} & K'_{13} \\ K'_{12} & K'_{22} & K'_{23} \\ K'_{13} & K'_{23} & K'_{33} \end{pmatrix} \begin{pmatrix} a_{11} & a_{12} & a_{13} \\ a_{21} & a_{22} & a_{23} \\ a_{31} & a_{32} & a_{33} \end{pmatrix} = \begin{pmatrix} a_{11} & a_{12} & a_{13} \\ a_{21} & a_{22} & a_{23} \\ a_{31} & a_{32} & a_{33} \end{pmatrix} \begin{pmatrix} K_{11} & 0 & 0 \\ 0 & K_{22} & 0 \\ 0 & 0 & K_{33} \end{pmatrix}$$

and reorganizing the above equation, we get nine equations:

$$\begin{aligned} K'_{11}a_{11} + K'_{12}a_{21} + K'_{13}a_{31} &= a_{11}K_{11} \\ K'_{11}a_{12} + K'_{12}a_{22} + K'_{13}a_{32} &= a_{12}K_{22} \\ \vdots \qquad\qquad & \vdots \qquad\qquad \vdots \\ \vdots \qquad\qquad & \vdots \qquad\qquad \vdots \\ K'_{13}a_{13} + K'_{23}a_{23} + K'_{33}a_{33} &= a_{33}K_{33} \end{aligned}$$

For a non-trivial solution, the determinant of the coefficients should be zero:

$$\begin{vmatrix} K'_{11} - K_{ii} & K'_{12} & K'_{13} \\ K'_{12} & K'_{22} - K_{ii} & K'_{23} \\ K'_{13} & K'_{23} & K'_{33} - K_{ii} \end{vmatrix} = 0$$

Solving the above equation, the principal dielectric constants are obtained. Taking the arithmetic average value of the three principal components, we have the dielectric value for each model material system:

C_4H_8	2.805
$C_{12}H_{22}O$	2.904
$C_8H_{14}O$	3.000
C_4H_6O	3.043

These absolute values are larger than the experimental values. This is because in our DFT calculations, the exchange-correlation functional is approximated using a local density approximation (LDA). However, the difference of the dielectric constants should be consistent

with experimental data since the errors due to approximation will be cancelled out. If we compare the value between C_4H_8 and C_4H_6O, the difference is 0.238. This difference value is very close to the reported experimental data [5].

Infrared and Raman spectroscopy

Infrared (IR) and Raman spectroscopy are complementary techniques, since transitions allowed in Raman may be forbidden in IR, which is due to the different selection rules for these two spectroscopic techniques. Vibrations that cause a change in the dipole moment of the molecule are IR-active while vibrations that change the molecular polarizability are Raman-active.

For a molecule containing N atoms, theoretically there are 3N modes considering each atom has 3 degrees of freedom in 3-dimensional space. After subtracting 3 translational modes and 3 (bent) or 2 (linear) rotational modes, the number of vibrational modes will be 3N-6 (bent) or 3N-5 (linear).

After calculating the spectral intensity and peak positions, we can determine the vibrational modes in a molecule by using nuclear site group analysis. The process is as follows:

1. Apply all symmetry operations to the molecule and determine how many atoms are not moved during a specific symmetry operation.
2. Multiply the number of atoms unmoved for each symmetry operation by a character contribution of that symmetry operation, to obtain a reducible representation. Here, the character contribution is equal to the trace of the matrix of the symmetry operation.
3. Decompose the reducible representation into a unique linear combination of irreducible representations using dot products.

For our crystalline polyethylene, the point group is mmm, which has 8 symmetry elements. These are: Identity, three mirror planes perpendicular to x, y, z directions, one inversion center, and three 2-fold rotation axes parallel to x, y, z directions. The character contributions of these symmetry operations can be obtained by calculating the traces of their matrices.

Following the process described above, the linear combination of vibrational modes (irreducible representation) can be obtained. The irreducible representation is

$$\Gamma_{irred}=3A_u+5B_{1u}+2B_{2u}+5B_{3u}+6A_g+2B_{1g}+5B_{2g}+2B_{3g}$$

By adding up all the coefficients the following is found:

$$3+5+2+5+6+2+5+2=30=3\times12-6=3N-6$$

which is consistent with the theoretical number of vibrational modes for a molecule containing 4 carbon atoms and 8 hydrogen atoms. Of all the vibrational modes, some of them are IR-active, some of them are Raman-active, and some are neither. Here we list the type of activity for each vibrational mode:

A_u Neither IR-active nor Raman-active
B_{1u} IR-active
B_{2u} IR-active
B_{3u} IR-active
A_g Raman-active
B_{1g} Raman-active
B_{2g} Raman-active

B_{3g} Raman-active
The calculated infrared spectra of pure and oxidized crystalline polyethylene C_4H_8, C_4H_6O, and $C_8H_{14}O$, are shown in Figure 64 through Figure 66.

The calculated infrared spectra of pure and oxidized crystalline polyethylene C_4H_8, C_4H_6O, and $C_8H_{14}O$, are shown in Figure 64 through Figure 66. From Figure 64, the calculated infrared spectrum of pure crystalline polyethylene C_4H_8 is seen to contain four peaks, which are located at 22 THz, 34 THz, 43 THz, and 86 THz with the one at 86 THz being the highest peak. Our result of pure crystalline polyethylene is in good agreement with published experimental work in which low density polyethylene is characterized by Fourier transform infrared spectroscopy. Further, Figure 65, there are two additional peaks appearing in oxidized polyethylene C_4H_6O, one at 4 THz and the other at 53 THz. These two peaks are due to the oxidization of the polyethylene. For the second oxidized model system, $C_8H_{14}O$, which has higher oxygen concentration, the locations of peaks are the same as the other oxidized model, however, the intensity of peak at 53 THz decreases while the intensity of peak at 86 THz increases.

The calculated Raman spectrum of pure crystalline polyethylene C_4H_8 contains a single large peak at 85 THz. By oxidizing the pure crystalline polyethylene, four more peaks, which are located at 19 THz, 25 THz, 33 THz, and 42 THz appear in both oxidized models C_4H_6O and $C_8H_{14}O$ due to the oxidization of polyethylene. In addition, the intensities of these four peaks increase when the concentration of oxygen is raised from model system $C_8H_{14}O$ to C_4H_6O.

The data shown in Figure 64 through Figure 66 are tabulated in Table 12, Table 13, and Table 14.

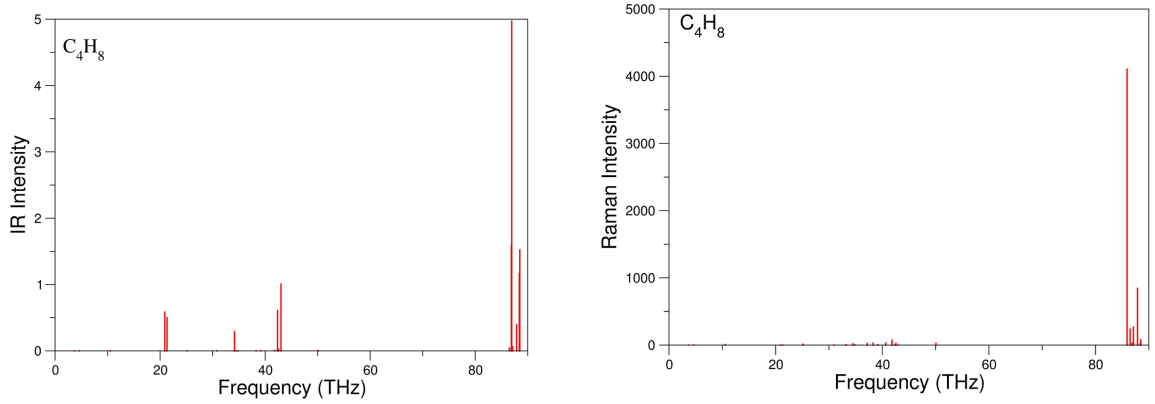

Figure 64. IR (left) and Raman (right) spectra of pure crystalline polyethylene.

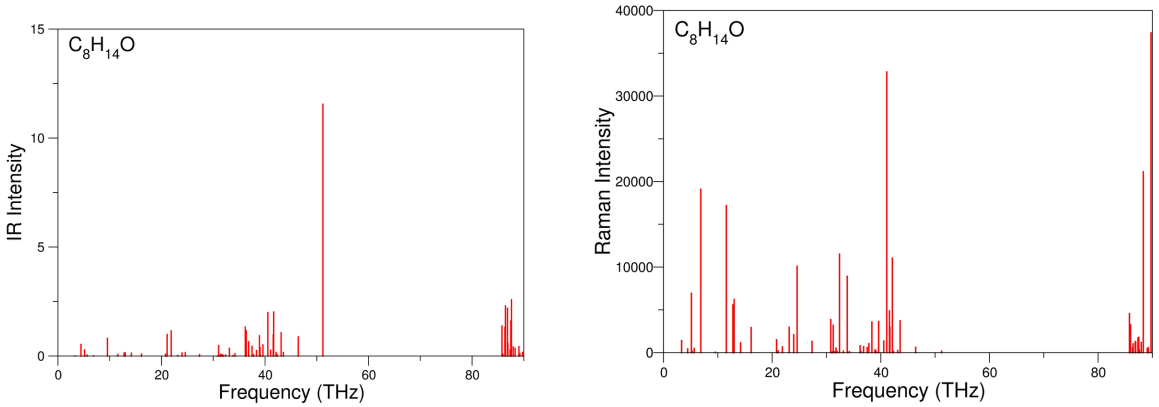

Figure 65. IR (left) and Raman (right) spectra of oxidized crystalline polyethylene $C_8H_{14}O$.

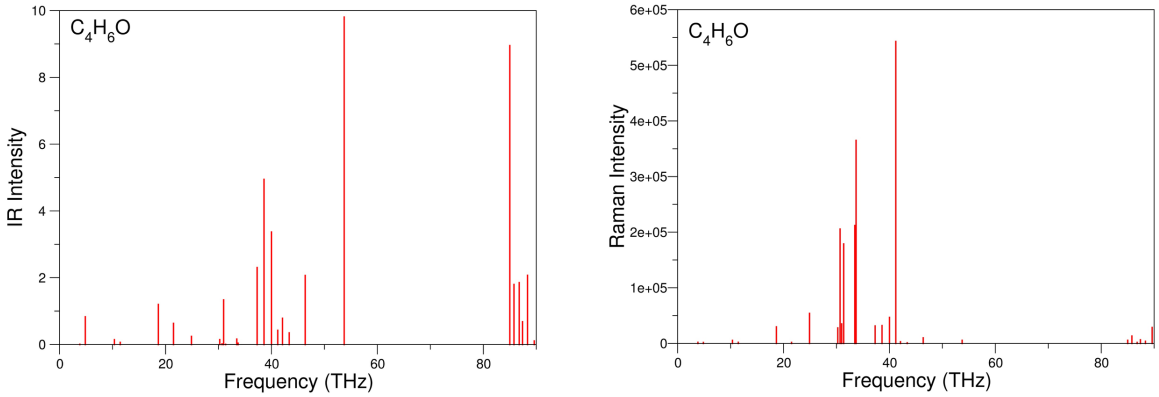

Figure 66. IR (left) and Raman (right) spectra of oxidized crystalline polyethylene C_4H_6O.

Table 12. Calculated Infrared and Raman-active modes of pristine polyethylene, C_4H_8.

# Mode	Wavenumber (cm^{-1})	Frequency (THz)	Intensity (IR)	Intensity (Raman)	Irreducible representation	IR or Raman active
1	122.01	3.6578	0.0012	0.1198	B_{1u}	I
2	154.75	4.6394	0.0008	0.9361	A_g	R
3	351.01	10.5229	0.0009	7.7143	B_{1u}	I
4	696.91	20.8928	0.5855	0.0137	B_{3u}	I
5	711.07	21.3175	0.5000	0.0242	B_{2u}	I
6	838.41	25.1348	0.0003	11.8306	A_u	
7	1027.90	30.8157	0.0015	0.0000	B_{3g}	R
8	1030.29	30.8874	0.0000	0.0090	B_{1g}	R
9	1107.55	33.2034	0.0000	5.0619	B_{2u}	I
10	1137.56	34.1032	0.0002	7.8441	A_g	R
11	1139.64	34.1656	0.2882	0.0000	A_u	
12	1150.44	34.4894	0.0002	18.1863	B_{2g}	R
13	1163.06	34.8675	0.0001	2.8217	A_g	R
14	1240.24	37.1813	0.0000	23.0600	B_{2g}	R
15	1276.80	38.2776	0.0007	28.6461	B_{1g}	R
16	1306.26	39.1605	0.0003	5.3859	B_{3g}	R
17	1355.59	40.6396	0.0000	27.3554	B_{3g}	R
18	1394.55	41.8075	0.0052	73.0887	A_g	R
19	1412.68	42.3512	0.6080	2.5661	B_{1g}	R
20	1419.66	42.5604	0.0242	26.2162	B_{2g}	R
21	1434.94	43.0184	1.0083	0.2397	B_{1u}	I
22	1670.30	50.0744	0.0060	26.1671	B_{3u}	I
23	2866.03	85.9213	0.0000	4106.5028	A_g	R
24	2885.40	86.5022	0.0421	235.6290	B_{2g}	R
25	2897.66	86.8698	1.5886	27.9149	B_{3u}	I
26	2900.45	86.9534	4.9717	0.2834	B_{1u}	I
27	2905.51	87.1051	0.0607	267.3734	B_{2g}	R
28	2931.10	87.8721	0.3959	833.3662	A_g	R
29	2948.23	88.3858	1.1686	23.3521	B_{1u}	I
30	2951.72	88.4903	1.5223	76.9992	B_{3u}	I

Table 13. Calculated Infrared and Raman-active modes of oxidized polyethylene, $C_8H_{14}O$.

# Mode	Wavenumber (cm^{-1})	Frequency (THz)	Intensity (IR)	Intensity (Raman)	Irreducible representation	IR or Raman active
1	110.92	3.3254	0.0011	1401.3398	B_{1u}	I+R
2	148.24	4.4441	0.5307	428.7735	A_g	I+R
3	171.07	5.1284	0.2786	6928.6960	B_{1u}	I+R
4	175.74	5.2685	0.0030	167.1607	B_{3u}	I+R
5	188.25	5.6436	0.0424	481.4127	B_{2u}	I+R
6	228.76	6.8581	0.0035	19094.7112	A_u	I+R
7	318.60	9.5514	0.8105	41.2938	B_{3g}	I+R
8	385.47	11.5561	0.0732	17180.4984	B_{1g}	I+R
9	426.16	12.7759	0.1344	5579.5052	B_{2u}	I+R
10	433.81	13.0052	0.1433	6211.5005	A_g	I+R
11	472.92	14.1777	0.1289	1146.5522	A_u	I+R
12	538.27	16.1370	0.0859	2933.9739	B_{3g}	I+R
13	693.79	20.7992	0.0850	1506.1341	B_{3g}	I+R
14	703.45	21.0890	0.9772	188.4064	A_g	I+R
15	729.65	21.8742	1.1510	671.2187	B_{1g}	I+R
16	771.85	23.1396	0.0237	2955.6701	B_{2g}	I+R
17	799.60	23.9714	0.1355	2087.8578	B_{1u}	I+R
18	820.10	24.5861	0.1509	10104.9039	B_{3u}	I+R
19	912.20	27.3470	0.0622	1305.2378	B_{3g}	I+R
20	1026.79	30.7823	0.0001	3865.5765	B_{3g}	I+R
21	1035.54	31.0447	0.4733	75.2618	A_g	I+R
22	1041.79	31.2321	0.0206	3186.3074	B_{1g}	I+R
23	1049.80	31.4721	0.0853	91.7623	B_{2g}	I+R
24	1059.61	31.7663	0.0522	525.2821	B_{1u}	I+R
25	1065.75	31.9503	0.0220	121.8801	B_{3u}	I+R
26	1080.60	32.3956	0.0424	11517.7941	B_{1u}	I+R
27	1104.82	33.1217	0.3527	172.4361	B_{3u}	I+R
28	1128.11	33.8197	0.0239	8920.2043	B_{2u}	I+R
29	1141.14	34.2105	0.0996	121.1356	A_u	I+R
30	1207.42	36.1975	1.3237	792.4809	B_{3g}	I+R
31	1213.51	36.3801	1.1450	99.6080	B_{1g}	I+R
32	1228.34	36.8248	0.6497	698.6402	B_{2u}	I+R
33	1250.54	37.4902	0.4382	592.4406	A_g	I+R
34	1260.82	37.7984	0.0648	1054.4470	A_u	I+R
35	1279.51	38.3586	0.2527	3570.5111	B_{3g}	I+R
36	1298.25	38.9207	0.9282	280.9180	B_{2u}	I+R
37	1301.94	39.0311	0.3873	300.2371	A_u	I+R
38	1308.10	39.2157	0.0055	56.0259	B_{3g}	I+R
39	1320.95	39.6011	0.5083	3633.4120	B_{1g}	I+R
40	1352.37	40.5431	1.9937	1350.8537	B_{1u}	I+R
41	1370.82	41.0960	0.2637	32812.5292	B_{3u}	I+R
42	1387.18	41.5865	0.9612	4871.4514	B_{3g}	I+R

43	1390.25	41.6786	2.0163	2991.0220	B_{3g}	I+R
44	1405.05	42.1225	0.1608	11042.0096	A_g	I+R
45	1412.59	42.3483	0.0554	119.9556	B_{1g}	I+R
46	1438.16	43.1150	1.0654	247.1746	B_{2g}	I+R
47	1452.43	43.5429	0.1615	3713.4127	B_{1u}	I+R
48	1548.41	46.4201	0.8781	620.2256	B_{3u}	I+R
49	1707.24	51.1818	11.5519	161.6319	B_{1u}	I+R
50	2861.09	85.7735	1.3783	4559.1014	B_{1u}	I+R
51	2867.76	85.9733	0.0821	3272.7137	B_{3u}	I+R
52	2879.77	86.3333	1.3098	559.4650	B_{3g}	I+R
53	2883.62	86.4487	2.2934	1030.7138	B_{3g}	I+R
54	2896.38	86.8314	2.1872	1287.8486	A_g	I+R
55	2899.19	86.9155	0.5768	1184.3328	B_{1g}	I+R
56	2913.60	87.3475	0.2756	1704.8269	B_{2g}	I+R
57	2918.08	87.4819	1.6037	1782.7100	B_{1u}	I+R
58	2922.51	87.6146	2.5822	298.3410	B_{3u}	I+R
59	2933.53	87.9449	0.4125	1202.4126	B_{1u}	I+R
60	2945.91	88.3160	0.3531	21133.5724	B_{1u}	I+R
61	2970.30	89.0473	0.4288	477.7084	B_{1u}	I+R
62	2977.17	89.2532	0.1018	577.7203	B_{3u}	I+R
63	2993.51	89.7432	0.1651	37385.5964	A_g	I+R

Table 14. Calculated Infrared and Raman-active modes of oxidized polyethylene, C_4H_6O.

# Mode	Wavenumber (cm^{-1})	Frequency (THz)	Intensity (IR)	Intensity (Raman)	Irreducible representation	IR or Raman active
1	127.33	3.8172	0.0084	1998.7890	B_{1u}	I+R
2	161.97	4.8558	0.8309	234.0200	A_g	I+R
3	345.08	10.3451	0.1443	5490.8368	B_{1u}	I+R
4	381.85	11.4475	0.0651	1916.6211	B_{3u}	I+R
5	622.13	18.6510	1.2003	29846.2428	B_{2u}	I+R
6	717.59	21.5127	0.6340	1821.2433	A_u	I+R
7	830.54	24.8990	0.2434	174.0300	B_{3g}	I+R
8	1008.76	30.2419	0.1466	27879.0003	B_{1g}	I+R
9	1023.39	30.6806	0.0197	205677.6425	B_{2u}	I+R
10	1032.90	30.9655	1.3363	35002.0666	A_g	I+R
11	1045.90	31.3552	0.2100	178889.4974	A_u	I+R
12	1116.00	33.4570	0.1632	211978.6427	B_{3g}	I+R
13	1123.72	33.6883	0.0406	365067.0539	B_{3g}	I+R
14	1244.14	37.2984	2.3051	31493.6732	A_g	I+R
15	1287.43	38.5949	4.9484	32103.4691	B_{1g}	I+R
16	1334.41	40.0047	3.3691	46715.4347	B_{2g}	I+R
17	1373.93	41.1894	0.4258	542876.8395	B_{1u}	I+R
18	1403.62	42.0766	0.7850	3042.8643	B_{3u}	I+R
19	1446.92	43.3519	0.3484	1234.5803	A_g	I+R
20	1546.28	46.3745	2.0683	10001.7349	B_{2g}	I+R
21	1792.12	53.7345	9.8082	5565.5083	A_g	I+R
22	2835.36	85.0041	8.9527	5653.6798	B_{1g}	I+R
23	2861.89	85.7875	1.7995	13317.1895	B_{2g}	I+R
24	2894.26	86.7731	1.8524	2642.1203	A_g	I+R
25	2915.62	87.3999	0.6825	6530.0081	B_{1g}	I+R
26	2946.96	88.3478	2.0733	3891.0518	B_{2g}	I+R
27	2989.06	89.6096	1.2300	28775.3547	B_{3u}	I+R

Summary and Key Conclusions

- Dielectric properties, infrared and Raman spectra have been calculated for crystalline polyethylene and oxidized crystalline polyethylene;
- The presence of oxygen atoms, in the form of carbonyl, causes an increase in calculated dielectric constant and introduces additional peaks in calculated infrared and Raman spectra.

References

1. C. Adamo and V. Barone, J. Chem. Phys. **110**, 6185 (1999).
2. A. D. Becke, J. Chem. Phys. **98**, 1372 (1993).
3. V. N. Staroverov, G. E. Scuseria, J. M. Tao, and J. P. Perdew, Phys. Rev. B **69**, 075102 (2004).
4. D. R. Hamann, M. Schlüter, and C. Chiang, Phys. Rev. Lett. **43**, 1494 (1979).
5. D. Vanderbilt, Phys. Rev. B **48**, 7892 (1990).

3.5 Validate models

This task concluded at the conclusion of the project, December 31, 2017.

Hypotheses

- Models describing aging mechanisms, i.e. changes in material composition and chemistry in response to environmental stressors, provide insight into processes of aging that are relevant to material performance;
- Models describing changes in material properties in response to environmental stressors underpin development of methods for monitoring material degradation.

Approach

Chemical reaction models were developed to describe chemical changes in response to thermo-oxidative aging of PE and XLPE stimulated by gamma irradiation. Molecular dynamics simulations were employed to predict changes in mechanical properties (stress-stain curves), infrared and Raman spectra for oxidized PE. A kinetic rate model was employed to model changes in the degree of cross-linking and chain scission that occurs in oxidized PE. Statistical analysis was applied to determine the most sensitive indicators of oxidative PE and XLPE aging, among many indicators measured experimentally. Multiple linear regression models were employed to construct equations that predict the values of the most sensitive aging indicator as a function of gamma radiation dose rate and total dose. Simulations were performed in COMSOL™ to select the best configuration of applied voltage, and choice of electrical shield, to obtain the best sensitivity to aging-related permittivity changes in the insulation material when measured via capacitive testing of intact cables.

Significant results

- Task 1.3 Thermal, mechanical, and chemical characterization of aged samples, page 19: Aging mechanisms (chemical changes) were deduced from thermal and chemical characterization of pristine and aged samples.
- Task 1.4 Dielectric, THz and infrared characterization of aged samples, page 41:
    - The PLS regression model works well in predicting total dosage from ATR-FTIR spectral data;
    - The PNN classification of sample groups according to aging temperature yields mean correct classification at 78 %.
- Task 1.5 Develop models of mechanical property changes and polymer changes due to aging, page 60:
    - Molecular dynamics simulations were employed to predict changes in mechanical properties (stress-stain curves), infrared and Raman spectra for polyethylene that has been oxidized to varying degrees;
    - A kinetic rate model that correctly captures the reactions occurring in irradiated polyethylene accounts for changes in the degree of cross-linking and chain scission that occur in the material as aging progresses;
    - Through molecular dynamics and kinetic rate model simulations, the mechanisms at work in radiation-induced, thermo-oxidative aging of polyethylene are better explained.
- Task 2 Identify spectral indicators due to aging, page 66:

    - Through statistical analysis the most sensitive indicators of polymer-based insulation material aging have been determined;
    - Multiple linear regression models have been used to construct equations that predict the values of one dimension as a function of dose rate and total dose (number of days of exposure).
- Task 3.4 Calculate spectra, page 83:
    - Dielectric properties and infrared spectra calculated for crystalline polyethylene and oxidized crystalline polyethylene support the experimental observations detailed in Task 1.4 Dielectric, THz and infrared characterization of aged samples, page 41;
    - The presence of oxygen atoms, in the form of carbonyl, causes an increase in calculated dielectric constant and introduces additional peaks in calculated infrared spectra, as observed experimentally, and in Raman spectra (not validated in this work).

Summary and Key Conclusions

- Chemical reactions associated with XLPE oxidative aging were identified and supported by experimental evidence;
- PLS regression modeling worked well in predicting total gamma radiation dose received by a sample, from ATR-FTIR spectral data measured on it;
- PNN classification of samples according to aging temperature worked correctly for 78 % of samples tested, using ATR-FTIR spectral data;
- Molecular dynamics simulations predicted successfully the changes in infrared spectra of PE due to oxidation that were observed experimentally;
- A kinetic rate model predicted successfully the trends observed experimentally in cross-linking and chain scission as radiation-induced aging of PE/XLPE proceeds;
- A satisfactory multiple linear regression model relating OIT and aging conditions was obtained;
- Molecular dynamics simulations predicted an increase in dielectric constant upon oxidation of PE, matching the observed trend.

Changes in Approach

Some minor changes in project approach were made during the project period. These changes and the reasons for them are listed below.

- In regards to Task 1.2 'Accelerated aging of samples,' it was originally proposed to consider polymer aging effects due to moisture whereas in fact we took advantage of the availability of the PNNL high-exposure facility to focus on *simultaneous* thermal and gamma-radiation induced aging, which has been poorly studied to date. In order to thoroughly research the effects of simultaneous thermal and radiation aging, moisture-induced aging was not considered.
- In regards to Task 1.3 'Thermal, mechanical, and chemical characterization of aged samples,' and Task 2 'Identify spectral indicators due to aging,' it was decided to characterize the entire sample set rather than only those samples considered as priority samples for elucidating aging mechanisms and validating models. The benefit of characterizing the entire sample set lies in improved statistics pertaining to the sensitivity of particular measurands as indicators of aging, the focus of Task 2.
- Additional characterization experiments, beyond those originally proposed, were performed for the purpose of elucidating the composition of the filled, commercial XLPE and the investigation of antioxidant depletion during aging.
- In regards to Task 1.4 'Dielectric, THz and infrared characterization of aged samples,' a new accessory for FTIR was purchased for the purpose of improving the low-wavenumber spectral data available, providing insight into XLPE aging in relation to the anti-oxidant behavior.
- In connection with the previous point, effort originally planned under Task 3.3 'Measure THz signals on aged cables' was redirected to the expanded effort under Task 1.4 'Dielectric, THz and infrared characterization of aged samples,' as just mentioned.

Changes of Key Personnel

- Co-investigator Prof. Scott Beckman moved from Iowa State University to Washington State University during Year 1 of this project, remaining as a co-investigator through a sub-contract from Iowa State University to Washington State University.
- Co-investigator Dr. Samy Madbouly departed Iowa State University during Year 1 of this project. His area of expertise was subsequently covered by Dr. Leonard S. Fifield of PNNL who was already a co-investigator on the project. [Note: the 'Request for Co-PI Change' was submitted by Iowa State University to U.S. Department of Energy on November 4, 2016.]

Products

Publications

Theses

1. Shuaishuai Liu, "Composition identification, aging mechanisms and nondestructive aging indicator of commercial filled cross-linked polyethylene (XLPE) cable insulation materials," PhD thesis, Dept. Mater. Sci. Engng., Iowa State Univ., Ames, IA, 2017. Online at: https://lib.dr.iastate.edu/cgi/viewcontent.cgi?article=7172&context=etd
2. Chamila De Silva, "Principal component analysis (PCA) as a statistical tool for identifying key indicators of nuclear power plant cable insulation degradation," MS thesis, Dept. Mater. Sci. Engng., Iowa State Univ., Ames, IA, 2017. Online at: https://lib.dr.iastate.edu/cgi/viewcontent.cgi?article=7127&context=etd
3. Mario V. Imperatore, "Dielectric Spectroscopy as a condition monitoring diagnostic technique for thermally aged PVC/EPR nuclear power plant cables," MS thesis, Dipartimento di Ingegneria Dell'energia Elettrica E Dell'informazione "Guglielmo Marconi" – DEI, Univ. Bologna, Bologna, Italy, 2016.

Journal papers

Published

1. N. Bowler and S. Liu, Aging Mechanisms and Monitoring of Cable Polymers, *Int. J. Prognostics and Health Management*, 6, (Special Issue Nuclear Energy PHM) 029, pages: 12, 2015. Online at: http://www.phmsociety.org/references/ijphm-archives/2015/Sp3

Submitted

1. Shuaishuai Liu, Stephen W Veysey, Leonard S Fifield, Nicola Bowler, "Quantitative analysis of changes in antioxidant in crosslinked polyethylene (XLPE) cable insulation material exposed to heat and gamma radiation," *Polymer Degradation and Stability*, revised July 2018.

In preparation

Seven journal manuscripts are being prepared.

1. Shuaishuai Liu, Leonard S. Fifield, and Nicola Bowler, "Aging Mechanisms of Filled Cross-linked Polyethylene (XLPE) Exposed to Simultaneous Thermal and Gamma Radiation," to be submitted.
2. Shuaishuai Liu, Nicola Bowler, Mark, K. Murphy, and Leonard S. Fifield, "Simultaneous versus Sequential Thermal and Gamma Radiation Aging of Cable Polymers," to be submitted.
3. Chien-Ping Chiou, Ying-Bin Gao, Shuaishuai Liu, Bo Z. Xu, Scott P. Beckman, Leonard S. Fifield, and Nicola Bowler, "Infrared spectroscopic indicators of thermal and radiation aging of polyethylene and filled cross-linked polyethylene (XLPE)," to be submitted.
4. Irmak Sargin, and Scott P. Beckman, "Crosslinking and chain scission of irradiated polyethylene," *IEEE Trans. Dielectr. Electr. Insul.*, to be submitted.
5. Chamila C De Silva, Scott P Beckman, Shuaishuai Liu, Leonard S. Fifield, and Nicola Bowler, "An informatics approach to identifying key indicators of cable insulation degradation," to be submitted.

6. Z. Shao, M. I. Byler, S. Liu, C.-P. Chiou, L. S. Fifield, M. K. Murphy, A. Gjersvik, and N. Bowler, "Dielectric Loss and Breakdown Response of XLPE to γ-Radiation and Thermal Exposure," *IEEE Trans. Dielectr. Electr. Insul.*, to be submitted.
7. Mario V. Imperatore, Leonard S. Fifield, Davide Fabiani, and Nicola Bowler, "Dielectric spectroscopy as a non-destructive method to assess the aging conditions of thermally aged PVC/EPR nuclear power plant cables," *Polymer Testing*, to be submitted.

Conference papers

Published

1. M. V. Imperatore, L. S. Fifield, D. Fabiani, and N. Bowler, Dielectric Spectroscopy on Thermally Aged, Intact, Poly-vinyl Chloride/Ethylene Propylene Rubber (PVC/EPR) Multipolar Cables, *Annual Conference on Electrical Insulation and Dielectric Phenomena*, Fort Worth, TX, USA, October 22-25, 2017, pp. 173-176. Online at: http://ieeexplore.ieee.org/document/8257522/
2. S. Liu, L. S. Fifield, and N. Bowler, Aging Mechanisms and Nondestructive Aging Indicator of Filled Cross-linked Polyethylene (XLPE) Exposed to Simultaneous Thermal and Gamma Radiation, *18th International Conference on Environmental Degradation of Materials in Nuclear Power Systems – Water Reactors*, Portland, Oregon, USA, August 13-17, 2017, pp. 65-75. Online at: https://link.springer.com/chapter/10.1007/978-3-319-68454-3_6
3. C. C. De Silva, S. P. Beckman, S. Liu, and N. Bowler, Principal Component Analysis (PCA) as a Statistical Tool for Identifying Key Indicators of Nuclear Power Plant Cable Insulation Degradation, *18th International Conference on Environmental Degradation of Materials in Nuclear Power Systems – Water Reactors*, Portland, Oregon, USA, August 13-17, 2017, pp. 11-23. Online at: https://link.springer.com/chapter/10.1007/978-3-319-68454-3_2
4. Z. Shao and N. Bowler, Capacitive Nondestructive Evaluation of Aged Crosslinked Polyethylene (XLPE) Cable Insulation Material, *18th International Conference on Environmental Degradation of Materials in Nuclear Power Systems – Water Reactors*, Portland, Oregon, USA, August 13-17, 2017, pp. 87-97. Online at: https://link.springer.com/chapter/10.1007/978-3-319-68454-3_8
5. S. Liu, L. S. Fifield, and N. Bowler, Towards Aging Mechanisms of Cross-Linked Polyethylene (XLPE) Cable Insulation Materials in Nuclear Power Plants, *Annual Conference on Electrical Insulation and Dielectric Phenomena*, Toronto, Canada, October 16-19, 2016. Online at: http://ieeexplore.ieee.org/document/7785636/
6. L. S. Fifield, S. Liu, and N. Bowler, Simultaneous Thermal and Gamma Radiation Aging of Cable Polymers, *Annual Conference on Electrical Insulation and Dielectric Phenomena*, Toronto, Canada, October 16-19, 2016. Online at: http://ieeexplore.ieee.org/document/7785479/
7. B. Z. Xu, N. Bowler, and S. P. Beckman, First Principles and Molecular Dynamics Modeling Investigation on Polyethylene, *Annual Conference on Electrical Insulation and Dielectric Phenomena*, Toronto, Canada, October 16-19, 2016. Online at: http://ieeexplore.ieee.org/document/7785553/

Accepted

1. Z. Shao, M. I. Byler, S. Liu, N. Bowler, L. S. Fifield, and M. K. Murphy, "Dielectric Response of Cross-Linked Polyethylene (XLPE) Cable Insulation Material to Radiation and Thermal Aging," *2nd IEEE International Conference on Dielectrics (ICD2018)*, Budapest, Hungary, July 1-5, 2018.

Conference presentations (without paper)

One oral presentation was given at the conference *Review of Progress in Quantitative Nondestructive Evaluation*, Atlanta, GA, USA, July 16-22, 2016. Presenter is underlined.

1. N. Bowler, S. Liu, M. I. Byler, and L. S. Fifield, "Capacitive Sensing for Nuclear Power Plant Cable Insulation Assessment."

Collaborations fostered

- **AMS**: Analysis & Measurement Services Corporation is a nuclear engineering consulting firm specializing in testing the instrumentation and control systems of nuclear power plants. AMS Corp. is a collaborator on our present project bringing expertise in reflectometry-based cable test methods and access to certain sample materials.
- **Fauske & Associates** provides engineering services to the nuclear industry, in particular in the testing and analysis of aging effects on cables at nuclear facilities. The team is in discussion with Fauske on the topic of development of interdigital capacitive sensors for cable health monitoring.
- **EPRI**: The team has developed relationships with Senior Technical Leaders at the Electric Power Research Institute (EPRI) in the areas of developing nondestructive evaluation (NDE) techniques for industrial applications, and EPRI cable research in Plant Engineering and Long Term Operation. The relationship brings good insight into the plant-based issues surrounding cable maintenance and access to the perspective of the DOE/NRC/EPRI research coordination and collaboration team.
- **University of Manchester, UK**: Discussions with researchers at the University of Manchester, UK, are ongoing with regards to possible future US-UK research collaborations.
- **University of Strathclyde, UK**: Discussions with researchers at the University of Strathclyde, UK, are ongoing with regards to possible future US-UK research collaborations.
- **University of Bologna, Italy**: MS student Mario V. Imperatore from the University of Bologna conducted his thesis research at Iowa State University, on this project, analyzing samples furnished by Pacific Northwest National Laboratory.
- **European Commission Joint Research Centre: Strategy and Work Programme**: L. S. Fifield, **N. Bowler**, F. Rossi, and D. Fabiani, "Advanced Electrical Methods for Cable Lifetime Management," January 2018 through December 2020, $674,000. Four-way collaboration between Iowa State University, USA, Pacific Northwest Laboratory, USA, the University of Bologna, Italy, and European Commission Joint Research Centre (JRC), Petten, Netherlands.

Inventions/Patent Applications

Invention disclosure "Cylindrical interdigital sensor for non-destructive evaluation of multi-layered single and multi-strand core cable" was submitted to Iowa State University Research Foundation for consideration but not pursued due to similar intellectual property existing.

Computer Modeling – Kinetic Rate Model of Polymer Chain Scission and Cross-Linking

a. Model description, key assumptions, version, source and intended use

The model of chain scission versus cross-linking described in Section 1.5 is a kinetic rate model. It is a mean field model that assumes the specimen is a homogenous isotropic material and that the distribution of O_2 is uniform. Other global assumptions include that the pristine sample contains only polyethylene (no fillers), and the presence of airborne species other than oxygen, such as nitrogen, carbon dioxide, etc, is ignored.

b. Performance criteria for the model related to the intended use

The performance criteria are that the model will reproduce the concentration of cross linking and chain scission sites as a function of irradiation rate and time.

c. Test results to demonstrate the model performance criteria were met (e.g., code verification/validation, sensitivity analyses, history matching with lab or field data, as appropriate)

We do not have experimental measurements available to validate this model but it was shown to correct a runaway reaction erroneously predicted by earlier published work.

d. Theory behind the model, expressed in non-mathematical terms

There exists a finite set of chemical reactions that exist in equilibrium. Exposing the material to radiation injects a set of radicals, removing the system from equilibrium. Over time the constituents re-establish equilibrium. The rate at which this occurs depends on a reaction rate. The reaction rate depends on the rate that reagents diffuse through the solid.

e. Mathematics to be used, including formulas and calculation methods

Chemical reaction, conservation of energy, and diffusion dependent reaction rate.

f. Whether or not the theory and mathematical algorithms were peer reviewed, and, if so, include a summary of theoretical strengths and weaknesses

This method is generally considered reasonable. It basically involves applying conservation of mass to follow the reactions. The particular family of chemical equations we considered also seem well established and peer reviewed.

g. Hardware requirements

Simple laptop computer.

h. Documentation (e.g., user guide, model code)

None available.

Computer Modeling – Density Functional Perturbation Theory for Calculation of Infrared and Raman Spectra

a. Model description, key assumptions, version, source and intended use

The density functional perturbation theory model of infrared (IR) and Raman spectra, described in Section 3.4, uses the Quantum Espresso software package. The theory has been developed over the past 60 years and the software for over 20 years. Theoretical background to this approach is provided in Appendix A. The fundamental assumptions are that a many-electron system can be treated a as single electron charge density and the rate of electron motion is significantly greater than ion motion.

b. Performance criteria for the model related to the intended use

The performance criteria are that the model will reproduce the vibrational modes, IR, and Raman spectra of molecular PE and derivatives.

c. Test results to demonstrate the model performance criteria were met (e.g., code verification/validation, sensitivity analyses, history matching with lab or field data, as appropriate)

We compared our computed results to measured spectra and verified the results.

d. Theory behind the model, expressed in non-mathematical terms

A many-electron system is treated as a single electron charge density and the rate of electron motion is assumed to be significantly greater than ion motion. The Hamiltonian in the Schrödinger equation is simplified to the Hamiltonian in the Kohn-Sham equations. The many-body effects are treated assuming that the electron distribution is slowly varying, i.e., the many body effects are a local functional of the charge density, and do not require long range considerations. The forces on atoms are simply the gradient of energy with respect to ion position. This allows the dynamical matrix to be directly calculated and the phonon frequencies (the eigenvalues of the dynamical matrix) to be determined.

e. Mathematics to be used, including formulas and calculation methods

Solving the Kohn-Sham equations. Finding the eigenvalues and eigenvectors of matrices.

f. Whether or not the theory and mathematical algorithms were peer reviewed, and, if so, include a summary of theoretical strengths and weaknesses

Highly peer reviewed and well accepted in the literature.

g. Hardware requirements

Calculations required 128+ processor cores, each with 8 GByte memory, to be available for weeks at a time.

h. Documentation (e.g., user guide, model code)

http://www.quantum-espresso.org/

Appendix A: Theoretical Background to Density Functional Perturbation Theory

A.1 Electronic Structure Problem

A major goal of electronic structure calculations is to solve the non-relativistic time independent Schrodinger equation,

$$\hat{H}\Psi = E\Psi \tag{A.1}$$

where $\hat{H}$ is the Hamiltonian for a system consisting of M nuclei and N electrons which are described by position vectors R_A and r_i, respectively. The distance between the i-th electron and A-th nucleus is $r_{iA}=|r_i- R_A|$; the distance between i-th and j-th electron is $r_{ij} =|r_i-r_j|$, and the distance between the A-th nucleus and B-th nucleus is $R_{AB} = |R_A-R_B|$. In atomic units (energy in Hartree and length in Bohr), $\hat{H}$ can be expanded as

$$\hat{H}_{elec} = -\sum_{i=1}^{N}\frac{1}{2}\nabla_i^2 - \sum_{i=1}^{N}\sum_{A=1}^{M}\frac{Z_A}{r_{iA}} + \sum_{i=1}^{N}\sum_{j\geq i}^{N}\frac{1}{r_{ij}} \tag{A.2}$$

In the above equation, M_A is the ratio of the mass of nucleus A to the mass of an electron and Z_A is the atomic number of nucleus A. The ∇_A^2 and ∇_i^2 are the Laplacian operators. The first two terms in Eq. (A.2) are for the kinetic energy of the electrons and nuclei, respectively. The third term represents the Coulomb attraction between electrons and nuclei. The fourth and fourth and fifth terms represent the repulsion between electrons and between nuclei, respectively. The compact form of Eq. (A.2) is as a result of using atomic units.

A.1.1 The Born-Oppenheimer Approximation

The Born-Oppenheimer approximation [1] plays a vital role in electronic structure calculations. The underlying rationale for this approximation is that the mass of the nuclei is much greater than that of the electrons. Even for the lightest nucleus, a proton, its mass is approximately 3000 times larger than that of the electron. Thus, in most cases, nuclei move much more slowly than electrons. Hence, in many cases, one can consider the electrons as moving in a field produced by the fixed nuclei. This is the qualitative rationale for separating the movement of electrons and nuclei. Under the Born-Oppenheimer approximation the second term in Eq. (A.2) is neglected, and the final term, the repulsion between nuclei, can be treated as a constant for a fixed configuration of the nuclei. The remaining terms in Eq. (A.2) are called the electronic Hamiltonian:

$$\hat{H}_{elec} = -\sum_{i=1}^{N}\frac{1}{2}\nabla_i^2 - \sum_{i=1}^{N}\sum_{A=1}^{M}\frac{Z_A}{r_{iA}} + \sum_{i=1}^{N}\sum_{j\geq i}^{N}\frac{1}{r_{ij}} \tag{A.3}$$

The solution to a Schrodinger equation involving the electronic Hamiltonian,

$$\hat{H}_{elec}\Psi_{elec} = E_{elec}\Psi_{elec} \tag{A.4}$$

is the electronic wave function

$$\Psi_{elec} = \Psi_{elec}(r_i, R_A) \tag{A.5}$$

which describes the motion of the electrons and explicitly depends on the electronic coordinates (r_i) but parametrically on the nuclear coordinates (R_A). Furthermore, to completely specify an electron, it is necessary to assign the corresponding spin (ω), so together with the spatial coordinates, we denote these four coordinates collectively by X,

$$X=\{r, \omega\} \tag{A.6}$$

and the wave function for an N-electron system is written as $\psi(X_1, X_2, \ldots, X_N)$.

The total energy of fixed nuclei will also include the constant nuclear repulsion term leading to,

$$E_{tot} = E_{elec} + \sum_{A=1}^{M} \sum_{B \geq A}^{M} \frac{Z_A Z_B}{R_{AB}} \tag{A.7}$$

Solving versions of Eq. (A.4) and (A.7) is the main focus of the research reported in this thesis and, indeed electronic structure calculations in general. In the following, the subscript "elec" will be dropped.

However, one should bear in mind that although we will solve versions of Eq. (A.4) and Eq. (A.7) in which the Born-Oppenheimer approximation is made, the Born-Oppenheimer approximation is certainly not universally valid. It is well known that the Born-Oppenheimer approximation will break down when there are multiple potential energy surfaces close to each other in energy or crossing each other. Dissociative adsorption of molecules on metal surfaces is a famous contemporary example. Similarly, reactions involving hydrogen and proton transfer may be susceptible to breakdowns in the Born-Oppenheimer approximation. More caution must be exerted when dealing with systems such as those [2, 3, 4, 5].

Despite the deceptively simple form of the Eq. (A.4), its exact solution for anything but the simplest of systems remains to the present day a major challenge. The difficulties in solving Eq. (A.4) lie in the electron-electron interaction, which includes all the quantum effects of the electrons. Despite the intractable nature of these interactions, many approximate methods have been developed to solve Schrodinger-like equations. Some of these approximate solutions, the ones made use of in this thesis, will be introduced in the following. However, the Slater determinant will be introduced first due to its fundamental role in many aspects of electronic structure theory.

A.1.2 Slater Determinants

Electrons are fermions and obey the Pauli exclusion principle. This requires that the wave function of electrons should be antisymmetric with respect to the interchange of the coordinates X of any two electrons,

$$\Phi\,(X_1, \dots, X_i, \dots, X_j, \dots, X_N) = -\,\Phi\,(X_1, \dots, X_j, \dots, X_i, \dots, X_N) \tag{A.8}$$

Slater determinants nicely satisfy this antisymmetric condition through an appropriate linear combination of Hartree products, which are the non-interacting electron wave functions. For example, consider a two-electron case in which we occupy the spin orbitals χ_i and χ_j. If we put electron one in χ_i and electron two in χ_j, we will have

$$\Phi_{12}\,(X_1, X_2) = \chi_i(X_1)\,\chi_j(X_2) \tag{A.9}$$

On the other hand, if we put the electron one in χ_j and electron two in χ_i, we will have

$$\Phi_{21}\,(X_1, X_2) = \chi_i(X_2)\,\chi_j(X_1) \tag{A.10}$$

by taking a linear combination of these two products,

$$\Phi\,(X_1, X_2) = 2^{-1/2}(\chi_i(X_1)\,\chi_j(X_2) - \chi_i(X_2)\,\chi_j(X_1)) \tag{A.11}$$

where the factor $2^{-1/2}$ is a normalization factor. It can be seen that the antisymmetry is guaranteed during interchange of the coordinates of electron one and electron two:

$$\Phi\,(X_1, X_2) = -\,\Phi\,(X_2, X_1) \tag{A.12}$$

The antisymmetric wave function of Eq. (A.11) can be rewritten as a determinant,

$$\Phi\,(X_1, X_2) = 2^{-1/2} \begin{vmatrix} \chi_i(X_1) & \chi_j(X_1) \\ \chi_i(X_2) & \chi_j(X_2) \end{vmatrix} \tag{A.13}$$

and this is called a Slater determinant. For an N-electron system, the Slater determinant becomes,

$$\Phi(X_1, X_2, \ldots, X_N) = (N!)^{-1/2} \begin{vmatrix} \chi_i(X_1) & \chi_j(X_1) & \ldots & \chi_k(X_1) \\ \chi_i(X_2) & \chi_j(X_2) & \ldots & \chi_k(X_2) \\ \vdots & \vdots & & \vdots \\ \chi_i(X_N) & \chi_j(X_N) & \ldots & \chi_j(X_N) \end{vmatrix} \quad (A.14)$$

Note that the rows of the N-electron Slater determinant are labeled by electrons: first row (X_1), second row (X_2), … , final row (X_N). The columns are labeled by spin orbitals: first column (χ_i), second (χ_j), … , final column (χ_N). Interchanging the coordinates of two electrons equals to the interchange of two rows of the Slater determinant that will change its sign. Thus the Slater determinant meets the requirement of antisymmetry. Furthermore, having two electrons occupying the same spin orbital corresponds to having two columns of the determinant identical, which leads to the determinant being zero, as it should. It is convenient to use a shorthand notation for a Slater determinant that only shows the diagonal elements:

$$\Phi(X_1, X_2, \ldots, X_N) = |\, \chi_i(X_1)\, \chi_j(X_2) \ldots \chi_k(X_N) \,\rangle \quad (A.15)$$

Furthermore, if the order of electrons is always to be $X_1, X_2, \ldots, X_N$, then

$$\Phi(X_1, X_2, \ldots, X_N) = |\, \chi_i\, \chi_j, \ldots, \chi_N \,\rangle \quad (A.16)$$

A.2 The Hartree-Fock Approximation

Among the approximate ways to solve Eq. (A.4), the Hartree-Fock (HF) method has a prominent status as it often paves the way toward more accurate calculations in modern quantum chemistry. At the same time, the HF method is also used extensively by itself to study various materials science problems, such as adsorption [6], defects in solids [7], and electronic structure of insulators [8]. In this section, we give a brief account of the HF method.

The Hartree-Fock method starts from using the single Slater determinant as an approximation to the wave function of the ground state of the N-electron system:

$$|\, \Phi \,\rangle = |\, \chi_i, \chi_j, \ldots, \chi_a, \chi_b, \ldots, \chi_N \,\rangle \quad (A.17)$$

Thus this choice of the approximation of wave function guarantees a proper description of the electron that obeys the Pauli exclusion principle as shown in the previous section. Then we need to determine the "best" approximate wave function. According to the variational principle, the "best" spin orbitals are those that make energy stationary,

$$E = \frac{\int \langle \Phi(X) | \hat{H} | \Phi(X) \rangle dX}{\int \langle \Phi(X) | \Phi(X) \rangle dX} \quad (A.18)$$

then we can systematically vary the spin orbitals $\{\chi_a\}$, while constraining that they are orthonormal, $\langle\, \chi_a \,|\, \chi_b \,\rangle = \delta_{ab}$, until the electronic minimum E_0 is reached. This leads to the HF energy expression,

$$E_{HF} = \langle \Psi_0 | \hat{H} | \Psi_0 \rangle = \sum_a \int \chi_a^*(1)(-\frac{1}{2}\nabla^2 - \frac{Z_A}{r_{iA}})\chi_a(1)dx_1$$
$$+\frac{1}{2}\sum_{ab}\int \chi_a^*(1)\chi_a(1)r_{12}^{-1}\chi_b^*(2)\chi_b(2)dx_1dx_2 \quad (A.19)$$
$$-\frac{1}{2}\sum_{ab}\int \chi_a^*(1)\chi_b(1)r_{12}^{-1}\chi_b^*(2)\chi_a(2)dx_1dx_2$$

Each term at the right-hand side in Eq. (A.19) will be explained in the following. The first term is the kinetic energy and potential energy for the attraction to the nuclei of a single electron. The last two terms in Eq. (A.19) are involving two electrons, and the first one is the Coulomb term and the other one is the exchange term which arises from the antisymmetric nature of the Slater determinant. For the Coulomb term, it has the classical interpretation that it represents the Coulomb interactions between two electrons. It is convenient to define a Coulomb operator,

$$J_b(1) = \int |\chi_b(2)|^2 r_{12}^{-1} dx_2 \quad (A.20)$$

Then the Coulomb term can be written as,

$$\int \chi_a^*(1)\chi_a(1)r_{12}^{-1}\chi_b^*(2)\chi_b(2)dx_1\,dx_2 = \langle \chi_a(1) | J_b(1) | \chi_a(1) \rangle \quad (A.21)$$

The exchange term, unlike the Coulomb term, has no simple classical interpretation but we can define an exchange operator by its effects when operating on $\chi_a(1)$

$$K_b(1)\chi_a(1) = [\int \chi_b^*(2)r_{12}^{-1}\chi_a(2)dx_2]\chi_b(1) \quad (A.22)$$

As evident from the above equation, $K_b(1)$ leads to an exchange of the variable in the two spin orbitals. Furthermore, the exchange operator, $K_b(1)$ is said to be a nonlocal operator, as the results of $K_b(1)$ operating on the spin orbital χ_a will depend on the value of χ_a throughout all space. Then the exchange term can be written as,

$$\int \chi_a^*(1)\chi_b(1)r_{12}^{-1}\chi_b^*(2)\chi_a(2)dx_1\,dx_2 = \langle \chi_a(1) | K_b(1) | \chi_a(1) \rangle \quad (A.23)$$

Up to this, we can write the Hartree-Fock equation as an eigenvalue equation:

$$[h(1) + \sum_{b\neq a} J_b(1) - \sum_{b\neq a} K_b(1)]\chi_a(1) = E_a\chi_a(1) \quad (A.24)$$

Furthermore, to eliminate the restriction on the summation ($b \neq a$), we define a new operator, the Fock operator, by

$$f(1) = h(1) + \sum_b J_b(1) - K_b(1) \quad (A.25)$$

The Fock operator is the sum of the operator h(1) and an effective one-electron potential operator called the Hartree-Fock potential $v_{(1)}^{HF} = \sum_b J_b(1) - K_b(1)$. From Eq. (A.25), Hartree-Fock theory is a single particle method. So then the Hartree-Fock equation becomes:

$$f | \chi_a \rangle = E_a | \chi_a \rangle \quad (A.26)$$

This is the usual form of the Hartree-Fock equation. Although, Eq. (A.26) is written as a linear eigenvalue problem, it will need to be solved by iterative procedures as the Fock operator has a functional dependence on $| \chi_a \rangle$ through the Coulomb and exchange operator.

A.3 Density-Functional Theory (DFT)

In the preceding section, we introduced the Hartree-Fock method as a way to solve, approximately,

the electronic Schrodinger equation. One feature of this method is that it relies on the many-body wave function as a central quantity. Once the wave function is known, the energy of the system and all related properties can be determined. But the wave function itself is a complicated quantity because it depends on 3N spatial variables together with the spin variable, where N is the number of electrons in the system. This severely limits the system sizes that can be treated with wave function-based methods. Certainly systems with hundreds of atoms and large basis sets are beyond reach for most practical studies with wave function based methods.

DFT differs from the wave function based methods by using the electron density $(\rho(r))$ as the central quantity. The advantage of using the electron density over the wave function is the much-reduced dimensionality. Regardless of how many electrons one has in the system, the density is always 3 dimensional. This enables DFT to be applied on much larger systems; consideration of hundreds or even thousands of atoms becomes possible. Partly for this reason, DFT has become the most widely used electronic structure modeling approach today in the condensed matter physics community. In this section, a basic introduction to DFT will be given. Authoritative and comprehensive discussions of DFT can be found in a range of excellent review articles [9, 10, 11, 12] and textbooks [13, 14].

A.3.1 Thomas-Fermi Theory

The history of using the electron density rather than the wave function begins with the early work of Thomas and Fermi [15, 16]. First, let us define the electron density

$$\rho(r) = N \int ... \int |\Psi(X_1, X_2, ..., X_N)|^2 \, dX_1 dX_2 ... dX_N \tag{A.27}$$

where $\rho(r)$ determines the probability of finding any of the N electrons within the volume with radius r but with arbitrary spin while the other N-1 electrons have arbitrary positions and spin in the state represented by Ψ. This is a nonnegative simple function of three variables, x, y, and z, integrating to the total number of electrons,

$$\int \rho(r) dr = N \tag{A.28}$$

In Thomas-Fermi theory, the kinetic energy of electrons is derived from the quantum statistical theory based on the uniform electron gas, but the interaction between electron-nucleus and electron-electron are treated classically. Within this model, the kinetic energy of the electrons is defined as,

$$T[\rho] = C_F \int \rho^{\frac{5}{3}}(r) dr \tag{A.29}$$

with $C_F = 2.871$.

From the above equation, the approximation is made that the kinetic energy only of the electron depends exclusively on the electron density. By adding the interaction between electron-nucleus and electron-electron into Eq. (A.29), a total energy in terms of electron density is obtained,

$$E[\rho] = C_F \int \rho^{\frac{5}{3}}(r) dr - Z \int \frac{\rho(r)}{r} dr + \frac{1}{2} \int \int \frac{\rho(r_1)\rho(r_2)}{|r_1 - r_2|} dr_1 \, dr_2 \tag{A.30}$$

The second and third terms are the electron-nucleus and electron-electron interactions, respectively.

The importance of this simple Thomas-Fermi model is not how well it performs in computing

the ground state energy and density but more as an illustration that the energy can be determined purely using the electron density.

A.3.2 Hohenberg-Kohn Theorem

Modern density-functional theory was born in 1964 with the paper of Hohenberg and Kohn [15]. The two key results of this paper are: (i) a one-to-one mapping between external potential and electron density was established; (ii) it was shown that the ground state density can be found by using a variational principle.

The first part was proved in a simple and extremely elegant manner using the principle of *reductio ad absurdum*, reproduced here for a non-degenerate system. Suppose there is a collection of electrons enclosed into a box influenced by an external potential $v(\mathrm{r})$. We assume we know the electron density of this system and it also determines $v(\mathrm{r})$ and thus all properties. If there is another external potential $v'(\mathrm{r})$ which differs from $v(\mathrm{r})$ by more than a constant that can also give the same electron density $\rho(r)$ for the ground state, then we will have two different Hamiltonians $\hat{H}$ and $\hat{H}'$ whose ground state electron density is the same but the normalized wave function Φ and Φ' would be different. Then we will have

$$\begin{aligned} E_0 < \langle \Phi' | \hat{H} | \Phi' \rangle &= \langle \Phi' | \hat{H}' | \Phi' \rangle + \langle \Phi' | \hat{H} - \hat{H}' | \Phi' \rangle \\ &= E'_0 + \int \rho(r)[v(r) - v(r)']dr \end{aligned} \tag{A.31}$$

where E_0 and E'_0 are the ground-state energies for $\hat{H}$ and $\hat{H}'$, respectively. Similarly, we can get

$$\begin{aligned} E'_0 < \langle \Phi | \hat{H} | \Phi \rangle &= \langle \Phi | \hat{H} | \Phi \rangle + \langle \Phi | \hat{H}' - \hat{H} | \Phi \rangle \\ &= E_0 - \int \rho(r)[v(r) - v(r)']dr \end{aligned} \tag{A.32}$$

Adding Eq. (A.31) and Eq. (A.32), we will obtain

$$E_0 + E'_0 < E'_0 + E_0 \tag{A.33}$$

This is an obvious contradiction. So, there are no two different external potentials that can give the same $\rho(r)$ and, thus, $\rho(r)$ uniquely determines $v(\mathrm{r})$ and all ground-state properties.

Now we can write the energy E explicitly as a function of the electron density $\rho(r)$:

$$\begin{aligned} E[\rho] &= T[\rho] + T_{ne}[\rho] + V_{ee}[\rho] \\ &= \int \rho(r) v(r)\, dr + F_{HK}[\rho] \end{aligned} \tag{A.34}$$

Here note that $F_{HK}[\rho]$ is only dependent on ρ and independent from any external potential $v(\mathrm{r})$. Thus $F_{HK}[\rho]$ is a universal functional of ρ.

The second Hohenberg-Kohn theorem demonstrates that that the ground state energy can be obtained variationally, with the density that minimizes the total energy being the exact ground state density. This is expressed as:

$$E_0[\rho_0] \leq E_v[\rho] \tag{A.35}$$

where $E_v[\rho]$ is the energy functional of Eq. (A.34). Following from the first part of the theorem, suppose the ground state wave function is Φ and its related electron density is ρ. Thus ρ uniquely

defines the external potential $v(\mathrm{r})$. If there is another wave function Φ' with a arbitrary variation from Φ and its electron density is ρ', then we can obtain,

$$\langle \Phi' | \hat{H} | \Phi' \rangle = \int \rho'(r) v(r) + F_{HK}[\rho'] = E[\rho'] \geq E[\rho] \tag{A.36}$$

So the energy will reach the minimum only when the electron density is the groundstate electron density.

A.3.3 The Kohn-Sham Equations

From the Hohenberg-Kohn theorem, we can get the ground-state energy by minimizing the energy functional,

$$E[\rho] = \int \rho(r) v(r)\, dr + F_{HK}(\rho(r)) \tag{A.37}$$

Although the Hohenberg-Kohn theorem provided a proof in principle that the total energy could be obtained from the ground state density it was not yet known how to obtain the $\rho(r)$ or $F_{HK}(\rho(r))$. In 1965, Kohn and Sham [16] published a paper that transformed density-functional theory into a practical electronic structure theory. Kohn and Sham recognized that the failure of Thomas-Fermi theory mainly resulted from the bad description of the kinetic energy. To address this problem they decided to re-introduce the idea of one-electron orbitals and approximate the kinetic energy of the system by the kinetic energy of non-interacting electrons. This led to the central equation in Kohn-Sham DFT, which is the one-electron Schrodinger-like equation, expressed as

$$(-\frac{1}{2}\nabla^2 + v(r) + \int \frac{\rho(r')}{|r - r'|} dr' + v_{xc}(r))\phi_i = \varepsilon \phi_i \tag{A.38}$$

Here ϕ are the Kohn-Sham orbitals and the electron density is expressed by,

$$\rho(r) = \sum_i^N |\phi_i|^2 \tag{A.39}$$

The terms on the left side of Eq. (A.38) are the kinetic energy of the non-interacting reference system, the external potential, the Hartree potential, and exchange-correlation potential, respectively. The parameter ε is the energy of the Kohn-Sham orbital. In addition, the exchange-correlation potential is given by,

$$v_{xc}(r) = \frac{\delta E_{xc}[\rho]}{\delta \rho(r)} \tag{A.40}$$

and $E_{xc}[\rho]$ is the exchange-correlation functional which will be discussed in Section A.3.4.

Furthermore, we can define an effective potential:

$$v_{eff} = v(r) + \int \frac{\rho(r')}{|r - r'|} dr' + v_{xc}(r) \tag{A.41}$$

This allows Eq. (A.38) to be rewritten in a more compact form,

$$(-\frac{1}{2}\nabla^2 + v_{eff})\phi_i = \varepsilon \phi_i \tag{A.42}$$

Clearly this is a Hartree-Fock like single particle equation, which needs to be solved iteratively. Finally, the total energy can be determined from the resulting density through

$$E = \sum_i^N \varepsilon_i - \frac{1}{2}\int\int \frac{\rho(r)\rho(r')}{|r-r'|} dr\, dr' + E_{xc}[\rho] - \int v_{xc}(r)\rho(r)\, dr \qquad \text{(A.43)}$$

Equations (A.42), (A.39), and (A.40) are the celebrated Kohn-Sham equations. Note that the v_{eff} depends on $\rho(r)$ through Eq. (A.41). So the Kohn-Sham equation must be solved self-consistently. The general procedure is to begin with an initial guess of the electron density, construct the v_{eff} from Eq. (A.41), and then get the Kohn-Sham orbitals. Based on these orbitals, a new density is obtained from Eq. (A.39) and the process repeated until convergence is achieved. Finally, the total energy will be calculated from Eq. (A.43) with the final electron density. If each term in the Kohn-Sham energy functional was known, we would be able to obtain the exact ground state density and total energy. Unfortunately, there is one unknown term, the exchange-correlation (xc) functional E_{xc}. E_{xc} includes the non-classical aspects of the electron-electron interaction along with the component of the kinetic energy of the real system different from the fictitious non-interacting system. Since E_{xc} is not known exactly, it is necessary to approximate it, which is the focus of the next section.

A.3.4 Exchange-Correlation Functionals

To use the Kohn-Sham equations we must know the form of the exchange-correlation energy functional. However, the exact form of E_{xc} is not known and may never be known (in some simple closed form). Thus since the birth of DFT approximations for E_{xc} have been used. By now there is an almost endless list of approximations with varying levels of complexity. Recently, a useful way for categorizing the many and varied E_{xc} functionals that exist has been proposed by Perdew and is known as "Jacob's ladder". In this scheme functionals are grouped according to their complexity on rungs of a ladder, which lead from the Hartree approximation on "earth" to the exact exchange-correlation functional in "heaven". We now very briefly discuss the first few rungs of this ladder as a means to introduce some of the most common types of exchange-correlation functionals in widespread use:

(a) The local-density approximation (LDA): This is the simplest approximation. The exchange-correlation energy density is taken to be that of a uniform electron gas of the same density. The exchange energy is known exactly and the correlation energy is obtained by fitting to the many-body studies of Gell-Mann and Brueckner, and Ceperly and Alder [17, 18]. Modern LDA functionals tend to be exceedingly similar, differing only in how their correlation contributions have been fitted to the many-body free electron gas data. The Perdew-Zunger (PZ) [19], Perdew-Wang (PW) [20], and Vosko-Wilk-Nusair (VWN) [21] functionals are all common LDA functionals. Strictly, the LDA is valid only for slowly varying densities. Experience with calculations of atoms, molecules, and solids shows that LDA can in general also be applied to these systems. Indeed LDA works surprisingly well and much current understanding of metal or semiconductor (Si or GaAs) surfaces comes from LDA simulations. A partial rationalization of the success of LDA is provided by the observation that it satisfies a number of so-called sum rules [22, 23, 24, 25].

(b) The generalised gradient approximation (GGA): These are the second-generation functionals (sitting on the second rung of Jacob's ladder). GGAs are "semi-local" functionals, comprising corrections to the LDA while (again) ensuring consistency with known sum rules. For many

properties, for example geometries and ground state energies of molecules, GGAs can yield better results than the LDAs. Although, for the properties of metals and their surfaces, GGA results are not necessarily superior to LDA results. The most widely used GGAs in surface physics are the PW91 [26] functional, and its close relative PBE [27]. PBE actually has several offspring; revPBE [28], RPBE, PBE-WC [29], and PBEsol [30]. RPBE is the most popular of the off-spring, although the latest addition to the PBE family, PBE-WC and PBEsol, offers promise for the simulation of solids and their surfaces. Also the specially designed functional, AM05 [31], dedicated to include the surface effect which has been shown to give a much improved performance for bulk properties, such as lattice constant and bulk modulus, and jellium surface energy, than PBE and PW91 [32].

A.4 Plane-Waves and Pseudopotentials

As with the wave function based methods, when it comes to the practical application of DFT, issues such as basis sets need to be considered. In calculations of solids or condensed matter, which will be the main types of systems that DFT is applied to in this thesis, the plane-wave basis set is a very common choice. In many cases, combined with plane-wave is the pseudopotential approach for treating the strong interactions between core electrons and nuclei. We will now briefly discuss plane-waves and then pseudopotentials.

A.4.1 Plane-Wave Basis Sets

When dealing with a crystal which has atoms periodically arranged, the electrons are in a periodic potential U(r) where U(r+R) = U(r) and R is the Bravais lattice vector. Starting from Bloch's theorem, the eigenstates of the one-electron Hamiltonian can be written as

$$\phi_{nk}(r) = \exp(ik \cdot r)\mu_{nk}(r) \tag{A.44}$$

where $\mu_{nk}(r)$ is a function with the same periodicity as the potential (U(r)) that μ_{nk}(r+R)= μ_{nk}(r). Furthermore, μ can be expanded as,

$$\mu_{ik} = \frac{1}{\Omega_{cell}} \sum_m c_{i,m} \exp(iG_m \cdot r) \tag{A.45}$$

where G is the reciprocal lattice vector.
We aim to solve the following Schrodinger-like equation and each electron moves in an effective potential v_{eff}(r)

$$\hat{H}_{eff}\phi_i(r) = [-\frac{1}{2}\nabla^2 + V_{eff}(r)]\phi_i(r) = \varepsilon_i\phi_i(r) \tag{A.46}$$

By the Bloch theorem, the eigenfunctions can be written as

$$\phi_i(r) = \sum_q c_{i,q} \frac{1}{\Omega} \exp(iq \cdot r) = \sum_q c_{i,q} \times |q\rangle \tag{A.47}$$

Here $c_{i,q}$ are the expansion coefficients and q = k+G, in the basis of the orthonormal plane-wave $|q\rangle$ satisfying

$$\langle q'|q\rangle = \frac{1}{\Omega}\int \exp(iq' \cdot r)\exp(iq \cdot r) = \delta_{q' \cdot q} \tag{A.48}$$

Inserting Eq. (A.47) into Eq. (A.46) with the orthogonality of Eq. (A.48) and multiplying from the left by $|q'\rangle$, leads to the Schrodinger-like equation in Fourier space,

$$\langle q' | [-\frac{1}{2}\nabla^2 + V_{eff}(r)] | q \rangle = \varepsilon_i q' | q \rangle c_{i,q} = \varepsilon_i c_{i,q} \tag{A.49}$$

Considering each term in the Hamiltonian. The first term, the kinetic energy operator, can be written as,

$$\langle q' | -\frac{1}{2}\nabla^2 | q \rangle = | q |^2 \, \delta_{q \cdot q'} \tag{A.50}$$

Second, for a crystal, the periodic potential $v_{eff}(\mathrm{r})$ can be expressed as a sum of Fourier components,

$$V_{eff}(r) = \sum_m V_{eff}(G_m) \exp(iG_m \cdot r) \tag{A.51}$$

Together with Eq. (A.50) and Eq. (A.51), Eq. (A.46) can be rewritten as

$$H_{m,m'}(k) c_{i,m'}(k) = \varepsilon_i(k) c_{i,m'}(k) \tag{A.52}$$

where

$$H_{m,m'} = \langle k + G_m | \hat{H}_{eff} | k + G'_m \rangle = | k + G_m |^2 + V_{eff}(G_m - G'_m) \tag{A.53}$$

Here q has been expanded as k + G. Eq. (A.52) and Eq. (A.53) are the basic Schrodinger-like equations of a periodic crystal with a plane-wave basis set.

A.4.2 Pseudopotentials

It is well established that most physically-interesting properties of solids are determined by the valence electrons rather than the core electrons. Meanwhile, the deeply bound core electrons within plane-wave basis sets require a huge number of basis functions for their description. This leads to a contradiction: that the less important core electrons will consume a lot of computational cost. To alleviate this problem, the pseudopotential approximation replaces the strong ionic potential with a weaker pseudopotential.

In general, there are two main purposes of the pseudopotential formalism. The first is to use a much weaker pseudopotential to replace core electrons which, due to their deep potential, need to be described by many plane-wave basis functions. The second is to eliminate the rapid oscillations of the valence electron wave function in the core region. These issues are shown in Figure 67. From Figure 67, we can see that the pseudopoential is much weaker than the all-electron potential and that the pseudo wave function has no radial node inside the core region. It is essential within the pseudopotential scheme that, outside the core region, the pseudo potential and wave function become identical with the corresponding all-electron ones (Figure 67). One important class of pseudopotentials are so called norm-conserving pseudopotentials. Norm conserving pseudopotentials require that the all-electron and pseudo wave function agree beyond a chosen radius (r_c) and that the integrated density inside r_c for the all electron wave function and pseudo wave function are the same ("norm conservation"). There are many types of norm-conserving pseudopotentials from different authors such as Troullier and Martins [33], Kerker [34], Hamann, Schluter, and Chiang, and Vanderbilt [35].

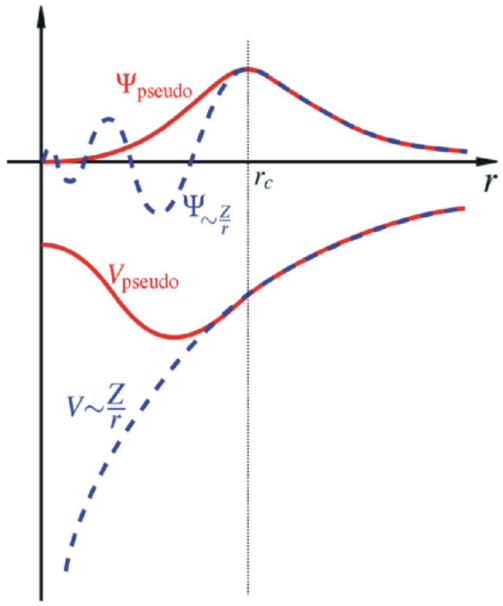

Figure 67. Schematic illustration of all-electron (dashed lines) and pseudopotential (solid lines) and their corresponding wave functions. The radius at which the all-electron and pseudo-electron values match is designated as r_c.

One problem with the norm-conserving pseudopotentials is that they cannot generate a smoother pseudo wave function than the all electron one when coming to the first row elements of the periodic table, like O, and the localized transition metals, like Ni, due to the "norm conservation" rule.

The combination of DFT, plane-wave basis set, and pseudopotentials has become a well-established methodology in electronic structure calculations of condensed matter. Usually such simulations are performed in periodic supercells to represent the physical system under consideration.

References

1. M. Born and R. Oppenheimer, Ann. Phys.(Leipzip) **84**, 457 (1927).
2. J. Behler, B. Delley, S. Lorenz, K. Reuter, and M. Scheffler, Phys. Rev. Lett. **94**, 036104 (2005).
3. J. Behler, K. Reuter, and M. Scheffler, Phys. Rev. B **77**, 115421 (2008).
4. A. M. Wodtke, J. C. Tully, and D. J. Auerbach, Int. Rev. Phys. Chem. **23**, 513 (2004).
5. A. C. Luntz, M. Persson, and G. O. Sitz, J. Chem. Phys. **124**, 091101 (2006).
6. P. Baranek, G. Pinarello, C. Pisani, and R. Dovesi, Phys. Chem. Chem. Phys. **2**, 3893 (2000).
7. S. Casassa, A. Ferrari, M. Busso, and C. Pisani, J. Phys. Chem. B **106**, 12978 (2002).
8. R. G. Parr, Ann. Rev. Phys. Chem. **34**, 631 (1983).
9. T. Ziegler, Chem. Rev. **91**, 651 (1991).
10. P. Geerlings, F. D. Proft, and W. Langenaeker, Chem. Rev. **103**, 1793 (2003).
11. R. O. Jones and O. Gunnarsson, Rev. Mod. Phys. **61**, 689 (1989); R. G. Parr and W. Yang, *Density-Functional Theory of Atoms and Molecules* (Oxford University

Press, New York, 1989).
12. M. R. Dreizler and E. K. U. Gross, *Density Functional Theory: An Approach to the Quantum Many-Body Problem* (Springer, Berlin, 1990).
13. L. H. Thomas, Proc. Camb. Phil. Soc. **23**, 542 (1927).
14. E. Fermi, Rend. Accad. Lincei. **6**, 602 (1927).
15. P. Hohenberg and W. Kohn, Phys. Rev. **136**, B864 (1964).
16. W. Kohn and L. J. Sham, Phys. Rev. **140**, A1133 (1965).
17. M. Gell-Mann and K. A. Brueckner, Phys. Rev. **106**, 364 (1957).
18. D. M. Ceperley and B. J. Alder, Phys. Rev. Lett. **45**, 566 (1980).
19. J. P. Perdew and A. Zunger, Phys. Rev. B **23**, 5048 (1981).
20. J. P. Perdew and Y. Wang, Phys. Rev. B **45**, 13244 (1992).
21. S. J. Vosko, L. Wilk, and M. Nusair, Can. J. Phys. **58**, 1200 (1980).
22. O. Gunnarsson and B. I. Lundqvist, Phys. Rev. B **13**, 4274 (1976).
23. O. Gunnarsson, M. Jonson, and B. I. Lundqvist, Sol. Stat. Comm. **24**, 765 (1977).
24. T. Ziegler, A. Rauk, and E. J. Baerends, Theor. Chim. Acta **43**, 261 (1977).
25. K. Burke, J. P. Perdew, and M. Ernzerhof, J. Chem. Phys. **109**, 3760 (1998).
26. J. P. Perdew, K. Burke, and Y. Wang, Phys. Rev. B **54**, 16533 (1992).
27. J. P. Perdew, K. Burke and M. Ernzerhof, Phys. Rev. Lett. **77**, 3865 (1996); **78**, 1396 (1197).
28. Y. Zhang and W. Yang, Phys. Rev. Lett. **80**, 890 (1998).
29. Z. Wu and R. E. Cohen, Phys. Rev. B **73**, 235116 (2006).
30. J. P. Perdew, A. Ruzsinszky, G. I. Csonka, O. A. Vydrov, G. E. Scuseria, L. A. Constantin, X. Zhou, and K. Burke, Phys. Rev. Lett. **100**, 136406 (2008).
31. R. Armiento and A. E. Mattsson, Phys. Rev. B **72**, 085108 (2005).
32. J. M. Tao, J. P. Perdew, V. N. Staroverov, and G. E. Scuseria, Phys. Rev. Lett. **91**, 146401 (2003).
33. A. D. Becke, J. Chem. Phys. **98**, 5648 (1993).
34. C. Lee, W. Yang, and R. G. Parr, Phys. Rev. B **37**, 785 (1988).
35. J. P. Perdew, M. Ernzerhof, and K. Burke, J. Chem. Phys. **105**, 9982 (1996).

Appendix B: Manuscripts submitted but not published at June 30, 2018

B.1 Quantitative analysis of changes in antioxidant in crosslinked polyethylene (XLPE) cable insulation material exposed to heat and gamma radiation

Submitted to: *Polymer Degradation and Stability*, revised July 2018.
Authors: Shuaishuai Liu[1], Stephen W Veysey[2], Leonard S Fifield[3], Nicola Bowler[1]
Affiliations:
[1]Department of Materials Science and Engineering, Iowa State University, Ames, IA 50011,USA
[2]Chemical Instrumentation Facility, Iowa State University, Ames, IA 50011, USA
[3]Pacific Northwest National Laboratory, Richland, WA 99354, USA

Abstract

Quantitative analysis of the antioxidant poly(1,2-dihydro-2,2,4-trimethylquinoline) (pTMQ) was conducted on pristine, thermally-aged, and gamma radiation-aged commercial cross-linked polyethylene-(XLPE-)based cable insulation material aged at temperatures 60, 90, and 115 °C, with gamma radiation exposure dose rates of 0, 120, 300, and 540 Gy/h for 15 days. The quantification of antioxidant was performed using pyrolysis gas chromatography-mass spectrometry (Py-GCMS). Oxidation induction time (OIT) was measured using differential scanning calorimetry (DSC) and correlation was made between the quantified depletion of antioxidant and measured OIT. It was observed that, in the case of isothermal aging, the quantity of antioxidant and OIT decreased with increasing gamma radiation dose. In the case of samples exposed to the same gamma radiation dose, the quantity of antioxidant and OIT were observed to decrease with increasing aging temperature. Depletion in the quantity of antioxidant relative to that in the pristine material ranged from 7 to 93 % for differently aged samples. The measured decline in OIT ranged from 0 to 80 %. Change in the quantity of antioxidant in the material was observed to follow the same trend as the change in OIT when the samples were aged under various conditions, with a correlation coefficient of 0.82. The observations are explained in terms of the reaction between the antioxidant and free radicals created during exposure of the samples to thermal and gamma radiation.

Introduction

As of February 2017, 61 commercial nuclear power plants (NPPs) with 99 nuclear reactors were operating in the United States [1]. Among the 99 reactors, 59 were pressurized water reactors (PWRs) and 40 were boiling water reactors (BWRs) [2]. Operation of a typical PWR requires thousands of kilometers, and a typical BWR requires hundreds of kilometers, of electrical cables [3]. The study of degradation and failure behavior of cable insulation materials is important because the integrity of the cables' polymeric insulation material is critical for safe and reliable operation of the NPP. The insulation materials suffer degradation through exposure to heat, gamma radiation and other environmental stressors throughout their service lifetime.

Polymer-based materials used for cable insulation are composites, consisting of a polymer matrix and various fillers and additives to protect the material against fire and degradation. Antioxidants (AOs) are important additives that protect the polymer from oxidative aging. Crosslinked

polyethylene (XLPE) is one of the most widely used polymers for cable insulation in NPPs due to its superior properties such as good resistance to thermal and gamma radiation and good mechanical properties [4,5,6,7]. Enormous research efforts have been made to study the effect of irradiation such as ultraviolet irradiation, electron beam irradiation and gamma irradiation on polyethylene with or without antioxidants or stabilizers in various fields such as wires and cables, biopharmaceuticals and biotechnology [8,9,10,11,12,13]. Researchers evaluate antioxidants by measurements such as yellowness index of the material under various irradiation conditions because aging causing the generation of carbonyl bonds which causes the material to appear yellowish in color [8]. To the best of our knowledge, however, there has been no study directly quantifying the changes in antioxidant caused by irradiation. For the application of wires and cables in NPPs, any change in the quantity of antioxidant under different aging conditions may be a key indicator of aging and is important for understanding the degradation behavior of these insulation materials. Evaluation of antioxidant depletion may help to determine the remaining service life of the cable.

In this paper, cross-linked XLPE-based cable insulation material was studied. The composition of this material was determined using a combination of analytical techniques: scanning electron microscopy-energy dispersive X-ray spectroscopy (SEM-EDX), Fourier transform infrared spectroscopy (FTIR), thermogravimetric analysis (TGA), Carbon-Hydrogen-Nitrogen (CHN) combustion, and pyrolysis gas chromatography-mass spectroscopy (Py-GCMS). Details of the method by which the material composition was established have been published elsewhere [14, 15], and the results are summarized in Table 1.

The XLPE-based cable insulation material was aged under various conditions, including three temperatures (60, 90, and 115 °C) and four gamma dose rates (0, 120, 300, and 540 Gy/h) for 15 days. This exposure time corresponds to total gamma doses of 0, 45, 110, and 190 kGy, respectively. The quantity of AO in the samples was analyzed following exposure using Py-GCMS.

Measurement of OIT is one of the evaluation methods of oxidative stability and has been used previously as a measure of oxidative degradation, antioxidant depletion, and antioxidant concentration in various types of polyethylene [16, 17, 18]. Little research has been conducted, however, to measure antioxidant depletion *directly and quantitatively* during polymer aging and to study the relationship between quantity of antioxidant and measured value of OIT. In this work, OIT was measured using differential scanning calorimetry (DSC) and correlations were made between the changes in OIT and in antioxidant.

Table 1. Composition of pristine XLPE-based cable insulation material studied, and function of the components.

Component	Approximate weight ratio (%)	Function
Cross-linked polyethylene	60	Polymer matrix
Decabromodiphenyl ether ($C_{12}Br_{10}O$)	10	Flame retardants
Octabromodiphenyl ether ($C_{12}H_2Br_8O$)	10	
Sb_2O_3	17	
ZnS		White pigment
Poly(1,2-dihydro-2,2,4-trimethylquinoline)	2	Antioxidant, metal deactivator
1,3,5-Triazine-2,4,6(1H,3H,5H)-trione	trace	Cross-linking booster

Sample Preparation

White XLPE-based insulation material studied in this work was obtained from commercially-available nuclear-grade instrumentation cable consisting of two 16AWG conductors, a laminated aluminum/polyester shield, a drain wire, and a chlorosulphonated polyethylene (CSPE) jacket (RSCC, product code I46-0021), Figure 1. According to the manufacturer, the XLPE insulation was cross-linked by electron-beam radiation. It was removed from the cables by first stripping off the jacket and other external components from the cable assembly, and then pulling out the conductor from the center of the insulation. The wall thickness of the resulting tubular insulation sample material was 0.70 ± 0.05 mm.

To accomplish accelerated aging, samples were suspended by clips on a rack placed in an oven located in the exposure zone of a Co-60 source in the High Exposure Facility (HEF) at Pacific Northwest National Laboratory. In this way, simultaneous thermal and gamma radiation aging of the samples was achieved. The dose rate to each individual sample was controlled by selecting the position of the sample with respect to the radiation source. Overall, 240 different aging conditions were achieved at three aging temperatures (60, 90, and 115 °C), 25 dose rates (ranging from 0 to 540 Gy/h), and five aging durations (5, 10, 15, 20, and 25 days). From this combination of conditions, samples were exposed to doses of gamma radiation in the range from 0 to 320 kGy. Details of the accelerated aging process and sample preparation can be found in a separate paper [19].

From the full set of 240 sample scenarios, 13 were selected for quantitative analysis of antioxidant, presented in this paper. The detailed aging conditions of the 13 selected sample sets are listed in Table 2.

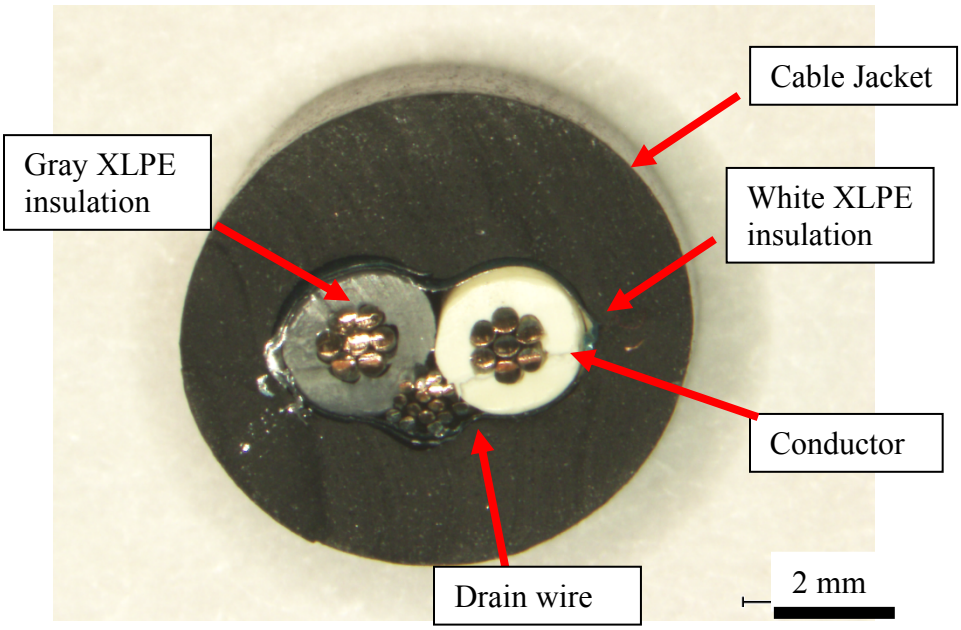

Figure 1. Cross section of the XLPE-based cable insulation material.

Table 2. Aging conditions under which the XLPE-based samples were prepared. Sample ID in the first column is a combination of aging temperature (in °C) and nominal radiation dose (in kGy). All samples other than the pristine sample were exposed for 15 days.

Sample ID	Aging temperature (°C)	Radiation dose rate (Gy/h)	Radiation dose (kGy)
Pristine	Room temp storage	0	0
60C-0	60	0	0
60C-45	60	120	45
60C-110	60	300	110
60C-190	60	540	190
90C-0	90	0	0
90C-45	90	120	45
90C-110	90	300	110
90C-190	90	540	190
115C-0	115	0	0
115C-45	115	120	45
115C-110	115	300	110
115C-190	115	540	190

Materials Characterization Methods

Pyrolysis gas chromatography-mass spectroscopy

The Waters® GCT Premier™ Mass Spectrometer is an accurate-mass time-of-flight (TOF) mass spectrometer coupled to an Agilent 6890 gas chromatograph (GC). The electron ionization (EI) source was used in this study. The Frontier 3030D sample introduction and furnace assembly were

mounted on the back inlet of the GC. For thermal desorption studies, the GC column used was a Restex Rxi-5HT, 30 m x 0.25 mm inner diameter x 0.25 micron film thickness. The carrier gas used for all measurements was ultra-high purity helium.

The brominated flame retardants present in the material-under-test, Table 1, are reactive compounds that interact with the surface of deactivated stainless steel sample cups and cause poor measurement reproducibility if stainless steel sample cups are used. In this study, deactivated glass sample cups were used in order to avoid this source of uncertainty. The type 'Eco-Cup G' from Frontier Lab was used.

An evolved gas analysis (EGA) test was conducted to determine the evolved temperature profile of each component in the material. The GC column was replaced with a two-meter-long deactivated Silcosteel transfer line for the EGA tests. The GC oven was held at 320 °C. A thin slice of sample (0.5 ± 0.02 mg) was cut from the cross section of the insulation material (Figure 1) and placed into the sample cup. The sample cup was then loaded into the pyrolyzer. The pyrolyzer was held at 80 °C for 2 min, after which the temperature was increased to 800 °C at 20 °C/min. The mass spectrometer total-ion-current (TIC) versus temperature profile of the test material was recorded during the EGA test. This profile was selected with the goal of maximizing signal-to-noise ratio for antioxidant for best quantitative analysis of antioxidant concentration in pristine and differently aged materials. The temperature program targeted complete evolution of the antioxidant from the test sample, while minimizing contamination to the instrument system from brominated flame retardant and XLPE polymer matrix decomposition residue. The EGA test indicated that holding the sample at 320 °C for 5 min met these objectives. From the TIC versus temperature data, multiple accurate masses were extracted from the TIC data to profile the desorption and pyrolysis of the various components under study.

Thermal desorption (TD) tests were conducted on pristine and differently aged materials using the GC column discussed previously. For accurate quantification of the antioxidant in each sample, 2,5-bis-2-(5-tert-butylbenzoxazolyl)thiophene (BBOT) was used as an internal standard. BBOT was dissolved in acetone at a concentration of 5.5 mg/100 mL. First, 3 μL of BBOT solution was injected into the sample cup. Then a thin slice of sample (0.260 ± 0.009 mg) was cut from the cross section of the insulation material and added to the sample cup after the acetone had evaporated. The sample cup was then loaded into the pyrolyzer. The pyrolyzer was held at 80 °C for 2 min, then ramped to 320 °C at 20 °C/min. The pyrolyzer was then held at 320 °C for 5 min, according to the EGA test result discussed in the previous paragraph. The GC column was then held at 40 °C for 5 min, followed by a temperature ramp up to 320 °C at 20 °C/min, holding there for 10 min.

The uncertainty of the TD GCMS measurements was estimated by running five replicates on pristine samples with BBOT as the internal standard. The studied compounds were quantified by integrating the corresponding peak areas. Figure 4 shows the weight-normalized AO peak areas of five measurements on pristine and gamma-irradiated sample material. Figure 5 shows the weight-normalized AO peak area on pristine and thermally-aged sample material. The average internal-standard-corrected antioxidant peak area of pristine material is 997, with a standard deviation of 66, which gives an uncertainty of 6.6 %, Table 3. Two replicates were measured for each aged sample scenario. A third replicate was generally measured when the standard deviation of the measured values on the two replicates was more than 6.6 %.

Oxidation Induction Time

Oxidation induction methods are based on the detection of the oxidation exotherm that occurs when a sample is heated in the presence of oxygen. OIT tests were conducted using a TA Instruments Q2000 differential scanning calorimeter. Samples with mass 10.0 ± 0.5 mg were used in each test. The temperature program is shown in Figure 2. The DSC cell was heated at 15 °C/min from 40 °C to 230 °C in nitrogen at a flow rate of 50 ml/min. When the specified temperature of 230 °C was reached, the specimen was held in nitrogen isothermally for 2 min, after which the atmosphere was changed to oxygen maintained at the same flow rate. The specimen was then held isothermally at 230 °C until the oxidative reaction was observed on the thermal curve. The time interval from when the oxygen flow is first initiated to the onset time of the oxidative reaction is referred to as the oxidation induction time. The threshold is defined as 0.1 W/g relative to (above) the baseline and the onset time of the oxidative reaction is defined by the intersection of the test curve with the threshold line, Figure 2. As also can be seen in Figure 2, the melting temperature range of the XLPE sample is from about 90 to 115 °C. The selected temperature for OIT testing, 230 °C, is above the melting temperature range of the tested sample.

Table 3. Internal standard (I.S.) peak area, weight normalized (wt. norm.) antioxidant peak area, and weight normalized antioxidant peak area after correction by the I.S. of five pristine samples.

Replicate	**1**	**2**	**3**	**4**	**5**	**Mean value**	**Standard deviation**	**Uncertainty (%)**
I.S. peak area (a.u.)	143	190	167	176	155	166	16.3	9.8
Wt. norm. antioxidant peak area (a.u.)	771	996	771	940	877	871	89.9	10.3
I.S. corrected antioxidant peak area	1024	996	877	1014	1075	997	65.6	6.6

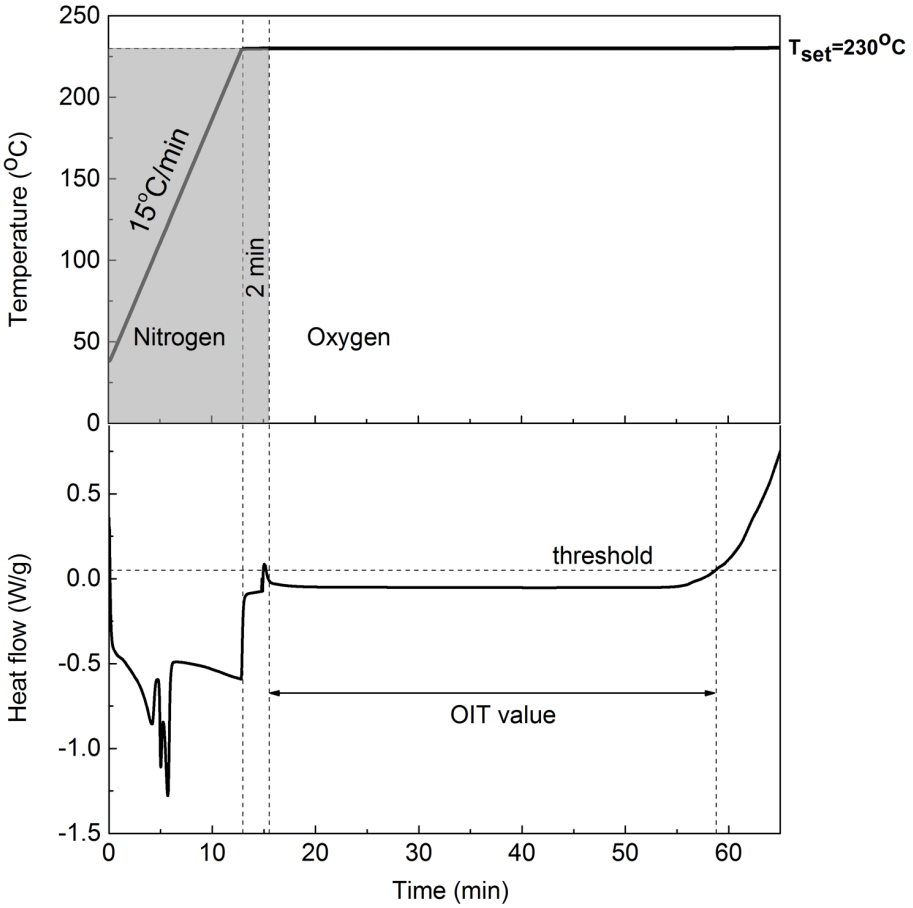

Figure 2. Temperature and gas profile and corresponding heat flow of OIT measurement. The example heat flow curve shown here is for pristine XLPE sample material.

Results

Figure 3 shows the evolved gas temperature profiles of a) the material as a whole, b) the XLPE polymer matrix, c) the brominated flame retardants, and d) the antioxidant. In Figure 3 a), it is shown that gases start to evolve from the test piece at around 150 °C, and this evolution continues until the ultimate temperature 800 °C of the pyrolyzer temperature program. Figures 3 b), c), and d) show that the XLPE polymer matrix starts to decompose between 300 and 400 °C and the majority of the polymer pyrolysis occurs between 400 and 500 °C. The brominated flame retardants show significant desorption and decomposition starting between 300 and 400 °C. The decomposition of antioxidant poly(1,2-dihydro-2,2,4-trimethylquinoline) (pTMQ) takes place mainly in the temperature range 200 to 350 °C.

Of the 13 sample scenarios studied in this work, the spectra of selected samples are displayed in Figures 4 and 5. Other spectra can be found in [19]. Figure 4 displays the mass spectra of samples that were aged at 60 °C for 15 days with gamma radiation exposure at doses of 0, 45, 110, and 190 kGy. Figure 5 displays the mass spectra of samples that were thermally-only aged for 15 days at

three different temperatures of 60, 90, and 115 °C. Main peaks of the antioxidant are marked with arrows in the spectrum of the pristine sample in Figure 4. It is observed that the height of antioxidant peaks decrease with increasing gamma radiation exposure and increasing aging temperature. Peak areas were calculated and the antioxidant quantities in pristine and different samples, normalized to the antioxidant content of the pristine sample, are plotted in Figure 6. At the same aging temperature, the antioxidant content decreases with higher gamma radiation dose. At the same radiation dose, the antioxidant content decreases with higher aging temperature. The sample that was aged at 115 °C with exposure to gamma radiation at the dose of 190 kGy showed maximum depletion (93 %) in the quantity of antioxidant. The sample that was aged at 60 °C without gamma radiation showed minimum depletion (7 %) in the quantity of antioxidant. The depletion of antioxidant of other samples lies in between 7 % and 93 %.

Figure 7 shows the measured OIT values of the same sample set. At the same aging temperature, the OIT decreases with higher gamma radiation dose. At the same radiation dose, the OIT decreases with higher aging temperature. The sample that was aged at 115 °C with exposure to gamma radiation at the dose of 190 kGy showed the maximum reduction of 80 % in OIT. The sample that was aged at 60 °C without gamma radiation showed no reduction in OIT. Figure 8 compares normalized antioxidant quantity and normalized OIT of the sample set. The trends of OIT and antioxidant quantity are well correlated, with calculated correlation coefficient 0.82.

Discussion

Generally speaking, the depletion of antioxidant may be caused by evaporation, sublimation, and chemical reactions with free radicals. Prior to further discussion on how and why the changes in antioxidant pTMQ vary in differently aged samples, the possible chemical reaction mechanisms of pTMQ with free radicals generated in the aging process are discussed as follows.

Most oxidative mechanisms characteristic of the degradation of polymers during processing, storage and long-term end-use involve free radicals induced thermally, catalytically, mechano-chemically, or by radiation [20]. Reactions (1) through (4) show one chain of reactions that may take place in the polymer degradation process without the involvement of antioxidant [21]. Bond scission causes the generation of free radicals $R^{\bullet}$, as shown in (1), which, in the presence of oxygen, react to produce more unstable free radicals as the oxidation process repeats itself in the polymer, as shown in (2), (3), and (4). The process in (1) is termed the degradation *initiation*, and the ensuing processes fall under degradation *propagation*. Degradation propagation processes take place at a much faster rate than degradation initiation [21].

The antioxidant used in the studied XLPE insulator is pTMQ, which is a type of hindered heterocyclic aminic stabilizer. The most widely used aminic stabilizers are grouped into two categories. One consists of aromatic and non-hindered heterocyclic amines, the classical antidegradants applied mainly in rubbers and to a lesser extent in polyolefins as antioxidants, heat stabilizers, antifatigue agents and antiozonant [20, 22, 23, 24, 25]. The second group consists of hindered heterocyclic amines introduced on the market in the 1970s. These rank among the currently most extensively studied additives [20]. Hindered amine stabilizers have been utilized almost exclusively in polyolefins and coatings as light stabilizers, photo-antioxidants, and heat stabilizers. The antioxidant pTMQ belongs to the second group, hindered heterocyclic aminic stabilizers, and efficiently stabilizes XLPE used as insulation material for electric cables exposed

to irradiation doses [26]. Generally speaking, interference with free-radical and peroxidic species resulting in polymer autoxidation, fatigue and photo-oxidation belong to the principal processes of polymer stabilization [20]. The detailed discussion of reaction mechanisms of various aminic stabilizers can be found in [22, 27, 28, 29]. Specifically, pTMQ has a broad application spectrum. It has been used for a long time as a heat stabilizer and antioxidant with some anti-flex-crack effect in the rubber industry and in polyolefins [30, 31]. pTMQ is generally more efficient than other common antioxidants in protecting against irradiation aging and thermal oxidation below 150 °C [32]. Abstraction of the hydrogen atom from the –NH group of TMQ according to Reaction (5) is the primary step of the antioxidant action [33].

When the samples are aged thermally, without gamma radiation, C-C bond breakage is most likely caused by thermal fluctuations, and the C-C bond breakage leads to the generation of free radicals. We speculate that the rate of generation of free radicals increases with increasing aging temperature. In the presence of gamma radiation, however, the rate of generation of free radicals is likely to be much higher than when gamma radiation is absent, due to the high photon energy of gamma radiation. The C-C bond energy is about 348 kJ/mol [34], and the photon energy from Co-60 radiation source is 1.17 MeV (1.129×10^8 kJ/mol) and 1.33 MeV (1.283×10^8 kJ/mol) [35], easily capable of breaking C-C bonds and generating free radicals. Moreover, the high energy photons generate secondary electrons which break additional polymer C-C bonds, producing more free radicals.

The melting temperature of pTMQ lies in the range from 70 to 108 °C [36], and its boiling temperature is higher than 315 °C [37]. When thermal aging takes place at 60 °C, sublimation and rate-limited chemical reactions might take place, causing depletion by only 15% as observed in Figure 6. When thermal aging takes place at 90 and 115 °C, evaporation, sublimation and rate-enabled chemical reaction take place simultaneously, causing a much faster depletion rate and explaining the observed depletion of approximately 60 and 70 % in these cases, respectively. Adding gamma radiation to the exposure environment causes the depletion of pTMQ to occur at a much faster rate, likely due to the faster generation of polymer free radicals as described in the previous paragraph.

The measured values of OIT and antioxidant content plotted together in Figure 8 are well correlated, with calculated correlation coefficient 0.82, suggesting that OIT can be used as an indicator of age-induced antioxidant depletion in XLPE-based cable insulation materials. The percentage changes observed for OIT and antioxidant content as a function of increased aging time are different, however, with the antioxidant quantity curve showing more pronounced changes with respect to aging conditions than the OIT curve. This suggests that depletion of antioxidant may not be the only factor that contributes to the change in OIT in the samples studied. Besides depletion of antioxidant, OIT may also be affected by the polymer type, polymer structure, and other additives and fillers. Scission of XLPE polymer chains and alteration of the crystalline and semi-crystalline content of the XLPE may lead to reducation in OIT in addition to changes caused by consumption of antioxidant.

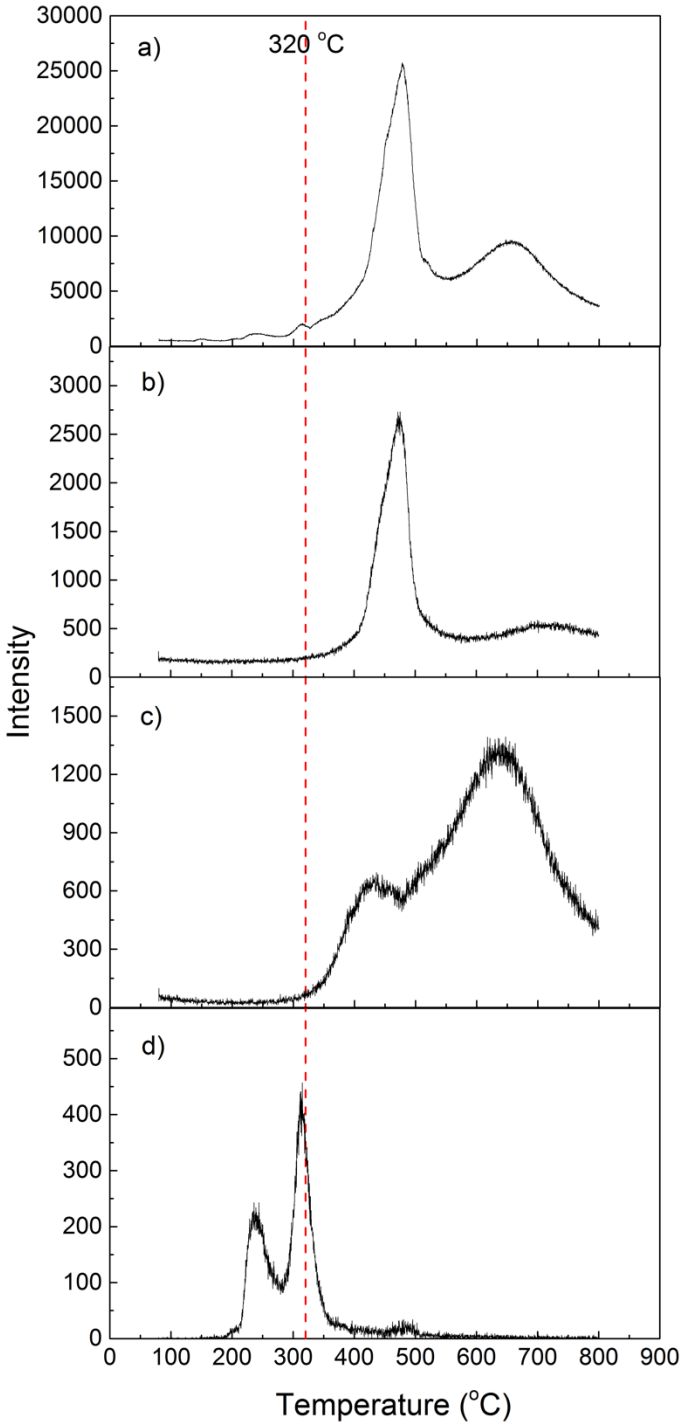

Figure 3. Evolved temperature profiles of major components in XLPE-based cable insulation material; a) evolved pyrolyzates from the whole sample piece; b) selected evolved pyrolyzates of XLPE polymer; c) evolved pyrolyzates from brominated flame retardants; and d) evolved pyrolyzates from antioxidant.

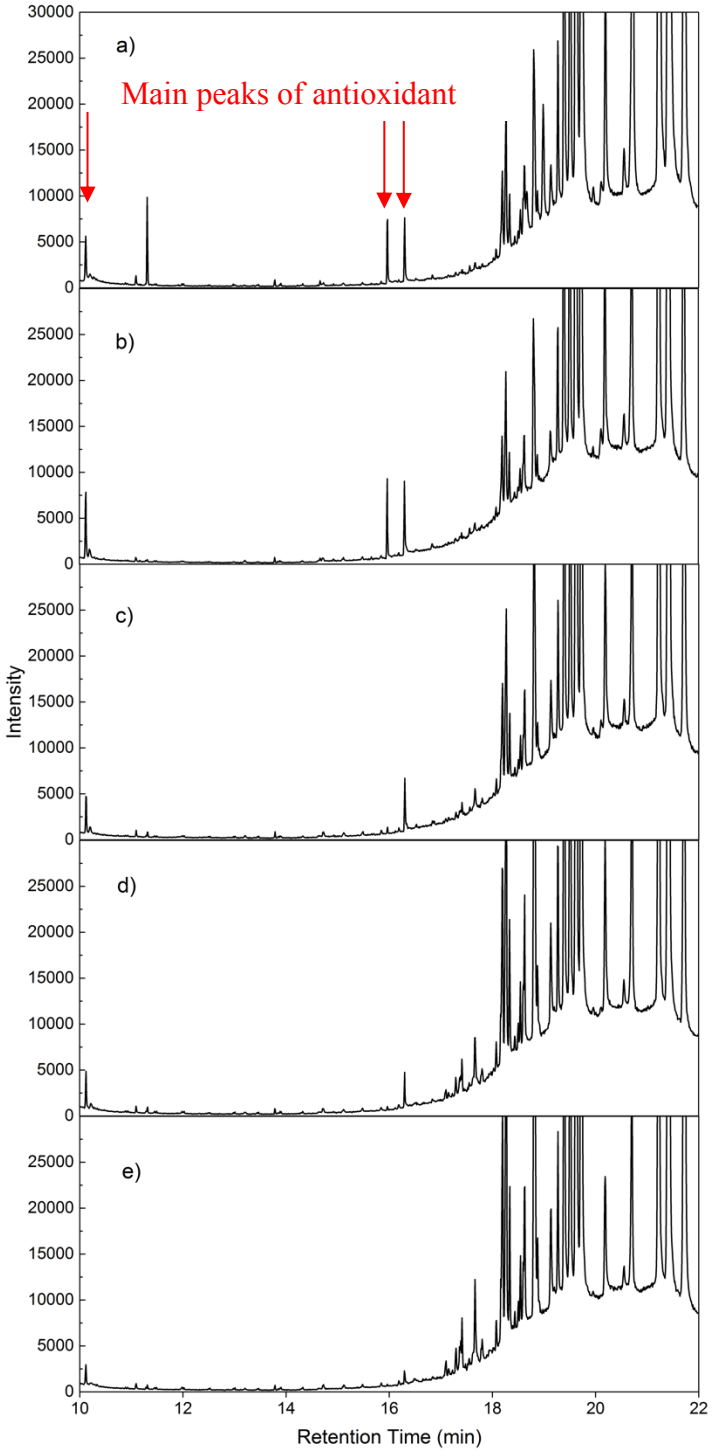

Figure 4. Mass spectra of XLPE-based samples a) pristine, and those that have been simultaneously thermal and gamma radiation aged at 60 °C for 15 days, with gamma radiation exposure of b) 0, c) 45, d) 110, and e) 190 kGy. Main peaks of the antioxidant are marked with arrows in the spectrum of the pristine sample. The peak at retention time of ~ 11.5 min that appears only in spectrum a) indicates the presence of residual cross-linking agent.

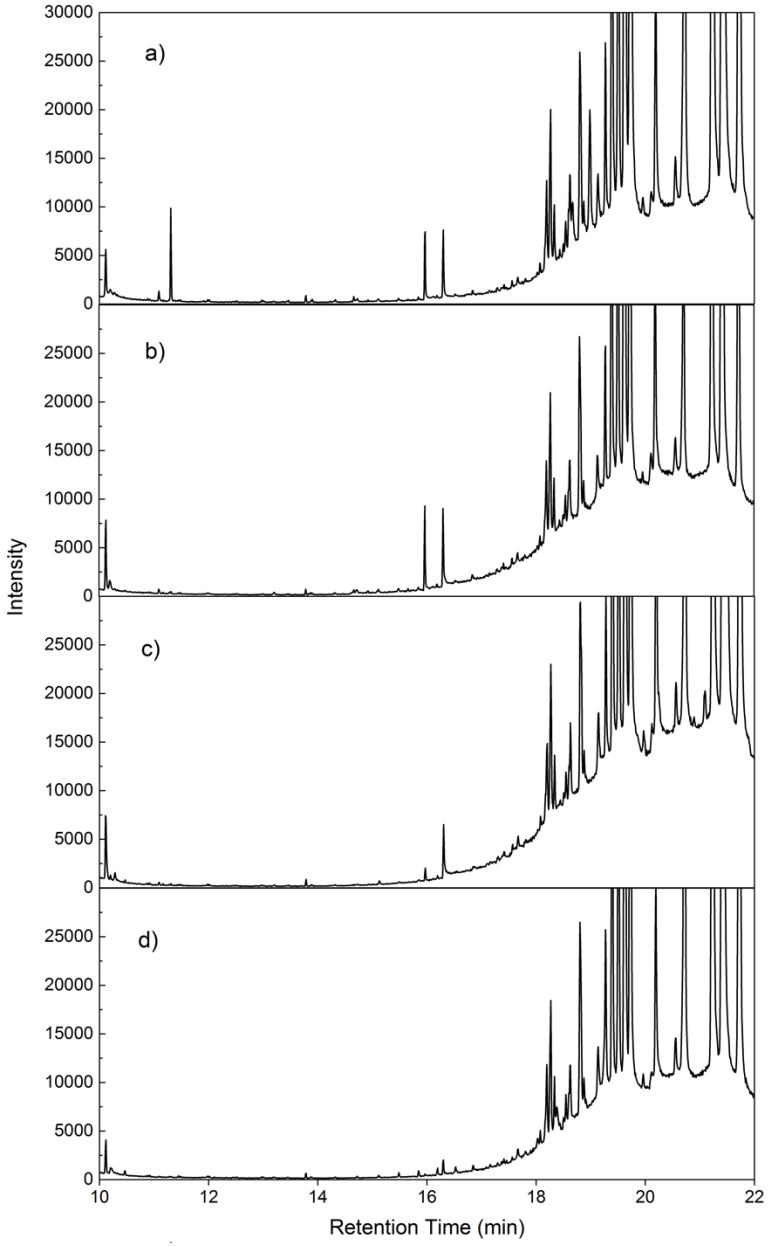

Figure 5. Mass spectra of XLPE-based samples a) pristine, and those that have been thermally aged at b) 60, c) 90, and d) 115 °C for 15 days, without gamma irradiation. The peak at retention time of ~ 11.5 min that appears only in spectrum a) indicates the presence of residual cross-linking agent.

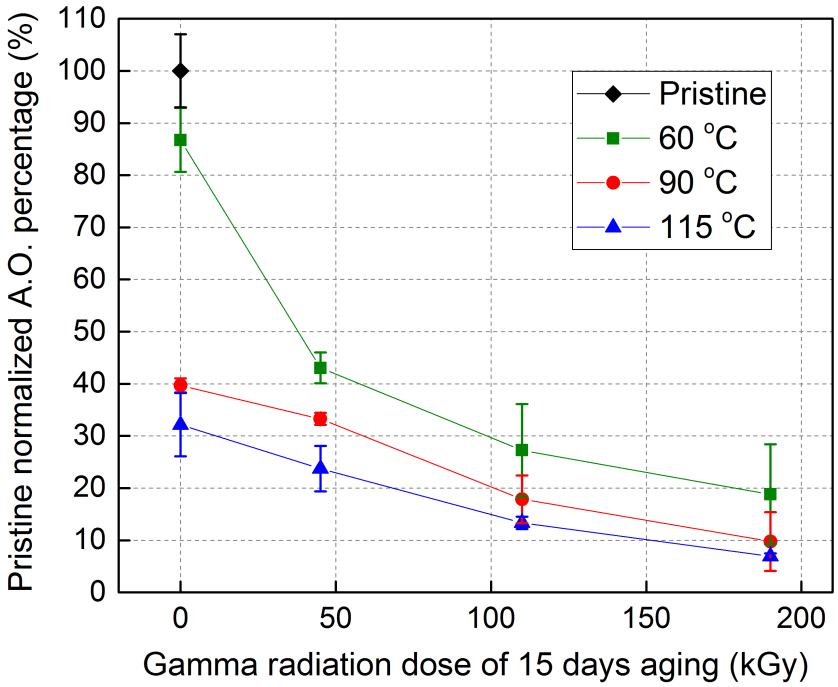

Figure 6. Antioxidant quantity in pristine and aged XLPE-based samples, normalized to the value for the pristine sample (997 area units).

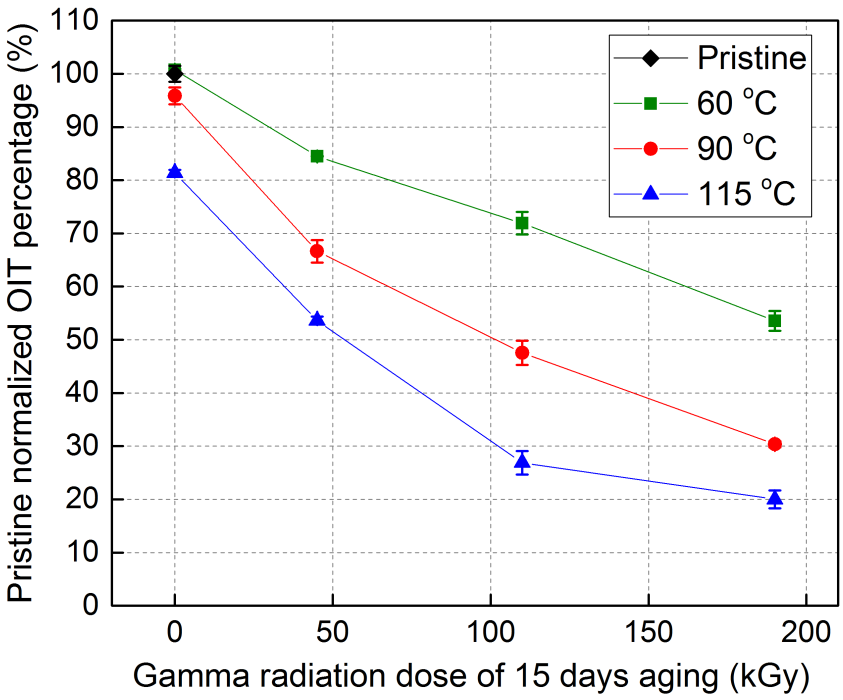

Figure 7. OIT for pristine and aged XLPE-based samples, normalized to the value for the pristine samples (48.6 min).

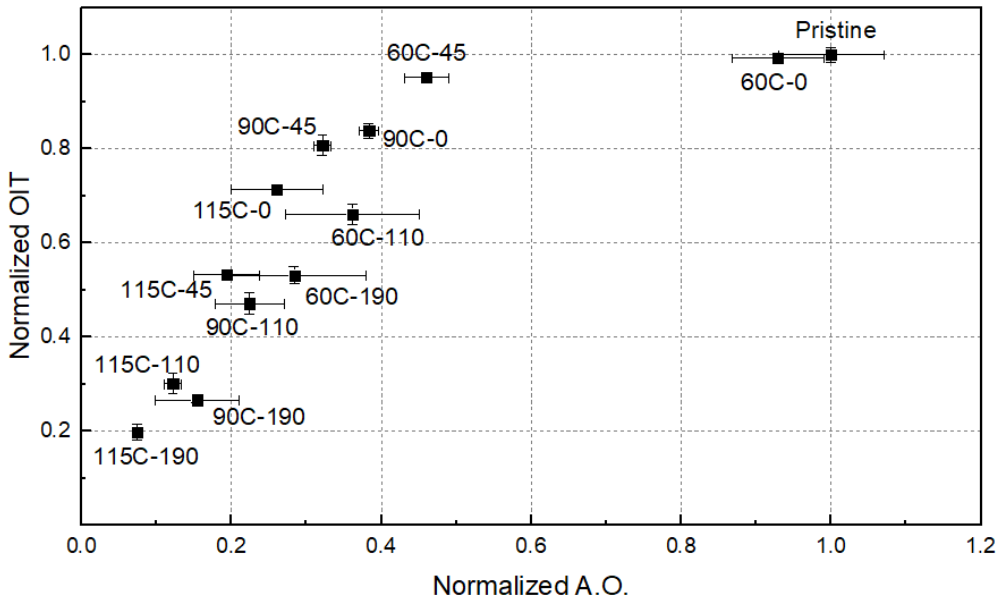

Figure 8. OIT and AO content normalized to values for the pristine sample.

$$R{-}R \longrightarrow 2R^{\bullet} \quad (1)$$

$$R^{\bullet} + O_2 \longrightarrow ROO^{\bullet} \quad (2)$$

$$ROO^{\bullet} + RH \longrightarrow ROOH + R^{\bullet} \quad (3)$$

$$ROOH \xrightarrow{h\nu} RO^{\bullet} + OH^{\bullet} \quad (4)$$

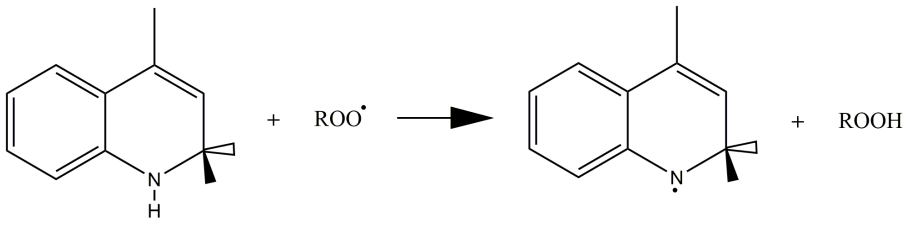

(5)

Conclusion

Quantitative analysis of antioxidant in a commercially-available, cross-linked polyethylene-based cable insulation material for nuclear power plant applications has been performed. Correlation between the antioxidant quantity in the material and the oxidation induction time (OIT) of the

material was made. For isothermal aging, the antioxidant quantity and OIT were observed to decrease with increasing gamma radiation dose. At fixed gamma radiation dose, they were observed to decrease with increasing aging temperature. The depletion of antioxidant quantity ranges from 7 % to 93 %, and the decrease of OIT ranges from 0 to 80 % for samples studied in this paper. The changes in the quantity of antioxidant in the material follow the same trend as the changes in OIT of the material when aged under various conditions, with a correlation coefficient of 0.82. We conclude that OIT can be an effective indicator of the antioxidant depletion severity in XLPE based cable insulation materials, while depletion of antioxidant is not the only factor that contributes to the reduction in OIT of the studied material. The way in which the antioxidant may slow the degradation process of the polymer by consuming the majority of the free radicals generated in the initial stages of degradation, so that the degradation propagation process is significantly reduced when antioxidant is present.

Acknowledgement

This work was funded by the DOE Office of Nuclear Energy's Nuclear Energy University Programs under contract number DENE0008269 and the DOE Office of Nuclear Energy's Light Water Reactor Sustainability Program. Exposure experiments were conducted at Pacific Northwest National Laboratory, which is operated by Battelle for the US DOE under contract DE-AC05-76RL01830. The authors acknowledge useful discussion with Andrew C. Kolbert, CTO of Avomeen Analytical Services, LLC.

References

[1] U.S. Energy Information Administration, (updated August 2017) http://www.eia.gov/tools/faqs/faq.cfm?id=207&t=3

[2] World Nuclear Association, (updated January 2018) http://www.world-nuclear.org/information-library/nuclear-fuel-cycle/nuclear-power-reactors/nuclear-power-reactors.aspx

[3] M. Subudhi. *Literature Review of Environmental Qualification of Safety-Related Electric Cables*, NUREG/CR-6384. BNL-NUREG-52480, Vol.1, 1995.

[4] Khonakdar, H. A.; Jafari, S. H.; Rasouli, S,; Morshedian, J.; Abedini, H. Investigation and Modeling of Temperature Dependence Recovery Behavior of Shape-Memory Crosslinked Polyethylene. *Macromol. Theory Simul.* 2007, 16, 43-52.

[5] Chodak, I. Properties of Crosslinked Polyolefin-Based Materials. *Prog. Polym. Sci.* 1995, 20, 1165-1199.

[6] Palmlof, M.; Hjertberg, T. Crosslinking of Poly(Ethylene-co-1,9-Decadiene) by Electron Beam Irradiation. *Polymer* 2000, 41, 6481-6495.

[7] Electric Power Research Institute (EPRI) (1994). Low-Voltage Environmentally-Qualified Cable License Renewal Industry Report; Revision 1. TR-103841.[5] N. Bowler, and S. Liu.

Aging Mechanisms and Monitoring of Cable Polymers. International Journal of Prognostics and Health Management 2016, 6, 029.

[8] F. Gaston, N. Dupuy, S R. A. Marque, D. Gigmes, and S. Dorey. Monitoring of the discoloration on γ-irradiated PE and EVA films to evaluate antioxidant stability. Journal of Applied Polymer Science. 2018, 135, 46114.

[9] H. Wang, L. Li, J. Guan, H. Jiang, R. Shen, X. Ding, J. Li, and Y. Li. Investigation on Molecular Structures of Electron-Beam-Irradiated Low-Density Polyethylene by Rheology Measurements. Ind. Eng. Chem. Res. 2018, 57, 4298-4310.

[10] B. Bartonicek, V. Placek, and V. Hnat. *Comparison of degradation effects induced by gamma radiation and electron beam radiation in two cable jacketing materials.* Radiation Physics and Chemistry 76(2007) 857-863.

[11] Jeon, D.H.; Park, G.Y.; Kwak, I.S.; Lee,K.H.; Park, H.J. *LWT* 2007, 40, 151.

[12] Bourges, F.; Bureau, G.; Dumonceau, J.; Pascat, B. *Packag. Technol. Sci.* 1992, 5, 205.

[13] Mortimer, R.J.; Varley, T.S. *Displays* 2011, 32, 35.

[14] S. Liu, L. S. Fifield, N. Bowler. *Towards aging mechanisms of cross-linked polyethylene (XLPE) cable insulation materials in nuclear power plants*, IEEE Conference on Electrical Insulation and Dielectric Phenomena, Toronto, Canada, 2016.

[15] S. Liu. Composition identification, aging mechanisms, and nondestructive aging indicator of commercial filled cross-linked polyethylene (XLPE) cable insulation materials, Graduate Theses and Dissertations, 2017.

[16] W. Mueller, I. Jakob. *Oxidative resistance of high-density polyethylene geomembranes.* Polymer Degradation and Stability 79(1), 161-173, 2003.

[17] Y.G. Hsuan, M. Li, *Temperature and pressure effects on the oxidation of high-density polyethylene geogrids*. Geotextiles and Geomembranes 23 (1), 55-75, 2005.

[18] M. Uhniat, S. Kudla, *Stabilisation of LDPE cross-linked in the presence of peroxides I. Kinetic study of oxidation*. Polymer Degradation and Stability 71(1), 69-74, 2001.

[19] L. S. Fifield, S. Liu, and N. Bowler. *Simultaneous thermal and gamma radiation aging of cable polymers*. IEEE Conference on Electrical Insulation and Dielectric Phenomena, Toronto, Canada, 2016.

[20] Pospisil J (1995), Aromatic and heterocyclic amines in polymer stabilizers, Advances in polymer science, vol 124, pp 87-189.

[21] Arvind Mafatlal group & Nocil Limited, (2010). http://www.nocil.com/Downloadfile/ETechnicalNote-Antioxidants-Dec2010.pdf

[22] Pospisil J (1984) In: Scott G (ed) Developments in polymer stabilization, vol 7. Elsevier, London, p 1

[23] Kuczkowski J (1990) In: Pospisil J, Klemchuk PP (eds) Oxidation inhibition in organic materials, vol 1. CRC Press, Boca Raton, p 247

[24] Pospisil J (1985) In: Klemchuk PP (ed) Polymer stabilization and degradation. ACS Symp Ser 280:157

[25] Pospisil J (1990) In: Pospisil J, Klemchuk PP (eds) Oxidation inhibition in organic materials, vol 1. CRC Press, Boca Raton, p 33

[26] Ray JW, Reynolds AB (1990) Nuclear Technol 91:394

[27] Pospisil J (1989) In: Patsis AV (ed) 11th Intern Confer on stabilization and degradation of polymers, 24-26 May 1989. Luzern, Proc p 163

[28] Pospisil J (1979) In: Scott G (ed) Developments in polymer stabilization, vol 1. Elsevier, Barking, p 1

[29] Denisov ET, Khudyakov IV (1987) Chem Rev 87: 1313

[30] Hoffman W (1989) Rubber technology handbook. Hanser, Munich

[31] Kememitsuya K, Tachibara T, Okruda T (1993) Jpn Kokai Tokkyo Koho 04 314, 752

[32] Richaud et al Polym Deg Stab 2009 94(3) https://doi.org/10.1016/j.polymdegradstab.2008.11.018

[33] Pospisil J (1995), Aromatic and heterocyclic amines in polymer stabilizers, Advances in polymer science, vol 124, pp 87-189.

[34] J. C. Earl. *Carbon-carbon bond energies*. Tetrahedron 9 (1-2), 65-66, 1960.

[35] J. K. Shultis and R. E. Faw. *Fundamentals of Nuclear Science and Engineering*, CRC Press Taylor & Feancis Group, Florida, 2008.

[36] Patent PL 114620 Polymeric 1,2-dihydro-2,2,4-trimethylquinoline By: Grzywa, Edward; Tarnowski, Jerzy; Zoledziowski, Wojciech; Szteke, Barbara; Straszewski, Jozef; Szulc, Henryk Assignee: Instytut Przemyslu Organicznego, Pol. 1982, Patent GB 1010247 Poly(2,2,4-trimethyl-1,2-dihydroquinoline) antioxidants for rubber Goodyear Tire & Rubber Co. 1965.

[37] Chemi book
https://www.chemicalbook.com/ChemicalProductProperty_EN_CB3222852.htm

B.2 Kinetic Rate Model of Crosslinking and Chain Scission of Irradiated Polyethylene

In preparation for submission to: *IEEE Trans. Dielectr. Electr. Insul.*
Authors: Irmak Sargin and Scott P. Beckman
Affiliation: School of Mechanical and Materials Engineering, Washington State University, Pullman, WA 99164, USA

ABSTRACT

Insulation cabling is an essential engineering component in nuclear power plants. The insulation around these wires is made of ethylene-propylene rubber and cross-linked polyethylene that are subjected to environmental and radiation damage. For the purpose of maintenance and reactor recertification, it is necessary to develop a non-destructive approach to testing the impact of damage on the insulation. Accelerated aging experiments are used to develop these methods, although it is unclear how to relate these experimental results to in situ aged specimen. Here we use a kinetic rate model to investigate the impact of radiation dose rate and total dose on the crosslinking and chain scission of polyethylene. Analytical expressions for the concentration of crosslinking and scission sites as a function of time and radiation rate both for during and post radiation and crossover point between these two are presented in terms of radiation rate and time. The scission reaction rate is significantly slower than crosslinking for lower total doses whereas the situation is changed for higher total doses causing the ambiguity between the accelerated aging and in-situ aging methods. Also, chain scission forming reactions can continue well after the radiation dosing has ended, whereas crosslink forming ones end almost immediately after the radiation is turned off.

Index Terms — **Polyethylene, radiation damage, crosslinking, and chain scission**

1 INTRODUCTION

ONE of the very important industrial application of polymers are insulation cabling and jacketing. In nuclear power plants insulation cabling is one of the essential component. The most frequently used ones are crosslinked poly ethylene (XLPE) and ethylene-propylene rubber (EPR). These two together makes the 72 % of the cables [1] The stressors that the cables are subjected to are radiation, thermal, mechanical, and moisture. Cables should endure those during their service life and during design basis accident conditions [1, 2]. The harsh environment that cables are subjected to cause degradation, i.e. aging, which cause structural changes affecting mechanical, physical, and electrical properties. The degradation of insulation cables and jacketing material may limit the operation of nuclear power plants since the aged cables may become more brittle and crack formation under environmental stresses becomes more probable. Crack formation results in intrusion of moisture into cable and causes corrosion, short circuits, shunting, and eventually failure [1, 3].

The aging mechanisms can be divided into chemical, which affects the molecular structure, and physical changing the composition of the polymer [3, 4]. The chemical degradation may take place via crosslinking, chain scission, free-radical formation, oxidation diffusion, and evolution of hydrogen [5–10]. On the other hand, physical degradation occurs by evaporation and migration of plasticizers and antioxidants [11].

Both the chemical and physical degradation cause changes in chemical, physical, mechanical, and electrical properties. Since the service life of the polymers are dependent of these properties, they can be used to determine remaining life of the aging cables. The key chemical, mechanical, and electrical indicators of cable aging are changes in melting, glass transition, and gel temperature; indenter modulus which is in correlation with the elongation at break; and finally dielectric strength, insulation resistance, and electrical conductivity [1, 3, 9, 12–17]. Currently, the industrially accepted in-situ procedures are visual testing and indentation measurements. The indentation measurement is the gold standard because it

Manuscript received on X Month 2018,in final form XX Month 2018.

can be related to the elongation-at-break and used in determining the remaining life of the cable. The structure's undeniable effect on this value, makes the changes taking place in the structure like crosslinking and chain scission very important and useful. However, correlation between these structural elements and changes in mechanical properties is not straightforward. There are other destructive and non-destructive testing methods for measurements of key indicators of aging but they can only detect flaws at this point in time [1, 8–10, 12, 18]. The search for more general non-destructive methods is an ongoing challenge, where availability of materials and missing knowledge of actual plant conditions are limiting factors [1, 9, 11].

In order to overcome the first limiting factor, availability of materials accelerated aging experiments are widely used [4, 13, 19]. Accelerated aging takes place at much higher radiation dose rates and much shorter dosing periods in comparison to in-situ aging. In order to extrapolate data from accelerating aging to in-situ aging superposition approach is used. This empirical approach has a long history in polymer research which starts with thermal aging predictions. Its extension to combined effect of radiation and temperature was applied first by Gillen et. al [20]. Regardless of its wide use, there are still discrepancies about the effect of dose rate, which may serve as the greatest problem for the superposition of accelerated aging effects along with diffusion-limited-oxidation [5, 9, 11, 19, 21–24]. Some studies suggested that only total dose is important for deformation [8, 21, 23], whereas many others suggested that dose rate is also important [4, 10, 17, 19, 25, 26]. In addition to this, the effect of dose rate is different for different polymers [5, 6, 24, 27]. The reason for these can be explained with the effect of oxidation at high and low dose rates [2, 5, 26, 28]. Besides these, the mentioned ambiguity on the effect of structure on key parameters [5] and complete ignorance of post-radiation effect serves as additional problems related to use of the superposition method.

In this study to answer the questions about extendibility of the accelerated aging results to in-situ aging, we have developed a kinetic model based on the chemical reactions taking place during radiation-induced aging of polyethylene by using different radiation rates, duration, and total dose. This kinetic model can simulated both controlled accelerated aging and in-situ aging. Also, we developed an analytical model which can give the crosslinking and chain scission concentration in terms of dose rate and duration again for both accelerated aging and in-situ aging conditions including post-radiation periods.

2 METHOD

2.1 KINETIC MODEL

The model developed here follows the approach used by Min et al. [29] to investigate oxidation of ethylene-propylene-diene copolymers, with a few critical differences and by only considering polyethylene (PE). In particular, there are two essential reactions that are absent in the previous work. It will be shown here that the absence of these reactions results in a physically unrealistic system.

Starting from PE, interaction with ionizing radiation creates an alkyl radical PE and hydrogen gas, H_2. The dot symbol, "·" symbolizes the unpaired electron associated with a radical specie. The ionization of PE to PE· is shown in Figure 1(a). The alkyl radical can react with oxygen gas, O_2, from the environment, to produce a peroxy radical, PEOO·, as shown in Figure1(b). Two peroxy radicals can react with each other to crosslink polyethylene chains, resulting in the crosslinked structure, PEOOPE, and oxygen gas, as shown in Figure 1(c). A second reaction to produce PEOOPE crosslinking, involves combining an alkyl radical with a peroxy radical, as shown in Figure 1(d). An isolated peroxy radical along the chain can react with ethylene to form a hydroperoxide, PEOOH, and alkyl radical, as shown in Figure 1(e). The hydroperoxide can further react to scission the chain, leaving a terminating acid structure, PECOOH, and terminating CH_3, as shown in Figure 1(f). Although the primary interest for characterizing radiation damage in polymers are crosslinking and scission products [5–7, 30–33], given by reactions in Figure 1(c), (d), and (f), other reactions that do not lead to this type of structural changes also are important because they directly impact the population of radicals. One such reaction involves two peroxy radicals combining to form a ketone, PECO, an alcohol, PEOH, and oxygen gas, O_2, as shown in Figure 1(g). A second involves the combination of two alkyl radicals to form a polyethylene alkene, PEA, as shown Figure 1(h). Details of these reaction can be found in literature [15, 16, 25, 29, 34, 35].

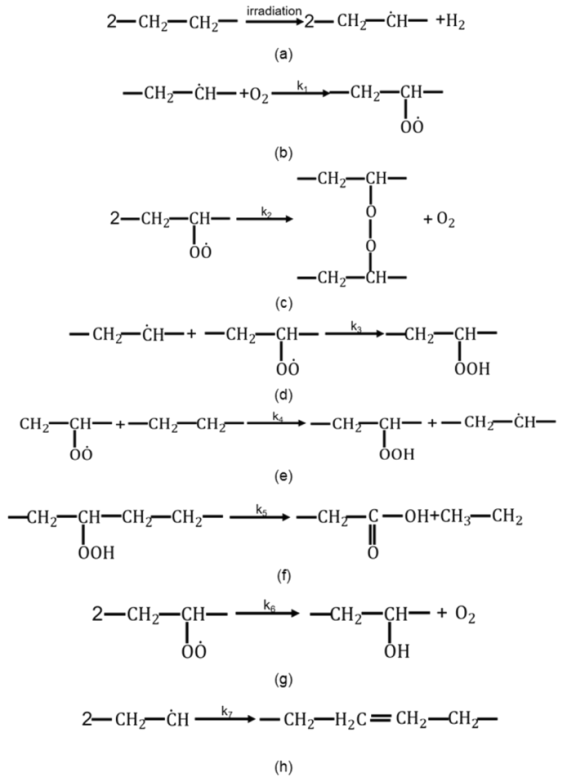

Figure 1. Radiation induced chemical reactions taking place in polyethylene in the presence of oxygen.

For each of the chemical reactions shown in Figure 1, rate equations can be written to describe the mass balance.

The kinetics of the reaction in Figure 1(a) is expressed

$$\frac{d[PE\cdot]}{dt} = 2\frac{d[H_2]}{dt} = -\frac{d[PE]}{dt} = \frac{\rho\dot{I}}{E_R} \tag{1}$$

where the square brackets indicate concentration, which is given here in units of molecule/m^3, and t is time in units of seconds (s). In Equation (1), the reaction rate scales directly with radiation dose rate, $\dot{I}$, in units of Gy/s and the density of PE mers in units of kg/m^3; it is inversely proportional to the energy required to create the alkyl radical, E_R in units of J/molecule. The reaction in Figure 1(b) is expressed

$$\begin{aligned}\frac{d[PEOO\cdot]}{dt} &= -\frac{d[PE\cdot]}{dt} = -\frac{d[O_2]}{dt} \\ &= k_1[PE\cdot][O_2]\end{aligned} \tag{2}$$

where the reaction rate is proportional to the concentration of the reagents, $PE\cdot$ and O_2, scaled by the rate constant k_1. Similarly, the remaining reactions in Figure 1 can be written:

$$\begin{aligned}\frac{d[PEOOPE]}{dt} &= \frac{d[O_2]}{dt} \\ &= -\frac{1}{2}\frac{d[PEOO\cdot]}{dt} \\ &= k_2[PEOO\cdot]^2,\end{aligned} \tag{3}$$

the reaction in Figure 1(d) is expressed

$$\begin{aligned}\frac{d[PEOOH]}{dt} &= -\frac{d[PE\cdot]}{dt} \\ &= -\frac{d[PEOO\cdot]}{dt} \\ &= k_3[PE\cdot][PEOO\cdot],\end{aligned} \tag{4}$$

the reaction in Figure 1(e) is expressed

$$\begin{aligned}\frac{d[PEOOH]}{dt} &= \frac{d[PE\cdot]}{dt} \\ &= -\frac{d[PEOO\cdot]}{dt} = -\frac{d[PE]}{dt} \\ &= k_4[PEOO\cdot],\end{aligned} \tag{5}$$

the reaction in Figure 1(f) is expressed

$$\frac{d[PECOOH]}{dt} = -\frac{d[PEOOH]}{dt} = k_5[PEOOH], \tag{6}$$

the reaction in Figure 1(g) is expressed

$$\begin{aligned}\frac{d[PECO]}{dt} &= \frac{d[PEOH]}{dt} = \frac{d[O_2]}{dt} \\ &= -\frac{1}{2}\frac{d[PEOO\cdot]}{dt} \\ &= k_6[PEOO\cdot]^2,\end{aligned} \tag{7}$$

the reaction in Figure 1(h) is expressed

$$\frac{d[PEA]}{dt} = -\frac{1}{2}\frac{d[PE\cdot]}{dt} = k_7[PE\cdot]^2. \tag{8}$$

All rate constants have units of m^3/molecule/s, with the exception of k_4 and k_5, which must have units s^{-1}.

From equations (1)-(6) it is possible to construct a set of 11 first order ordinary differential equations that determine the time evolution of the system from a given initial condition:

$$\frac{d[PE]}{dt} = -\frac{\rho\dot{I}}{E_R} - k_4[PEOO\cdot], \tag{9}$$

$$\begin{aligned}\frac{d[PE\cdot]}{dt} = \frac{\rho\dot{I}}{E_R} &- k_1[PE\cdot][O_2] \\ &- k_3[PEOO\cdot][PE\cdot] \\ &+ k_4[PEOO\cdot] - 2k_7[PE\cdot]^2,\end{aligned} \tag{10}$$

$$\frac{d[H_2]}{dt} = \frac{1}{2}\frac{\rho\dot{I}}{E_R}, \tag{11}$$

$$\begin{aligned}\frac{d[PEOO\cdot]}{dt} &= k_1[PE\cdot][O_2] + 2k_2[PEOO\cdot]^2 \\ &- k_3[PEOO\cdot][PE\cdot] \\ &- k_4[PEOO\cdot] - 2k_6[PEOO\cdot]^2,\end{aligned} \tag{12}$$

$$\frac{d[O_2]}{dt} = k_1[PE\cdot][O_2] + 2k_2[PEOO\cdot]^2 + k_6[PEOO\cdot]^2, \tag{13}$$

$$\begin{aligned}\frac{d[PEOOPE]}{dt} &= k_2[PEOO\cdot]^2 \\ &+ k_3[PEOO\cdot][PE\cdot],\end{aligned} \tag{14}$$

$$\frac{d[PEOOH]}{dt} = k_4[PEOO\cdot] - k_5[PEOOH], \tag{15}$$

$$\frac{d[PECOOH]}{dt} = k_5[PEOOH], \tag{16}$$

$$\frac{d[PECO]}{dt} = k_6[PEOO\cdot]^2, \quad (17)$$

$$\frac{d[PEOH]}{dt} = k_6[PEOO\cdot]^2, \quad (18)$$

$$\frac{d[PEA]}{dt} = k_7[PE\cdot]^2. \quad (19)$$

The density of PE, ρ, is assumed to be $1x10^3$ kg/m^3. According to the previous study [29] E_R is approximately 20 eV-30 eV based on the paper by Chapiro [36], however this seems extremely large. Revisiting the cited study we verified that the bond energies of any of the bonds present in polyethylene, expectedly around 2.5-5eV, are much smaller than the energy deposited as a result of irradiation (20-30 eV). It is also stated in the work by Chapiro [36] that there is far more available energy than required to break any bond present in PE. Based on this, we use 2.5 eV/molecule ($4x10^{-19}$ J) as E_R. The radiation dose in terms of Gray (Gy), i.e. J/kg, and the dose rate is in Gy/hr.

We calculate and estimate the reaction coefficients, k, based on the study by Min et al. [29]. The k_1 is expressed

$$k_1 = 4\pi r_c D_{O_2}[\exp(r_c/r_{b_1}) - 1]^{-1}, \quad (20)$$

by solving Fick's second law since it depends on diffusion of the species [29, 37–41]. Here r_c is the Coulombic radius [29, 31] and it defines the characteristics of recombination based on the distance between molecules along with minimum distance, r_b. If the distance between molecules is smaller than r_c but larger than r_b, then diffusion-controlled recombination takes place, whereas if the distance between molecules are smaller than r_b complete recombination takes place. r_c values was given as 1.47 x 10^{-8} m at 100℃ based on their calculation following to relative permittivity measurements on EPDM sheets. They also assumed that r_{b_1} is $0.6x10^{-9}$m. They further assumed that diffusion coefficient of O_2, D_{O_2}, is $2x10^{-12}$ m^2/s at 100 ℃. This yields $8.46x10^{-30}$. Similarly

$$k_2 = 4\pi r_c D_{POO\cdot}[\exp(r_c/r_{b_2}) - 1]^{-1}, \quad (21)$$

Using assumptions from Min et. al again, r_{b_2} is $1.0x10^{-9}$m and $D_{POO\cdot}$ is $4.15x10^{-19}$ m^2/s at 100 ℃, making k_2 $6.33x10^{-32}$.

For k_3, we do not have any reference because this reaction was not considered in the previous study. Still it shows similarity with the reaction given in Equation 5 since both depends on the diffusion of $POO\cdot$. In other words, both depends on $D_{POO\cdot}$. Using this diffusion coefficient along with r_b value given for the reaction in Equation 5 in the previous study, we assume that k_3 is $8.02x10^{-34}$ as an initial test value.

According to Min et al.[29] ,

$$k_4 = 4\pi r_c(2D_{POO\cdot})[\exp(r_c/r_{b_4}) - 1]^{-1}, \quad (22)$$

and as stated above this would yield a reaction coefficient of $8.02x10^{-34}$. However, this underestimates the reaction rate since the reaction doesn't require diffusion. As show in Figure 1(e) the reaction involves $PEOO\cdot$ reacting with the PE next to it. The value of k_4 should have a relatively larger value k_5, which Min et al. assumes to be $2.51x10^{-7}$. Therefore, in these calculations we approximate that k_4=$2.51x10^{-6}$ and k_5=$2.51x10^{-7}$ at 100 ℃.

$$k_6 = 4\pi r_c(2D_{POO\cdot})[\exp(r_c/r_{b_6}) - 1]^{-1}, \quad (23)$$

Using again the assumption from the previous study r_{b_6} is $1.4x10^{-9}$ m finds k_6 $4.22x10^{-30}$. Parameter k_7 was again not considered in the previous study, so as a test, it is accepted as $1.78x10^{-35}$.

2.2. Analytical Model

Afterwards, we use the results that we obtain under different radiation conditions changing dose rate, dose duration, and total dose from kinetical model to build an analytical model. This analytical model predicts the crosslinking and chain scission as a function of time and radiation rate. We try this model for rates and duration simulating both in situ and accelerating conditions. We have also developed and analytical model estimating the cross over and the period after radiation turn-off is on-going.

Firstly, we find the mathematical representation of the crosslinking and chain scission curves as a function of time for different radiation rates from 0.001 Gy/hr to 1000 Gy/hr for 40 years to develop the analytical model. We choose 40 years and include very low radiation rate to be able to simulate in situ aging conditions. At this point we have one functional form with different coefficients corresponding to different radiation rates. So, the next step is finding the functional forms of each coefficient where the variable parameter is radiation rate.

3 RESULTS

3.1 Kinetic Model

The kinetic model was used to examine the evolution of polyethylene during and after irradiation. The impact of dose rate is examined. For all of the calculations it is assumed that the diffusion of O_2 into and out of the polyethylene is instantaneous, which is reasonable considering the typical

specimen geometry, rates of reaction, and time scales examined.

The first set of calculations, was designed to examine the impact of dose rate. Each of the calculations involved a total dose of 12,000 Gy, but the rates were varied as shown in Table 1. For the fourth calculation in the series the dosage was cyclically turned on and off to achieve the total dose of 12,000 Gy. The cyclic schedule was 1 day on, followed by 9 days off, for a total of 5 exposures. All of the simulations were conducted for 2400 hours to allow observation of the post-radiation evolution. The concentration profiles of the crosslinking and chain scission sites are shown in Figure 2.

Table 1. Summary of different conditions used in the study.

Condition Number	Dosage Rate (Gy/hr)	Dosage Duration (hr)	Off Duration (hr)
1	500	24	2376
2	100	120	2280
3	10	1200	1200
4	100	24 x 5 (cyclic)	216x5(cyclic)+1200

The amount of crosslinking at the end dosing period is almost independent of the exposure rate and exposure duration, which suggests that it depends only on total dose since at the end of dosing period the total amount produced is almost same for all conditions (Figure 2). On the other hand, of course the rate of reaching the total amount depends strongly on the dose rate and/or pattern of irradiation.

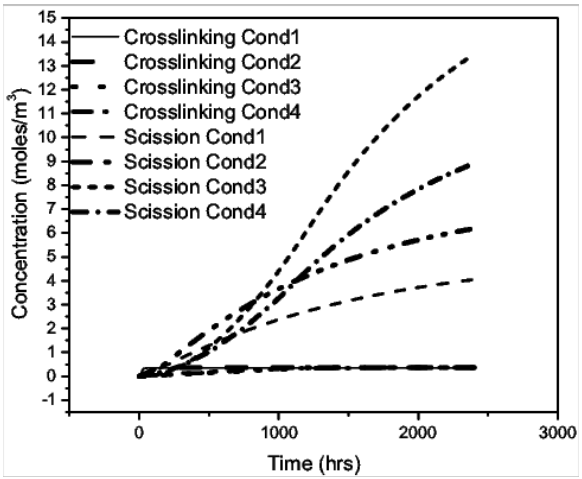

Figure 2. Concentration of scission and crosslinking for the exposure conditions given in Table 1.

To examine this point further, we calculated the crosslinking for the same duration at different rates. Here, the irradiation pattern is hundred days of radiation and hundred days of no radiation. The result for selected radiation rates covering both in situ (a) and accelerated (b) aging conditions are given in Figure 3. As it can be seen more clearly, in the accelerated aging conditions where the rates increased incrementally, the final amount produced is also changing incrementally. Considering the duration is same, the produced amount is a function of total dose which depends on with what rate production happens.

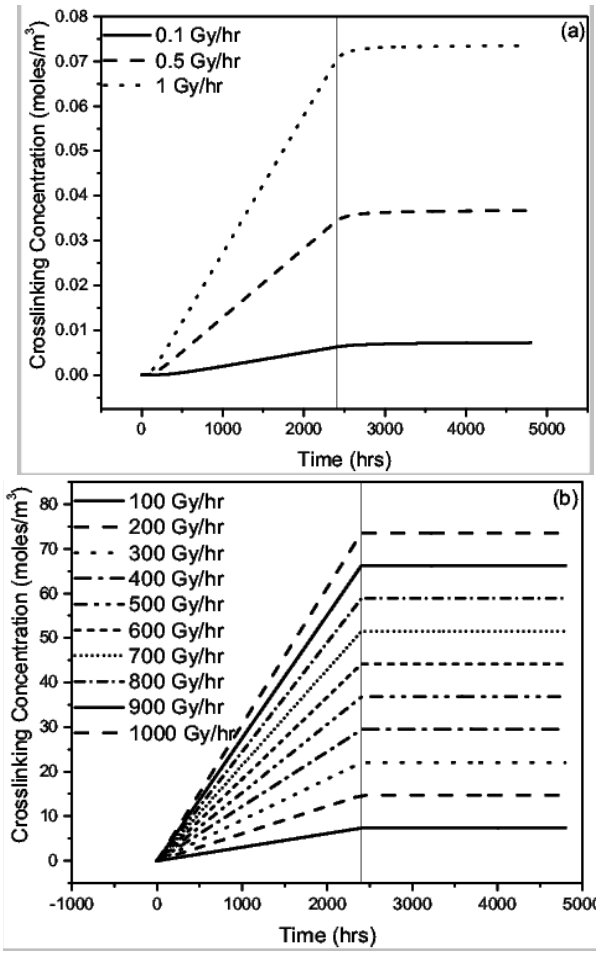

Figure 3. Crosslinking, i.e. concentration of PEOOPE at (a) low dosing rates and (b) high dosing rates.

Another important point that Figure 3 shows is the production of PEOOPE ends with the ending of dosing period. Reasoning of aforementioned points can be understood by examining the precursor reactions of PEOOPE formation. The formation of PEOOPE, can occur through two reactions. The first involves bonding between two peroxy radicals and the second peroxy radical reacting with an alkly radical:

$$2\mathrm{PEOO}\cdot \rightarrow \mathrm{PEOOPE} + \mathrm{O_2} \qquad (24)$$

where $k=6.33\times10^{-32}$

$$\mathrm{PE}\cdot + \mathrm{PEOO}\cdot \rightarrow \mathrm{PEOOPE} + \mathrm{O_2} \qquad (25)$$

where $k=8.02\times10^{-34}$.

These reactions only depend on the concentration of radicals and their proximity. Figure 4 shows the concentration of the radicals for the different conditions.

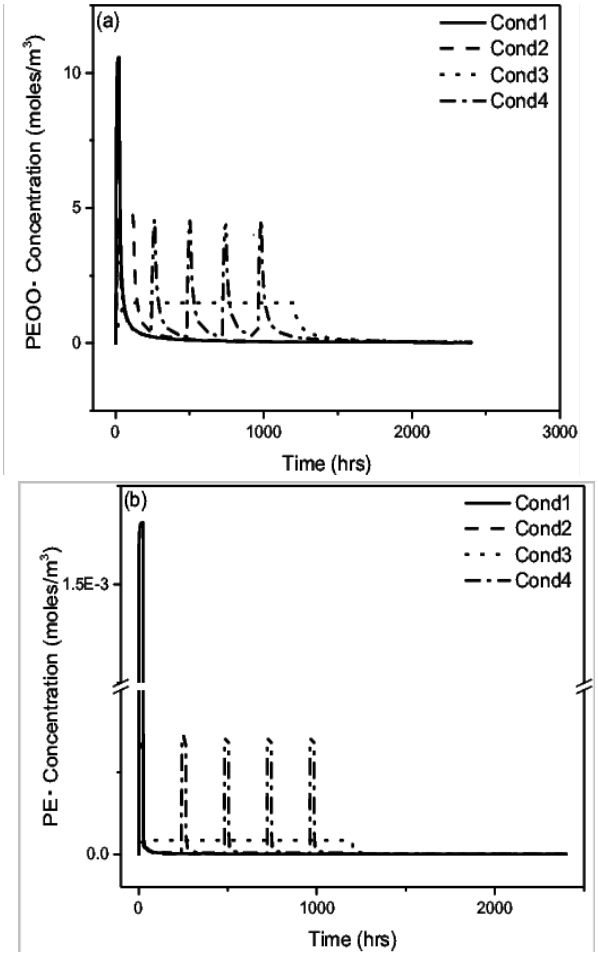

Figure 4. Concentration of radial, (a) peroxy and (b) alkly, which combines and causes crosslinking for the exposure conditions in Table 1.

The concentration of both radicals goes to zero almost instantly after turning off the radiation and as a result, almost only during radiation PEOOPE is produced. Therefore, the production of crosslinking sites depends mainly on the total dose.

In contrast, scission seems to have a strong dependence on exposure time, i.e., the longer the exposure the greater the concentration of scission sites. This also can be understood by looking at the precursor reaction for forming PECOOH and also for the radicals which are used in other reactions. The reaction for formation of scission (PECOOH) involves the decomposition of hydroperoxide, PEOOH, to generate inactive acids, alcohols, and water. The reaction is

$$\mathrm{PEOOH} \rightarrow \mathrm{PECOOH} + \mathrm{CH_3} \qquad (26)$$

where k=2.51x10^{-7}. The concentration and the production rate of hydroperoxide depends highly on the radiation rate (Figure 5). The highest concentration is observed for the greatest exposure time just as in the case of PECOOH.

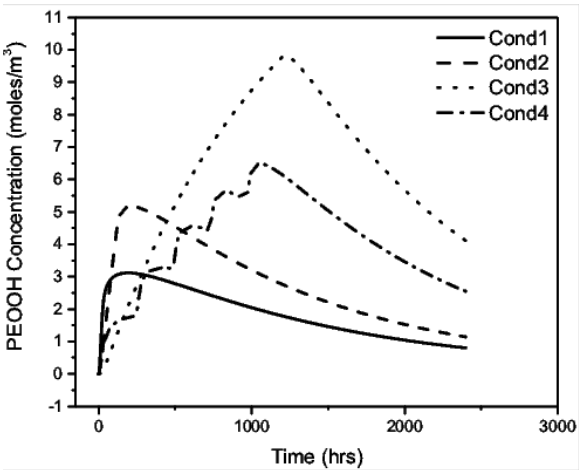

Figure 5. Concentration of hydroperoxide, PEOOH, for the exposure conditions given in Table 1.

We have also examined this point by using simulation for the same duration at different rates. As Figure 6 shows the production of PECOOH continues well after the radiation turned off although eventually it becomes stationary. Also, the produced amount is a function of exposure rate, exposure period, and total dose.

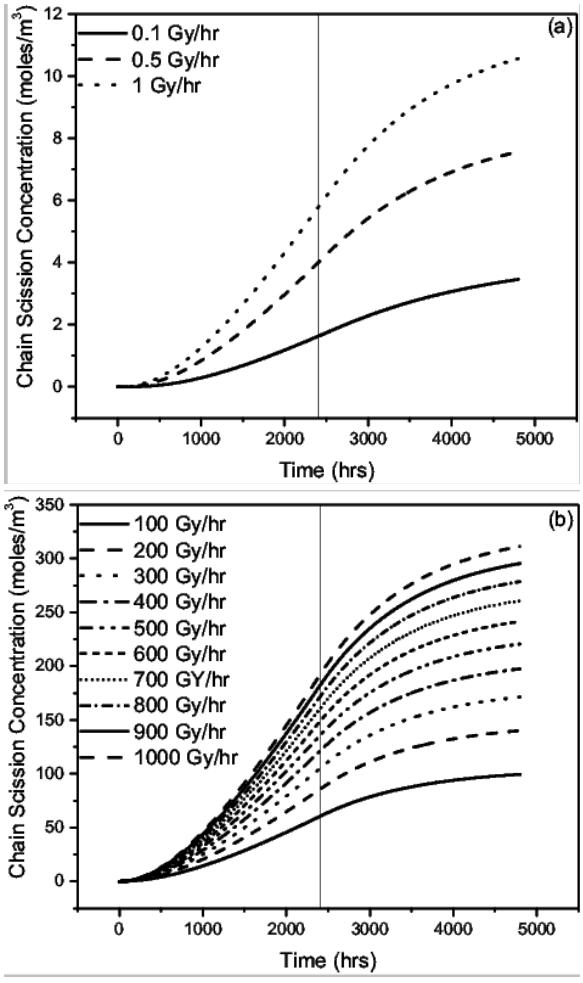

Figure 6. Chain scission, i.e. PECOOH, concentration at (a) low dosing rates and (b) high dosing rates.

3.2 Analytical Model

As it is stated above for developing analytical model, we represent the concentration of crosslinking and chain scission as a function of time for radiation on periods. The mathematical representation of both the crosslinking and chain scission curves are second-degree polynomial with the equation,

$$\begin{aligned}\mathrm{Conc}_{\mathrm{PEOOPE/PECOOH}} &= \mathrm{A} + \mathrm{B} \times \mathrm{time(hr)} \\ &+ \mathrm{C} \times \mathrm{time(hr)}^2\end{aligned} \qquad (27)$$

regardless of the radiation rate. The radiation rate changes coefficients; A, B, and C, as expected. After that we obtain these polynomial coefficient as a function of radiation rate.

The polynomial coefficients A and C depend on radiation rate linearly for both PEOOPE AND PECOOH for in situ aging periods. The coefficient B in PEOOPE, on the other hand, depends linearly on radiation rate, whereas for PECOOH the dependency follows a power law. These are summarized in Table 2.

Table 2. Dependence of the polynomial coefficients on radiation rate for both PEOOPE and PECOOH at in situ radiation periods.

	Dependence on $\dot{I}$	
Coefficient	PEOOPE	PECOOH
A	$\frac{a + b\dot{I} + c\dot{I}^2 + d\dot{I}^3}{1 + e\dot{I} + f\dot{I}^2 + g\dot{I}^3}$	$\frac{a + b\dot{I} + c\dot{I}^2 + d\dot{I}^3}{1 + e\dot{I} + f\dot{I}^2 + g\dot{I}^3}$
B	$y_o + a\dot{I}$	$a\dot{I}^b$
C	$y_o + a\dot{I}$	$y_o + a\dot{I}$

The constants in the radiation dependence of the polynomial coefficients A and B and C are given in Table 3 and Table 4, respectively.

Figure 7 shows the comparison of kinetic and analytical models for two different radiation rate and time periods. The first row, (a) and (b) shows the simulation of in situ aging duration, which is 40 years, whereas the second row shows the simulation of accelerated aging times, 100 days. Instead of very low rates and very short periods, e.g., around or less than 0.5 Gy/hr and less than 10 days, one analytical model \with the same constants can predict the result of the kinetic model almost perfectly.

Table 3. Radiation rate dependency constants of the time dependency constant A.

Constant	a	b	c	d	e	f	g
PEOOPE	-3.17×10^{-4}	-6.98×10^{-3}	-1.13×10^{-3}	-6.62×10^{-6}	1.27	3.72×10^{-2}	3.48×10^{-5}
PECOOH	-7.46×10^{-1}	-9.68	-1.53	-8.91×10^{-3}	1.29	3.79×10^{-2}	3.57×10^{-5}

Table 4. Radiation rate dependency constant of the time dependency constants B and C.

	B	C
PEOOPE	$y_o = 9.43 \times 10^{-10}$, $a = 3.07 \times 10^{-5}$	$y_o = 1.94 \times 10^{-16}$, $a = 6.40 \times 10^{-20}$
PECOOH	$a = 4.27 \times 10^{-3}$, $b = 5.00 \times 10^{-1}$	$y_o = 7.83 \times 10^{-12}$, $a = 1.72 \times 10^{-13}$

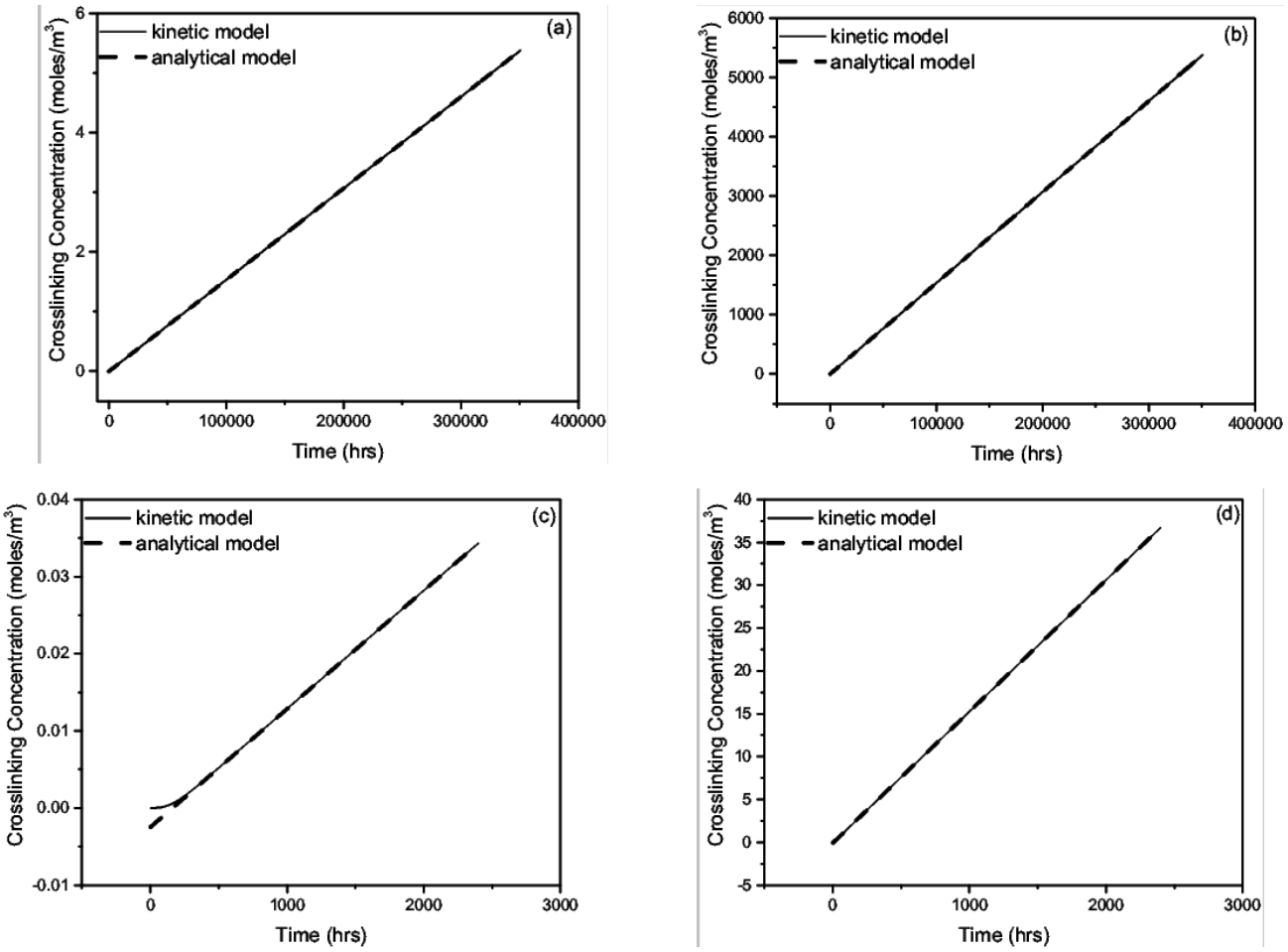

Figure 7. Comparison of analytical and kinetic model for crosslinking: (a) radiation rate 0.5 Gy/hr and (b) radiation rate 500 Gy/hr for 40 years; (c) radiation rate 0.5 Gy/hr and (d) radiation rate 500 Gy/hr for 100 days.

In contrast, the analytical model obtained for chain scission by using long periods falls short for predicting accelerated aging results. So, we need two different analytical models for these two different durations of radiation. In accelerated aging conditions, the time dependency becomes a third-degree polynomial,

$$\begin{aligned}\mathrm{Conc_{PECOOH}} = \mathrm{A} + \mathrm{B} \times \mathrm{time(hr)} \\ + \mathrm{C} \times \mathrm{time(hr)}^2 \\ + \mathrm{D} \times \mathrm{time(hr)}^3\end{aligned} \quad (28)$$

Dependency of all polynomial constants on the radiation rate is a three-parameter power law,

$$\mathrm{A, B, C, or\ D} = y_o + a\dot{I}^b \quad (29)$$

Again y_o, a , and b are different for A, B, C, and D, and given in Table 5.

Table 5. Radiation rate dependency constant of the time dependency constants for accelerated aging analytical model.

Constant	A	B	C	D
y_o	9.60×10^{-3}	-1.86×10^{-4}	2.30×10^{-8}	2.36×10^{-12}
A	-2.63×10^{-2}	2.09×10^{-4}	1.48×10^{-6}	-2.12×10^{-10}
B	4.95×10^{-1}	5.07×10^{-1}	4.99×10^{-1}	4.99×10^{-1}

Figure 8 given below visualizes two important points. Firstly, the shape of the PECOOH vs time curves varies with dosing duration regardless of radiation rate. Secondly, by using two different analytical models, it is possible to estimate both in situ aging, first row Figure 8, and accelerated aging, the second row, for a very wide range radiation rate.

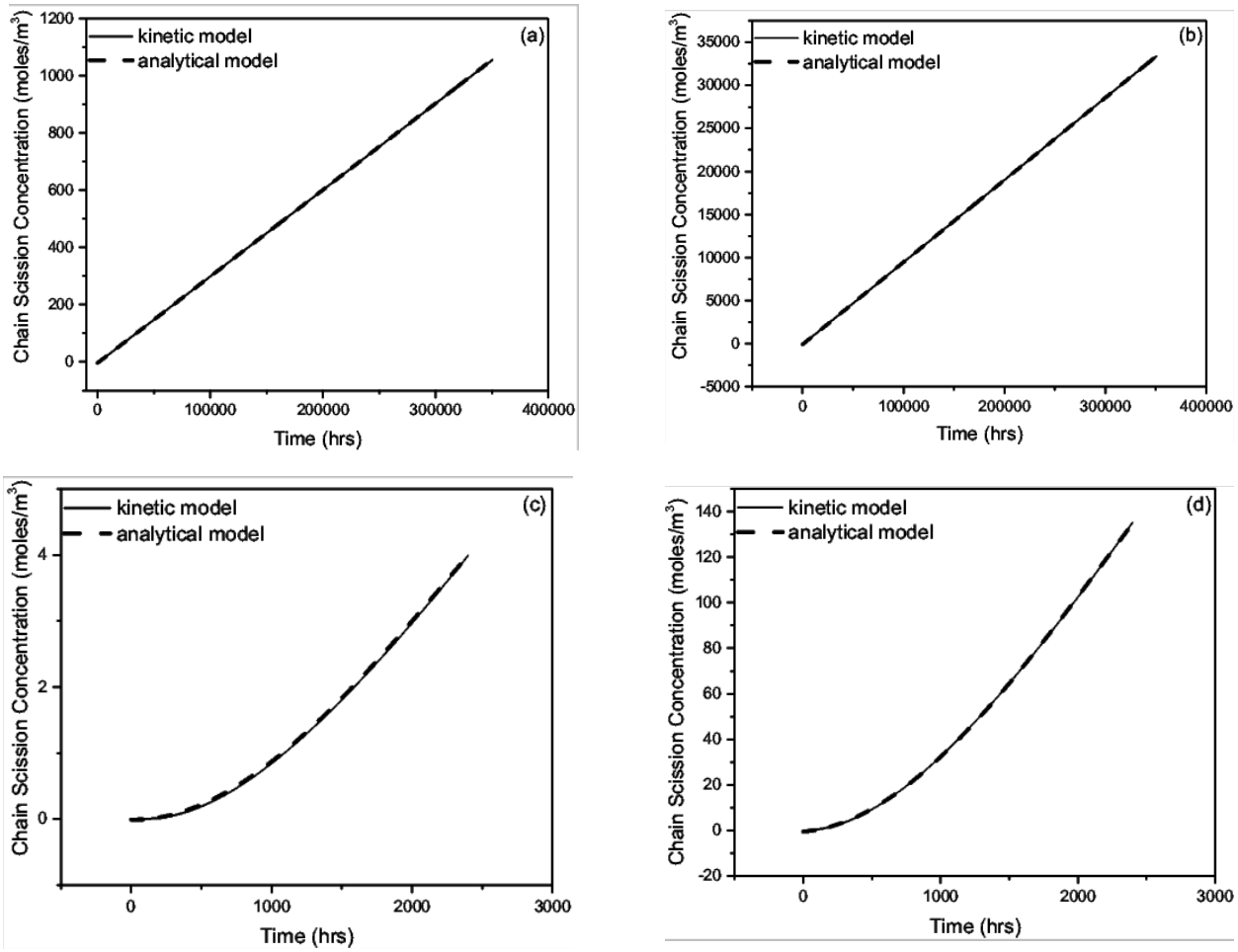

Figure 8. Comparison of analytical and kinetic model for chain scission: (a) Radiation rate 0.5 Gy/hr and (b) radiation rate 500 Gy/hr for 40 years; (c) radiation rate 0.5 Gy/hr and (d) radiation rate 500 Gy/hr for 100 days.

Finally, we have tried to develop analytical expressions for both crosslinking and chain scission concentrations at the periods where radiation is turned off. We followed the same steps above with an additional first one. This step involves the rescaling of time and concentration by using the final values at the radiation on. Rescaling is required for the generalization of model since the parameters in the analytical model are based on the radiation on values.

The dependence of PEOOPE and PECOOH concentration on time are shown in Eq.30 and 31, respectively.

$$Norm\mathrm{Conc}_{\mathrm{PEOOPE}} = \frac{\mathrm{A} + \mathrm{B}(\mathrm{time}_{\mathrm{norm}})}{1 + \mathrm{C}(\mathrm{time}_{\mathrm{norm}})} \qquad (30)$$

$$\begin{aligned}\mathrm{NormConc}_{\mathrm{PECOOH}} &= \mathrm{A} + \mathrm{B} \times \mathrm{time}_{\mathrm{norm}} \\ &+ \mathrm{C} \times \mathrm{time}_{\mathrm{norm}}{}^{2} \\ &+ \mathrm{D} \times (\mathrm{time}_{\mathrm{norm}})^{3}\end{aligned} \qquad (31)$$

However, when the dependence of the coefficients on radiation rate is examined it became obvious that they are almost not possible to be expressed as mathematical equations if they are not examined in different radiation rates. So, here instead of doing this, we are presenting the time dependency coefficients dependency on radiation rate in graphical form as seen in Figure 9 and Figure 10.

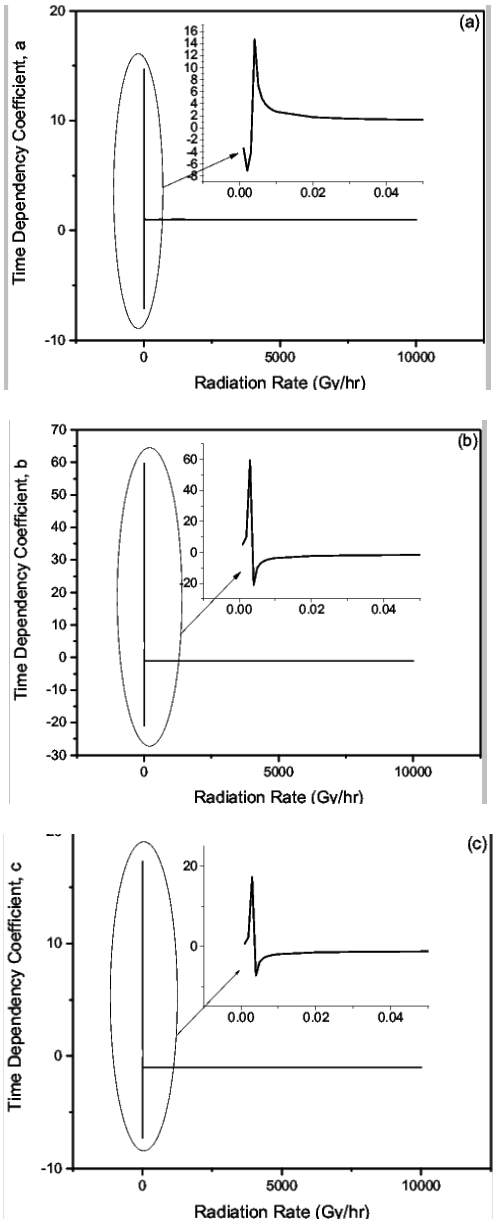

Figure 9. Time dependency coefficients of PEOOPE for radiation-off period. The insets show the low radiation rate part in detail.

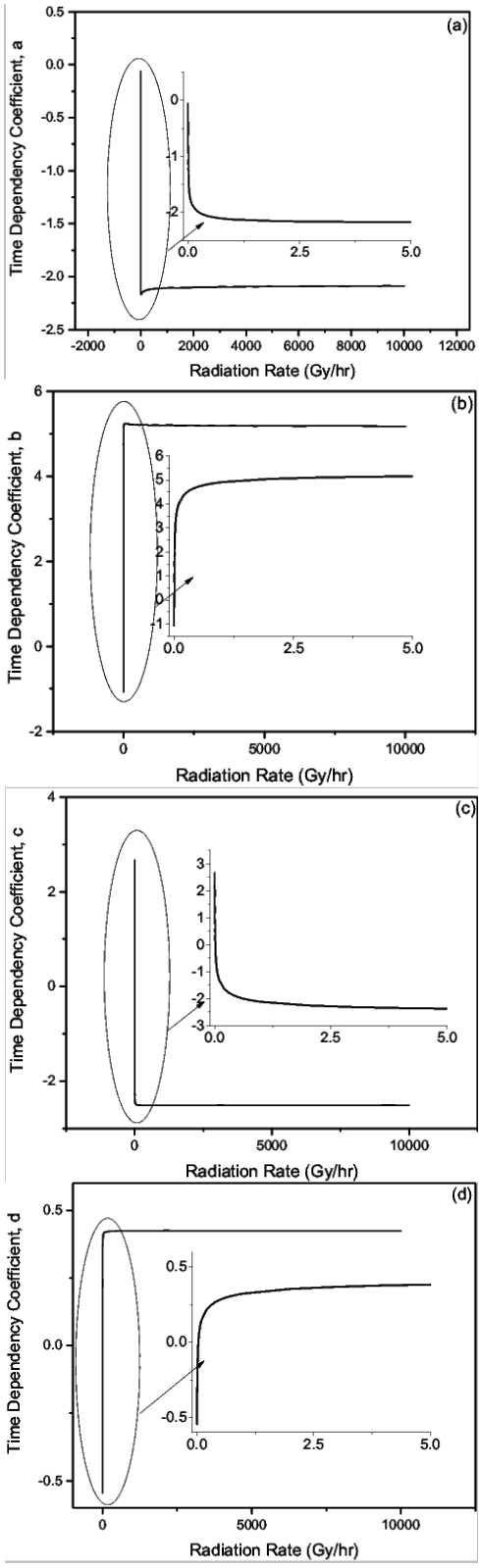

Figure 10. Time dependency coefficients of PECOOH for radiation-off period. The insets show the low radiation rate period in detail.

Finally, we have obtained the analytical expression of the cross-over point between crosslinking and chain scission reaction as a function of radiation rate. When we checked for the crossover point at different radiation rate, we have seen that until 8 Gy/hr there is no crossover point. Also, as it is seen in Figure 11(a) after 6000 Gy/hr the dependency of crossover point on radiation rate changes to a different mathematical function. Because of these discrepancies we limit our analytical model to radiation rates in the range of 8 – 5000 Gy/hr. The analytical expression is a double-rectangular hyperbola

$$\text{Crossover point} = \frac{a \times \dot{I}}{b + \dot{I}} + \frac{c \times \dot{I}}{d + \dot{I}} + e \times \dot{I} \qquad (32)$$

where $\dot{I}$ is the radiation rate. The coefficients are given in Table 6. This analytical relationship is very successful at estimating the crossover point as the comparison between analytical the model and the kinetic model shows in Figure 11(b).

Table 6. Radiation rate dependency coefficients of the crossover point

Coefficients	a	b	c	d	e
	1.09×10^{2}	1.94×10^{1}	3.08×10^{2}	4.84×10^{2}	2.82×10^{-1}

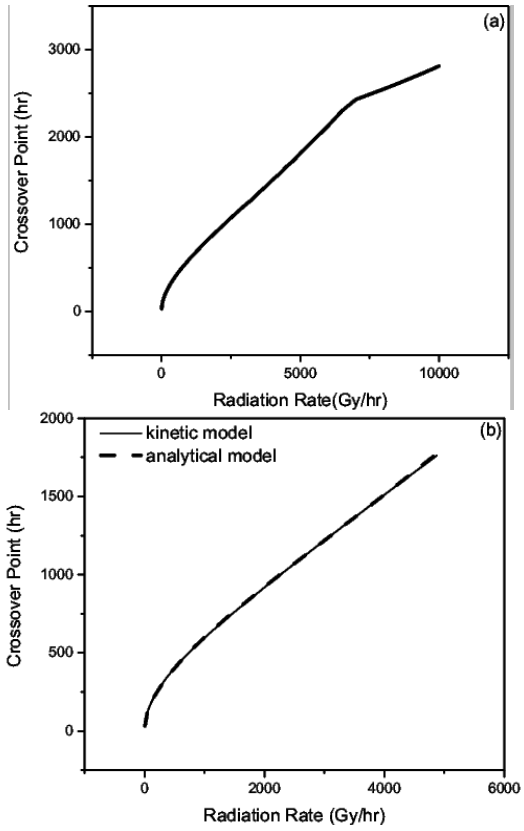

Figure 11. (a) Crossover point as a function of radiation rate and (b) Comparison of kinetic and analytical model for crossover point.

4 DISCUSSION

4.1 Kinetic model

In this study we have used Debye-Smoluchowski equation [42] which is one form of the Smoluchowski's time-dependent rate constant equation for a diffusion-controlled reaction [41, 43] for calculation of reaction constants in our diffusion-controlled reaction problem by following the study by Min et. al [29]. This theory assumes the homogeneous or steady-state distribution density of reacting ions and thermal equilibrium at the time throughout the diffusion process [44]. Another assumption is isolation of reagents from the medium, which may not be entirely valid for the problem at the hand. As many studies in the literature shows when the multi-radical effect is considered a notable improvement is observed [39–41, 45–47] in different problems. Other important assumptions include the independency of diffusion coefficients from the composition. The independency of composition is a general assumption for most of the diffusion related problems and it is mostly relaxed for increasing accuracy. An important simplification of this theory is that one of the reactants is assumed to be stationary which can introduce errors to the reaction constants that we calculate since that is not correct and some of the reactant even disappear with time [41]. Another point that our model does not take into account is the effect of temperature, which is important for the diffusion coefficients and its stand alone and combined effect during radiation. These are some of the assumption that can be problematic in our case however offering corrections for these are beyond the scope of this study.

In addition to these, there are also some uncertainties related to parameters used in the calculation of the reaction constants some parameters, i.e. r_bs, since it is not well-stated their origin and/or calculation. Besides, there are some reactions which were not present in the previous study and we needed to estimate. These suggest that the quantitative part in this study may have errors. In order to understand the accuracy limits we have employed a sensitivity study. We have measured the sensitivity of our models to variation values of reactions coefficients using condition 2 from Table 1. This sensitivity analysis served us also as a precision analysis and tells us the uncertainly in the results due to uncertainty in the values used for the reaction rates. We increased the reaction coefficients by 5% across 130 different combinations, from increasing just one coefficient to increasing all seven together. We examined the results in terms of changes in the crossover between crosslinking and scission. As a quantitative measure, we examined the crossing point for the concentration of crosslinking and scission sites. The crosslinking concentration always begins higher than the scission because the scission product requires multiple reaction steps, as discussed earlier, but over time the scission sites always becomes greater. Figure

12 shows the crossing point for the different coefficient values. The red line indicates the cross point when the parameters are as reported and the circles are variation from these. The expected value, when no changes are made to the coefficients, is 480 hours. For this series of tests, the standard deviation is found to be 17.23 hours and the maximum deviation is 45 hours. We conclude that a 5% change in the reaction rate coefficients results at the greatest a 10% change in the crossover point.

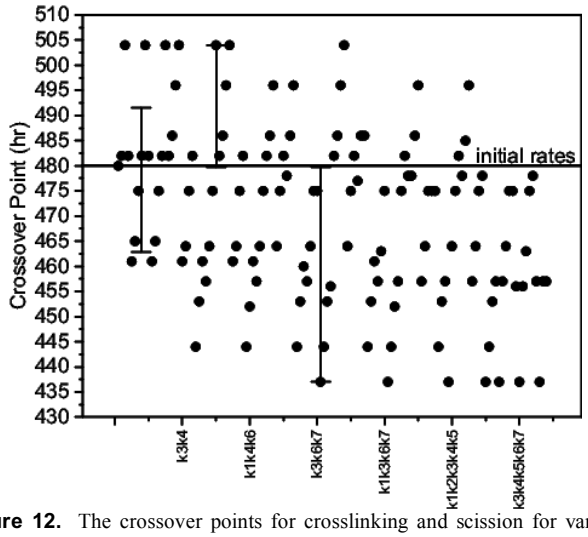

Figure 12. The crossover points for crosslinking and scission for varying values of the reaction rate coefficient. The arrow at the left shows the standard deviation (17.23 hours) and the ones in the middle and at the right show the maximum differences.

4.2 Comparison to prior model

We also compared our model with the kinetic model presented previously by Min et. al. in 2016 [29]. The comparison summarized in Figure 13 using exposure condition 2 from Table 1. For both the crosslinking and chain scission products the previous model predicted significantly greater concentrations. This alone is not damning, but the long ranging tail of the previously reported model at the concentration of scission sites does not asymptote to a constant value, and instead continues to increase.

There are two primary reasons for the differences: first, reactions were added that consume spurious radicals, preventing run away calculations in our model; and second, the prior model assumed the energy to produce an alkyl radical was 20 eV, which is about an order of magnitude higher than realistic, which we took to be 2.5 eV.

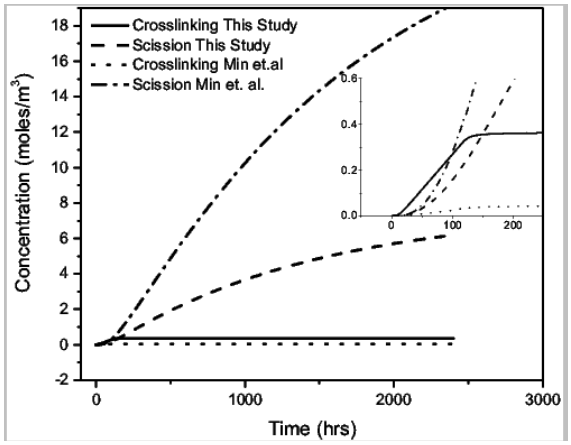

Figure 13. Comparison of kinetic models presented in this study and previous study under condition 2 given in Table 1. The inset shows the crossover point of both models.

4.3 Effect of dose rate on structure

It is well known that some materials are sensitive to radiation rate effects if the degradation takes place via radiation induced oxidation, chain scission formation [5, 14, 15, 48] and the low rate has a higher impact on degradation in comparison to high rate for the same total dose [2, 5]. Our study agrees well with these findings. In our first test where we keep the total dose constant and varied the radiation rate, we see that the rate is not important for crosslinking formation which only depends on total dose, whereas the concentration of chain scission is higher for the longer duration of radiation or in other words slower dose rate. This is explained with limited diffusion of oxygen at high dose rates or shorter times. In experimental condition this may also result in a non-homogeneous concentration profile along the depth of cable [5, 8].

4.4 Post-radiation effects

The radiation-induced degradation in air can be examined in two different stages. The first one chemical modification during actual exposure which is followed by a gradual post-irradiation stage which can continue for months and years of storage in air due to slow decomposition of hydoperoxides [22] and forming chain scission. It is another point that our model estimated correctly. In the literature, it is possible to find reports of cables which are examined right after and years after their extraction and shows the very similar properties [11]. This is not a discrepancy between our model and these findings. Because our model also showed that before 8 Gy/hr, which is a lot higher than in-situ aging radiation rates, there is no crossover between crosslinking and chain scission. In other words, crosslinking dominates and as a result of them, the post-radiation effects are minimal.

CONCLUSION

In this study, we have developed a kinetic model for radiation-induced degradation of polyethylene under oxygen. We have calculated the reaction constants by following Debye-Smoluchowski equation. Our model agrees well with the experimental studies on ethylene-propylene-diene copolymers or crosslinked polyethylene in the literature qualitatively. We cannot make quantitative comparisons because most cable studies includes real cables with lots of additives which can change the oxidation kinetics. Our results shows that for low total doses the crosslinking reactions are dominant. This changes at the crossover point and chain for polyethylene, the critical rate is 8 Gy/hr. The post-irradiation effects are results of the continuing formation of chain scission after the radiation is turned off. In addition to this, the rate effects that are observed during aging of polyethylene is also related to chain scission reaction. These two points make it clear that the crossover point is also a critical point for comparison of accelerated and in-situ aging. In addition to this, we have developed analytical models for crosslinking and chain scission concentrations both irradiation and post-irradiation durations and crossover points. The agreement between the kinetic and analytical model shows that this kind of studies can be used as an alternative to empirical superposition approach.

REFERENCES

1. Glass, S. W., Fifield, L. S., Dib, G., Tedeschi, J., Jones, A. M., and Hartman, T. S. "State-of-the-Art Assessment of NDE Techniques for Aging Cable Management in Nuclear Power Plants FY2015, PNNL-24649" no. September (2015).

2. Anandakumaran, K. "Condition Assesment of Cable Insulation Systems in Operating Nuclear Power Plants" 6, no. 3 (1999): 376–384.

3. Simmons, K. L., Ramuhalli, P., Brenchley, D. L., Coble, J. B., Hashemian, H. M., Konnick, R., and Ray, S. "Light Water Reactr Sustainability (LWRS) Program-Non-Destructive Evaluation R&D Roadmapfor Determining Remaining Useful Life of Aging Cables in Nuclear Power Plants" no. September (2012):

4. Kim, J.-S. and Lee, D.-J. "Evaluation of Nuclear Plant Cable Aging Through Condition Monitoring" Journal of the Korean Nuclear Society 36, no. 5 (2004): 475–484.

5. Wilski, H. "The Radiation Induced Degradation of Polymers" International Journal of Radiation Applications and Instrumentation. Part C. Radiation Physics and Chemistry (1987): doi:10.1016/1359-0197(87)90054-3

6. Wilski, H. "Radiation Stability of Polymers" International Journal of Radiation Applications and Instrumentation. Part (1990): doi:10.1016/1359-0197(90)90082-S

7. Gheysari, D., Behjat, A., and Haji-saeid, M. "The Effect of High-Energy Electron Beam on Mechanical and Thermal Properties of LDPE and HDPE" 37, (2001): 295–302.

8. Verardi, L., Fabiani, D., and Montanari, G. C. "Electrical Aging Markers for EPR-Based Low-Voltage Cable Insulation Wiring of Nuclear Power Plants" Radiation Physics and Chemistry 94, no. 1 (2014): 166–170. doi:10.1016/j.radphyschem.2013.05.038

9. Banford, H. M. and Fouracre, R. A. "Nuclear Technology and Ageing" IEEE Electrical Insulation Magazine 15, no. 5 (1999): 19–27. doi:10.1109/57.793826

10. Agarwal, V. K., Banford, H. M., Bernstein, B. S., Brancato, E. L., Fouracre, R. A., Montanari, G. C., Parpal, J. L., Seguin, J. N., Ryder, D. M., and Tanaka, J. "The Mysteries of Multifactor Ageing" IEEE Electrical Insulation Magazine 11, no. 3 (1995): 37–43. doi:10.1109/57.387831

11. Gillen, K. T., Celina, M., and Clough, R. L. "Density Measurements as a Condition Monitoring Approach for Following the Aging of Nuclear Power Plant Cable Materials" Radiation Physics and Chemistry 56, no. 4 (1999): 429–447. doi:10.1016/S0969-806X(99)00333-3

12. Simmons, K. L., Fifield, L. S., Westman, M. P., Ramuhalli, P., Pardini, A. F., Tedeschi, J. R., and Jones, A. M. "Determining Remaining Useful Life of Aging Cables in Nuclear Power Plants: Interim Status for FY2013" Northwest National Laboratory (PNNL), Richland, WA (US), 2013. no. September (2013):

13. Shimada, A., Sugimoto, M., Kudoh, H., Tamura, K., and Seguchi, T. "Degradation Mechanisms of Silicone Rubber (SiR) by Accelerated Ageing for Cables of Nuclear Power Plant" IEEE Transactions on Dielectrics and Electrical Insulation 21, no. 1 (2014): 16–23. doi:10.1109/TDEI.2014.6740721

14. Rivaton, A., Cambon, S., and Gardette, J.-L. "Radiochemical Aging of Ethylene-Propylene-Diene Monomer Elastomers. I. Mechanism of Degradation under Inert Atmosphere" Journal of Polymer Science Part A: Polymer Chemistry 42, no. 5 (2004): 1239–1248. doi:10.1002/pola.11095, Available at http://doi.wiley.com/10.1002/pola.11095

15. Rivaton, A., Cambon, S., and Gardette, J. L. "Radiochemical Ageing of EPDM Elastomers. 2. Identification and Quantification of Chemical Changes in EPDM and EPR Films γ-Irradiated under Oxygen Atmosphere" Nuclear Instruments and Methods in Physics Research, Section B: Beam Interactions with Materials and Atoms 227, no. 3 (2005): 343–356. doi:10.1016/j.nimb.2004.09.008

16. Rivaton, A., Cambon, S., and Gardette, J. L. "Radiochemical Ageing of EPDM Elastomers. 3. Mechanism of Radiooxidation" Nuclear Instruments and Methods in Physics Research, Section B: Beam Interactions with Materials and Atoms 227, no. 3 (2005): 357–368. doi:10.1016/j.nimb.2004.09.009

17. Clough, R. L. and Gillen, K. T. "Radiation-Thermal Degradation of PE and PVC: Mechanism of Synergism and Dose Rate Effects" Radiation Physics and Chemistry (1981): doi:10.1016/0146-5724(81)90189-8

18. Fothergill, J. C., Montanari, G. C., Stevens, G. C., Laurent, C., Teyssedre, G., Dissado, L. A., Nilsson, U. H., and Platbrood, G. "Electrical, Microstructural, Physical and Chemical Characterization of HV XLPE Cable Peelings for an Electrical Aging Diagnostic Data Base" IEEE Transactions on Dielectrics and Electrical Insulation 10, no. 3 (2003): 514–527. doi:10.1109/TDEI.2003.1207480

19. Gasa, J. V., Liu, Z., and Shaw, M. T. "Relationship between

Density and Elongation-at-Break of Naturally and Artificially Aged Cable Materials Used in Nuclear Power Plants" Polymer Degradation and Stability 87, no. 1 (2005): 77–85. doi:10.1016/j.polymdegradstab.2004.07.009
20. Gillen, K. T. and Clough, R. L. "Time-Temperature-Dosae Rate Uperposition: A Methodology for Extrapolating Accelerated Radiation Aging Data to Low Dose Rate Conditions" Polymer Degradation and Stability 24, no. 2 (1989): 137–168. doi:10.1520/D0850-11.1
21. Seguchi, T., Tamura, K., Ohshima, T., Shimada, A., and Kudoh, H. "Degradation Mechanisms of Cable Insulation Materials during Radiation-Thermal Ageing in Radiation Environment" Radiation Physics and Chemistry 80, no. 2 (2011): 268–273. doi:10.1016/j.radphyschem.2010.07.045, Available at http://dx.doi.org/10.1016/j.radphyschem.2010.07.045
22. Carlsson, D. J., Dobbin, C. J. B., Jensen, J. P. T., and Wiles, D. M. "Polypropylene Degradation by Gamma-Irradiation in Air" Polymer stabilization and degredtion: based on a symposium sponsored by the Division of Plymer Chemistry at the 187th meeting of the Americn Chemical Society, St. Louis, Missouri (1985): 359–371. doi:10.1520/D0850-11.1
23. Plaček, V., Bartoníček, B., Hnát, V., and Otáhal, B. "Dose Rate Effects in Radiation Degradation of Polymer-Based Cable Materials" Nuclear Instruments and Methods in Physics Research, Section B: Beam Interactions with Materials and Atoms 208, no. 1–4 (2003): 448–453. doi:10.1016/S0168-583X(03)00626-8
24. Hanisch, F., Maier, P., Okada, S., and Schönbacher, H. "Effects of Radiation Types and Dose Rates on Selected Cable-Insulating Materials" International Journal of Radiation Applications and Instrumentation. Part (1987): doi:10.1016/1359-0197(87)90141-X
25. Zaharescu, T., Setnescu, R., Jipa, S., and Setnescu, T. "Radiation Processing of Polyolefin Blends. I. Crosslinking of EPDM-PP Blends" Journal of Applied Polymer Science (2000): doi:10.1002/1097-4628(20000801)77:5<982::AID-APP4>3.0.CO;2-F
26. Reynolds, A. B., Bell, R. M., Bryson, N. M. N., Doyle, T. E., Hall, M. B., Mason, L. R., Quintric, L., and Terwilliger, P. L. "Dose-Rate Effects on the Radiation-Induced Oxidation of Electric Cable Used in Nuclear Power Plants" Radiation Physics and Chemistry 45, no. 1 (1995): 103–110. doi:10.1016/0969-806X(94)E0003-2
27. Kuriyama, I., Hayakawa, N., and Nakase, Y. "EFFECT OF DOSE RATE ON DEGRADATION BEHAVIOR INSULATING POLYMER MIATERIALS from the Wd F Ws" IEEE Transactions on Electrical Insulation (1979): 272–277.
28. Gillen, K. T. and Clough, R. L. "Occurence and Implications of Radiation Dose-Rate Effects for Material Aging Studies" Radiation Physics and Chemistry (1981): doi:10.1016/0146-5724(81)90191-6
29. Min, D., Li, S., Hirai, N., and Ohki, Y. "Modeling of Oxidation Process and Property Changes of Ethylene-Propylene-Diene Copolymer" IEEE Transactions on Dielectrics and Electrical Insulation 23, no. 1 (2016): 537–546. doi:10.1109/TDEI.2015.005400, Available at http://ieeexplore.ieee.org/document/7422602/
30. Dadbin, S., Frounchi, M., Haji Saeid, M., and Gangi, F. "Molecular Structure and Physical Properties of E-Beam Crosslinked Low-Density Polyethylene for Wire and Cable Insulation Applications" Journal of Applied Polymer Science 86, no. 8 (2002): 1959–1969. doi:10.1002/app.11111
31. Ratzsch M., Arnold M., Borsig E., Bucka H., R. N. "Radical Reactions on Polypropylene in the Solid State - GetInfo" Progress in polymer science 27, (2002): 1195–1282. doi:10.1016/S0079-6700(02)00006-0, Available at https://getinfo.de/app/Radical-reactions-on-polypropylene-in-the-solid/id/BLSE:RN114974018
32. Odonnell, J. "Chemistry of Radiation Degradation of Polymers" Radiation Effects on Polymers (1990): doi:10.1021/bk-1991-0475.ch024
33. Davenas, J., Stevenson, I., Celette, N., Cambon, S., Gardette, J. L., Rivaton, A., and Vignoud, L. "Stability of Polymers under Ionising Radiation: The Many Faces of Radiation Interactions with Polymers" Nuclear Instruments and Methods in Physics Research, Section B: Beam Interactions with Materials and Atoms (2002): doi:10.1016/S0168-583X(02)00628-6
34. Carlson, W. D. "POLYMORPHS OF CaCO//3 AND THE ARAGONITE-CALCITE TRANSFORMATION." Reviews in Mineralogy 11, (1983): 191–225. Available at http://www.scopus.com/inward/record.url?eid=2-s2.0-0020947885&partnerID=tZOtx3y1
35. Planes, E., Chazeau, L., and Vigier, G. "Role of Temperature during Ageing under Gamma Irradiation of Filled EPDM: Consequences on Mechanical Properties" Journal of Polymer Science, Part B: Polymer Physics (2010): doi:10.1002/polb.22030
36. Chapiro, A. "General Consideration of the Radiation Chemistry of Polymers" Nuclear Inst. and Methods in Physics Research, B 105, no. 1–4 (1995): 5–7. doi:10.1016/0168-583X(95)00861-6
37. Smoluchowski, M. "Three Lectures on Diffusion, Brownian Movement and Coagulation of Colloidal Particles" Physikalische Zeitschrift (1916):
38. Kuppermann, A. and Belford, G. G. "Diffusion Kinetics in Radiation Chemistry. I. Generalized Formulation and Criticism of Diffusion Model" J.Chem.Phys. 36, no. 1962 (1962): 1412–1426. doi:10.1063/1.1732759
39. Clifford, P., Green, N. J. B., Pilling, M. J., and Pimblott, S. M. "Stochastic Models of Diffusion-Controlled Ionic Reactions in Radiation-Induced Spurs. 1. High-Permittivity Solvents" J. Phys. Chem 91, no. 6 (1987): 4417–4422. doi:10.1021/j100300a043, Available at http://pubs.acs.org/doi/abs/10.1021/j100300a043
40. Wolf, K. and Bartzcak, M. W. "Dynamics of Diffusion-Controlled Recombination of Ions in Ionic Solutions. Limits of Validity If the Debye-Smoluchowski Equation" Proc. SPIE 4412, (2001): 137–148. doi:ADP010487
41. Al-Samra, E. H. and Green, N. J. B. "Scavenging and Recombination Kinetics in Radiation Chemistry" Phys. Chem. Chem. Phys. 19, no. 30 (2017): 20016–20028. doi:10.1039/C7CP04184E, Available at http://xlink.rsc.org/?DOI=C7CP04184E
42. Debye, P. "Reaction Rate in Ionic Solutions" Transactions of The Elecrtochemical Society 82, no. 1 (1942): 265.
43. Smoluchowski, M. V. "Mathematical Theory of the Kinetics of the Coagulation of Colloidal Solutions" Z. Phys. Chem. 92, (1917): 129–168.

44. Rice, S. A., Butler, P. R., Pilling, M. J., Baird, J. K., and Rice, S. A. “Dilute Solution Rate of Reaction of Ions in Dilute Solution” 4001, no. 1979 (2012): doi:10.1063/1.438020
45. Green, N. J. B., Pilling, M. J., Pimblott, S. M., and Clifford, P. “Stochastic Models of Diffusion-Controlled Ionic Reactions-Induced Spurs. 2. Low-Permittivity Solvents” The Journal of Physical Chemistry 93, no. 24 (1989): 8025–8031. doi:10.1021/j100361a014, Available at http://pubs.acs.org/doi/abs/10.1021/j100361a014
46. Bartzcak, M. W. and Hummel, A. “Computer Simulation of Ion Recombination in Irradiated Nonpolar Liquids” Journal of Radioanalytical and Nuclear Chemistry 101, no. 2 (1986): 299–306.
47. Bartzcak, M. W. and Hummel, A. “Monte Carlo Calculation of Diffusion-Controlled Ion Recombination for Single and Multiple Ion Pairs in a Nonpolar Liquid” International Journal of Radiation Applications and Instrumentation. Part C. Radiation Physics and Chemistry 27, no. 1 (1986): 71–72.
48. Carlsson, D. J., Wiles, D. M., and Dobbin, C. J. B. “Direct Observations of Macroperoxyl Radical Propagation and Termination by Electron Spin Resonance and Infrared Spectroscopies” Macromolecules 18, no. 10 (1985): 2092–2094. doi:10.1021/ma00152a053

B.3 Dielectric Response of Cross-Linked Polyethylene (XLPE) Cable Insulation Material to Radiation and Thermal Aging

Presented at: *2nd IEEE International Conference on Dielectrics (ICD2018)*, Budapest, Hungary, July 1-5, 2018.
To be published in: *IEEE Xplore.*
Authors: Zhihui Shao, Michael I. Byler, Shuaishuai Liu, Nicola Bowler, Leonard S. Fifield, and Mark K. Murphy

Dielectric Response of Cross-Linked Polyethylene (XLPE) Cable Insulation Material to Radiation and Thermal Aging

Zhihui Shao, Michael I. Byler, Shuaishuai Liu, Nicola Bowler
College of Engineering, Iowa State University
Ames, Iowa 50011, USA
nbowler@iastate.edu

Leonard S. Fifield, Mark. K. Murphy
Pacific Northwest National Laboratory
Richmond, Washington 99354, USA
leo.fifield@pnnl.gov

***Abstract*—This work seeks dielectric indicators of the aged state of cross-linked polyethylene (XLPE) that has been simultaneously irradiated and thermally aged. The XLPE samples studied here were of the same material formulation as XLPE insulation found in RSCC I46-0021 instrumentation cable, formed into tapes with dimensions approximately 20 x 0.7 x 100 mm^3. Aging was conducted by suspending the samples from a rack within an oven and subsequently exposing oven and samples to gamma radiation. Samples were aged at 60, 90, and 115 °C, with gamma-radiation dose rates from 0 to 450 Gy/h with total received doses from 0 to 216 kGy. The dielectric spectra of these samples were measured over the frequency range 1 Hz to 1 MHz using custom electrodes and a Novocontrol dielectric spectrometer before dielectric breakdown strength was measured on the same samples. Dielectric loss tangent was observed to increase as a function of dose, dose rate and exposure time for XLPE samples exposed as described above. Dielectric loss tangent did not, however, show sensitivity to thermal aging for the range of temperatures studied. Dielectric breakdown strength initially increased as the material oxidized, then decreased for more extreme aging, due to chain scission. It is concluded that dielectric loss tangent is a promising indicator of XLPE aging due to gamma radiation exposure.**

Keywords—dielectric losses; dielectric breakdown; cable insulation

I. Introduction

The safe operation of nuclear power plants (NPPs) relies upon the proper functioning of low-voltage power, control and instrumentation cables [1]. Approximately 1,000 km of low-voltage cables are found in each United States NPP and cross-linked polyethylene (XLPE) is the mostly widely used insulation material for such cables. This work studies the electrical response of XLPE to exposure to simultaneous thermal and gamma radiation, seeking potential nondestructive indicators of insulation age.

II. Sample Preparation

A. XLPE Insulation Material

XLPE-based insulation material found in RSCC I46-0021 instrumentation cable was provided by the manufacturer in the form of tapes with dimensions approximately 20 x 0.7 x 100 mm^3, Figure 1. The material is a composite consisting of approximately 60 wt. % XLPE, 20 wt. % organic flame retardants, 17 wt. % inorganic flame retardant and white pigment, 2 wt. % antioxidant, and a small amount (< 1 wt. %) of residual cross-linking agent [2].

B. Accelerated Aging

The tape samples were suspended within an oven that itself was placed in a gamma-ray field from an encapsulated cobalt-60 source at Pacific Northwest National Laboratory's high exposure facility (HEF). Samples were exposed at temperatures 60, 90, and 115 °C for 0, 5, 10, 15 and 20 days at dose rates 0, 140, 280, 350, and 450 Gy/h (dose in terms of air kerma). A set of 13 independent samples resulted, as detailed in Table 1, with naming convention 'DR *dose rate* D *days exposed*'.

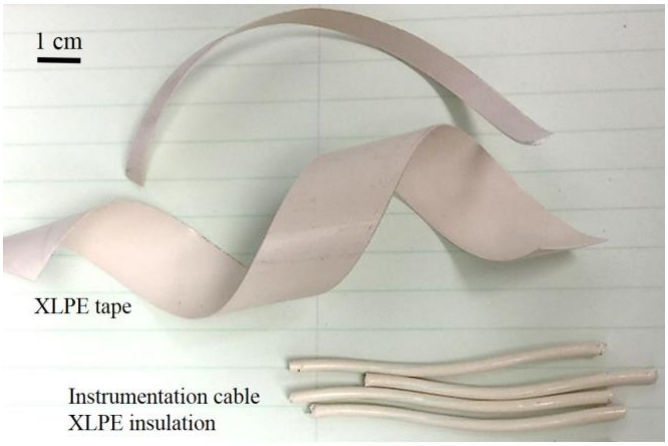

Fig. 1. XLPE samples. The material formulation is the same as insulation found in RSCC I46-0021 instrumentation cable.

This work was funded by the U.S. Department of Energy's Nuclear Energy University Program and Light Water Reactor Sustainability Program.

978-1-5386-6389-9/18/$31.00©2018 IEEE

TABLE I. SAMPLE SET

Sample	Dose Rate (Gy/h)	Exposure Time (d)	Total Dose (kGy)	Thickness (mm)
DR0D0	0	0	0	0.70 ± 0.02
DR0D5	0	5	0	0.75 ± 0.07
DR0D10	0	10	0	0.76 ± 0.04
DR0D15	0	15	0	0.75 ± 0.05
DR0D20	0	20	0	0.76 ± 0.04
DR450D0	450	0	0	0.70 ± 0.02
DR450D5	450	5	54	0.70 ± 0.05
DR450D10	450	10	108	0.73 ± 0.04
DR450D15	450	15	162	0.70 ± 0.05
DR450D20	450	20	216	0.74 ± 0.03
DR140D20	140	20	67	0.72 ± 0.03
DR280D20	280	20	134	0.74 ± 0.04
DR350D20	350	20	168	0.72 ± 0.05

III. EXPERIMENTAL MEASUREMENTS

A. *Dielectric Spectra*

For dielectric measurements, a custom sample cell was designed to fit the sample dimensions while boosting the measured capacitance to maximize the signal-to-noise ratio. Rectangular electrodes were machined from brass and mounted in a poly-methyl methacrylate holder to maintain parallel electrode faces while the sample was sandwiched between them. The areas of the bottom and top electrodes were, respectively, 50 x 20 mm^2 and 40 x 15 mm^2. The four corners of each electrode were rounded with radius of curvature approximately 2 mm. For each measurement, the sample cell was connected to the input ports of a Novocontrol dielectric spectrometer and the capacitance and dissipation factor obtained from 1 Hz to 1 MHz. Spectral measurements were made at three different locations on each sample, with three measurements recorded per location, and the averaged data are presented. Dielectric spectra were measured under ambient conditions with temperature 20.3 °C and 26 % relative humidity.

B. *Dielectric Breakdown Strength*

Dielectric breakdown strength of the XLPE-based samples was measured using a dielectric rigidity 6135 test apparatus that is capable of supplying alternating voltage up to 60 kV. The upper electrode was machined from titanium with hemi-spherical tip of radius 0.5 mm. The lower electrode was cylindrical, of brass, with a flat, circular tip of diameter 5 mm. Immediately prior to each breakdown test, the sample surface was wiped with acetone and allowed to dry. The sample and electrode assembly were then immersed into an insulating liquid bath filled with Envirotemp® FR3® fluid to avoid surface flashover during the breakdown test. Alternating voltage (50 Hz) was increased at rate 0.5 kV/s with applied current of 0.1 mA until breakdown occurred. Breakdown voltage was measured at 20 nominally identical points on each sample. Sample thickness was measured at five points on each sample using a digital indicator with accuracy ~1 µm. The mean and standard deviation of measured thickness values are reported in Table 1. The value of dielectric breakdown strength was obtained by dividing the measured breakdown voltage by the sample thickness.

IV. RESULTS AND DISCUSSION

A. *Dielectric Spectra*

1) *Effect of aging time*

The dielectric loss tangent of samples aged at 60 °C, with radiation exposures detailed in Table 1, is shown in Figure 2. Comparing Figure 2(a) with Figure 2(b), it can be seen that the dielectric response of the material changes dramatically following exposure to gamma radiation. Exposure to gamma radiation causes depletion of antioxidant due to chemical reactions with free radicals, along with evaporation and sublimation [2]. The prevalence of these mechanisms depends on the aging temperature. Brominated flame retardants in the material also decompose into smaller brominated molecules. Chain scission and chain cross-linking also take place simultaneously during aging, with chain scission dominating when the material is exposed to gamma radiation at 60 °C [2].

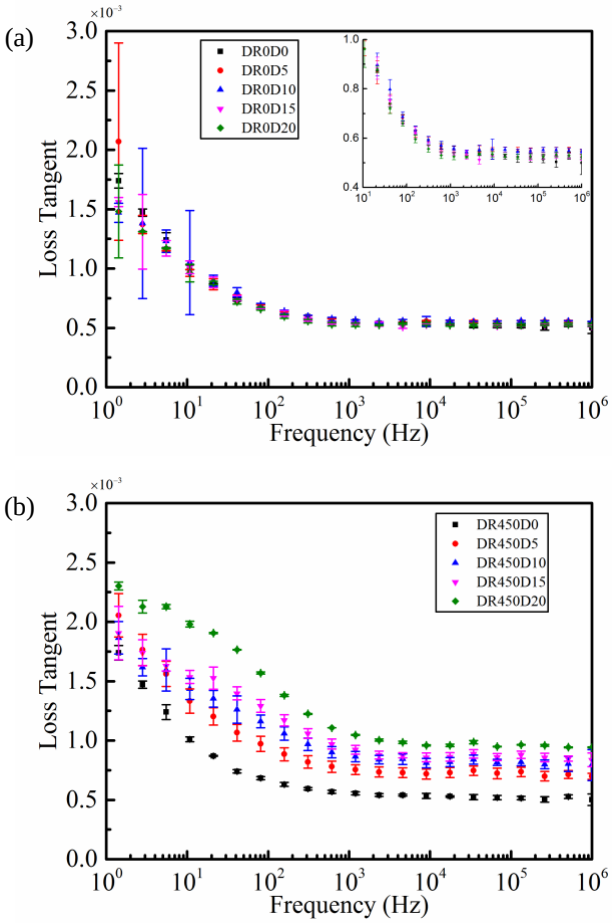

Fig. 2. Dielectric loss tangent as a function of frequency for samples aged for up to 20 days (a) thermally and (b) with simultaneous thermal and gamma radiation at dose rate 450 Gy/h. Inset in (a) shows expanded view.

To facilitate direct comparison between the dielectric response of samples aged with and without gamma radiation, dielectric loss tangent measured at frequencies 100 Hz and 1 MHz is plotted in Figure 3 as a function of exposure time, for samples aged without and with gamma radiation at dose rate 450 Gy/h. Loss tangent is a sensitive function of aging time for samples exposed to gamma radiation, but not for samples aged only thermally. Similar results have been obtained for samples aged at 90 and 115 °C [2].

2) Effect of dose rate

The dielectric loss tangent of XLPE samples aged at different dose rates is presented in Figure 4, for five and 20 days of exposure. As depicted in Figure 4, the dielectric loss tangent increases with the dose rate of gamma radiation for almost the entire frequency range from 1 Hz to 1 MHz. Dielectric loss tangent measured at frequencies 100 Hz and 1 MHz is plotted in Figure 5 as a function of dose rate. The dielectric loss tangent increases almost linearly with dose rate for the range of values studied here, and the slope is higher for 20 than for five days of exposure.

B. Dielectric Breakdown Strength

Figure 6 shows the Weibull plot for dielectric breakdown of XLPE samples aged without and with exposure to gamma radiation. For samples aged thermally only, the breakdown strength shifts to lower values when compared with the response of the pristine sample, Figure 6(a).

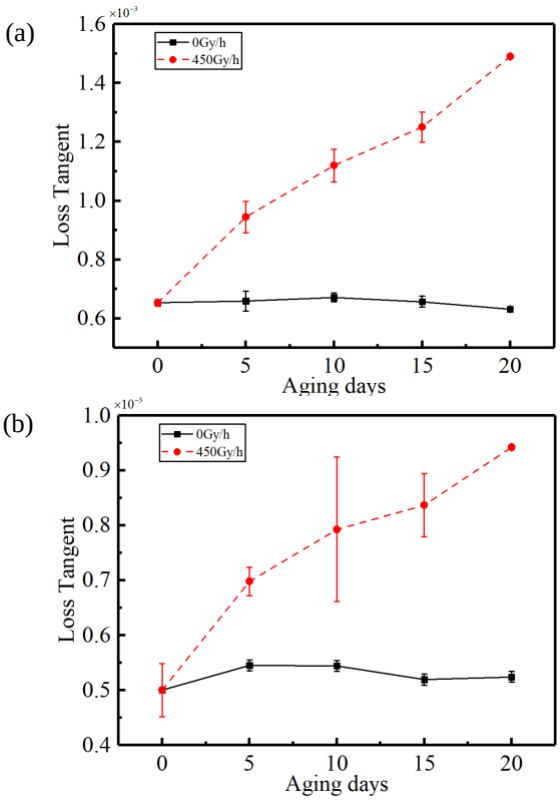

Fig. 3. Dielectric loss tangent as a function of aging time for samples aged thermally and with simultaneous thermal and gamma radiation at dose rate 450 Gy/h, for (a) 100 Hz and (b) 1 MHz.

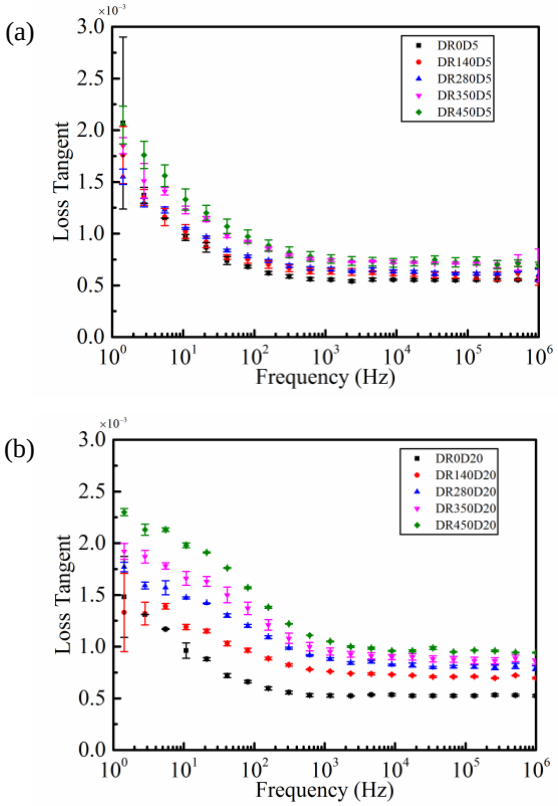

Fig. 4. Dielectric loss tangent as a function of frequency for samples aged with simultaneous thermal and gamma radiation at various dose rates for (a) five and (b) 20 days.

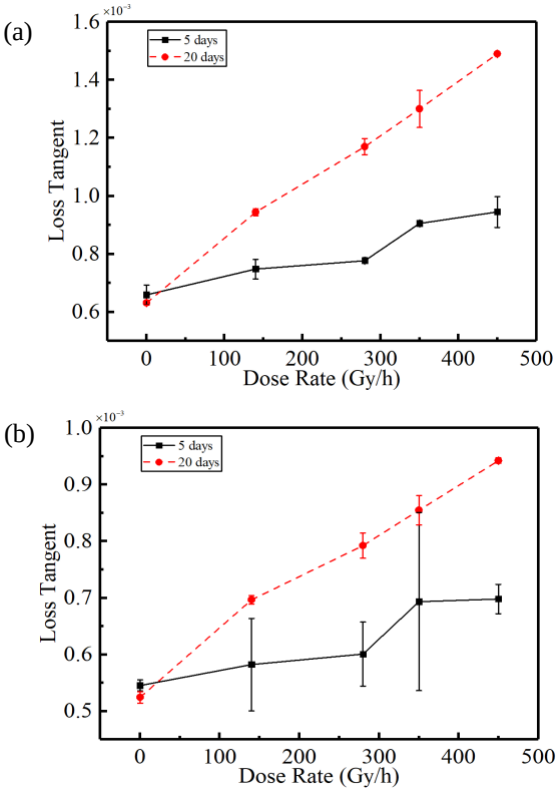

Fig. 5. Dielectric loss tangent as a function of dose rate for samples aged for five and 20 days, for (a) 100 Hz and (b) 1 MHz.

This shows that the dielectric breakdown strength of the material is reduced after thermal exposure at 60 ºC. In the presence of gamma radiation, Figures 6(b) and (c), the observations suggest an initial increase of the dielectric breakdown strength i.e. for five and 10 days of aging at 450 Gy/h, Figure 6(b), or for dose rate 140 Gy/h, Figure 6(c), with a subsequent weakening as aging continues at this temperature, for 15 and 20 days of aging at 450 Gy/h, Figure 6(b), and for dose rate 450 Gy/h, Figure 6(c). Taking the average of these data for each sample confirms the observations from the Weibull plots, that the average breakdown strength decreases for thermal aging in the absence of gamma radiation even after only five days of aging. In the presence of gamma radiation, however, the average breakdown strength increases slightly for five and 10 days of aging at 450 Gy/h before subsequently declining as the aging time increases further. Similarly, the average breakdown strength increases for 20 days aging at low dose rate (140 Gy/h) before declining as the dose rate increases to 280 Gy/h and higher.

The observed early increase of breakdown strength may be caused by oxidation of the carbon bond in XLPE. The oxygen atoms have higher electronegativity, which can prevent the electrons from accelerating, increasing the breakdown strength slightly. When aging time or dose rate increase, however, chain scission starts to dominate and increases the free volume inside the sample, which in turn increases the acceleration path of electrons and subsequently decreases the breakdown strength of the material [3]. Further, free radicals generated in the process of chain scission also serve to decrease the dielectric breakdown strength [2].

Although these two factors (oxidation and chain scission) have some effect, the observed shifts in the position of the Weibull plot are relatively small when compared with the range of data values measured for each sample. The reason may be that the maximum aging time (20 days) studied here is too small to allow such factors to take their effect.

V. Conclusion

Instrumentation cable used in NPPs may be exposed to gamma irradiation and/or elevated temperature during service. Long-term operation of NPPs presents the need to understand changes in cable insulation materials, such as commonly used XLPE, that may affect cable function. Dielectric loss tangent was demonstrated, here, to be a promising indicator of XLPE aging due to gamma radiation exposure, showing significant increase while dielectric breakdown strength declined. Dielectric loss tangent measured at 1 MHz increased by 140 % for the most heavily aged sample studied here, whereas mean dielectric breakdown strength declined by 8 % for the same sample. This suggests that dielectric loss tangent is a sensitive indicator of material changes associated with decline in insulation function.

References

[1] N. Bowler, and S. Liu, "Aging mechanisms and monitoring of cable polymers," Int. J. Prognostics and Health Management., vol. 6, pp. 1-12, 2015.

[2] S. Liu, "Composition identification, aging mechanisms and nondestructive aging indicator of commercial filled cross-linked polyethylene (XLPE) cable insulation materials," PhD thesis, Dept. Mater. Sci. Engng., Iowa State Univ., Ames, IA, 2017.

[3] L. A. Dissado and J. C. Fothergill, *Electrical Degradation and Breakdown in Polymers* (IEE Materials and Devices Series 9). London, United Kingdom: Peter Peregrinus (IEE), 1992.

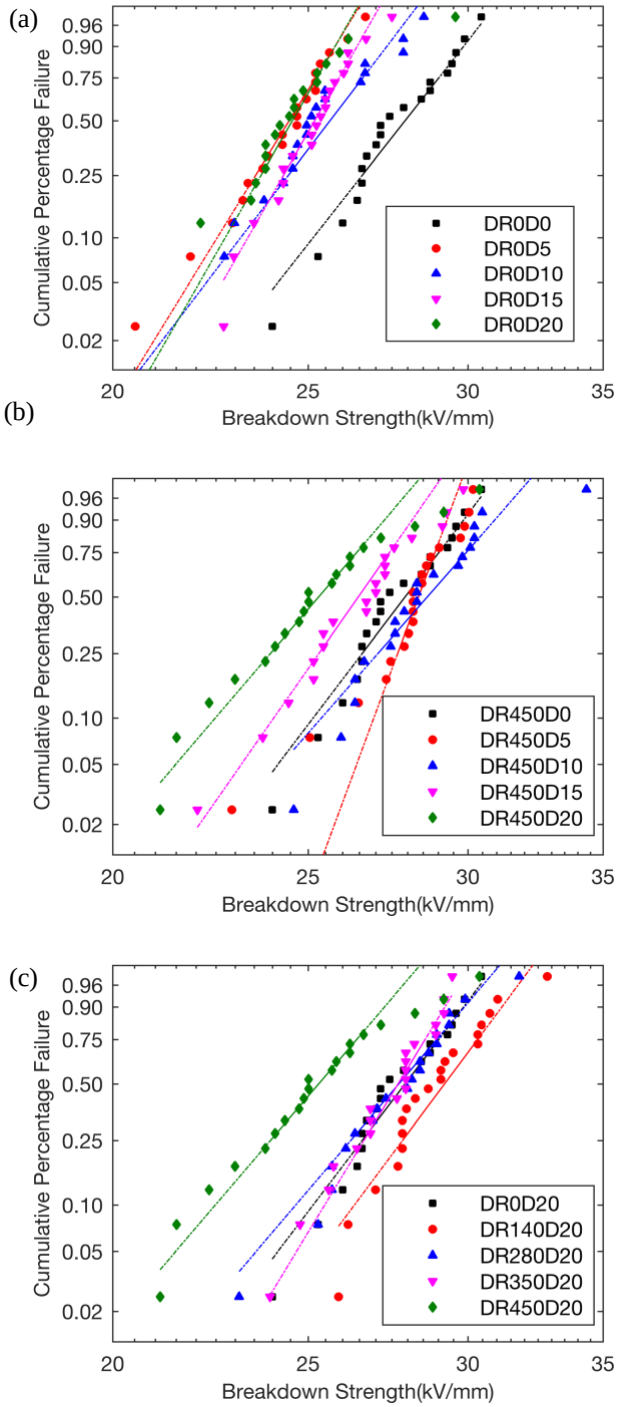

Fig. 6. Dielectric breakdown strength for samples aged (a) thermally, (b) with simultaneous thermal and gamma radiation for different numbers of days at dose rate 450 Gy/h, and (c) for samples aged with simultaneous thermal and gamma radiation at various dose rates for 20 days.